AD A104772

LEVEL

DTIC
S
SEP 2 9 1981
H

FROM—
THE UNIVERSITY, UNIVERSITY PARK, NOTTINGHAM
NG7 2RD

Grant No. AFOSR-78-3717

CORROSION CHEMISTRY IN INHIBITED HDA

Final Scientific Report
30th November 1980

REPRODUCIBLE COPY

AD A104772

REPORT DOCUMENTATION PAGE	READ INSTRUCTIONS BEFORE COMPLETING FORM	
1. Report Number AFRPL-TR-81-81	2. Govt Accession No. AD A104 772	3. Recipient's Catalog Number
4. Title (and Subtitle) CORROSION CHEMISTRY IN INHIBITED HDA.		5. Type of Report & Period Covered Final Scientific 30 Sept. 1978 - 30 Sept. 1980
		6. Performing Org. Report Number
7. Author(s) Norman/Logan Michael F.A./Dove		8. Contract or Grant Number AFOSR-78-3717
9. Performing Organization Name and Address Department of Inorganic Chemistry, University of Nottingham, Nottingham, NG7 2RD. U.K.		10. Program Element, Project, Task Area & Work Unit Numbers 62302F 3058/10ED
11. Controlling Office Name and Address Air Force Rocket Propulsion Laboratory/ LKCP Edwards AFB, CA 93523		12. Report Date 30 November 1980
		13. Number of Pages 337
14. Monitoring Agency Name and Address European Office of Aerospace Research and Development/LNC Box 14, FPO New York, 09510.		15.
16. & 17. Distribution Statement Approved for public release; distribution unlimited.		
18. Supplementary Notes		
19. Key Words HNO_3-N_2O_4 Mixtures. HDA. Spectroscopy. Electrochemistry. Aluminium and Stainless Steel Corrosion. Cathodic Protection. Inhibitors. Corrosion Products. Metal Fluorides. Metal Difluorophosphates.		

20. Abstract The constitution of uninhibited HDA has been examined by Raman spectroscopy. The behaviour of known and potential inhibitors of aluminium and stainless steel corrosion in HDA has been studied by n.m.r. spectroscopy, electrochemical techniques, X-ray photoelectron spectroscopy and scanning electron microscopy. The mechanism of inhibition has been established for both aluminium and stainless steel. For stainless steel, inhibition occurs because of plugging of anodic sites, which prevents growth and breakdown of the existing chromium (III) oxide film. Film breakdown on stainless steel in uninhibited HDA has been shown to be due to the transpassive effect. For aluminium, inhibition is also due to a film plugging mechanism which appears to inhibit pitting. Long term storage of Standard HDA in aluminium generates a very thick film on the metal surface which appears to contain α-AlF_3 and α-$AlF_3.H_2O$ as principal components. A number of new metal difluorophosphates has been synthesised, some of which are likely to resemble authentic Modified HDA corrosion products, and reactions of a range of metal fluorides with difluorophosphoric acid have been examined.

FORM 1473

AFRPL-TR-81-81

Grant Number: AFOSR-78-3717

CORROSION CHEMISTRY IN INHIBITED HDA

Norman Logan
Michael F.A. Dove
Department of Chemistry
University of Nottingham
University Park,
Nottingham, NG7 2RD
United Kingdom

30th November 1980

Final Scientific Report, 30th September 1978-30th September 1980

Approved for public release; distribution unlimited

Prepared for:

AFRPL/LKCP EDWARDS AFB, California 93523

and

EUROPEAN OFFICE OF AEROSPACE RESEARCH AND DEVELOPMENT
London, England.

81 9 29 036

ASSEMBLY/COLLATING GUIDE - 1-274

CLASSIFICATION	TRIM SIZE	JOB NUMBER
Unclassified	8 1/2 x 11	

TITLE Corrosion Chemistry in Inhibited HDA

ORDERING ACTIVITY	TOTAL COPIES

ADDITIONAL INSTRUCTIONS (X = Blank Page) (F=Fold Out)

TOTAL PAGES

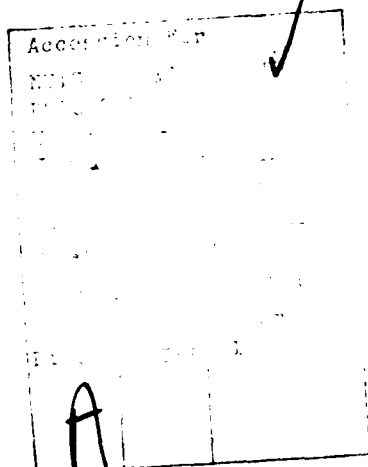| CIRCLE FOLIO	PAGE NUMBER OR OTHER IDENTIFICATION	LINE	HALF-TONE	CIRCLE FOLIO	PAGE NUMBER OR OTHER IDENTIFICATION	LINE	HALF-TONE
1	Cover			66	28		
2	Notice			67	29		
3	Form 1473			68	30		
4	X BLANK			69	31		
5	i			70	Fig 3.5		
6	ii			71	32		
7	iii			72	33		
8	iv			73	34		
9	v			74	Fig 3.6		
10	vi			75	35		
11	vii			76	36		
12	viii			77	37		
13	ix			78	Fig 3.7		
14	x			79	38		
15	xi			80	39		
16	xii			81	40		
17	xiii			82	41		
18	xiv			83	Fig 3.8		
19	xv			84	42		
20	xvi			85	43		
21	xvii			86	44		
22	xviii			87	45		
23	xix			88	Fig 3.9		
24	xx			89	46		
25	xxi			90	Fig 3.10		
26	xxii			91	Fig 3.11		
27	xxiii			92	47		
28	xxiv			93	48		
29	xxv			94	Fig 4.1		
30	xxvi			95	49		
31	xxvii			96	50		
32	X BLANK			97	Fig 4.2		
33	1			98	51		
34	2			99	Fig 4.3a		
35	3			100	Fig 4.3b		
36	4			101	52		
37	5			102	53		
38	6			103	Fig 4.4		
39	7			104	Fig 4.5		
40	8			105	54		
41	9			106	55		
42	10			107	56		
43	Fig 2.1			108	Fig 4.6		
44	11			109	57		
45	12			110	Fig 4.7		
46	13			111	58		
47	14			112	Fig 4.8		
48	Fig 2.2			113	59		
49	Fig 2.3			114	60		
50	15			115	61		
51	Fig 2.4			116	62		
52	16			117	63		
53	17			118	64		
54	18			119	Fig 4.9		
55	19			120	Fig 4.10		
56	20			121	65		
57	21			122	Fig 4.11		
58	22			123	66		
59	23			124	Fig 4.12		
60	24			125	Fig 4.13		
61	25			126	67		
62	Fig 3.1 + Fig 3.2			127	68		
63	26			128	Fig 4.14		
64	Fig 3.3 + Fig 3.4			129	Fig 4.15		
65	27			130	69		

CIRCLE FOLIO	PAGE NUMBER OR OTHER IDENTIFICATION	LINE	HALF-TONE	CIRCLE FOLIO	PAGE NUMBER OR OTHER IDENTIFICATION	LINE	HALF-TONE
131	Fig 4.16			203	Fig 5.4 + 5.5		
132	Fig 4.17			204	Fig 5.6		
133	70			205	108		
134	71			206	109		
135	Fig 4.18			207	Fig 5.7		
136	Fig 4.19			208	110		
137	Fig 4.20 + 4.21			209	Fig 5.8		
138	72			210	111		
139	73			211	112		
140	74			212	113		
141	75			213	Fig 5.9		
142	Fig 4.22 + 4.23			214	Fig 5.10		
143	76			215	114		
144	Fig 4.24 + 4.25			216	Fig 5.11		
145	77			217	Fig 5.12		
146	Fig 4.26			218	115		
147	Fig 4.27			219	Fig 5.13		
148	78			220	Fig 5.14		
149	Fig 4.28			221	116		
150	79			222	Fig 5.15		
151	80			223	Fig 5.16		
152	81			224	117		
153	82			225	118		
154	83			226	Fig 5.17		
155	84			227	" 5.18		
156	85			228	" 5.19		
157	Fig 4.29 + 4.30			229	" 5.20		
158	Fig 4.31			230	" 5.21		
159	Fig 4.32			231	119		
160	86			232	120		
161	87			233	121		
162	88			234	122		
163	Fig 4.33 + 4.34			235	123		
164	Fig 4.35 + 4.36			236	124		
165	89			237	Fig 5.22		
166	90			238	125		
167	Fig 4.37 + 4.38			239	Fig 5.23		
168	Fig 4.39 + 4.40			240	" 5.24		
169	91			241	126		
170	Fig 4.41 + 4.42			242	Fig 5.25		
171	Fig 4.43 + 4.44			243	127		
172	92			244	128		
173	Fig 4.45 + 4.46			245	Fig 5.26		
174	Fig 4.47			246	129		
175	Fig 4.48 + 4.49			247	Fig 5.27		
176	93			248	130		
177	Fig 4.50 + 4.51			249	131		
178	94			250	132		
179	Fig 4.52 + 4.53 + 4.54			251	133		
180	Fig 4.55 + 4.56			252	134		
181	95			253	135		
182	Fig 4.57 + 4.58			254	136		
183	Fig 4.59 + 4.60			255	137		
184	Fig 4.61 + 4.62			256	138		
185	Fig 4.63 + 4.64			257	139		
186	96			258	140		
187	97			259	141		
188	98			260	142		
189	Fig 4.65 + 4.66			261	Fig 6.1		
190	Fig 4.67 + 4.68			262	143		
191	99			263	144		
192	100			264	145		
193	101			265	146		
194	102			266	147		
195	Fig 5.1			267	148		
196	103			268	149		
197	Fig 5.2			269	150		
198	104			270	151		
199	105			271	152		
200	106			272	153		
201	Fig 5.3			273	154		
202	107			274	155		

ASSEMBLY/COLLATING GUIDE - 1-274		CLASSIFICATION	TRIM SIZE	JOB NUMBER
TITLE		ORDERING ACTIVITY		TOTAL COPIES
ADDITIONAL INSTRUCTIONS (X = Blank Page) (F=Fold Out)				TOTAL PAGES

CIRCLE FOLIO	PAGE NUMBER OR OTHER IDENTIFICATION	LINE	HALF-TONE	CIRCLE FOLIO	PAGE NUMBER OR OTHER IDENTIFICATION	LINE	HALF-TONE
1	Fig 6.2			66			
2	156			67			
3	Fig 6.3			68			
4	157			69			
5	Fig 6.4			70			
6	158			71			
7	Fig 6.5			72			
8	159			73			
9	Fig. 6.6			74			
10	160			75			
11	Fig 6.7			76			
12	161			77			
13	Fig 6.8			78			
14	162			79			
15	163			80			
16	Fig 6.9			81			
17	164			82			
18	Fig 6.10			83			
19	165			84			
20	166			85			
21	Fig 6.11			86			
22	167			87			
23	168			88			
24	169			89			
25	170			90			
26	171			91			
27	172			92			
28	Fig 6.12			93			
29	173			94			
30	174			95			
31	Fig 6.13			96			
32	175			97			
33	176			98			
34	177			99			
35	Fig 6.14			100			
36	178			101			
37	179			102			
38	180			103			
39	181			104			
40	182			105			
41	183			106			
42	184			107			
43	185			108			
44	186			109			
45	187			110			
46	188			111			
47	189			112			
48	Fig. 7.1			113			
49	191			114			
50	192			115			
51	193			116			
52	194			117			
53	195			118			
54	196			119			
55	197			120			
56	198			121			
57	199			122			
58	200			123			
59	Fig A1			124			
60	201			125			
61	Fig B1			126			
62	202			127			
63	203			128			
64				129			
65				130			

FINAL SCIENTIFIC REPORT, 1980

TABLE OF CONTENTS

(iii)

(iv)

LIST OF FIGURES

(x)

(xvii)

(xviii)

LIST OF MICROGRAPHS

LIST OF CHARTS

LIST OF ABBREVIATIONS AND SYMBOLS

Reagents and Materials

HDA (UHDA)	High Density Acid, i.e., 56 Wt % HNO_3 + 44 Wt % N_2O_4
Standard HDA (SHDA)	HDA containing <u>ca</u> 0.6 Wt % HF
Modified HDA (MHDA)	HDA containing <u>ca</u> 0.6 Wt % PF_5
Inhibisol	1,1,1-Trichloroethane
Methcol	97% ethanol + 3% methanol
Nujol	Liquid Paraffin
Kel-F	Chlorotrifluoroethylene Polymer
FEP	Fluorinated Ethylene Propylene copolymer
Teflon PTFE	Polytetrafluoroethylene
Teflon PFA	Perfluoroalkoxy fluorocarbon resin

Spectroscopy

IR (ir)	Infra-red
UV	Ultra-violet
N.m.r.	Nuclear magnetic resonance
XPS (ESCA)	X-ray photoelectron spectroscopy
SEM	Scanning electron microscopy
EDAX	Energy dispersive analysis by X-rays

Spectra

Infrared

ν_s Symmetric stretching   s   strong

ν_a Antisymmetric stretching   m   medium

δ_s Symmetric deformation   w   weak

δ_a Antisymmetric deformation br broad

ρ_r Rocking deformation   sp   sharp

ρ_w Wagging deformation   sh   shoulder

π Out-of-plane deformation v   very

N.m.r. δ Chemical shift (ppm)

                                     J Coupling constant (Hz)

XPS   BE Binding energy

Units   Å angstrom = 10^{-10} m

                                     eV electron volt = 1.6022×10^{-19} J

                                     psig pound per square inch guage = 6.89476×10^{3} N m^{-2}

                                   Torr (1 mm Hg) = 10135/760 Pa

Symbol

                            [ ] Concentration

ELECTROCHEMISTRY

a	Activity (thermodynamic concentration)
b	Tafel coefficient, Tafel slope
c or [ ]	Concentration
E	Electrode potential
$E^{\ominus}$	Standard electrode potential
E_F	Flade (passivation) potential
E_{rp}	Electrode rest potential (the measured potential relative to the reference electrode at zero overpotential)
F	Faraday's constant (96.5 kJ V^{-1} mol^{-1})
i	Current density
i_{corr}	The corrosion current
i_o	Exchange current density
R	Gas constant (8.31 J mol^{-1} K^{-1})
S/V	Surface area to Volume ratio / cm^{-1}
z	Total number of electrons transferred in the electrochemical reaction
β	Symmetry factor ($\sim$ 0.5)
$\dfrac{\Delta E}{\Delta i}$	Polarisation resistance
$\Delta G_M^{\ominus}$	The chemical free energy change accompanying the deposition of 1 mole of M^{2+} on to the metal surface

η Overpotential

Subscripts a and c denote anodic and cathodic respectively.

Arrows denote the direction of current flow.

Equations

The Nernst Equation

The general form is

$$E = E^{\ominus} + \frac{RT}{zF} \ln \frac{a_{oxidized\ species}}{a_{reduced\ species}}$$

(As a first approximation activities may be replaced by

concentrations)

The Stern-Geary Equation

$$\frac{\Delta E}{\Delta I} = \frac{1}{2.303} \cdot \frac{b_a |b_c|}{b_a + |b_c|} \cdot \frac{1}{i_{corr}} \qquad (|\ | \text{ represents modulus})$$

The Tafel Equations

$$b_a = 2.303\ RT/\beta zF$$

$$b_c = -\,2.303\ RT/(1-\beta)zF$$

(Where β is usually assumed to be 0.5).

1. INTRODUCTION

The research on corrosion chemistry in inhibited HDA (commencing 30 September 1978), described here and in a previous report[1.1] continues earlier USAF-sponsored investigations[1.2] of the fundamental chemistry of the corrosion of stainless steels and aluminium alloys in contact with the rocket propellant oxidiser High Density Acid (HDA), i.e., inhibited high density red fuming nitric acid containing approximately 55% HNO_3, 44% N_2O_4, 0.4% H_2O and 0.6% HF ("Standard" HDA) or PF_5 ("Modified" HDA).

The study of this topic in the Department of Inorganic Chemistry at the University of Nottingham, UK, has aimed to provide as comprehensive a coverage as possible of all relevant aspects, using an extensive range of chemical and physical techniques. It has sought to elucidate the mode of action of HF and PF_5 as corrosion inhibitors in this medium, to identify the conditions under which they can exert their optimum inhibitory effect and to produce an understanding of rocket engine problems, such as filter-clogging and valve and pump malfunctions in order that such undesirable phenomena , related to the presence of precipitated or colloidal corrosion products, can be predicted and eliminated.

The earlier report[1.1] provided a detailed account of the work carried out during the first year of the programme (30 September 1978 to 30 September 1979) and is a substantial

document, which it would be superfluous to duplicate here, although its status as an interim statement was stressed. It includes studies of corrosion rates, the application of X-ray photoelectron spectroscopy and related techniques to metal surfaces, authentic corrosion products, synthetic corrosion products, spectroscopy of solution species and the preliminary results of a new electrochemical approach to the interaction of metals with HDA.

This Final Scientific Report presents the detailed results (including those outlined in Progress Reports[1,3]) obtained in the second year of the grant period (1 October 1979 to 30 September 1980). It will be noted that major emphasis has been placed on electrochemical studies of the corrosion in HNO_3/N_2O_4 mixtures of 6061-T6 aluminium alloy (Section 4) and 321 and 347 stainless steels (Section 5) supported by non-electrochemical corrosion rate measurements (aluminium) and X-ray photoelectron spectroscopy of metal surfaces (aluminium and stainless steel). The extensive electrochemical work has included exploratory experiments involving inhibitors other than HF or PF_5, as reported in Section 4 (H_3PO_4 and P_4O_{10}) and Section 5 (H_2SO_4 and As_2O_3). Furthermore, it was necessary to precede these Sections on the application of electrochemistry to metal and propellant oxidiser systems of interest by an account of the theory and practice of electrochemistry in nitric acid-dinitrogen tetroxide mixtures, and this constitutes Section 3.

Due attention to other aspects of the work has, however, been maintained during the second year, and since spectroscopic monitoring of solution species is of obvious relevance to electrochemical studies, detailed spectroscopic results (Section 2) again precede the electrochemistry, as in the interim report.[1.1] Since HPO_2F_2 is a principal product of the reaction of PF_5 with HDA[1.2] and is likely to generate insoluble metal salts in the medium, its stability in HDA as a function of temperature, concentration and time is clearly of considerable interest. In this connection, a preliminary ^{19}F n.m.r. study as a function of temperature and time has already been reported[1.1] and the results of a more detailed ^{31}P n.m.r. investigation of this type are now presented here (Section 2.2).

The presence of H_2PO_3F, albeit as a minor solvolysis product of PF_5 in HDA, renders a study of its own solvolysis and metal corrosion inhibiting characteristics of relevance. Unfortunately, it has not yet proved possible to obtain this acid in pure form, however, the aluminium corrosion inhibitory characteristics of a sample obtained in our laboratories were considered to be worthy of electrochemical and XPS studies and these are reported in Section 4. Since this sample was not suitable for n.m.r. investigation, it was considered that Na_2PO_3F, which is obtainable commercially in a satisfactory degree of purity, should permit the evaluation of monofluorophosphate solvolytic stability in red-fuming nitric

acid media. Na_2PO_3F is, unfortunately, of low solubility in HDA but it was considered that its behaviour in 100% HNO_3 was of sufficient relevance to justify the ^{31}P n.m.r. investigation also reported in Section 2.2.

The possibility of P_4O_{10} acting as an efficient corrosion inhibitor at modest concentrations in HDA was also deemed worthy of examination since it should exert the dual effect of dehydrating HDA (known to be beneficial) giving rise, via its solvolysis, to phosphorus (V) oxo-acids which are proven inhibitors of metal corrosion. It was considered that a study of this kind should also give more information on the solvolytic characteristics of HDA and both electrochemical (Section 4.2) and n.m.r. (Section 2.2) studies of this system were therefore undertaken.

Concerning the n.m.r. studies, it must be noted that the ^{19}F probe was damaged in May 1980 and work on phosphorus-fluorine species, during the final four months of the grant period, was restricted to the recording of ^{31}P resonances.

An authentic corrosion product has now been isolated from the experiment involving Standard HDA in an aluminium tank (see Section 4.1) and its characterisation is described in Section 6. Experiments involving synthetic corrosion products have been continued and are also reported in Section 6 where studies relevant to both Standard and Modified HDA are described.

So far as the Appendices are concerned, only new experimental details, not already given in the earlier report[1.1], are to be found here.

Reference 1.1 and the present report must therefore be taken together in order to obtain a full account of the 24 month research programme, carried out under Grant No. AFOSR-78-3717, however in Section 7 we have attempted to draw together some overall conclusions and recommendations arising from the work described in both reports.

Personnel

Formally, the research work under Grant Number AFOSR-78-3717 has been carried out by Dr John W Bailey, Dr Barrie Mellor and Mr Clifford LE Cole, with Dr N Logan (Principal Investigator) and Dr. MFA Dove as Joint Research Supervisors, and Professor CC Addison as Consultant. In fact, this area of research work has become so closely identified with the interests of the Inorganic Chemistry Department at Nottingham that two other research workers, Mr Richard C Hibbert and Mr Paul G Cheeseman have also made very substantial contributions. Both these workers were supported financially by grants from the UK Science Research Council but their work has been included in the present report, together with some experimental contributions made by Mr A Aziz M Moharum, who is supported financially by the University of Khartoum, Sudan. The names of these research workers are given alongside the headings to the Sections of the Report describing experiments for which they were responsible.

The advice and assistance of Dr Peter J Boden,
Senior Lecturer in Metallurgy and Materials Science,
University of Nottingham,is once again gratefully
acknowledged.

2. SPECTROSCOPIC STUDIES

2.1 The Raman Spectrum of Uninhibited HDA (A.A.M. Moharum)

Both Raman[2.1] and infrared[2.2] spectroscopic investigations of the ionisation of N_2O_4 in HNO_3 were reported by DJ Millen and his co-workers. The Raman spectrum[2.1] of an 8.7wt % (0.95 molal) solution of N_2O_4 in HNO_3 gave bands attributable to HNO_3, NO^+ and NO_3^- but not N_2O_4 or NO_2 and it was concluded that the concentration of non-ionised N_2O_4 is small in this solution. In the publication on infrared spectroscopy,[2.2] the spectrum of a 7 molal (64.4wt %) solution of N_2O_4 in HNO_3 is illustrated and includes absorption bands assignable to undissociated N_2O_4 (although not NO_2), however, the authors appear to have overlooked the fact that at ambient temperature HNO_3-N_2O_4 is a two phase liquid system[2.3] over the region 6-10 molal.

We have now recorded the Raman spectrum of uninhibited HDA (which is 4.8 molal in N_2O_4) and the band positions, polarisation properties, qualitative intensities and assignments to species are presented in Table 2.1.

The bands assigned to N_2O_4 have the frequencies and polarisation properties expected[2.4] for five of the six Raman-active fundamental vibrations of the usual planar $(D_{2h})O_2NNO_2$ form of the molecule. The sixth N_2O_4 band will be obscured by that at 678 cm^{-1}, assigned to HNO_3, which should be depolarised if assignable to N_2O_4. No indication of bands at ca. 750, 1318 and 1618 cm^{-1}, expected for NO_2[2.4], was observed. The rather low frequency of the band assigned to the NO^+ ion we attribute to interaction with

Table 2.1

The Raman Spectrum of UHDA

Band/cm^{-1}		Intensity	Assignment
265.5	(pol)	vvs	N_2O_4
484	(depol?)	vw,b	N_2O_4
626	(depol)	w	HNO_3?
678	(pol)	m	HNO_3
714	(pol)	w	NO_3^-
809	(pol)	m,vsp	N_2O_4
934	(pol)	s	HNO_3
1042	(pol)	s	NO_3^-
1265	(depol)	w,sh	?
1306	(pol)	s	HNO_3
1381	(pol)	m,sp	N_2O_4, NO_3^-
1450	(depol?)	vw,b	HNO_3?
1676	(depol)	w	HNO_3
1717	(depol)	vw	N_2O_4
2235	(pol)	vs	NO^+
2374	(?)	vw	?
2545	(?)	vvw	?
3390		m,vb	HNO_3
3553		w,sh,b	?

pol	polarised	w	weak	v	very
depol	depolarised	m	medium	sp	sharp
		s	strong	sh	shoulder

the NO_3^- ion (rather than NO_2, as originally proposed by Millen[2.1], although later retracted[2.2]), a situation somewhat analogous to that encountered for the species $NO_3^-.3NO^{+}$[2.5] . These results indicate that the heterolytic equilibrium

$$N_2O_4 \rightleftharpoons NO^+ + NO_3^-$$
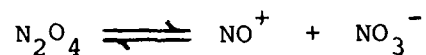
occurs in uninhibited HDA, whereas, in spite of the rather intense colour of the liquid, the homolytic dissociation $N_2O_4 \rightleftharpoons 2NO_2$ is much less significant.

2.2 N.m.r. Spectroscopic Studies (J.W. Bailey, R.C. Hibbert, A.A.M. Moharum)

(a) Introduction

The use of the Bruker n.m.r. spectrometer (^{19}F studies at 235 MHz and ^{31}P at 101 MHz) for investigating solution species in HDA has enabled us to extend our studies to include more dilute solutions. This has been especially important for MHDA studies involving [31]P n.m.r. spectroscopy, although the length of time needed to collect sufficient data for the most dilute solutions (0.4 wt% PF_5) is still considerable (0.5-1 hour). The importance of [31]P n.m.r. spectroscopy is that it permits us to look for orthophosphoric acid, H_3PO_4, a species which must be considered as a possible active corrosion inhibitor in these media. It must also be recognised that wherever possible both nuclei (P and F) should be investigated for every sample of MHDA since the concentration of both H_3PO_4 and HF ought to be determined in order to obtain a complete picture of the solute species present in this acid system.

(b) Solutions of HF in Nitric Acid and in HDA

This solute produces a single, somewhat broadened resonance whose chemical shift is markedly dependent on the sample temperature. A set of typical spectra are depicted in Figure 2.1. The chemical shift, - 175 ppm in HNO_3 and -159 ppm in SHDA

at 293 K is in the region which corresponds to hydrogen bonded HF molecules rather than to HF_2^- or even F^-.[2.6]

(c) Solutions of PF_5 in HDA

A mixture containing 6 wt% PF_5 in HDA was prepared and the n.m.r. of the supernatant solution, above the slurry of crystals of (presumably) $NOPF_6$ and NO_2PF_6, investigated at regular intervals, 5 hours, 33 days, 59 days and 83 days, by [19]F n.m.r.

TEMP/°K

223

233

243

253

263

273

283

293

Chem. shift from CF_4Cl/ppm

0

−100

−200
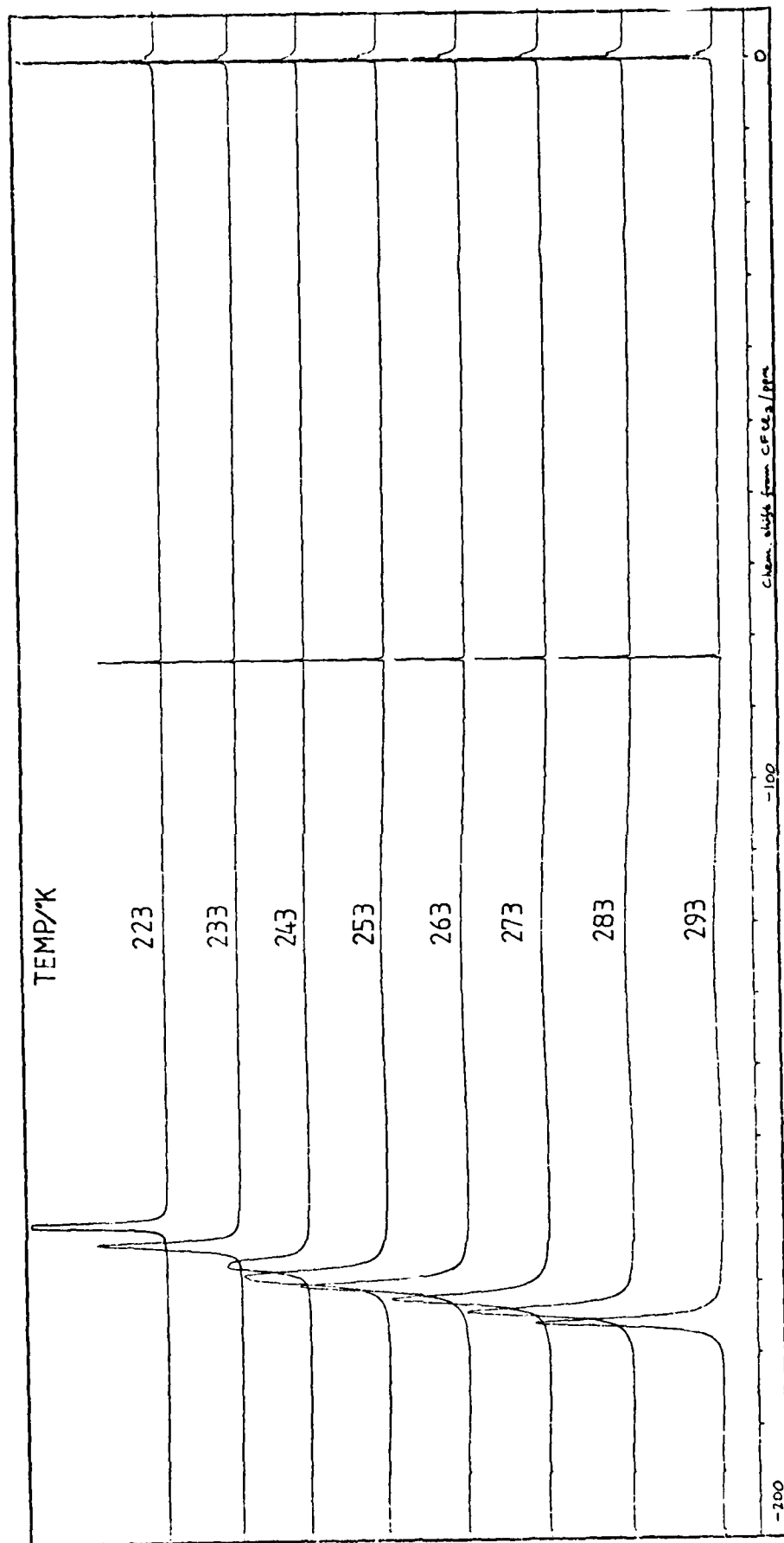
FIG 2·1 ^{19}F nmr Spectrum of 5.8% HF in HNO_3

spectroscopy. The presence of HF in the solution was not sought for at first; however, the scan range was increased and HF was readily detected after 33 days and thereafter. The chemical shifts and coupling constants for this solution and also a 0.7 wt% PF_5 solution are listed in Table 2.2.

The relative concentrations of the various F-containing solutes in the more concentrated solution, buffered with PF_6^- by the presence of undissolved salts, are summarised in Table 2.3. Although the presence of H_3PO_4 in this sample cannot be inferred from these results its concentration was shown at a later stage to be too small to be detected by ^{31}P n.m.r. The data in Table 2.3 are molar concentrations relative to $\left[PF_6^-\right]$ which has been set arbitrarily to 100. A significant feature of these results is that the rate of hydrolysis of HPO_2F_2 at room temperature is concurrent with that of PF_6^-, although it is less rapid; in other words, all three fluoro-phosphate species can co-exist in this system. It must also be remembered that the observed concentrations of HF in the solution are unlikely to be reliable, since it is known that HF (as well as N_2O_4 and H_2O) diffuses through the walls of the fluoroplastic n.m.r. tubes. Clearer evidence for this is provided below.

A more dilute (and completely homogeneous) solution, 0.7 wt% PF_5 in HDA, was also prepared at the same time and investigated in the same way. Here it is possible to discuss the results in a more quantitative manner by assuming that the P:F ratio remained at 1:5 in the sample. The results are

Table 2.2

^{19}F Chemical Shifts (at 293K) and F-F Coupling Constants of the Fluorine - Containing Species Detected in 0.7 wt % and 6 wt % PF_5 in HDA

Species	Chemical Shift/ppm (relative to $CFCl_3$ in $CDCl_3$ external standard) *		Coupling Constant/Hz	
	0.7 wt % PF_5	6 wt % PF_5	0.7 wt % PF_5	6 wt % PF_5
PF_6^-	-70.6	-70.5	708.0	708.0
HPO_2F_2	-84.0	-84.1	982.7	982.7
H_2PO_3F	-76.6	-76.6	952.3	952.3
HF	-157.0	-157.8	-	-

* Negative chemical shift indicates shift to lower resonance frequency, i.e., shift to higher field.

Table 2.3

Variation with Time of the Concentration of Fluoride-Containing Species
Detected by ^{19}F n.m.r. in the Supernatant Solution of 6 wt % PF_5 in HDA

Species	Sample			
	5 hours	33 days	59 days	83 days
PF_6^-	100	100	100	100
HPO_2F_2	51.5	109	116	172
H_2PO_3F	0.8	1.9	2.1	4.4
HF	(not sought)	78	69	216

depicted in Figure 2.2 which shows the variation with time

of the relative concentrations of PF_6^-, HPO_2F_2 H_2PO_3F

and HF as determined from the integrations of the n.m.r.

spectra and Figure 2.3 shows the spectrum obtained after

83 days. The very broad signal centred at <u>ca</u> - 122 ppm

is attributed to the fluoroplastic sample tubing. ^{31}P studies

have since confirmed that the concentrations of H_3PO_4 are

negligible and hence it is possible to calculate the HF

concentration. The results of this check are included in

Figure 2.2 and show good agreement at 33 days: however,

the calculated values after 59 days and 83 days are greater

than the observed values and therefore we conclude that HF

is lost from the samples through the walls of the fluoroplastic

tube. The following trends are apparent: that $\left[HPO_2F_2\right]$

increases in a regular manner as $\left[PF_6^-\right]$ diminishes whereas

$\left[H_2PO_3F\right]$ remains relatively static. If the relative concentra-

tions of PF_6^- and HPO_2F_2 are put into the equation

$$HNO_3 + PF_6^- + 2H_2O \rightleftharpoons HPO_2F_2 + 4HF + NO_3^-$$

an equilibrium constant can be written as

$$K_1 = \frac{\left[HPO_2F_2\right]\left[HF\right]^4}{\left[PF_6^-\right]}$$

if we ignore the species derived from the solvent whose

activities or concentrations will remain effectively constant.

The value of K_1 determined from the integrations of the n.m.r.

spectra recorded at 33, 59 and 83 days (see e.g., Fig. 2.3) was

found to be reasonably constant ($\pm$ 13%).

Fig. 2·2 Variation with Time of species Detected by ^{19}F nmr of MHDA

Moles product per 100 moles fluorophosphates

100

50

Legend:
- ⬡ PF_6^-
- ⊡ HPO_2F_2
- △ H_2PO_3F
- ⊙ HF observed ÷ 2
- ⊗ HF calculated ÷ 2

20   40   60   80
Time/days
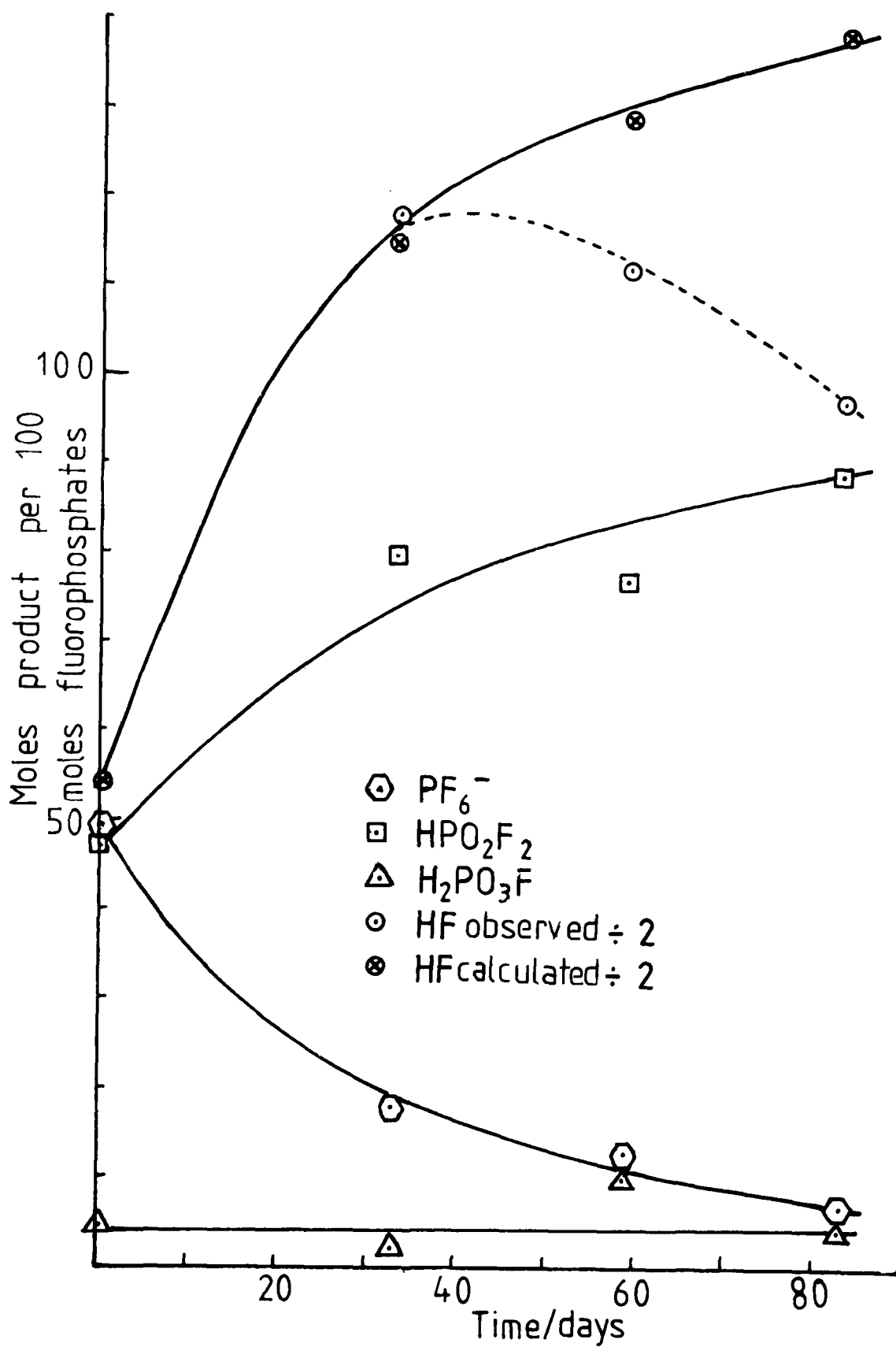
Fig. 2.3 ^{19}F NMR Spectrum of 0.7 wt% PF_5 in HDA, after 83 days
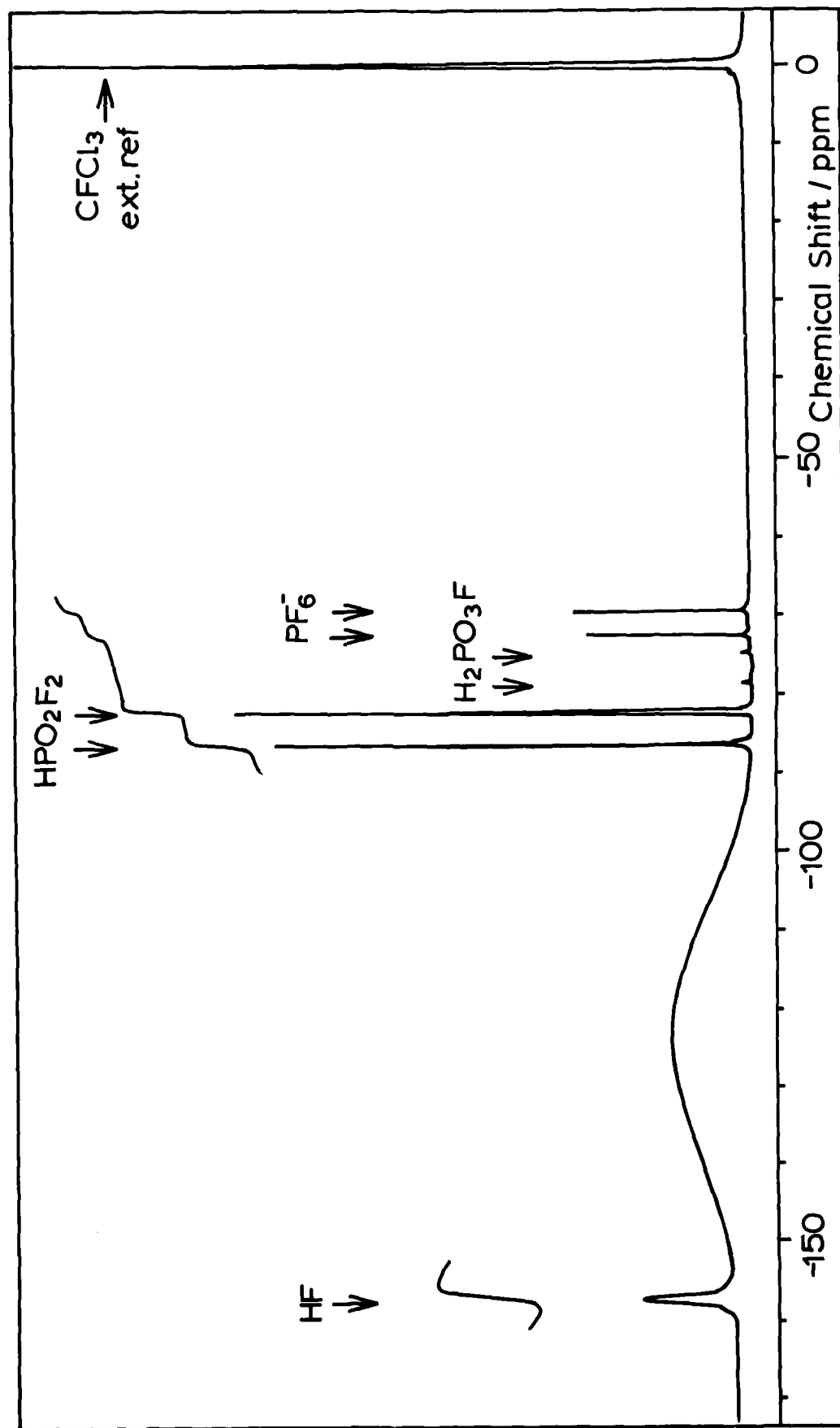
In a separate series of experiments the effect of added water or N_2O_5 on the hydrolysis of PF_5 by HDA has been studied. Samples containing 0.7 wt % PF_5 were prepared from:-

(i)   HDA as prepared in our laboratories[2.7] (water content ca 0.25 wt%).

(ii) "Wet" HDA, i.e., (i) with 0.2 wt % H_2O added to give a total water content of ca 0.45 wt % and,

(iii) "Dried" HDA, i.e., (i) with sufficient N_2O_5 added to remove 0.25 wt% water, and therefore, with a water content of ca 0.0 wt%.

The ^{31}P n.m.r. spectra of these solutions, taken approximately 1 hour after preparation, are shown in Fig. 2.4. The signal-to-noise ratio is greatly improved in comparison to the ^{31}P spectra reported earlier.[2.7] Table 2.4 presents the PF_6^-: HPO_2F_2 mole ratios determined from the integrals recorded for the spectra shown in Fig. 2.4.

From these experiments, drying the HDA with N_2O_5 is seen to have no effect on the ratio of the species produced initially, which suggests that the observed products arise primarily from reaction of PF_5 with HDA, (rather than with H_2O). However, added H_2O can then bring about further "hydrolysis". On the other hand, the addition of 0.2 wt % H_2O has a large effect on the PF_6^-:HPO_2F_2 ratio.

(d) Solutions of HPO_2F_2 in HDA

Solutions of 27.0, 10.6 and 4.1 wt % HPO_2F_2 in HDA were prepared in fluoroplastic tubes, together with a solution of 19.0 wt % HPO_2F_2 in HNO_3 for comparison. ^{31}P Nmr spectra have been recorded after various time intervals, the tubes being

Fig 24 ^{31}P nmr Spectra of 0.7 wt% PF_5 in HDA
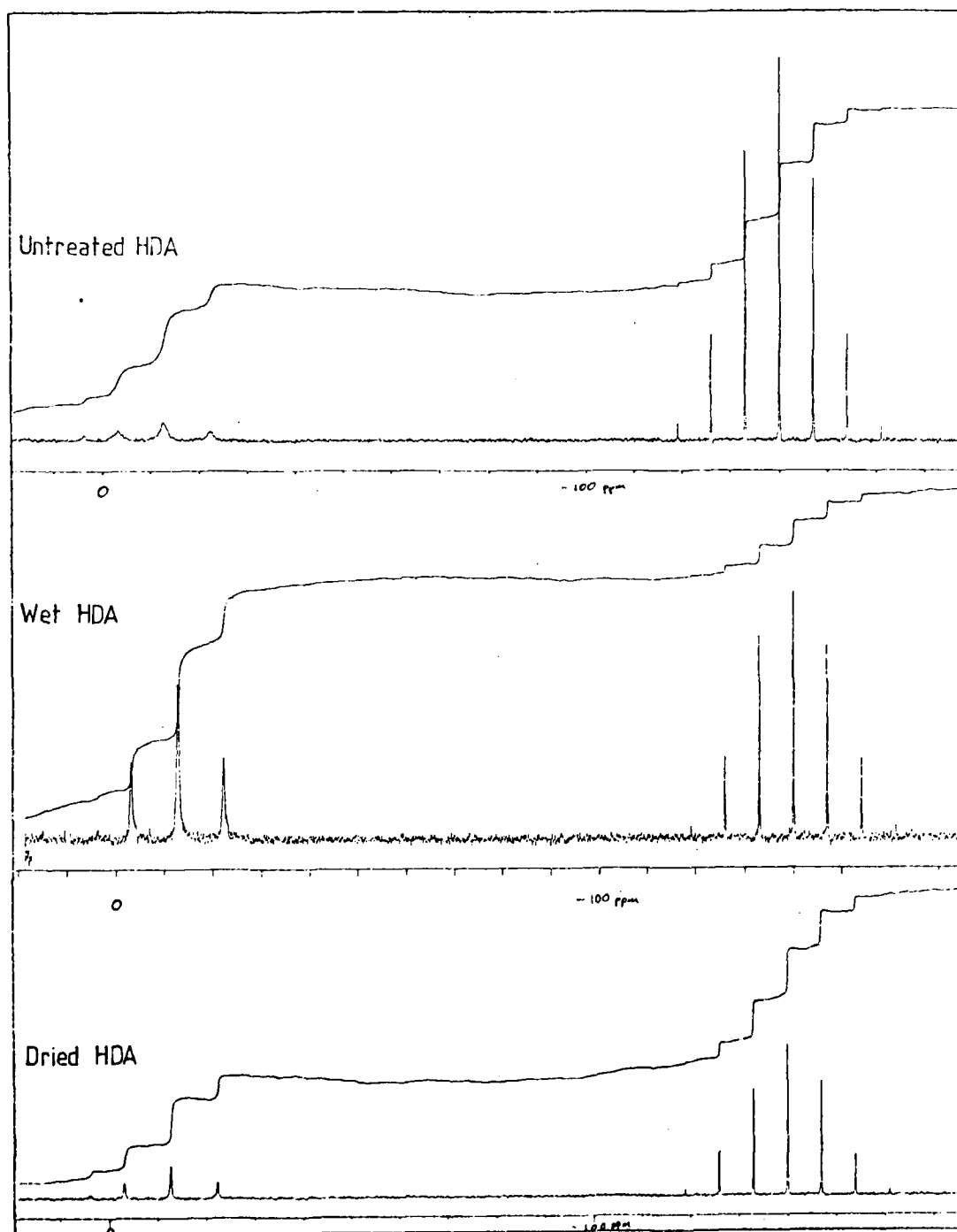
Table 2.4

Mole Ratios of Species Detected by ^{31}P n.m.r. in HDA Containing 0.7 wt % PF_5 with Variations in Water Content

System	Mole Ratio Found PF_6^- : HPO_2F_2		Estimated Values for % H_2O	molality H_2O	H_2O:PF_5 mole ratio
Preliminary Results (Refs 2.7 & 2.8)	3	: 1			
(i) HDA as prepared.	1.63	: 1	0.25	0.140	2.5
(ii) "Wet" HDA ((i) + 0.2 wt % H_2O)	0.47	: 1	0.45	0.250	4.5
(iii) "Dried" HDA ((i) - 0.25 wt % H_2O)	1.60	: 1	"0"	"0"	"0"

stored in a freezer at $-20^\circ C$ during these intervals. The results are summarised in Table 2.5.

H_2PO_3F is rapidly produced by the solvolysis of HPO_2F_2 in HDA (in contradiction to earlier results[2.7]). The H_2PO_3F:HPO_2F_2 ratio increases as the initial concentration of HPO_2F_2 is decreased, i.e., as the H_2O:HPO_2F_2 ratio in HDA is increased. The hydrolysis of HPO_2F_2 to H_2PO_3F in HNO_3 is much more extensive. The H_2PO_3F concentration increased with time in both the 4.1 wt % HPO_2F_2 solution in HDA and the 19.0 wt % HPO_2F_2 solution in HNO_3.

This work confirms the impression gained from studies of solutions of PF_5 in HDA, namely that HPO_2F_2 undergoes hydrolysis in HDA to give H_2PO_3F. Resonances arising from very small amounts of H_3PO_4 and PF_6^- have also been observed in the ^{31}P nmr spectra but concentrations have so far been too small to be measurable.

(e) Solutions of Na_2PO_3F in HNO_3

A solution of 4.3 wt % Na_2PO_3F in HNO_3 was prepared in a fluoroplastic tube. Na_2PO_3F was used in place of H_2PO_3F since attempts to prepare the latter in pure form have proved unsuccessful. HNO_3 was used because the solubility of Na_2PO_3F in HDA is quite small. ^{31}P nmr spectra were obtained after 7 days and 23 days. Hydrolysis of monofluoro-phosphate to orthophosphate was rapid. The ratio of

Table 2.5

Mole Ratios of Species Present in Solutions of HPO_2F_2, Determined by ^{31}P N.m.r. Spectroscopy

System[†]	Mole Ratios								
	HF^*	:	H_3PO_4	:	H_2PO_3F	:	HPO_2F_2	:	PF_6^-
27.0 wt % HPO_2F_2 HDA 1 day	1	:	O	:	1	:	46.3	:	O
10.6 wt % HPO_2F_2 HDA 1 day	1	:	v. small	:	1	:	34.6	:	O
4.1 wt % HPO_2F_2 HDA 19 days	1	:	v. small	:	1	:	29.7	:	-
44 days	1	:	v. small	:	1	:	18.6	:	v. small
19.0 wt % HPO_2F_2 HNO_3 1 day	1	:	v. small	:	1	:	6.5	:	-
30 days	1	:	v. small	:	1	:	4.6	:	-
55 days	1	:	0.014	:	1	:	4.4	:	v. small

[†] Concentrations of ca 1 wt % phosphorus (e.g., 3-4 wt % P_4O_{10} or HPO_2F_2), or greater, were chosen for practical reasons; the time to accumulate ^{31}P spectra at concentrations below ca 1 wt % phosphorus was prohibitively long.

* HF determined by difference.

- Species not sought in ^{31}P spectrum.

monofluorophosphate:orthophosphate after 1 week was
2.7:1 and after 23 days 2.3:1.

(f) Solutions of P_4O_{10} in HDA and HNO_3

A study of the behaviour of P_4O_{10} in HDA and HNO_3 has
been made using ^{31}P n.m.r. spectroscopy.

Solutions of 1.3, 4.2 and 5.5 wt % P_4O_{10} in HDA and
4.3 wt % P_4O_{10} in HNO_3 were prepared, and the effect of
addition of 3.7 wt % water to a solution of 3.3 wt % P_4O_{10}
in HDA, using a calibrated micropipette was also examined.
The results are summarised in Table 2.6 and show that HNO_3
is a more effective hydrolysing medium than HDA. In
particular HNO_3 is far more effective in breaking down the
cyclic and higher polyphosphorus (V) acids than is HDA.

(g) The Composition of MHDA After Storage in Al Vessel (see also Section
4.1)

A sample was removed from the aluminium tank used in
the long term corrosion rate experiment involving MHDA after
the experiment had proceeded for 700 days at room temperature.
The identity and mole ratio of phosphorus species present in
the HDA was examined by ^{31}P n.m.r. spectroscopy. The results
are summarised in Table 2.7.

A signal due to PF_6^- was observed but no integral could be
obtained for it because the concentration of PF_6^- was
exceedingly small. The disappearance of PF_6^- can be

- 19 -

Table 2.6

Phosphorus (V) Oxo-Acids Detected by ^{31}P N.m.r. Spectroscopy in solutions of P_4O_{10} in HDA, Expressed as Percentage of Total Phosphorus Content

System	H_3PO_4	$H_4P_2O_7$	Cyclic and Higher Polyphosphorus (V) Acids
1.3 wt % P_4O_{10} in HDA			
7 days	21.0	26.2	52.8
4.2 wt % P_4O_{10} in HDA			
17 days	6.89	26.72	66.37
48 days	11.35	41.21	47.44
73 days	13.09	47.97	38.93
5.5 wt % P_4O_{10} in HDA			
17 days	3.46	28.59	67.95
48 days	7.41	41.75	50.84
73 days	13.02	55.17	31.80
4.3 wt % P_4O_{10} in HNO_3			
24 days	34.64	55.56	9.80
40 days	41.09	53.58	5.33
72 days	45.17	49.17	4.90
3.3 wt % P_4O_{10} 3.7 wt % added H_2O in HDA 7 days	Only distinct peak in spectrum	–	very broad peak

Table 2.7 Mole Ratio of Phosphorus Species in MHDA After 700 Days Storage in Al Vessel At Room Temperature

Species	PF_6^-	HPO_2F_2	H_2PO_3F	H_3PO_4
Mole Ratio	O	18.3	7.3	1

$$HPO_2F_2:H_2PO_3F \quad \text{Ratio} \quad 2.5:1$$

attributed to removal of F^- (HF) by Al leading to a shift

in the equilibrium (1) (see above) which will result in the

ultimate removal of PF_6^-.

H_2PO_3F and H_3PO_4 are present but HPO_2F_2 is still the

major constituent after 700 days.

3. ELECTROCHEMISTRY OF METALS IN NITRIC ACID - DINITROGEN TETROXIDE MIXTURES: THEORY AND PRACTICE (P.G. Cheeseman)

3.1 Theoretical Considerations

(a) Origin of Electrode Potential[3.1, 3.2]

A metal electrode placed in a solution of its ions will have an electrochemical potential associated with it. This potential arises from the electrode holding on its surface a negative charge adjacent to a plane of positively charged ions. E_M the single potential of the M/M^{2+} (e.g., Fe/Fe^{2+}) electrode on the standard hydrogen scale is given by equation (3.1)

$$E_M^{\ominus} = - \Delta G_M^{\ominus} / zF \qquad (3.1)$$

where $\Delta G_M^{\ominus}$ is the chemical free energy change accompanying the deposition of 1 mole of M^{2+} onto the metal surface.

On the basis of this equation, it is possible to construct a series of single potentials for various metals. This series is, of course, the well-known electrochemical series and standard single electrode potentials relate to a metal ion concentration of 1 molar. When metals are immersed in 4 wt % aqueous sodium chloride solution (approximating to the composition of sea water) each takes up a rest potential (corrosion potential) in this medium (which is also influenced by the presence of surface films) and the resulting series of potentials is known as the galvanic series.

-23-

The rest (corrosion) potentials of a number of metals
have now been examined in 100% nitric acid and a similar
series has been established. Table 3.1 shows this 'nitric
acid series' for the metals investigated so far. Rhodium
and platinum are the only noble metals; gold and stainless
steel corrode noticably despite their noble/passive character
and copper and mercury both react with notable vigour.
Aluminium and calcium, despite their expected base metal
character, do not react to any noticable extent. Aluminium
is protected by insoluble Al_2O_3 and calcium by its nitrate
which is also highly insoluble in nitric acid. Platinum and
rhodium are assigned a potential of zero because they act
as inert electrodes and take up the potential of the
$NO_2^+/\frac{1}{2}N_2O_4$ redox couple in nitric acid. It should be noted
that the reduced species in this couple was referred to as
NO_2 in ref. 1.1, but further experimental work in our
laboratories has established that $\frac{1}{2}N_2O_4$ is the correct
designation.

(b) Polarisation Theory[3.1,3.3]

If a metal electrode in solution is at equilibrium,
i.e., not corroding, then the rate of dissolution as
solvated ions is equal to the rate of deposition. Since charged
entities are involved, two equal and opposite electric
currents can be considered: $(\vec{i}=\overleftarrow{i}=i_o)$, the magnitude of which
defines the exchange current density, i_o.

- 24 -

Table 3.1

"Nitric Acid Series" of Electrochemical Potentials

Metal	Potential/V	
Rhodium, Platinum	0.00	
Stainless Steel, Gold	-0.15	±0.05
Mercury	-0.70	±0.1
Aluminium, Calcium	-0.75	±0.05
Copper, Silver	-0.90	±0.05
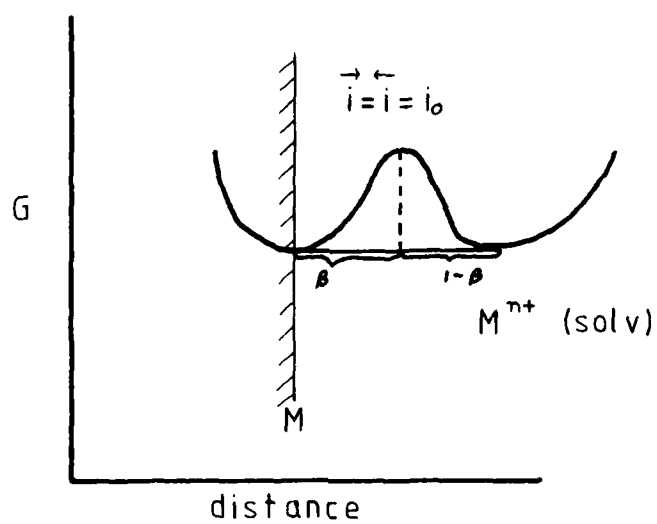
Figure 3·1   Energy — distance profile for
metal in solution at equilibrium.
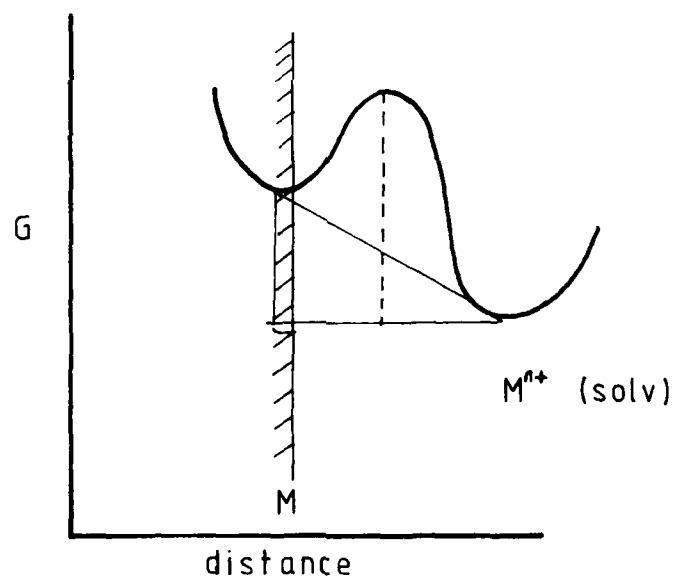
Figure 3·2   Energy — distance profile
for metal in anodically polarised
state.

The equilibrium at the electrode surface can be considered in an energy-distance profile. (Fig. 3.1). If an external e.m.f. is imposed on the electrode (i.e., the electrode is polarised) then the energy-distance profile is changed to that represented in Figure 3.2. The potential applied to the electrode, the overpotential η, is related to the net current that flows by the Tafel equations.

$$\eta_a = b_a \ \log \ (i_a/i_o) \qquad\qquad (3.2)$$

$$\eta_c = b_c \ \log \ (i_c/i_o) \qquad\qquad (3.3)$$

a = anode, c = cathode

where b_a and b_c are the Tafel constants, such that

$$b_a = 2.3 \ RT/\beta z F) \qquad\qquad (3.4)$$

$$b_c = -2.3 \ RT/(1-\beta)zF \qquad\qquad (3.5)$$

The Tafel relations were initially determined experimentally but theoretical derivations have now been made. β is a symmetry factor (normally between 0.4 and 0.6)and is as shown in Figure 3.1.

Figure 3.3 shows the Tafel plots for a metal/metal ion system under cathodic and anodic activation polarisation. If the metal is corroding in the medium, metal dissolution is the anodic reaction and there must be a corresponding cathodic reaction taking place elsewhere on the metal surface. Figure 3.3 shows the Tafel slopes for the hypothetical cathodic couple Z^+/Z on the metal and the (coordinates of the)

Figure 3·3   Theoretical   Tafel plots for metal M
and reactant couple Z/Z^+
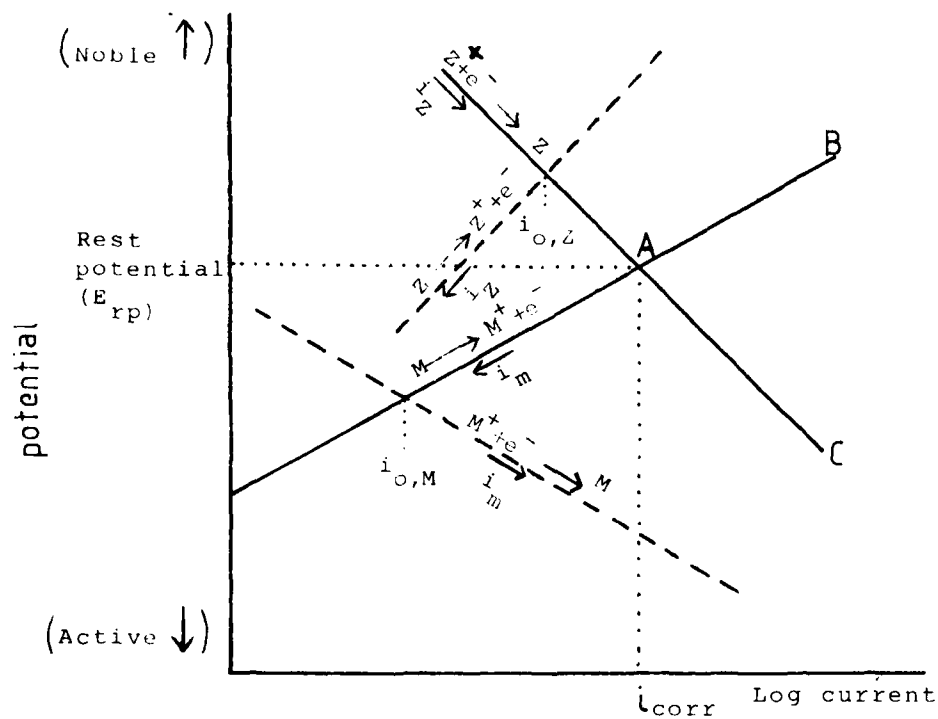
Figure 3·4 Experimental   Polarisation
Curves
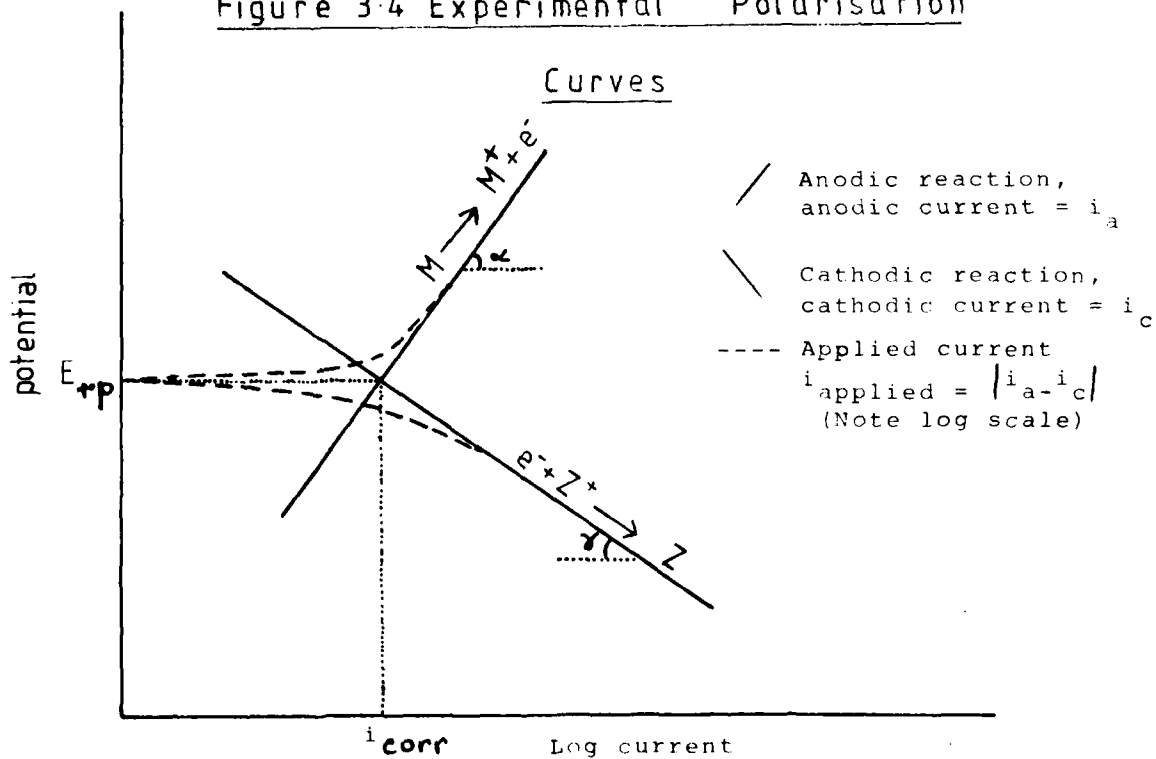
intersection between the reduction of z^+ and metal

dissolution curves corresponds to the corrosion potential,

E_{rp}, and the corrosion current, i_{corr}, for this particular

system.

It should be noted that not only is the corrosion rate

very dependent on the individual single potentials but also

on the exchange current density for the z^+/z couple on the

metal surface. Table 3.2 lists the approximate exchange current

densities for the hydrogen couple $H^+/\frac{1}{2}H_2$, on metals at 25^OC.

Values for the $NO_2^+/\frac{1}{2}N_2O_4$ couple are not available but will

be similar, at least in relative degree, to those for the

hydrogen couple. This follows because the oxidized and reduced

species are of similar character for each reaction, i.e.,

z^+ and $Z\cdot$, a positive ion and an adsorbed radical (which dimerizes).

(c) <u>Estimation of Corrosion Rate</u>[3.1, 3.3]

In polarisation experiments the straight lines (AB, AC

in Figure 3.3) for anodic and cathodic polarisation are not

obtained. The current measured, i_{app}, is not equal to

i_a or i_c but rather is the difference between them at any

particular overpotential. Hence for cathodic polarisation,

$i_{app} = i_c - i_a$ and the curve only becomes a straight line

when $i_c >> i_a$, i.e., When the overpotential, η_c, is sufficiently

high (>80mV). This explains the curvature observed in

experimentally determined Tafel plots (e.g., Figure 3.4).

By extrapolating the straight portion, the corrosion current

may be estimated from the intersection between the straight

line portion and the line $y = t_{rp}$ It is usual to extrapolate

Table 3.2

Approximate Exchange Current Densities for the Hydrogen Couple
$H^+/\frac{1}{2}H_2$ on Metals at 25 $^{\circ}$C

Metal	Exchange Current Density A cm^{-2}
Pb, Hg	10^{-13}
Zn	10^{-11}
Sn, Al, Be	10^{-10}
Ni, Ag, Cu, Cd	10^{-7}
Fe, Au, Mo	10^{-6}
W, Co, Ta	10^{-5}
Pd, Rh	10^{-4}
Pt	10^{-2}

only the cathodic portion as the cathodic area can reasonably be equated with the measured electrode area. The anodic reaction occurs only at particularly susceptible sites such as grain boundaries, dislocations, kink sites etc., it is therefore not valid to equate the anodic area with the total area.

This method of determining the corrosion current, the "Tafel Extrapolation Method", involves a considerable change in the equilibrium of the metal. A superior method which involves far smaller overpotentials is the "Polarisation Resistance Method".

This method allows determination of the instantaneous corrosion rate of a component. If a small potential increment $\pm\Delta E$ is applied to the freely-corroding component, the current through the external circuit used to apply the potential increases from zero to $\pm\Delta i$. This current increment is directly proportional to the corrosion rate. It is simple to show that if the corrosion process is under activation control as opposed to diffusion control, the corrosion current, i_{corr}, is related to Δi by the equation:

$$i_{corr} = \frac{1}{2.3} \cdot \frac{b_a |b_c|}{b_a + |b_c|} \cdot \frac{1}{(\Delta E/\Delta i)} \qquad (3.7)$$

$\Delta E/\Delta i$ has units of ohms and is called the polarisation resistance. Experimentally $\Delta E/\Delta i$ is obtained by plotting ΔE vs Δi not exceeding 10mV overpotential. This method has largely been employed in $HNO_3-N_2O_4$ solutions for determination of aluminium corrosion rates (Section 4.2) and is a rapid

and facile method which involves little disturbance to the metal itself. This method is employed quite widely in real corroding situations on industrial plants where the corrosion rate of tanks and pipes is periodically monitored using this technique.

(d) Passivation[3.1, 3.2, 3.4]

Many metals owe their corrosion resistance to the formation of a passive film on the surface. Gold, the most noble of metals has been observed to corrode in pure nitric acid and it is therefore concluded that no metal will be corrosion resistant in pure nitric acid, unless a passive film is present.

In aqueous solutions, water molecules in the Helmholtz double layer at the metal surface tend to orientate with their oxygen atoms towards the metal. Oxidation then occurs because the metal can conduct electrons away to a suitable electron sink. The oxidation is an electrochemical reaction, and there will therefore exist a standard single potential for oxide formation given by:

$$E^{\ominus}_{M/M_xO_y} = \frac{G^{\ominus}_{M_xO_y} - yG^{\ominus}_{H_2O}}{2yF} \qquad (3.8)$$

for the reaction.

$$xM + yH_2O \rightarrow M_xO_y + 2yH^+ + 2ye^- \qquad (3.9)$$
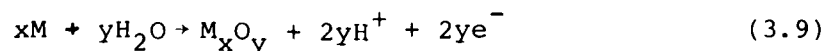
When the potential of a metal is raised above its reversible

value, $E_M^{\ominus}$, the electrode will obey the Tafel equation,
however, when the potential exceeds that corresponding to
equilibrium between metal and one of its oxides ($E_{M/M_xO_y}^{\ominus}$)
we should expect the appropriate oxide or hydroxide to form
on the metal surface; such a film retards the dissolution
process and the metal can then be regarded as passive. The
E vs log i curve shown in Figure 3.5, demonstrates the effect
of passivation on the shape of the anodic polarisation curve.
The potential at which minimum current density is reached
is called the Flade potential, E_f, and is in practice 0.3 to
1.0 V above $E_{M/M_xO_y}^{\ominus}$, the theoretical potential for oxide
formation. Passivation is also characterised by a critical
current density, i_{crit}, the maximum current that passes
before passivation begins.

Once passivation has occurred, the anode current density
at any potential becomes limited by one of three consecutive
processes:

    (i)   Movement of cations from metal into the oxide.

    (ii) Movement of cations and or oxide anions through
          the oxide.

    (iii) Movement of cations from oxide into solution.

The rate of each of these processes is dependent on the
electric field in the region   where it occurs, which in
turn, is a function of the total potential drop between the
metal and the solution. If the anode potential is raised
from one steady value to another, the current density increases
momentarily and falls as the film thickens by ion transport.

Figure 3·5
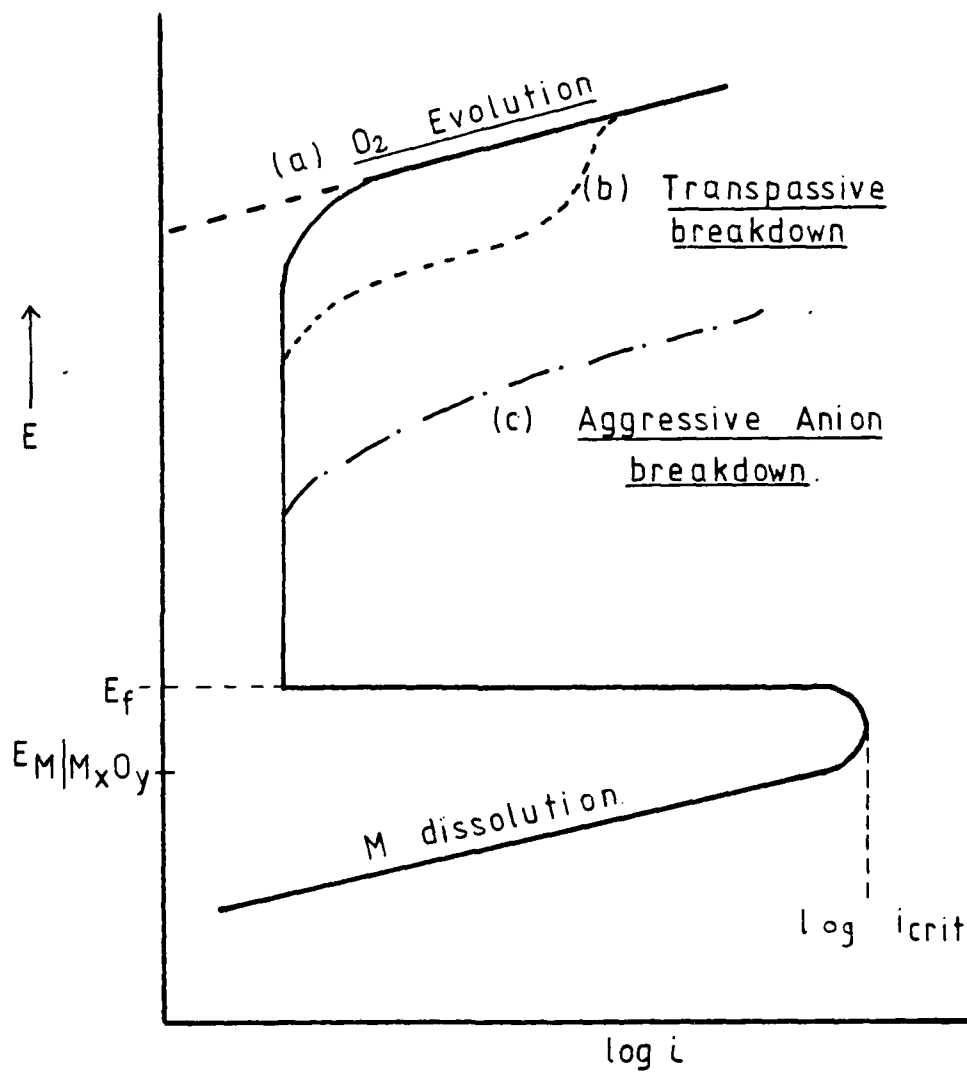
Passivation and breakdown of a metal film by anodic polarisation.

Metals can be taken into the passive region by
application of an external potential, but in an oxidising
environment many metals self-passivate. Titanium and
chromium have sufficiently low Flade potentials to pass-
ivate in non-oxidising acids, but Iron will only exhibit
self-passivity if the acid is sufficiently oxidising.
70% nitric acid is a good example of such an acid, for
which the passivating effect is now well documented.

Potential-time curves are a method of monitoring
the passivation process. The potential of a passivated
electrode in any solution is related to the degree of
passivation ; this in turn depends upon where the cathodic
curve cuts the anodic passivation curve. However, when a
piece of metal is first immersed in an oxidising environment
the air-formed film on its surface is very thin and oxide
film build-up must occur for the film to attain its
equilibrium thickness. This process is monitored using
potential-time curves; the more noble the potential, the
greater is the degree of passivation. In ideal cases, because
the film thickens logarithmically with time, and because of
the relation between electric field and film thickness, a plot
of potential vs log t is a straight line. In some cases the
film existing on the metal surface prior to immersion is of a
different nature to that which will be finally present. In
such a situation the primary film may be stripped off by
the oxidising medium as a first stage. This process is
indicated in potential-time observations by a decrease of
potential corresponding to film stripping.

(e)   Film Breakdown[3.1, 3.2, 3.4]

Above E_f the metal is passivated and the current will remain low unless at higher potentials other anodic reactions are possible, or due to aggressive anions in solution the film suffers breakdown. Oxygen evolution shown in Figure 3.5, curve (a), is a common reaction in aqueous systems but such a reaction is unlikely in HNO_3-N_2O_4 solutions, although NO_2/N_2O_4 oxidation to NO_2^+ must be possible. Oxygen evolution in aqueous systems occurs according to the following equation:

$$4OH^- \rightleftharpoons O_2 + 2H_2O + 4e^- \qquad (3.10)$$
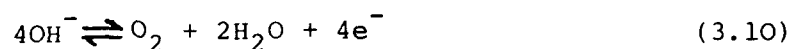
The existence and effect of dissolved oxygen in nitric acid media is not known but in the light of the fact that dissolved oxygen aids the passivation reaction in aqueous solution, a parallel investigation in nitric acid would be most informative.

Transpassivity, shown by (b) in Figure 3.5, is a further reaction which may occur; this is dealt with in more detail in Section 5, and essentially involves the anodic oxidation of the scarcely soluble passivating oxide to a soluble substance. This phenomenon is only prevalant for metals which are able to form oxides of high oxidation state, e.g., vanadium (V_2O_5), chromium (CrO_3) and manganese (Mn_2O_7).

Transpassivation is rarely a cause of film breakdown because of the highly oxidising conditions needed to form the high oxidation state oxide. However, the breakdown

- 33 -

of films by anions is a very general process which may
occur at quite low anode potentials. Curve (c) of Figure 3.5
represents just such a situation. The chloride ion is the
anion normally associated with such a breakdown and is
particularly aggressive in contact with stainless steels,
but bromide, chlorate, sulphate and phosphate all may act
in this way in certain circumstances. The pits formed at
the points of breakdown are not crystallographic, but are
approximately hemispherical and are electro-brightened.
They tend to form preferentially at the grain boundaries
of the metal and at other locations where the oxide film
is, presumably,   imperfect.

The mechanism of breakdown by anions is still
rather unclear and many theories have been advanced. It
seems that the breakdown process occurs in two distinct
stages; anion adsorption at the metal surface involving
displacement of solvent molecules at the surface, followed
by anion penetration of the film leading to its subsequent
breakdown. T P Hoar[3.5] devised a diagram to summarise the
effect of anion concentration and electrode potential on
the passivated state of the metal surface. Figure 3.6,
shows such a diagram, the numbered regions of which
correspond to the following:-

(1)   Anodic passivation.

(1')   Activation - the Flade reaction.

(2)   Activation by adding "corrosive" anion.

(3)   Transpassivation by raising anode potential.

(3')   Re-passivation by lowering anode potential.

(4)   Breakdown, via pitting, leading to anodic brightening,
by raising anode potential.
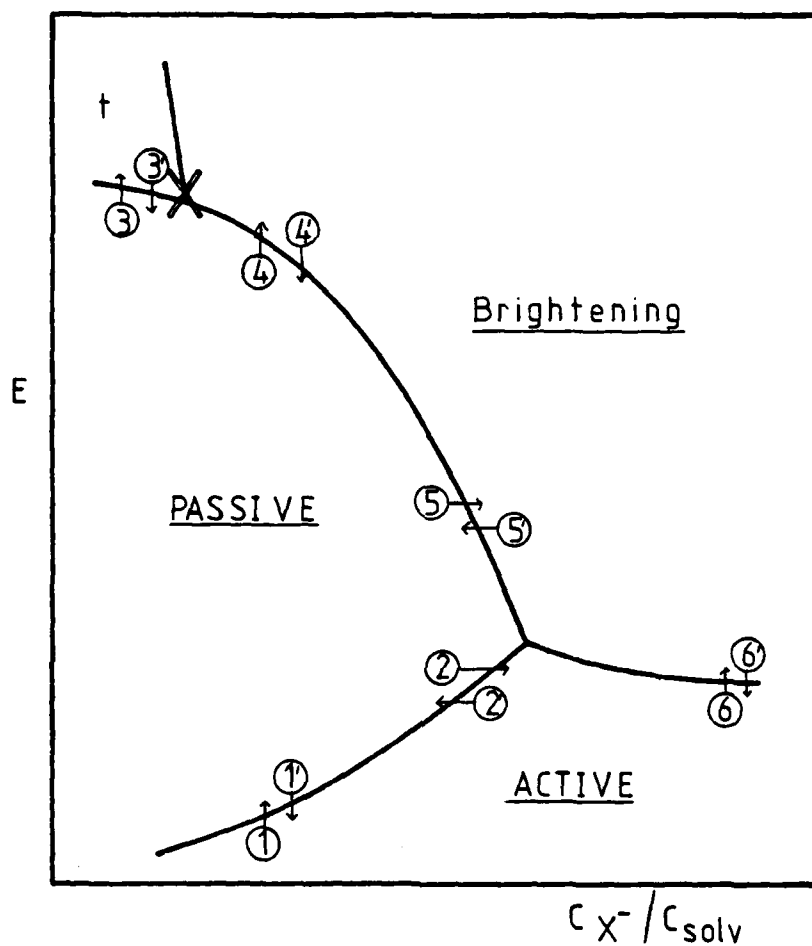
Figure 3·6. Scheme showing anode behaviour at various potentials in solutions of various anion/solvent concentration ratios.

(t = transpassive region)

(see text for key to numbered reactions)

(4') Re-passivation by lowering anode potential.

(5) Breakdown, via pitting, leading to anodic brightening, by adding "corrosive" anion.

(5') Re-passivation by removing "corrosive" anion.

(6) Anodic brightening by raising anode potential in concentrated solution.

(6') Anodic etching of brightened metal, by lowering potential in concentrated solution.

In nitric acid-dinitrogen tetroxide solutions only the upper half of the Hoar diagram is relevant for any metal in such an oxidising system. The concept of brightening is also of dubious relevance as most anions to be considered in these media form insoluble salts with the cations that are produced from film breakdown. It is supposed that the inhibition of corrosion in nitric acid - dinitrogen tetroxide media corresponds to the region X in Figure 3.6, and that the actual protection afforded is directly related to the solubility or insolubility of the corrosion products formed in this region. Hence stainless steel is moderately protected in pure nitric acid inhibited by H_2SO_4, due to the formation of an insoluble iron sulphate, but is afforded far greater protection if the nitric acid is inhibited with hF, where upon a fluoro-species of chromium provides a highly protective insoluble film. This phenomenon of protection by insoluble salt formation is little encountered in aqueous systems where most common salts are found to be soluble. A more detailed discussion of this subject is given in Section 5.

3.2 Electrochemical Instrumentation [3.3, 3.6, 3.7]

The Potentiostat

The potentiostat is a device used in polarisation

studies for the plotting of Tafel and passivation curves.
The potentiostat maintains the potential between the
working (specimen) electrode and the reference electrode
equal to some signal generator potential which may be a
constant voltage or a time-varying signal if automatic
polarisation is being employed. The current which arises
from the change in working electrode potential is passed
through a negative feed-back circuit which contains a third
counter electrode, and this operation is performed so
that insignificant current passes through the reference
electrode. Early potentiostats were cumbersome and
inaccurate but the last 25 years has seen the development
of high performance electronic devices, especially with
the discovery of the operational amplifier.

In our laboratories, two potentiostats, a H B Thompson
and Associates Model 401 and a Wenking Model PCA 72, have
been used. The former is the most up-to-date type with
a response time of 10^{-9} seconds and, with an appropriate
counter resistor, will allow measurements of currents as
low as 10^{-7} or 10^{-8} amp. This particular model has a
maximum output current of 1.0 amp and output voltage of
43 volts. The Wenking potentiostat has a response time
of 10^{-6} seconds and an inbuilt current meter which will allow
measurement of currents down to 10^{-6} amp.

The Thompson 401 potentiostat has been employed
(Section 4.2)
exclusively in work with aluminium(and has also been used
for electrochemical studies of stainless steel in fluoride-
inhibited HDA   (Section 5.5). All other experiments
described in this report have used the Wenking potentiostat.

In order to record polarisation curves automatically,

- 36 -

the potentiostat may be supplied with a time-varying signal from an external potential-generating source. In our laboratories we have used two instruments to effect this.

(1) A potential step generator; this device (constructed in our electronic workshops) enables the automatic polarisation of an electrode to the desired overpotential in a total of 32 potential increments. The step time interval can be varied from 1 to 1,000 seconds and the magnitude of each increment can be varied from 1 to 100 mV. This enables a whole range of polarisation rates to be obtained and current and potential readings were recorded on a Keithley 750 printer which was linked to a Keithley 172A multimeter.

(2) A linear sweep generator; this was used exclusively with the Wenking potentiostat and was a model manufactured by Chemical Electronics Co. The varying external EMF is produced by a motorized rheostat, and different polarisation rates are obtained via complicated mechanical gearing. Total polarisation time can be varied from 2 minutes to 20 hours and the maximum polarisation overpotential from 0 to 6 V. This instrument has the disadvantages associated with a mechanical device but has the advantage of an automatic reverse for plotting depolarisation curves. Furthermore E vs ι or E vs log ι (incorporating a linear-log converter) curves can be plotted directly onto a chart recorder and this greatly reduces result processing time.

Figure 3.7 illustrates the two types of automatic potential control discussed above. The different effects of the two types of control on the shape of polarisation

Figure 3.7 ; automatic polarisation methods
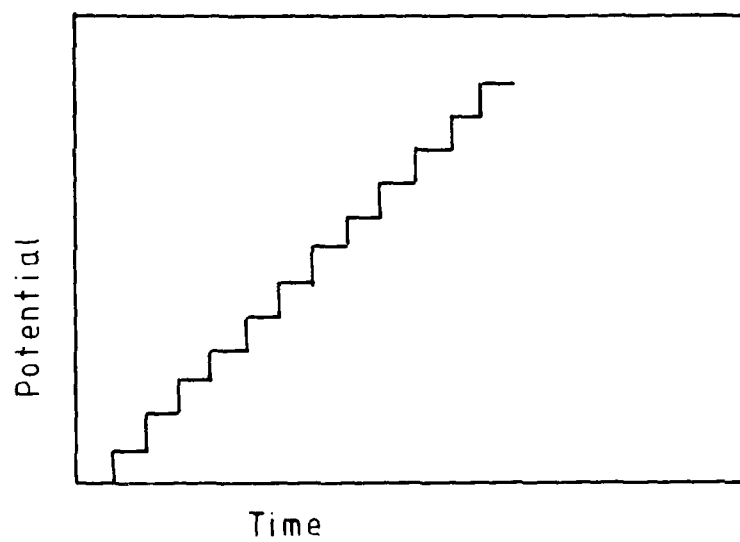
a) Potential step method
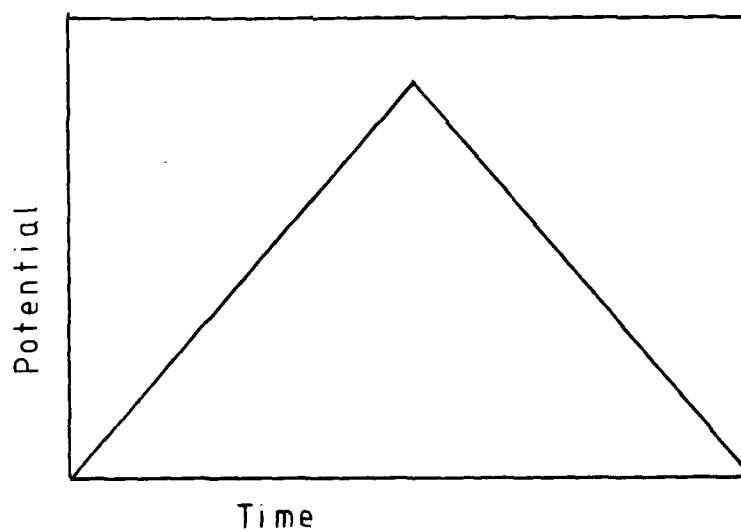
b) Potential sweep method.

curves has been studied[3.7] and the difference has been found to be minimal.

3.3 The Electrochemical Cell[3.6, 3.7, 3.8]

The optimum characteristics for cell and electrodes for electrochemical studies are now well documented in the literature and as far as possible these have been adopted in our electrochemical investigation of HNO_3 - N_2O_4 solutions. The system under study has certain properties which must be reflected in the experimental approach chosen.

(1) Nitric acid - dinitrogen tetroxide solutions are highly conducting and this minimizes IR drop (internal resistance) in the solution between the electrodes.

(2) The cathodic reaction;

$$NO_2^+ + e^- \rightarrow \tfrac{1}{2}N_2O_4 \hspace{2cm} (3.11)$$

occurs in solution without evolution of gas which might collect on electrode surfaces altering their effective area.

(3) The corrosive and oxidative nature of the system limits error due to contamination (organic impurities are oxidised) but this corrosivity does present problems in practical design, especially for solutions which contain HF or other fluoride-species which attack glass.

The Specimen Electrode

The specimen electrode must be free of any foreign impurities as even the smallest amounts may affect the electrochemical behaviour. The effect of surface roughness on the shape of polarisation curves has been demonstrated, and it has been shown that the more polished the surface, the more representative and reproducible are the results

obtained. In most of the electrochemical work described in subsequent Sections of this Report, aluminium and stainless steel specimens were first abraded with a series of silicon carbide abrasive papers before polishing on 8 and 1 μm diamond wheels. The aluminium was subjected to one further step, being finally polished with 0.1 μm aluminium oxide paste. Such a degree of polish is probably not absolutely necessary for the electrochemical work but the highly polished surface produced is ideal for optical microscopy studies.

Ideally in electrochemical studies the specimen surface should consist of only one face. In aqueous systems the pressure moulding of the specimen into a range of plastic mounts has long been practiced, but in $HNO_3-N_2O_4$ solutions the penetrating nature of the N_2O_4 and the corrosivity of the nitric acid has so far made this mounting procedure impossible. The specimens used for electrodes in our laboratories have been either metal discs or cylindrical rod sections. The use of such specimens, which introduce edges as well as plane surfaces into the experiment, is justified at least by the recognition that they more adequately represent a real situation. It is presumed that edges and corners etc, if absent in storage tanks, no doubt exist in rocket engine assemblies. The specimens are mounted on glass or teflon rods depending on whether a fluoride inhibitor is present and sucn electrodes have already been detailed.[3.9]

To avoid excessive contamination by air the specimens are polished immediately prior to use and are degreased in inhibisol before being dried and placed in the $HNO_3-N_2O_4$ solution.

The Counter Electrode

This electrode must be able to sustain large amounts of current and be able to act as an efficient anode or cathode. Ideally, it should be separated from the main cell by a sintered glass plate or similar membrane to avoid contamination of the main cell. The area of the counter electrode should be as large as practically possible and the counter electrode should be positioned as far away from the working electrode as possible. In HNO_3-N_2O_4 solutions, a platinum plate has been used as the counter electrode with an area generally between 2 and 4 cm^2. This electrode is placed in a HNO_3-N_2O_4 solution of composition similar to that in the main cell.

The Reference Electrode

A rhodium wire in a HNO_3-N_2O_4 solution will act as a very satisfactory reference electrode. The establishment of rhodium as a reference electrode and its use also as an indicator electrode is dealt with later in this Section; the following discussion deals exclusively with its practical use as a reference electrode.

The rhodium wire electrode has been used in two forms in our laboratories. For simple experiments in uninhibited HNO_3-N_2O_4 solutions, and for all solutions containing HF, a bare rhodium wire has been used. This may be sealed directly into glass, clamped in Teflon or sealed into FEP plastic tubing. The reference electrode must be positioned as close as possible to the working electrode to avoid the potential gradient between working and counter electrode, and to minimize the

effect of solution resistance. Problems are, however,

encountered if the reference electrode is positioned too close

to the working electrode; during polarisation, reaction

products generated at the working electrode may contaminate

the reference electrode, consequently altering its potential.

The reference wire of this type should be as short as possible,

as the potential monitored by it will be the sum of the

infinite number of potentials corresponding to the infinite

number of points comprising the wire surface. An alternative

to a very short reference wire is a wire which lies parallel

to the specimen surface about 2 mm from it. Reference wires

generally have a diameter of 0.2-1.0 mm. A far more satisfactory

reference electrode system is one where the reference wire is

contained in its own cell and is effectively brought up to the

working electrode surface by a Luggin capillary. Figure 3.8a

shows an electrochemical cell which incorporates such an

arrangement. The capillary generally used has an external

diameter of 1 mm and internal diameter of 0.5 mm, and is

positioned between 1 and 2 mm from the working electrode

surface. The potential monitored between the reference and

working electrode is that between the Luggin capillary tip and

the area of specimen surface adjacent to it. This arrangement

is equivalent to placing a rhodium disc of negligible thickness,

and diameter, 1-2 mm from the specimen surface. In the

comparative operation of the Luggin capillary arrangement

with that of a bare wire reference electrode

the former gave the better performance, although

the difference was not crucial.

Fig 3.8a Glass electrochemical cell

3.8b Stainless steel cell
         (for use with HF inhibited solutions)

3.8a

Rhodium ref electrode

(glass sinter)   (Glass sinter)

Platinum
counter electrode

Working
electrode

Luggin capillary

3.8 b

teflon

321 stainless
steel tube

KEL-F electrode
support

stainless steel
(working) electrode.

stainless steel
clamping screw

Rhodium reference
electrode

Platinum counter
electrode

teflon
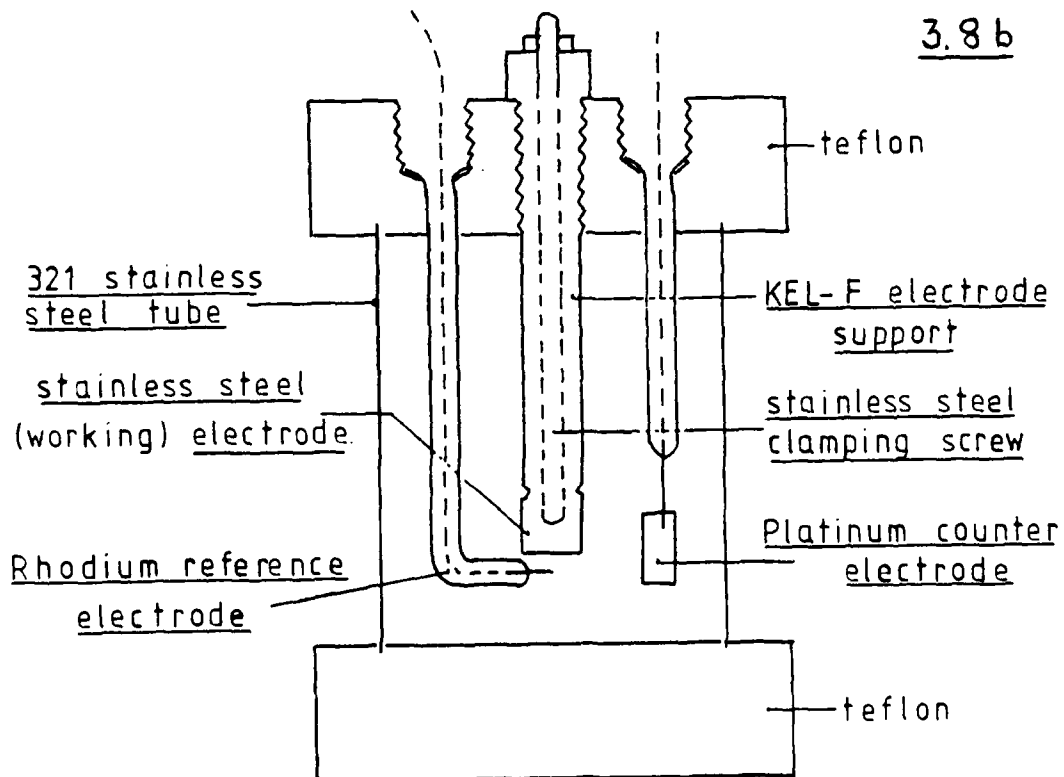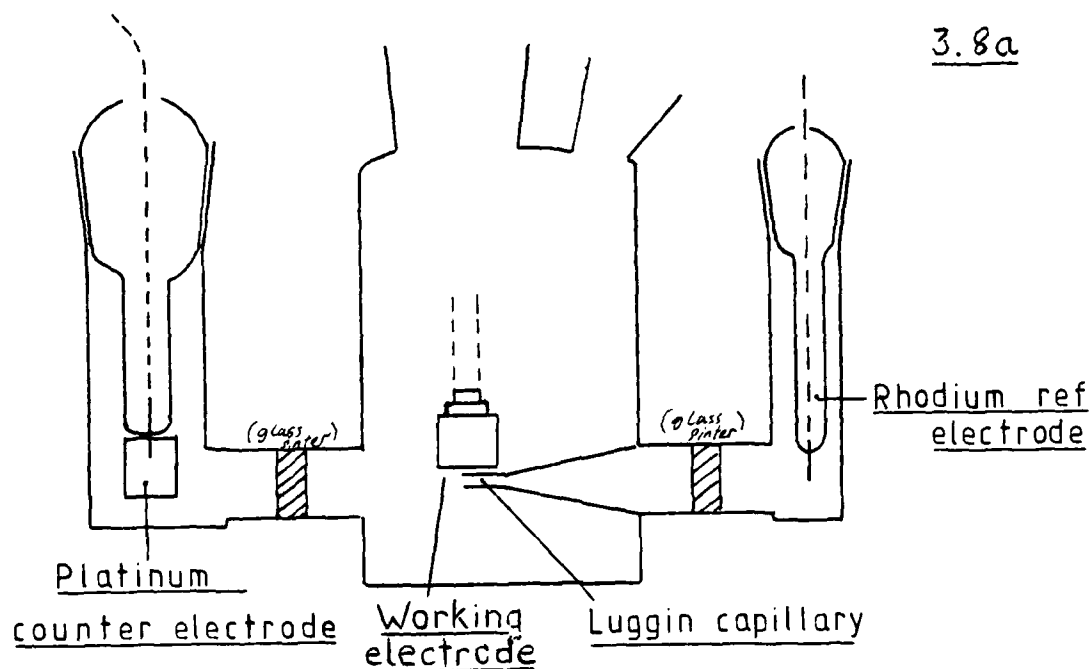
The Salt Bridge

A membrane (sintered glass plate etc) which separates a reference cell from the main cell may have a "liquid junction potential" associated with it if the ions on either side differ greatly in type or concentration. The existence of a liquid junction potential will give erroneous potential readings and such junctions should be eliminated if at all possible. The effect of this in HNO_3-N_2O_4 solutions is thought to be minimal although experiments have yet to be performed to verify this. To completely rule out any possible liquid junction potentials, a salt bridge may be used between the reference cell compartment and the main cell. In some experiments, pure nitric acid saturated with potassium nitrate (3M) has been used to eliminate these potentials and such a salt bridge has been found to behave satisfactorily.

Cell Design

Electrochemical cell designs for use with HNO_3-$N_2O_4^-$HF solutions have previously been described,[3.9]. Figure 3.8b shows an improved cell design for use with inhibited HNO_3-N_2O_4 and an alternative to those originally used for uninhibited systems. The stainless steel tube for this second cell is protected by the fluoride inhibitor present in solution. The stainless steel tube may be pretreated with a fluoride filming solution to limit fluoride depletion of the test solution. Electrochemical experiments with such a cell rarely extend beyond one week and such an arrangement is considered to be entirely satisfactory.

3.4   The Rhodium Redox Reference Electrode

To make an electrochemical study of any system it is
necessary to have a reference electrode, an electrode which
has a constant and reproducible potential to which other
potentials can be reliably related.   In aqueous systems
all potentials are related to the standard hydrogen electrode
(reversible potential of the $H^+/\frac{1}{2}H_2$ couple) set at 0.00 V.
In practice, a number of more convenient reference electrodes
are used, e.g., Cu/Cu^{2+}, $Hg,HgCl_2|Cl^-$, and $Ag,AgCl|Cl^-$.
The use of such classical reference systems in nitric acid-
dinitrogen tetroxide mixtures was initially thought inadvisable
and a rhodium redox reference electrode has been developed.
The rhodium electrode is reversible to the $NO_2^+/\frac{1}{2}N_2O_4$ couple,
which exists in $HNO_3-N_2O_4$ solutions, and therefore gives
a constant and stable potential (with respect to time),
characteristic of the NO_2^+/N_2O_4 ratio present in solution.
As yet it has been impossible to relate the potentials
measured to the standard hydrogen electrode and the reversible
potential of a solution of 0.1 molal N_2O_4 in HNO_3 (1.0 wt%)
has been chosen as an arbitary zero; this particular
concentration is convenient because between -20 and +20°C, thé
reversible potential shows zero temperature dependence.

Rhodium was tested as a reference electrode according to
the following established criteria.[3.6, 3.8]

1. It should be reversible and obey the Nernst equation with respect to the appropriate species in the electrolyte. This has been tested with the rhodium electrode, which has been found to be correctly responsive to changes in concentration of NO_2^+ and N_2O_4, the oxidised and reduced species respectively.

2. The potential of the reference electrode should remain constant with time, i.e., be stable. This has been tested with rhodium over a period of several days and the potential has been found to remain constant within 1 mV. Potential decay is, however, likely if the temperature of the acid is allowed to exceed $0^{\circ}C$, as nitric acid decomposition is then able to occur to a noticeable extent.

3. The reference electrode potential should return to its initial potential after small currents have been passed. An extensive polarisation study has been made to assess this property. The anodic and cathodic curves obtained were symmetrical about the common axis and both NO_2^+ reduction and N_2O_4 oxidation were found to occur reversibly as an overpotential was applied to the rhodium electrode (i.e., the polarisation curves showed no hysteresis).

4. The exchange current density, i_o, (See Section 3.1(b)) should be sufficiently high to swamp the possible effects of alternative reactions which might be introduced through surface or solution contamination. The exchange current density for the $NO_2^+/\frac{1}{2}N_2O_4$ couple on rhodium at 0^oC has been found to be $10^{-3.8}$ A cm^{-2}. Comparison with i_o values for the hydrogen reaction on various metals, listed in Table 3.2, shows that this value is comparatively high and more than satisfactory for a reference electrode.

Rhodium has thus been established as a reference electrode for use in $HNO_3-N_2O_4$ solutions and because of its reversible redox character, it can also be used as an indicator electrode for solution analysis.

3.5 Determination of N_2O_4 Concentration

Figure 3.9 shows the variation of potential with N_2O_4 concentration from 0-15 wt %. Up to 1 wt %, N_2O_4 the curve is seen to obey the Nernst equation (E α $-\log\left[N_2O_4\right]$) but above 1 wt % the curve deviates from its straight line form due to $\left[NO_2^+\right]$ suppression, caused by increasing $\left[NO_3^-\right]$, arising from ionized N_2O_4. Figure 3.9 provides a useful thermodynamic calibrated scale, so that the potential (and free energy) of any N_2O_4 solution up to 15 wt % may be related in terms of thermodynamics to any other solution.

NOTE

The half cell Rh|0.1 molal N_2O_4-HNO_3 is assigned
the arbitary potential of 0.00V because of the
potentials zero dependance on temperature at this
concentration. This 'Standard potential' is sometimes
designated simply as '0.1 molal'.
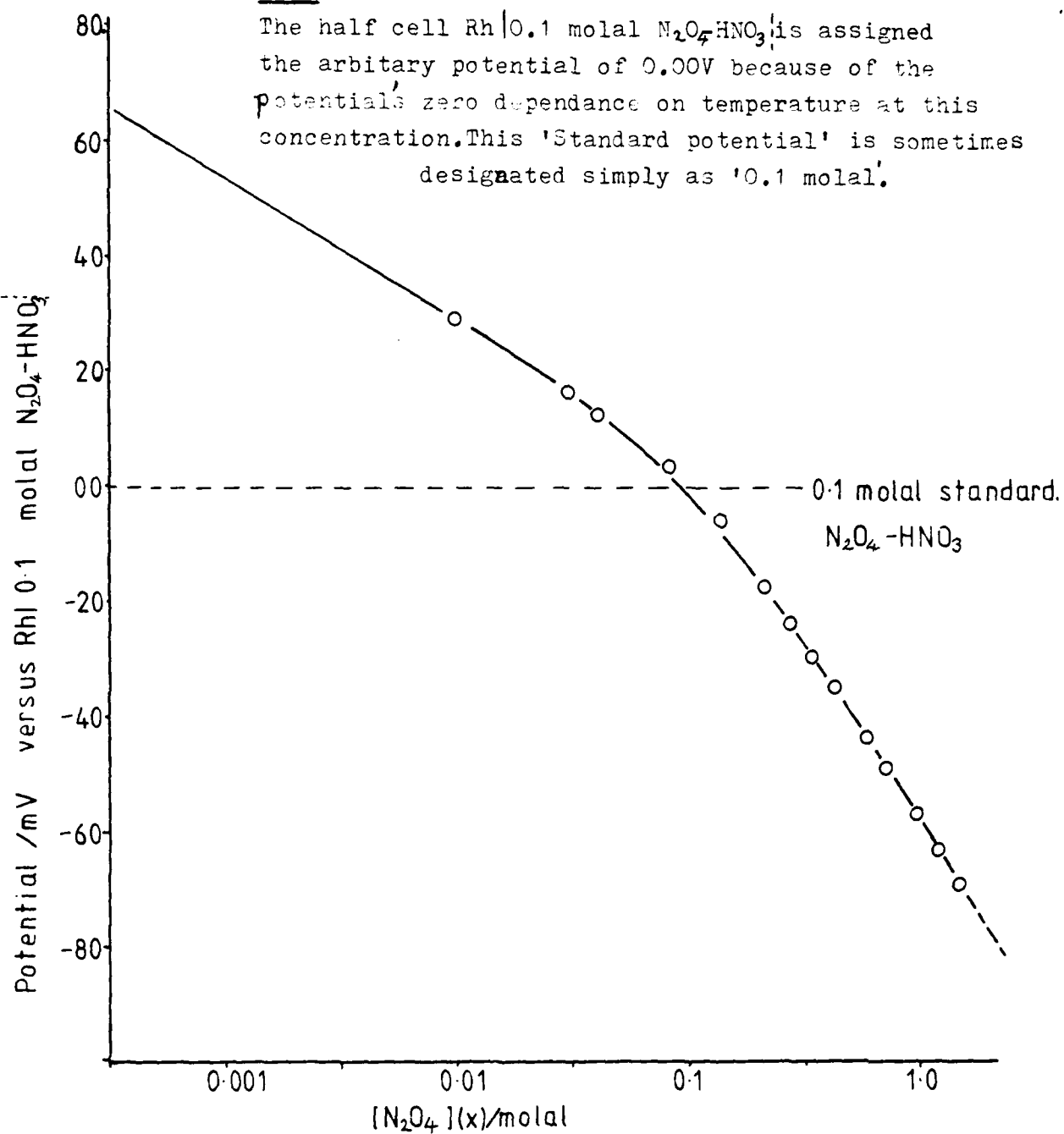
Figure 39   Potential of the Cell

Rh| x molal N_2O_4-HNO_3| 0.1 molal N_2O_4-HNO_3 | Rh

versus x molal N_2O_4

3.6   Determination of Water Content in HDA

The potential of laboratory prepared HDA on the above described scale has been measured as ca -196.5 mV vs 0.1 molal standard. This value, however, represents acid which contains water additional to that produced from the auto-ionization. This is clearly shown in Figure 3.10, which shows the effect of adding water to HDA previously enriched with N_2O_5. (N_2O_5 ionizes to $NO_2^+ + NO_3^-$). The mid point of this acid-base type curve corresponds to the situation $\left[NO_2^+\right] \equiv \left[H_2O\right]$ and represents dry HDA. (No excess water). This dry acid has a reversible potential of -139.5 mV and by expanding the relevant portion of Figure 3.10, the laboratory acid can be seen to contain 0.24 ± 0.02 wt % H_2O. AAM Moharum has determined the water content of HDA prepared in our laboratories, by near IR spectroscopy[3.9], obtaining a value of 0.23 wt %. This value is in very good agreement with that obtained electrochemically but the electrochemical method has the advantage of being more rapid with an estimated accuracy of within 0.01 wt %. Figure 3.11 shows a plot of potential versus wt % H_2O between 0.2 and 1.0 wt %, for determination of HDA water contents up to 1.0 wt%.

Figure 3.10
Electrochemical Titration of
Water into N_2C_5(ca 0.2molal)—
enriched HDA.

--- corresponds to wet HDA
containing 0.24wt% residual H_2O

Figure 3.11
Determination of water content in HDA
by redox potential measurements.

Water/wt% added to 'wet' (laboratory) HDA

Potential/mV vs that of 'dry' HDA
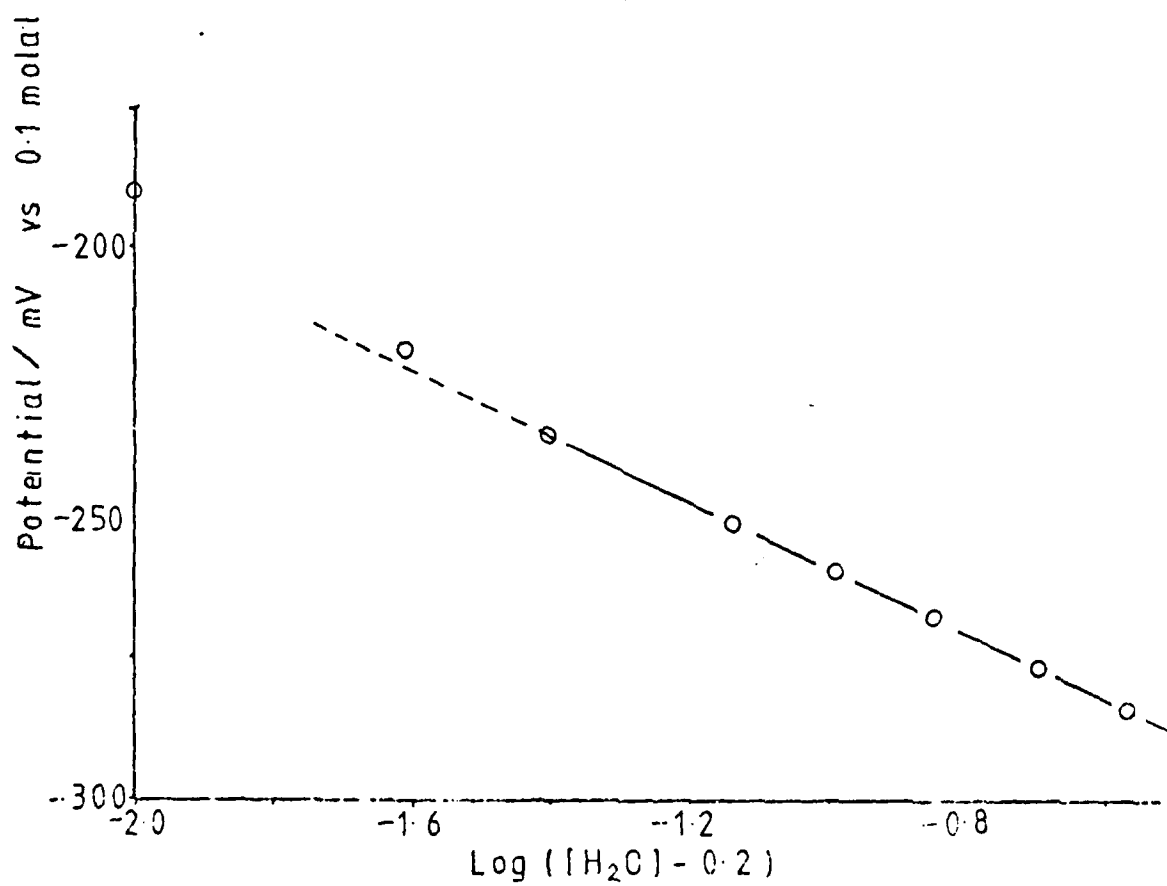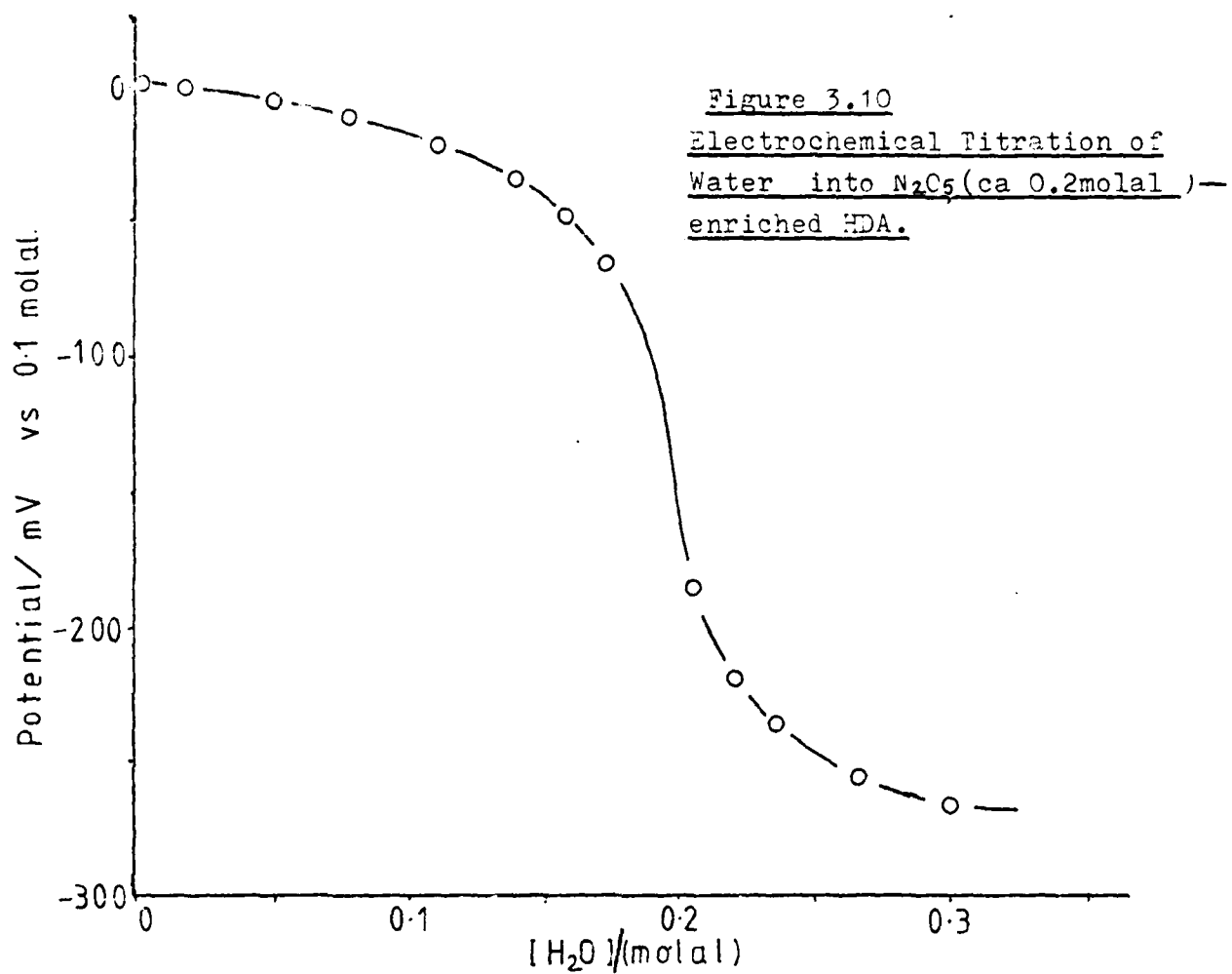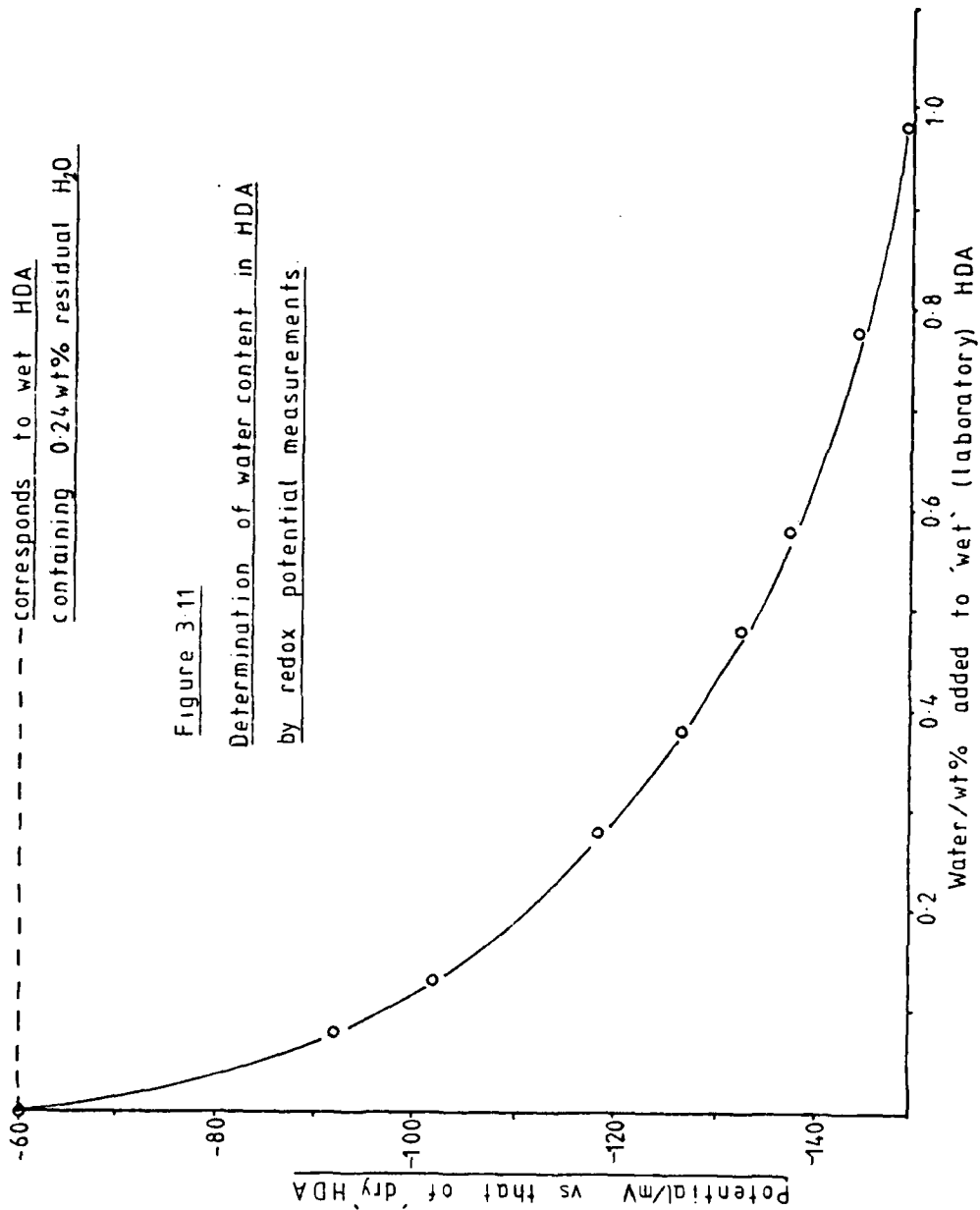
4. THE CORROSION OF ALUMINIUM IN HNO_3/N_2O_4 MIXTURES

4.1 The Corrosion of Aluminium in SHDA and MHDA (R.C. Hibbert)

The tanks and experimental procedures used in the long term corrosion rate study of 6061-T6 aluminium alloy in SHDA and MHDA have already been described.[4.1] Initially it had been planned to terminate the experiment after 20 months but due to the low concentration of aluminium in solution, this was thought inadvisable. The contents of the tanks were eventually filtered after 28 months. It was not possible to isolate any authentic aluminium corrosion products by this means. It was possible, however, to scrape a small amount of a white solid product off the walls of the SHDA tank. This material is discussed in Section 6.

The results of tank sampling are presented in Table 4.1, and Figure 4.1.

Figure 4.1 shows the sharp rise in corrosion rate for MHDA between 200 and 275 days. For SHDA a similar effect is observed after 527 days.

This type of behaviour has been observed elsewhere[4.2] (e.g., stainless steel in MHDA after 344 days) and may be ascribed to inhibitor depletion. Nevertheless, even up to 680 days the corrosion rates in both systems are very small.

Table 4.1   Corrosion of Aluminium in SHDA and MHDA

Time/ days	Aluminium concn./ ppm	Total weight loss/ mg
SHDA		
171	3.3 ± 0.7	0.8 ± 0.2
336	6.9 ± 2.0	1.6 ± 0.5
527	11.0 ± 1.5	2.4 ± 0.3
680	21.0 ± 2.0	4.5 ± 0.4
MHDA		
171	1.6 ± 0.5	0.4 ± 0.1
336	13.6 ± 0.8	3.1 ± 0.2
527	24.5 ± 2.0	5.3 ± 0.4
680	43.5 ± 0.8	9.3 ± 0.2

Time period	Weight loss during period/mg	Average corrosion rate during period/g m^{-2} hr^{-1}
SHDA		
0-171 days	0.8 ± 0.2	1.6×10^{-5}
171-336 "	0.8 ± 0.7	1.8×10^{-5}
336-527 "	0.8 ± 0.8	1.6×10^{-5}
527-680 "	2.1 ± 0.9	5.1×10^{-5}
MHDA		
0-171 days	0.4 ± 0.1	8.0×10^{-6}
171-336 "	2.7 ± 0.3	6.0×10^{-5}
336-527 "	2.2 ± 0.6	4.4×10^{-5}
527-680 "	4.0 ± 0.6	9.6×10^{-5}

Fig. 4·1

Graph of Weight loss vs. Time for Al tanks

⊙ .... MHDA

+ .... SHDA

Weight loss/ mg

Time/ Days
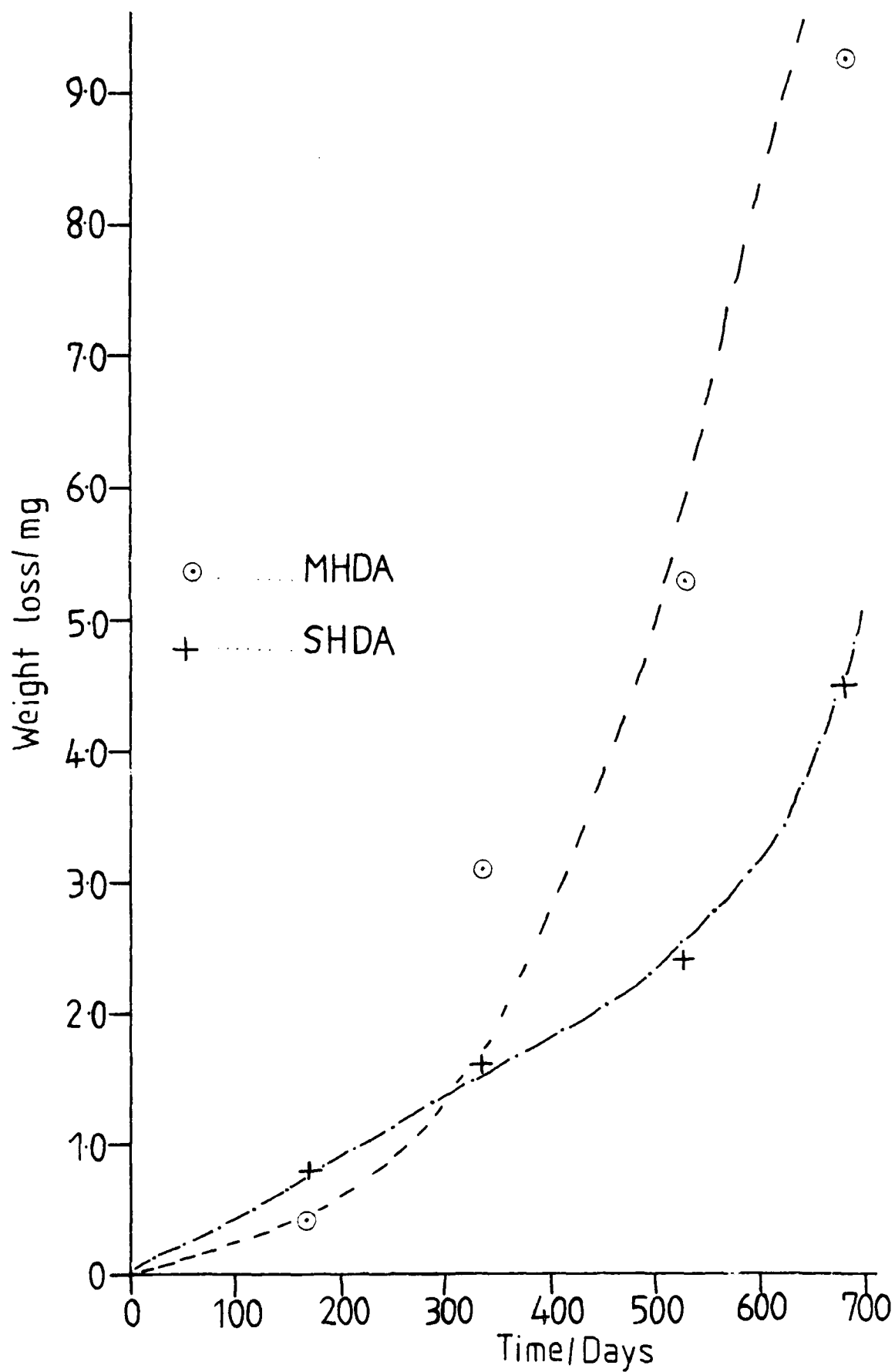
4.2 Electrochemical Studies   (C.L.F. Cole and R.C. Hibbert)

(a) Aluminium in the 100% HNO_3 System

The Al/HNO_3 system was investigated using polarisation
and potential-time   methods and formed a necessary
preliminary to work on uninhibited HDA.

A notable feature of the polarisation curves of Al
in HNO_3 was that the rest potentials were found, using
the same Al sample in different samples of HNO_3 at
various times, to range widely. The discrepancy was
approximately 250mV; for example, a typical spread
of rest potentials would be ca. -510mV to -733mV.
An explanation for this behaviour probably lies in
the nature of the oxide film on Al.

Al forms a passive film of Al_2O_3 on exposure to air,
which can vary from ca 20 to 100 Å in thickness. Both
natural and thermally-formed oxide films consist of
a layer of barrier-type oxide, the thickness of which
depends on the temperature, and a porous layer whose
thickness depends on the environment and the exposure
time. The porous film is formed by the action of
moisture on the barrier film, and clearly the nature
and extent of these layers will influence the final
rest potential of the Al.

Pretreatment of aluminium

The method of pretreatment of Al is not considered to
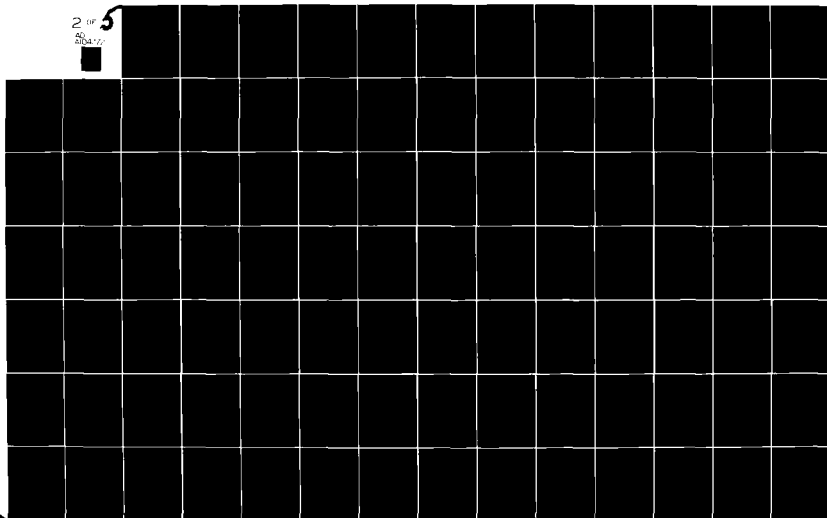
have any long-term effect on the beha\

100% HNO_3 or possibly also in UHDA.]

and Towner[4.3] showed that for Al in cor

the thickness of the film formed on th

as measured by ellipsometry, rose to a

a certain time and then fell to a cons

various pretreatments being used. All

used, however, produced this maximum,

a different value. This behaviour is

the potential-time curve of Al in 100%

after a fairly rapid rise in potential

to film formation, the potential falls

values before achieving a steady rest

The pretreatment of aluminium used in th

for studies of the Al/100% HNO_3 system

abrading the sample on SiC paper, poli

1μ diamond wheels and a final polish w

paste. This procedure was also adopte

of Al/UHDA at 0^OC. Other pretreatment

of the Al/UHDA system at room temperat

examined and will be described in Sect

An observation which suggests that the

decreases upon continued cathodic pola

effect on the Tafel slope; this is fou

with continued polarisation. This can

when it is realised that β, the symmet

is affected by such factors as a film

of a metal and the electrical double l
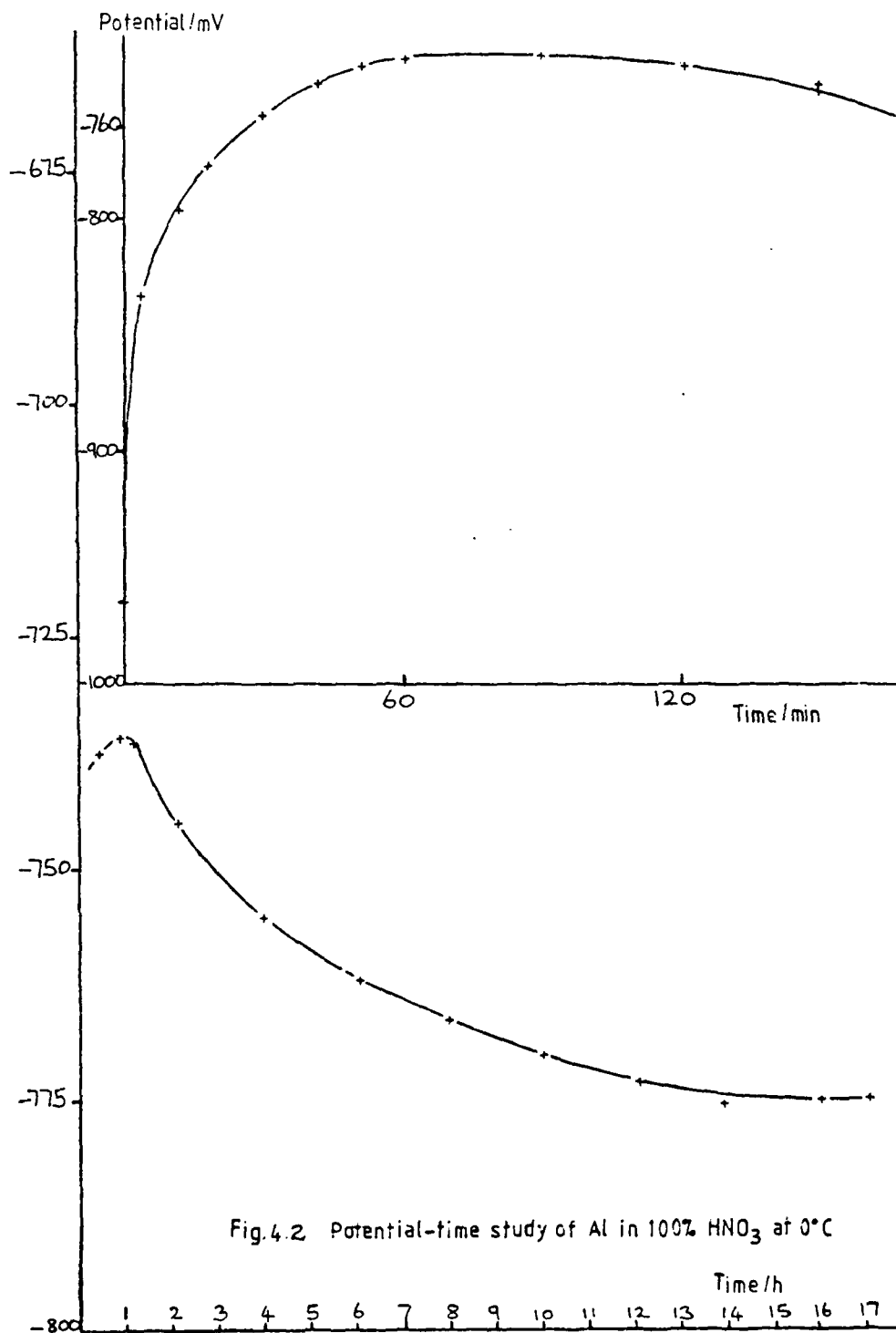
Fig. 4.2 Potential-time study of Al in 100% HNO_3 at 0°C

Fig. 4.3(a) shows cathodic polarisation curves of Al/100% HNO_3 obtained using Pt counter and reference electrodes (these electrodes were used in all uninhibited work), Fig. 4.3(b) shows the corresponding anodic polarisation curves. The curvature of the cathodic plot is typical of this system, and is not affected by stirring. This shows that the curvature is not due to concentration polarisation, but is indicative of a fast reaction, (Levich-Dogonadse theory).[4.4]

Corrosion Rate of Al in 100% HNO_3 at $0^{\circ}C$

The corrosion rate is difficult to evaluate using the Tafel extrapolation method since the cathodic slopes vary in magnitude, and the anodic slope corresponding to metal dissolution could not be found. This dissolution is assumed to be

$$Al \rightarrow Al^{3+} + 3e^-$$
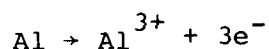
and should have a Tafel slope of 0.036 V^{-1} decade at $0^{\circ}C$. However, corrosion rates were estimated by extrapolating the Tafel-like slope to the rest potential, E_{rp}, assuming that the cathodic area approximates to the total area of the specimen. A number of corrosion currents for Al in 100% HNO_3 are presented, together with several other parameters, in Table 4.2. As can be seen,

Fig.4.3a Comparison of AL/100% HNO₃ at 0°C with and without stirring-polarisation curves

$E_{rp} = -697.3 \, mV$ ①

$E_{rp} = -697.4 \, mV$ ②

slope① = − 0·092 V decade⁻¹
slope② = − 0·0925 V decade⁻¹

① = not stirred (+)
② = stirred (⊕)

Potential/mV

Current/mA

Fig.4. 3bAl/100% HNO_3 at 0°C (stirred) - anodic polarisation curve

$E_{r.p} = -722.2$ mV
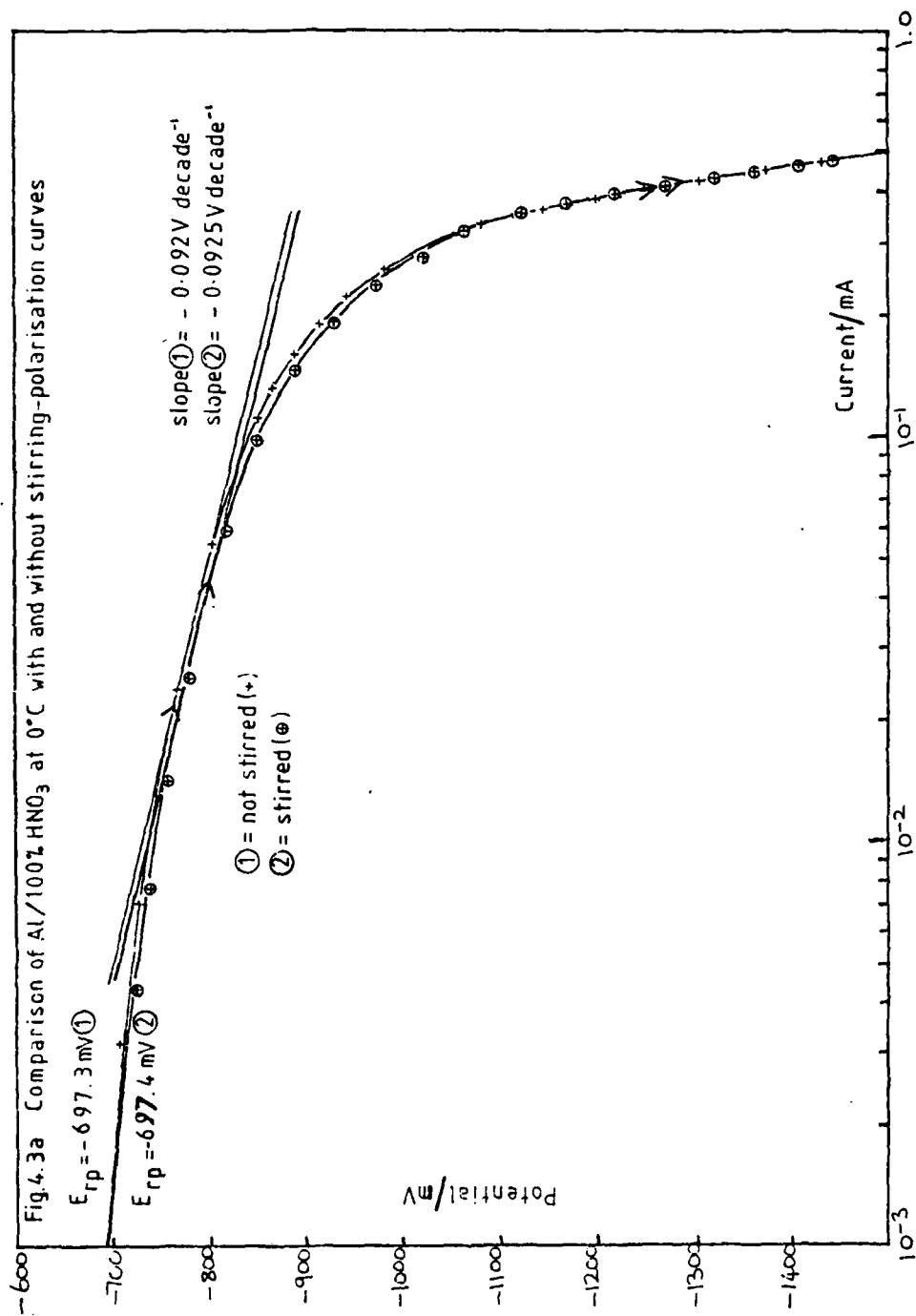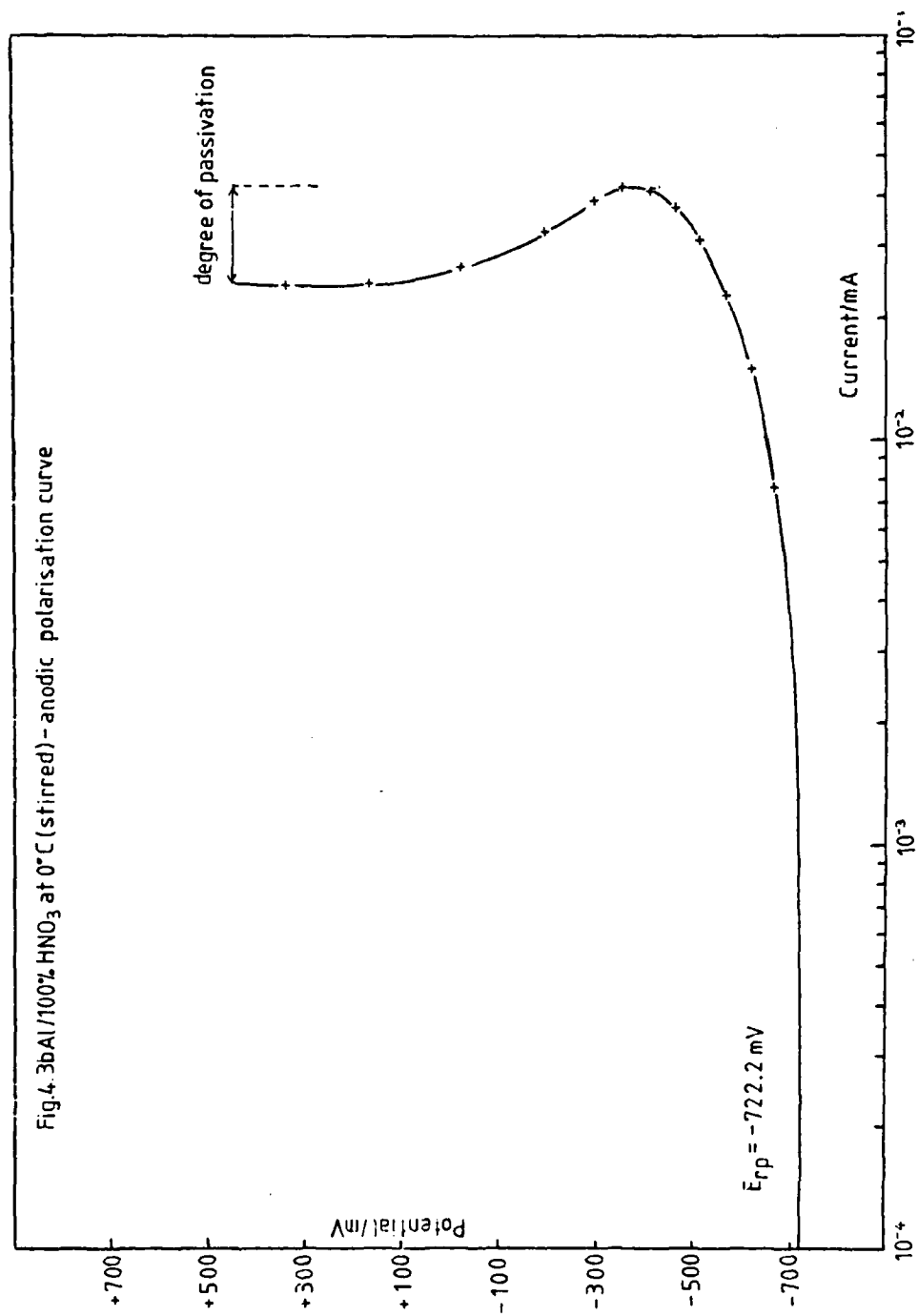
Table 4.2

Some Electrochemical Parameters for Al in HNO_3 ** at $0^\circ C$

Date	Solution†	Rate of scan/ mV s^{-1}	Tafel Slope/ V decade^{-1}	Rest potential (cathodic)/mV (E_{rp})	i_{corr}/Acm^{-2}
31/1/80	(1)	25/20	-0.144	-712.4	4.23×10^{-7}
31/1/80	(1)	25/20	-0.142	-715.5	4.01×10^{-7}
1/2/80	(1)	10/120	-0.1415	-735.2	5.55×10^{-7}
5/2/80	(2)	35/20	-0.133	-586.0	4.11×10^{-7}
5/2/80	(2)	20/20	-0.1285	-638.8	9.78×10^{-7}
5/2/80	(2)	25/10	-0.120	-654.8	1.09×10^{-6}
5/2/80	(2)	25/40	-0.117	-662.5	1.09×10^{-6}
6/2/80	(2)	25/20	-0.120	-655.0	1.03×10^{-6}
6/2/80	(2)	25/20	-0.107	-668.3	9.78×10^{-7}
6/2/80	(2)	25/20	-0.1085	-668.1	9.54×10^{-7}
7/2/80	(2)	25/20	-0.093	-692.5	8.94×10^{-7}
7/2/80	(2)	25/20	-0.0935	-694.0	8.33×10^{-7}
7/2/80	(2)	25/20	-0.092	-697.3	8.57×10^{-7}
7/2/80	(2)	25/20	-0.0925	-697.4	8.10×10^{-7}

** The S/V value for all these measurements is 0.088 cm^{-1}

† The number in this column identifies the set of results obtained for a particular solution (ie experimental "run")

all the electrochemical parameters (Tafel slope, Rest potential, i_{corr}) show some variation from one polarisation run to the next. However all the cathodic slopes are reasonably consistent with a 1 electron reaction, being in the range -0.092 to -0.144 V decade^{-1} compared with the theoretical value of -0.108 V decade^{-1}.[*] The corrosion currents are quite small indicating that there is a protective film on the aluminium surface in 100% HNO_3. The rest potentials are however quite negative. These negative rest potentials are probably due to the high electrical resistance of the film. A highly resistive film would mean that electrons would not be readily available for the cathodic reaction:-

$$NO_2^+ + e^- \longrightarrow \tfrac{1}{2}N_2O_4.$$
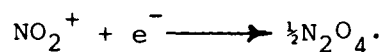
Noble rest potentials are to be expected when the anodic reaction is inhibited by film formation but cathodic inhibition can give rise to quite negative rest potentials. It is therefore likely that cathodic inhibition is taking place.

Addition of H_2O to the Al/100% HNO_3 system

The potential time graph of Al in 100% HNO_3 + 1 wt % added water is shown in Fig. 4.4. It can be seen that upon addition of the water the potential decreases by approximately 220 mV and finally reaches an equilibrium value of -793 mV.

The polarisation plot (Fig.4.5) shows that the shape of the cathodic curve is considerably affected by the addition of H_2O. (cf. Fig.4.3a). It is probable that a different cathodic reaction is now taking place, since the addition of H_2O will affect the concentration of both NO_2^+ and N_2O_4. Addition of

*See footnote to p.60
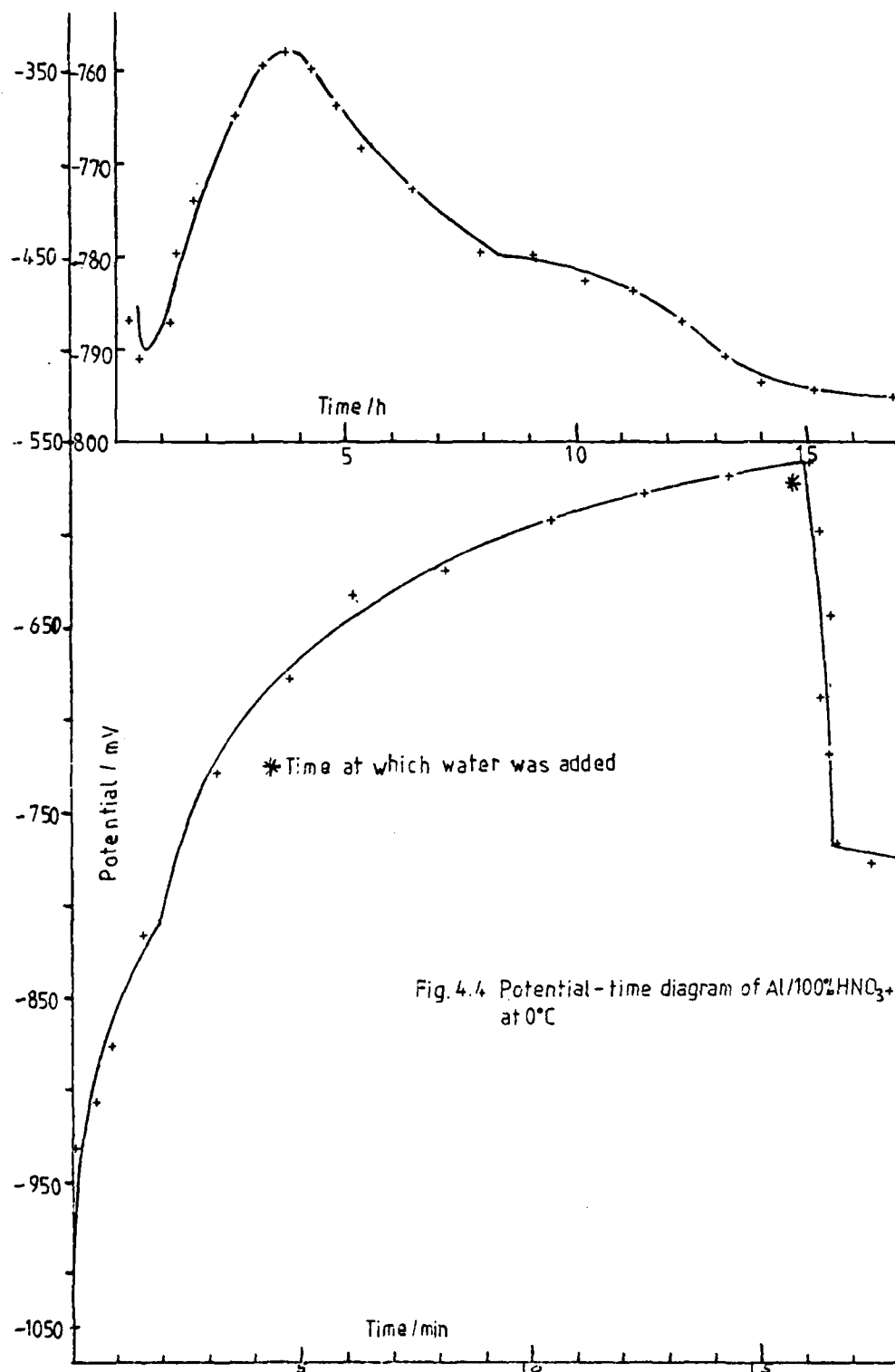
Fig. 4.4 Potential-time diagram of Al/100%HNO$_3$+1%H$_2$O at 0°C

*Time at which water was added

Fig. 4.5 Al/100% HNO_3 + 1% H_2O at 0°C (stirred) - polarisation curves
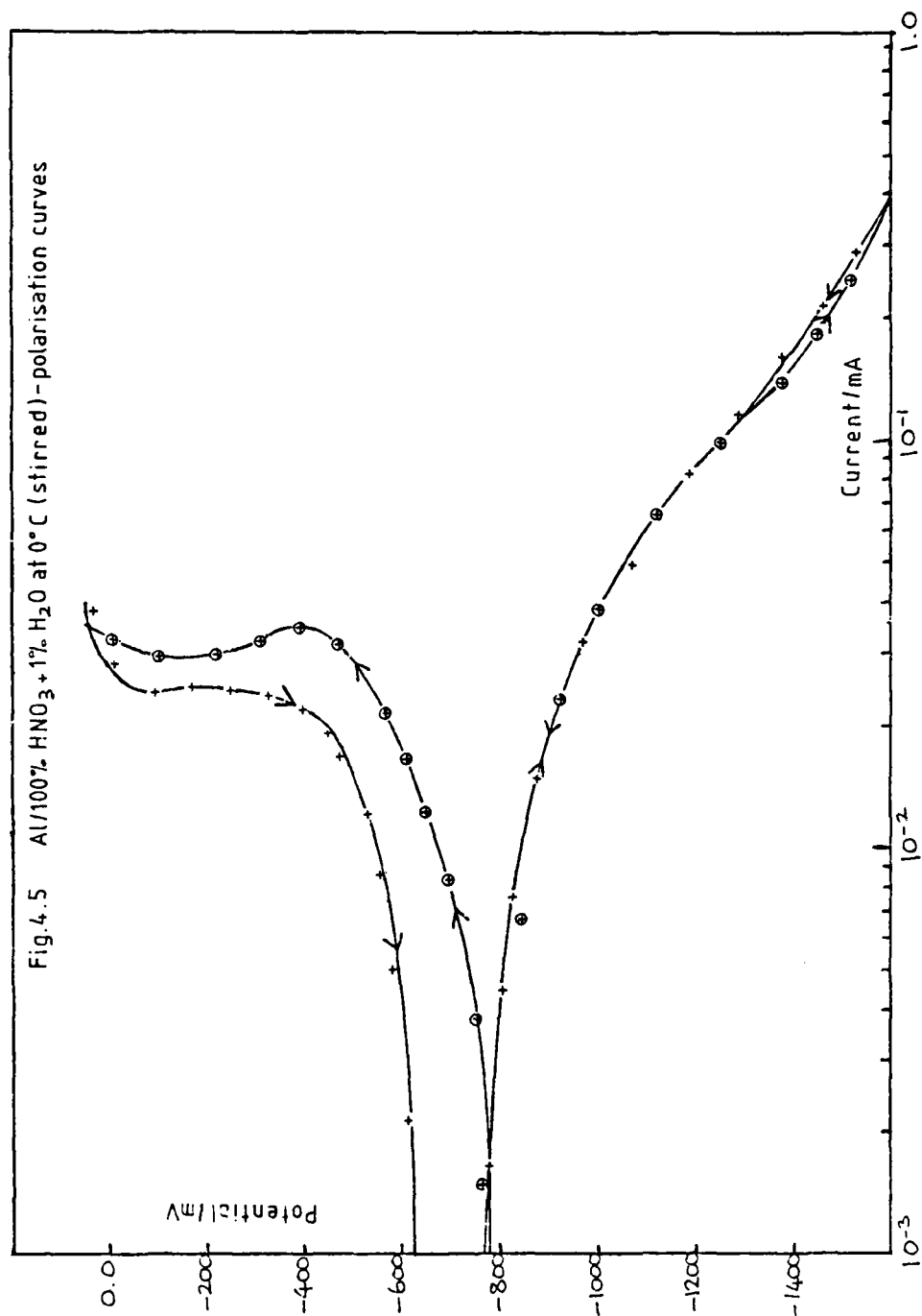
H_2O will suppress the NO_2^+ concentration arising from the self-dissociation of HNO_3:-

$$2 \ HNO_3 \rightleftharpoons NO_2^+ + NO_3^- + H_2O$$
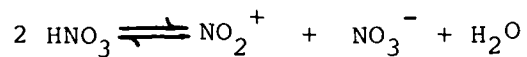
N_2O_4 will be removed by the following mechanism:-

$$N_2O_4 \longrightarrow NO^+ + NO_3^-$$

$$NO^+ + H_2O \longrightarrow HNO_2 + H^+$$

$$3 \ HNO_2 \longrightarrow HNO_3 + H_2O + 2NO$$
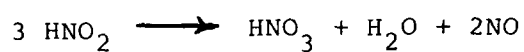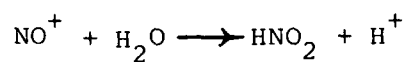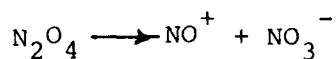
The absence of Tafel-like behaviour in the cathodic reaction indicates that there is more than one cathodic reaction taking place. The change of cathodic reaction may also account for the decrease in rest potential.

The polarisation resistance method (see also Section 3.1(c))

A method of obtaining more accurate corrosion currents
would obviously be of great advantage in the discussion of
rest Potentials,   the effect of water and i_{corr}.

It was decided, therefore, to employ the polarisation
resistance method. This technique provides an alternative
to the conventional Tafel method of determining the corrosion
current. A small potential increment ($\pm\Delta E$) is applied to the
freely corroding specimen and the current which flows through
the external circuit applying the potential increases from zero
to $\pm\Delta i$. The slope of the polarisation curve   at the corrosion
potential is given by

$$\left(\frac{di}{dE}\right)_{E\rightarrow 0}$$

This slope defines the polarisation resistance, R_p, and
shows its relationship to the corrosion current, i_{corr}, by the
equation

$$\left(\frac{di}{dE}\right)_{E\rightarrow 0} = \frac{1}{R_p} = \frac{2.3 i_{corr}}{B}$$

R_p is inversely proportional to the corrosion current
and, hence, the corrosion rate. The constant of proportionality
can be deduced from the Tafel slopes (included in the constant
B), or it can be determined empirically.

The method has a number of advantages. Chiefly, it is
insensitive to deviations from Tafel behaviour which make
extrapolations of polarisation slopes inaccurate. The method

- 55 -

is very rapid, requiring, approximately, ten minutes only. Since the potential is disturbed by only $\pm$ 10 mV from the rest potential, compared with hundreds of mV in the Tafel method, the film is disturbed very little. Thus, this method can be used with some reliance in conjunction with potential-time studies.

The polarisation resistance technique was, therefore, applied to the $Al/100\%$ HNO_3 system and a corrosion current, i_{corr}, of 3.38×10^{-7}A cm^{-2} was obtained, using values of 0.036 and -0.108 V decade^{-1} for the anodic and cathodic slopes respectively; the graph of η $\Big/$ mV $\underline{vs}$ i $\Big/$ mA $\Big/ \overset{x\,10^{-4}}{}$ is shown in Fig. 4.6. This i_{corr} was obtained for a E_{rp} of -726.10 mV and indicates again that a more negative E_{rp} does not necessarily correspond to a greater i_{corr}. However, further experiments concerning addition of water to the 100% HNO_3 system need to be performed in order for definite conclusions to be drawn. Experiments involving the addition of water to the Al/UHDA system would also be useful for comparison purposes.

Fig.4.6 Polarisation resistance graph of Al exposed to 100% HNO_3 at 0°C (not stirred)
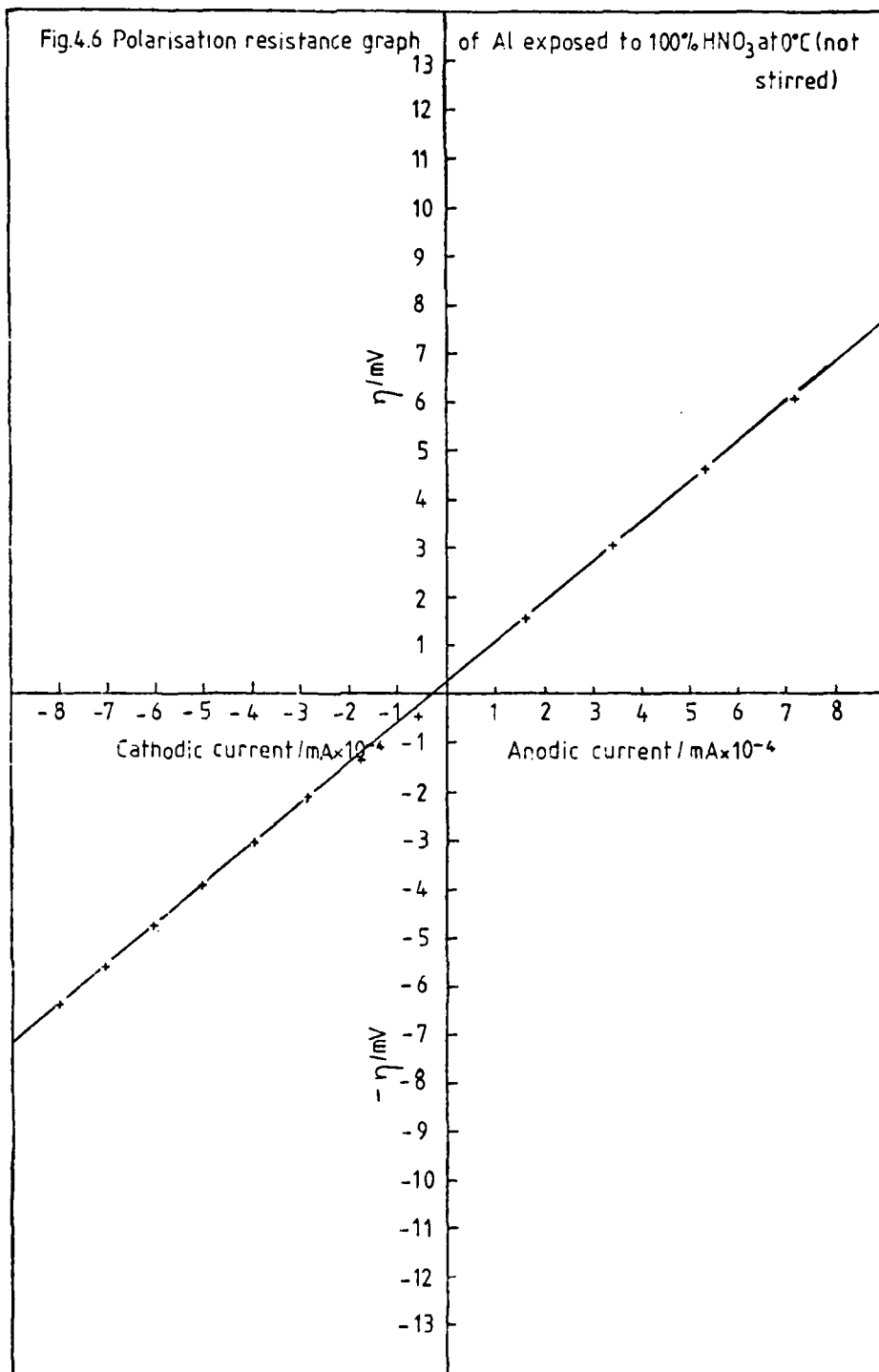
For certain types of inhibition e.g. involving organic and pickling inhibitors* the rest potential can actually become more negative[4.5,4.6]. This is due to cathodic rather than anodic inhibition taking place. Upon the addition of H_2O to HNO_3 the cathodic reaction is actually changed; a change of cathodic reaction can also cause the rest potential to become more negative.

Addition of P_4O_{10} (0.75 wt %) to the Al/100 % HNO_3 System

P_4O_{10} was added to 100 % HNO_3 in the hope that it would reduce the water content arising from self-dissociation and hence the corrosion rate. Above ca 25 wt % aqueous HNO_3, the corrosion rate of aluminium decreases with increasing HNO_3 concentration.

The anodic polarisation curve (Fig.4.7) is indicative of a metal passivated in its environment. The vertical portion of the curve occurs at quite a low current value (ca 8×10^{-4} mA) and indicates that P_4O_{10} is acting as an inhibitor in 100% HNO_3. The electrochemical parameters are recorded in Table 4.3.

* i.e. adsorption inhibitors (e.g. benzoate) which owe their initial corrosion inhibiting action to adsorption onto either the metal or its oxide.

- 57 -

Fig. 4.7   Al / 100% HNO_3 + 0.5 g(0.75 wt.%) P_4O_{10} at 0°C (stirred)
—anodic polarisation curve

Potential/mV

+200
+100
0.0
-100
-200
-300
-400
-500

10^{-4} 10^{-3} 10^{-2} 10^{-1}
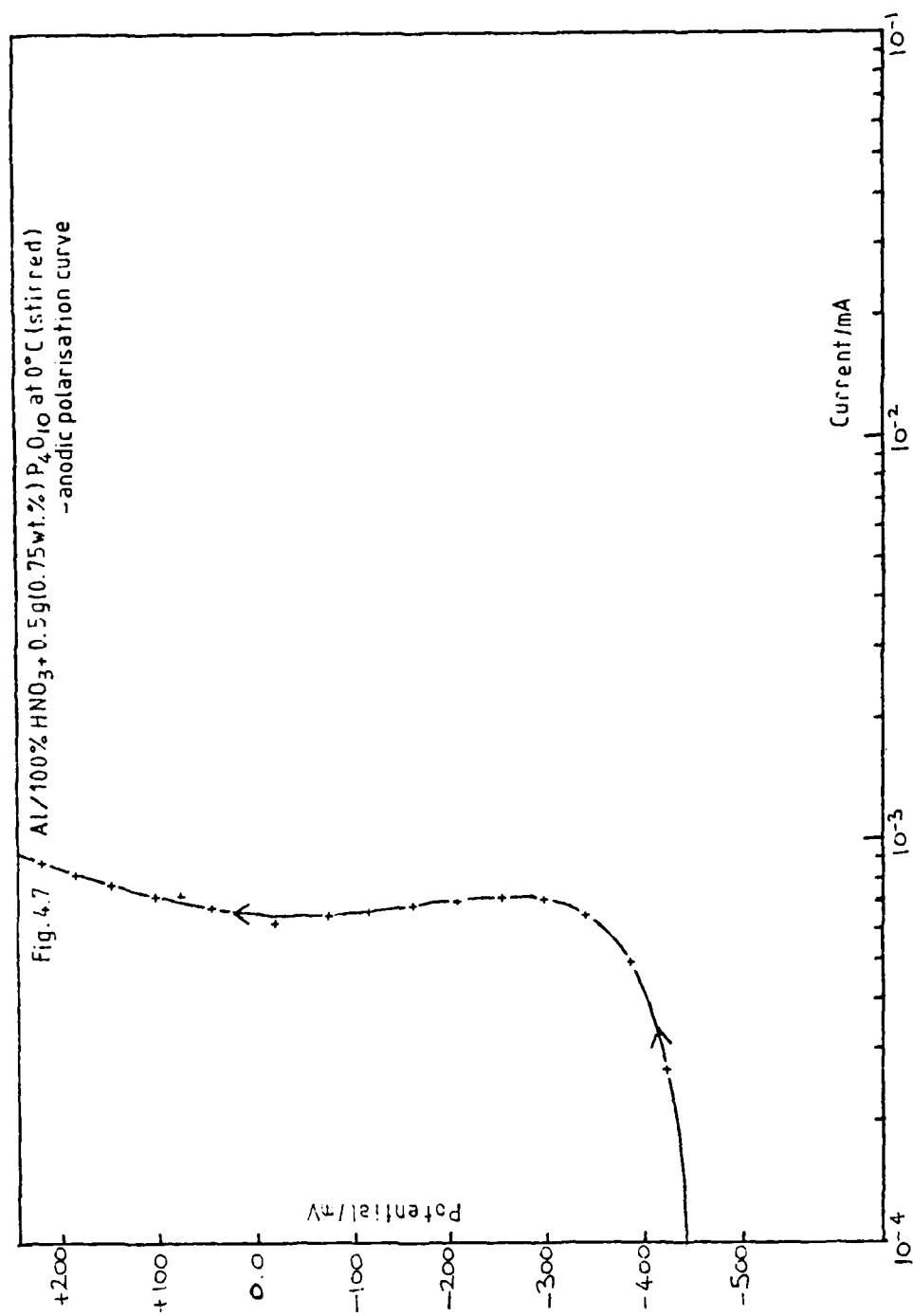
Current/mA

A corrosion current cannot be obtained from Fig.4.8
since the presence of two Tafel slopes invalidates the Tafel
extrapolation method.

It was decided to add the calculated amount of water,
sufficient to restore that removed by the P_4O_{10}, to
determine whether the anodic curve moved back to its
original position. The rest potential shifted to a
more negative value by ca 30 mV, but after a few seconds
it had returned to the value before addition of water. No
change was observed in the position of the anodic or
cathodic curve.

The P_4O_{10} will hydrolyse in 100% HNO_3 to phosphorus
(V) oxo-acids (see Section 2.2(f)) which can produce an
aluminium phosphate film on the metal surface.

Fig. 4.8 Al/100% HNO$_3$ + 0.50g(0.75wt.%) P$_4$O$_{10}$ at 0°C (stirred) – cathodic polarisation curve

Slope ① = – 0.222V decade^{-1}
Slope ② = – 0.121V decade^{-1}

E_{rp} = –436.0mV
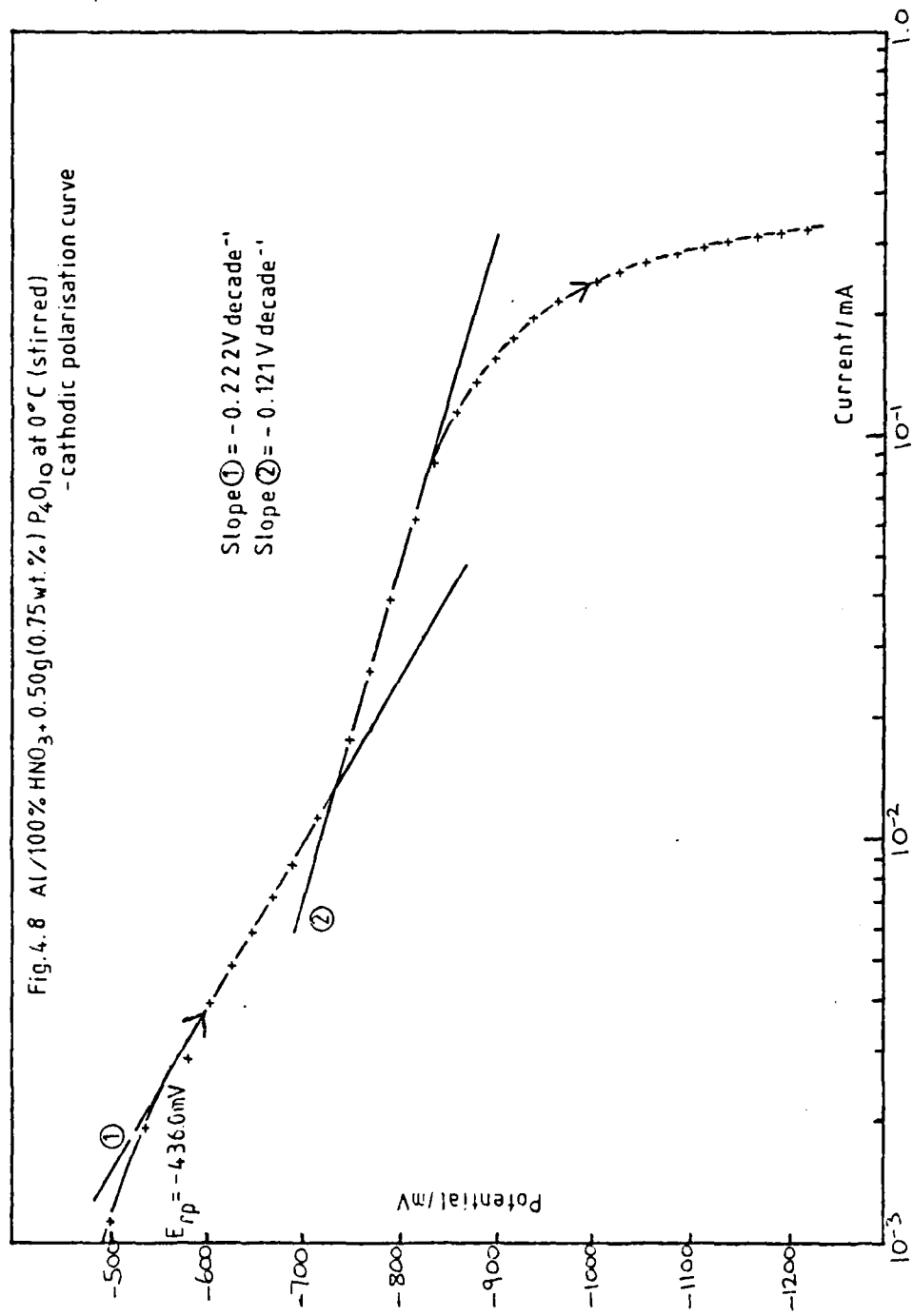
Table 4.3

Electrochemical Parameters for Al in 100% HNO_3 Containing 0.75 wt%

$\underline{P}_4\underline{O}_{10}$ at $0^{\circ}C$

(S/V = 0.086 cm^{-1} for all Measurements)

Date	Soln.	Tafel Slope/ V decade^{-1}	E_{rp}/mV
8/2/80	(1)	-0.222	} -436.0
		-0.121	
8/2/80	(1)	-0.255	} -40 3.2 (after anodic polarisation)
		-0.118	
11/2/80	(1)	-0.2085	} -455.5
		-0.137	
11/2/80	(1)	-0.217	} -456.7 (after anodic polarisation)
		-0.134	
12/2/80	(1)	-0.245	} -473.3
		-0.1425	

(b) Al in HNO_3/N_2O_4 Mixtures

No detailed statements can be made at the present time concerning corrosion rates in these systems, (with the exception of UHDA - see Section 4.2(c)), since the Tafel slope varies to a large extent, and the range of corrosion currents appears to lie in a narrow band. However, work is currently in progress using the polarisation resistance technique.

Tentative measurements using the Tafel method suggest however, that the corrosion rate decreases with addition of N_2O_4 up to about 10 wt % and then increases up to the UHDA concentration (44 wt%).

(c) The Al/Uninhibited HDA System

The cathodic polarisation curves for Al in UHDA are more difficult to explain than those for HNO_3. It was originally thought that, as in the HNO_3 system, continued cathodic polarisation would lead to a progressive improvement in the Tafel slope, i.e., it would tend towards a value of -0.108 V decade^{-1} at 0°C.* This was not found, however; in fact the slope tended towards higher values, and figures close to -0.108 V decade^{-1} were very difficult to obtain.

*i.e. the idealised value obtained from the Tafel equation for a one-electron reaction at 0°C, assuming β (eq 34) $= 0.5$

The closest value was -0.110 V decade^{-1}, and the most common one appeared to be at <u>ca</u> -0.126 V decade^{-1}.

The relevant parameters for Al in UHDA are given in Tables 4.4 and 4.5, the format being the same as for Al/100% HNO$_3$.

A comparison of Tables 4.2 and 4.4 reveals that the rest potential is more noble (more positive) in uninhibited HDA than in 100% HNO$_3$. However the corrosion current (i$_{corr}$) is lower in 100% HNO$_3$ than uninhibited HDA. The explanation is that a thicker film is formed in 100% HNO$_3$ than in uninhibited HDA, which inhibits the cathodic rather than the anodic reaction due to its high electrical resistivity. The cathodic slopes observed in uninhibited HDA are consistent with a 1 electron reaction.

Table 4.4

Electrochemical Parameters for Al in Uninhibited HDA

(S/V = 0.093 cm^{-1} for Soln. (1) and 0.085 cm^{-1} for Soln.(2) at 0°C

Date	Soln.	Rate of Scan/ mV s^{-1}	Tafel Slope/ V decade^{-1}	Rest Potential (cathodic)/ mV	i_{corr}/Acm^{-2} ×10^{6}
26/2/80	(1)	35/20	-0.119	-303.60	2.85
26/2/80	(1)	10/20	-0.1315	-292.00	2.05
26/2/80	(1)	10/20	-0.1315	-295.40	2.15
26/2/80	(1)	10/120	-0.1295	-296.60	2.05
28/2/80	(1)	10/20	-0.138	-285.50	1.67
28/2/80	(1)	10/20	-0.1355	-289.60	1.69
3/3/80	(2)	25/20	-0.1205	-404.00	7.20
3/3/80	(2)	10/20	-0.1245	-404.7	5.56
3/3/80	(2)	10/20	-0.105	-412.40*	2.42

* The sample was polarised first anodically, then cathodically before measurement of the rest potential

Table 4.5

Electrochemical Parameters for Al in Uninhibited HDA at $0°C$

(For Solns. (3), (4) and (5) the S/V Ratio's are 0.087,

0.054 and 0.0935 cm^{-1} Respectively)

Date	Soln.	Rest Potential (anodic)/mV
19/11/79	(3)	-484.60
18/12/79	(4)	-368.80
29/ 2/80	(1)	-288.00
3/ 3/80	(2)	-406.20
4/ 3/80	(2)	-447.00
7/ 3/80	(2)	-481.50
12/ 3/80	(5)	-338.40

Fig. 4.9 shows the anodic curve for solution (2) obtained on 4/3/80. The arrows pointing upward denote that anodic polarisation is proceeding in the noble direction and the arrows pointing downward, that successive depolarisations have been performed, at certain time intervals (2 mins, 25 mins and 65 mins). This procedure was adopted in order to establish whether the anodic film was capable of surviving in the UHDA over any length of time. As the diagram shows, the film is very rapidly destroyed since at the point of depolarisation the corresponding current value is at least as high as the point at which anodic polarisation stopped. The curves do show however, that the anodic film is readily reformed upon applying an appropriately high potential.

Fig. 4.10 shows the anodic curve of solution(2) obtained on 7/3/80. A passive region can clearly be seen, but at ca +900 mV a phenomenon similar to breakdown or evolution of a gas can be seen, although no gas was actually observed. This situation is similar to that encountered for Al in 100% HNO_3.

Fig.4.9 Al / HDA at 0°C (stirred)-polarisation curves

② taken after 2 mins.
③ "   "   25 "
④ "   "   65 "

Fig. 4.10 Al / HDA at 0°C (stirred)-anodic polarisation curve
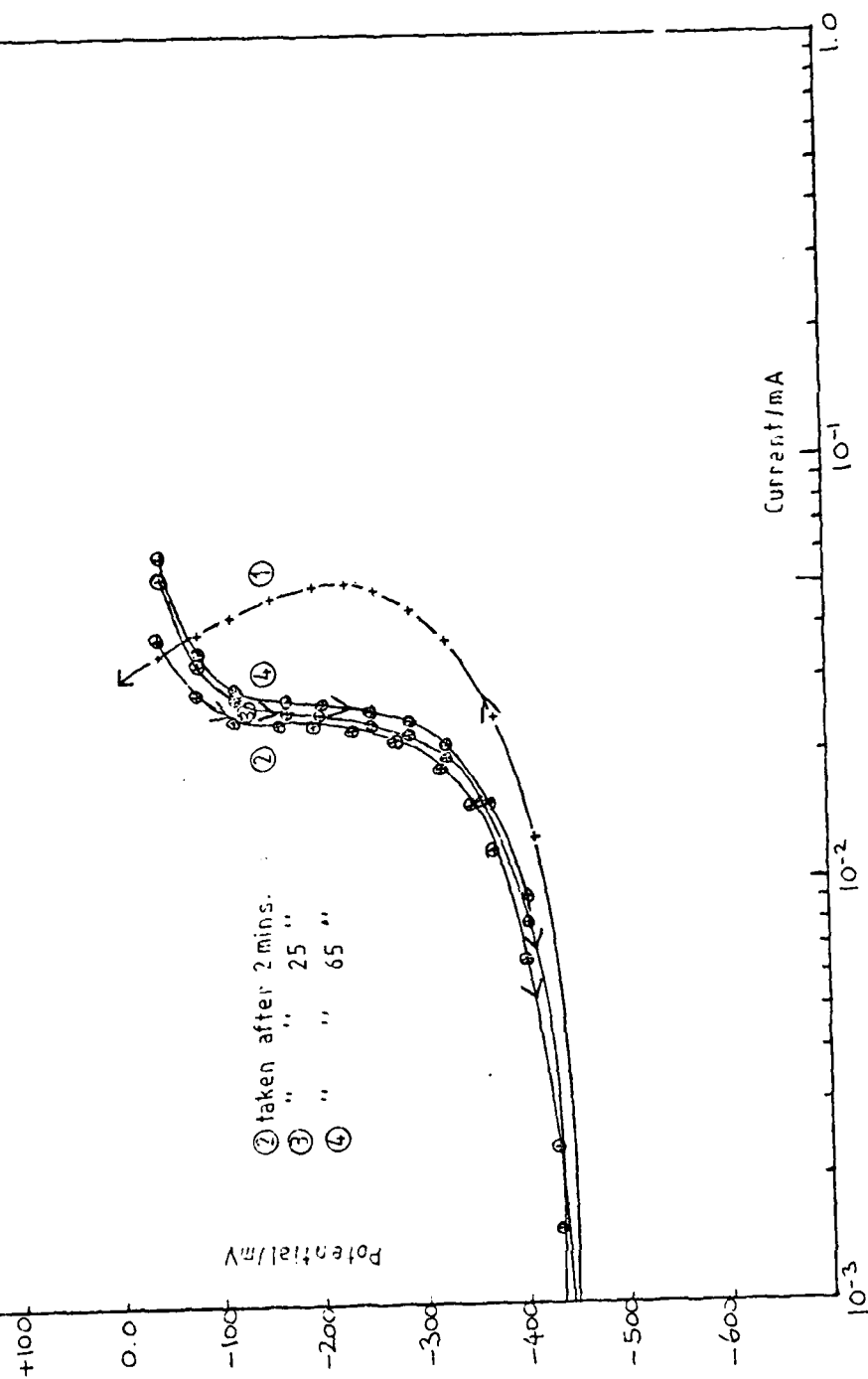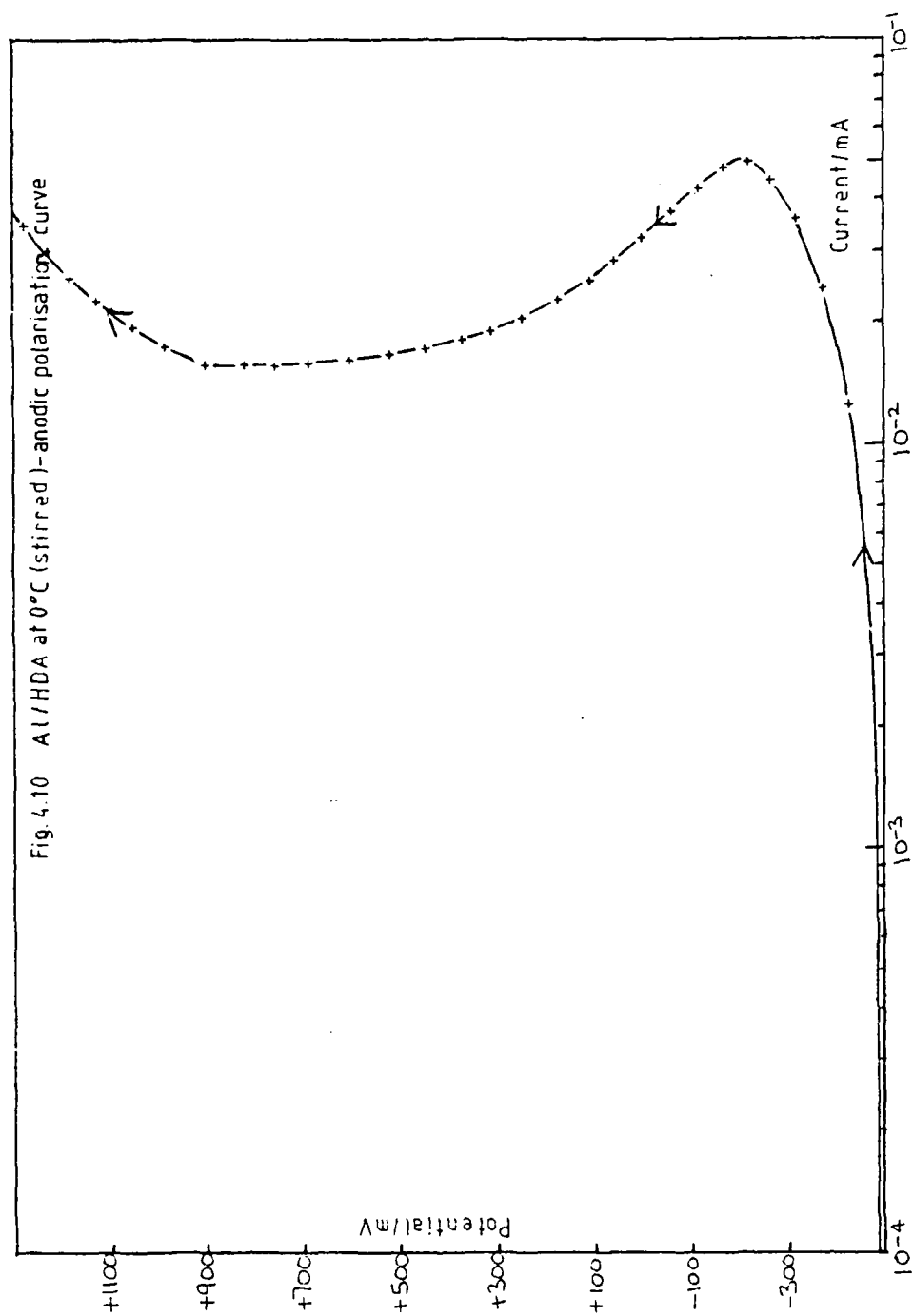
Fig.4.11 shows the anodic curve of solution (1) obtained on
28/2/80.   A comparison of Figs.4.10 and 4.11 indicates that
the degree of secondary passivation is dependant upon the
rest potential.   The more noble the rest potential the
smaller the degree of secondary passivation observed upon
(anodic) polarisation.   A similar phenomenon was observed
in the AL/100% HNO_3 system.

Corrosion rate of Al in Uninhibited HDA at 0^OC

From Table 4.4 it appears that a fairly representative corrosion
current would be ca 2.00 x 10^{-6} Acm^{-2} (6.70 x 10^{-3} gm^{-2} hr^{-1}),
while from polarisation resistance techniques a figure of
1.14 x 10^{-6} Acm^{-2} (3.80 x 10^{-3} gm^{-2} hr^{-1}) was obtained.   This
compares reasonably well with the value obtained by previous
workers in these laboratories[4.7] from atomic absorption and
weight loss measurements, i.e., 1.2 x 10^{-2} gm^{-2} hr^{-1} (S/V =0.25cm^{-1})
at 20^OC.   The corrosion rate of Al/UHDA compared to Al/100% HNO_3
can be seen to be at least a factor of two greater, although an
exact comparison is difficult.

Aluminium in Uninhibited HDA at Room Temperature

The metal specimen was in the form of a machined disc.
The surface pretreatment consisted of degreasing in acetone
followed by heating in an aqueous solution containing potassium
dichromate (20 g) and orthophosphoric acid (23 cm^3) per litre
at 70-75 ^OC, for 10 minutes.   The specimen was then removed,

Fig. 4.11   Al / HDA at 0°C (stirred) - anodic polarisation curve
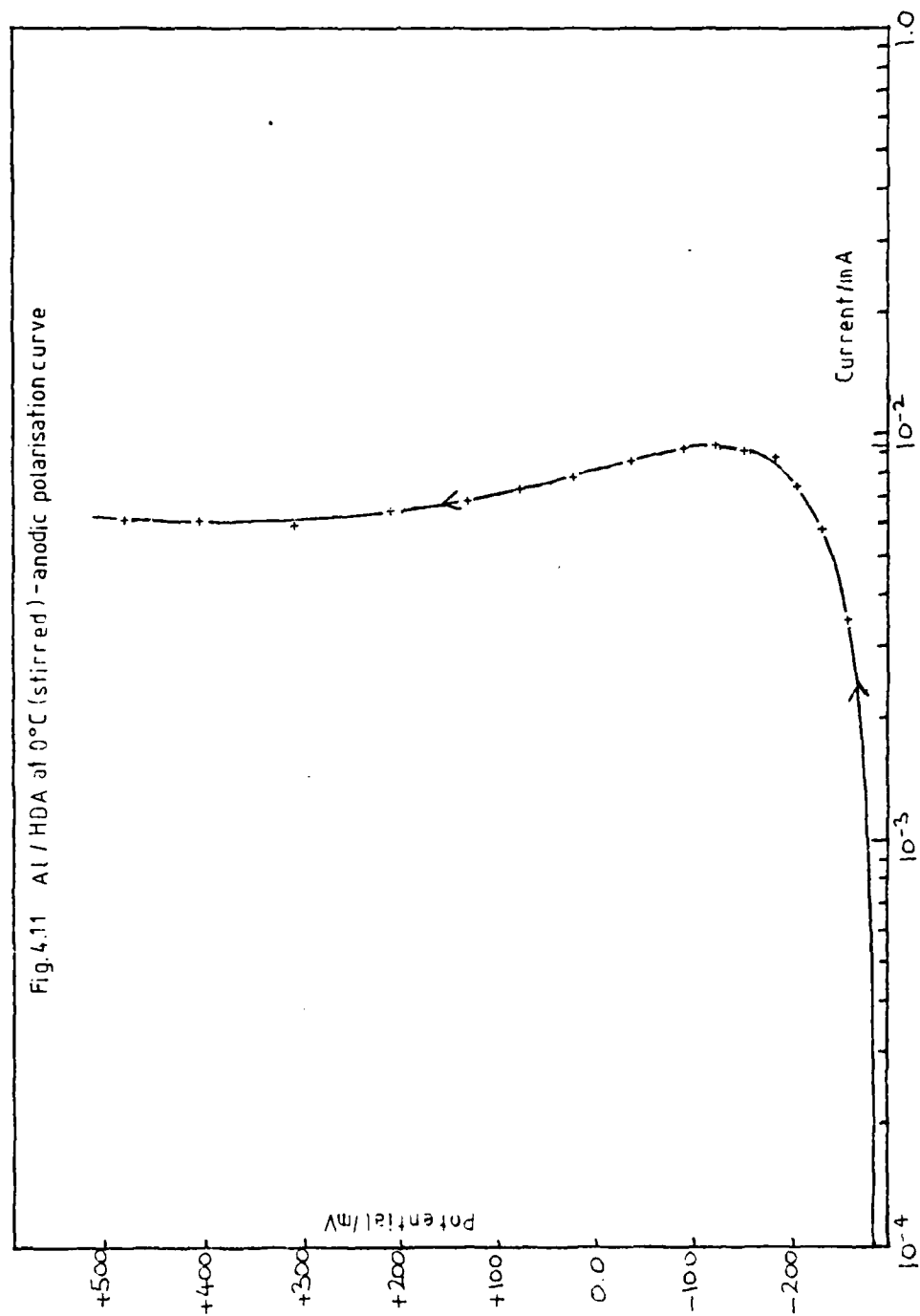
washed thoroughly with water and then inhibisol and finally

dried in a current of argon. This pre-treatment was also

used in the aluminium/HDA corrosion rate experiment[4.8] and also

in the aluminium tank experiment (see p.47, this report).

A series of polarisation curves was obtained for

aluminium in HDA (see Figs. 4.12 and 4.13). The cathodic

portion exhibits the expected Tafel behaviour for a 1 electron

reaction $(NO_2^+ + e^- \longrightarrow \tfrac{1}{2}N_2O_4)$. The anodic portion of the

curve displays a passivation 'nose'; this must be some form

of secondary passivation. The corrosion current (i_{corr}) is

sufficiently low to indicate that aluminium is passive in HDA.

At anodic overpotentials greater than 600 mV the curve indicates

film thickening behaviour. This film may actually be an

aluminium nitrate. Although this nitrate would be expected

to have a fairly high solubility in HDA it may be unable to

diffuse away from the surface (fast enough to dissolve) at high

anodic overpotentials, thereby producing an extra barrier to

corrosion. Alternatively, the film may be an aluminium oxide.

As the sample is anodically polarized the anodic and cathodic

reactions are still able to take place on the surface of the

oxide. However, at a certain current density, defects in the

film are healed and a passivation 'nose' is observed. Beyond

this current density the film simply grows thicker and no

increase in current is observed as the potential is raised.

Fig. 4.12   Polarisation Curve of Al in HDA

Temp. 20°C., Step Time 60 s
Step Voltage 40 mV, Scan Rate 0.67 mV s^{-1}
S/V 0.04 cm^{-1}

$E_{rp} = -695$ mV

$i_{corr} = 3.6 \times 10^{-6}$ A cm^{-2}

Current Density / A cm^{-2}

Potential / mV

Fig. 4·13

Anodic Polarisation Curve of Al in HDA

Potential/mV

	Temp.	Step Time
+	....20°C..............	....60 s
□	....20·5°C.........	....600 s
o	....20°C............	....60 s

	Step Voltage	Scan Rate
+	....45 mV.........	....0·75 mV s^{-1}
□	....45 mV........	....0·075 mV s^{-1}
o	....45 mV........	....0·75 mV s^{-1}

$S/V = 0·04$ cm^{-1}

Current Density/ A cm^{-2}
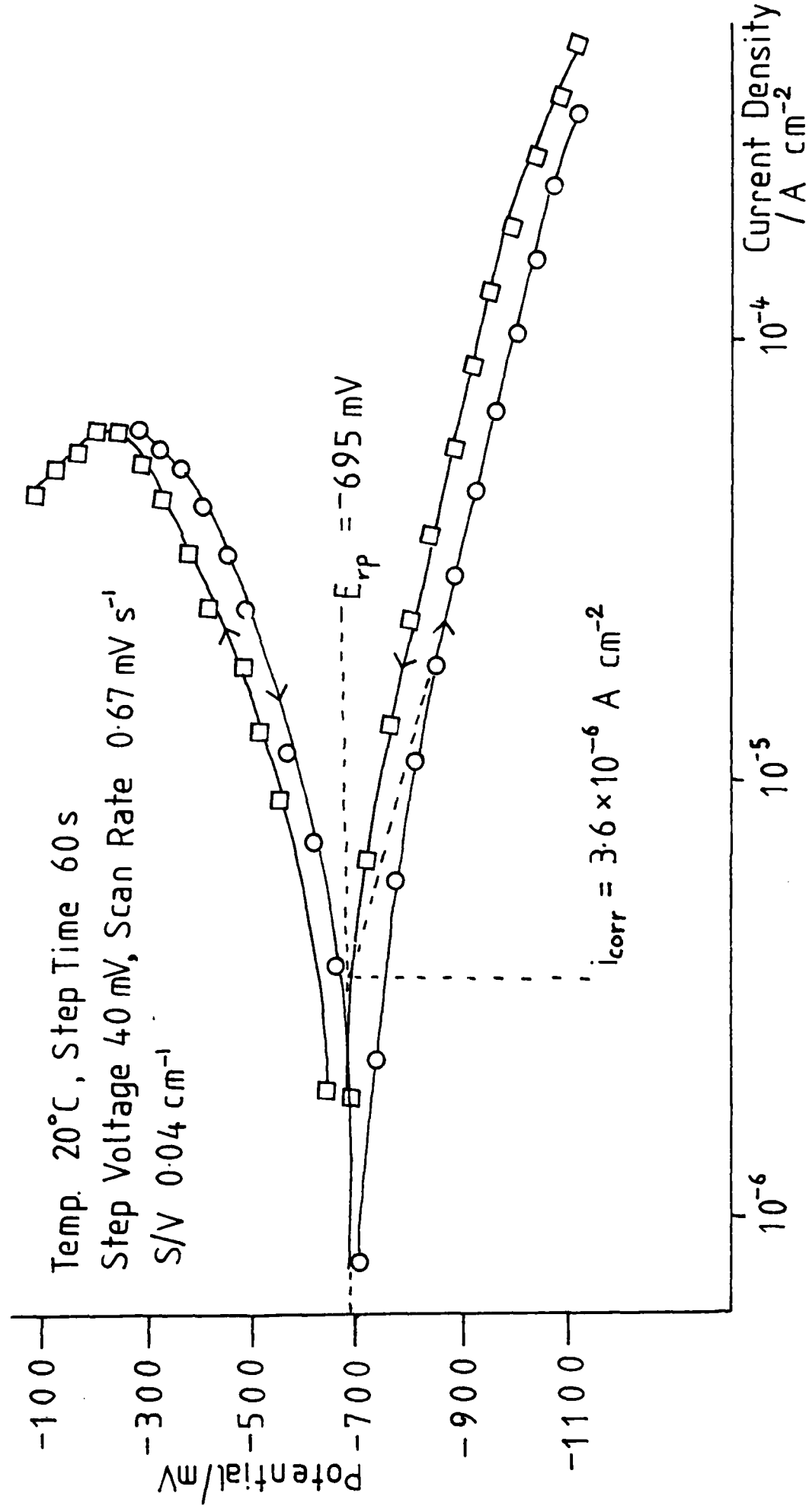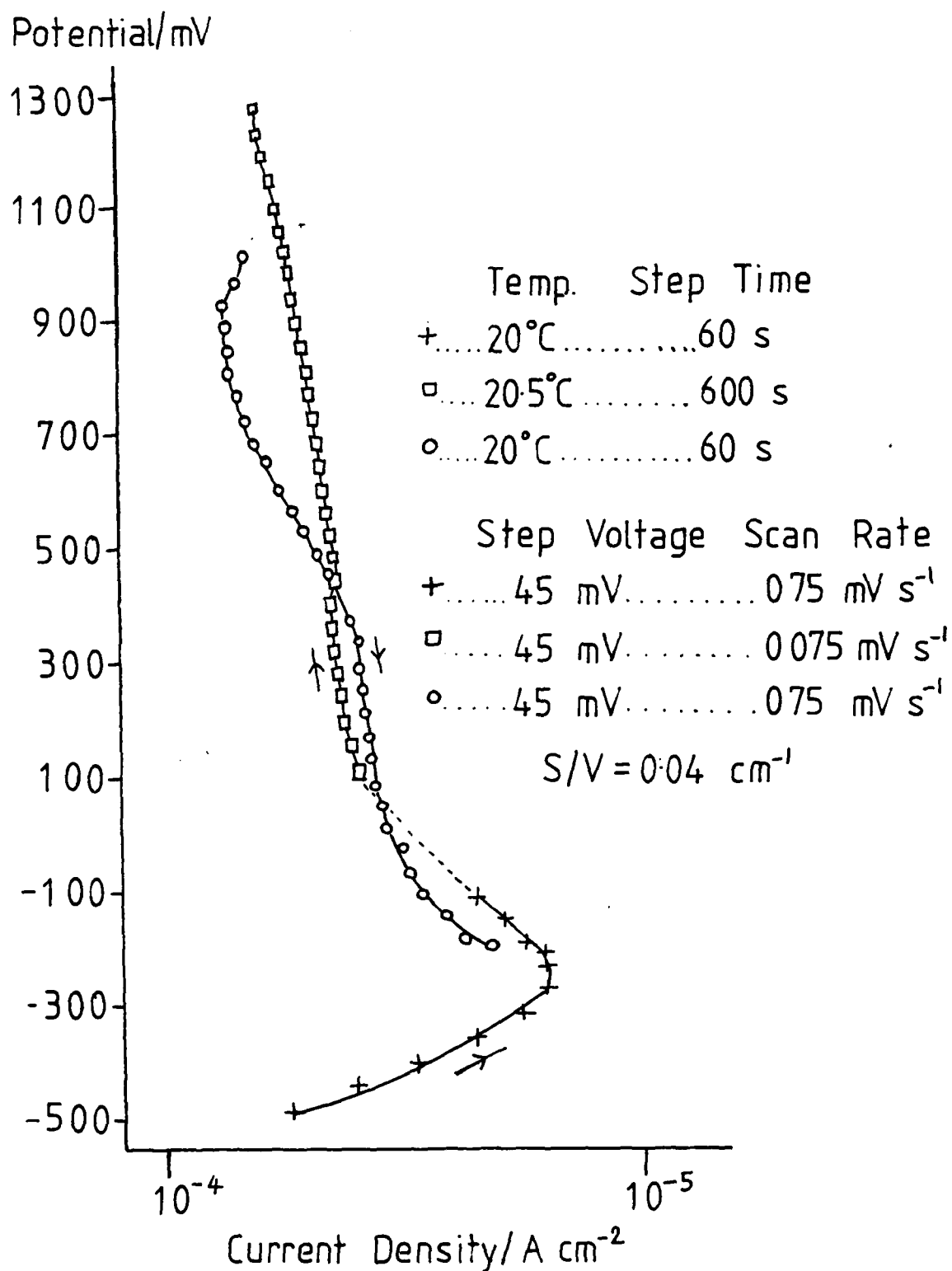
(d) <u>Al in HDA + P$_4$O$_{10}$ (0.84 wt%) at 0°C</u>

Results are presented in Table 4.6. The corrosion
currents are of the order of those obtained from Al in
pure UHDA, for comparable rest potentials

The cathodic curve (Fig. 4.14)
shows only one Tafel slope compared to two for Al/HNO$_3$
+ P$_4$O$_{10}$, possibly indicating different phosphate
species present. The anodic curve (Fig. 4.15) shows
that the 'nose' has been shifted to slightly lower
current values   (<u>ca</u> 1.60 x 10^{-2} mA) compared
to <u>ca</u> 5 x 10^{-2} mA for Al/UHDA, indicating that some
form of inhibition is taking place, though this
is very much less effective than for Al in HNO$_3$ + P$_4$O$_{10}$

Table 4.6   Electrochemical Parameters for Al in HDA + P_4O_{10} (0.84 wt %) at $0^{\circ}C$

($S/V = 0.090 \text{ cm}^{-1}$)

Date	Soln.	Tafel Slope $/V \text{ decade}^{-1}$	Rest Potential $/mV$	i_{corr} $/A cm^{-2}$
19/2/80	(1)	-0.169	-439.9	5.07×10^{-6}
19/2/80	(1)	-0.160	-448.2	3.86×10^{-6}

Fig 4.14 Al / HDA + 0.58g(0.84wt.%) P_4O_{10} at 0°C(1stirred) -cathodic polarisation curve

$E_{rp} = -439.9$ mV

Slope = - 0.169 V decade^{-1}

Current/mA

Potential/mV

Fig.4.15   Al / HDA + P_4O_{10} (0.58g , 0.84wt.%) at 0°C (stirred) - polarisation curves
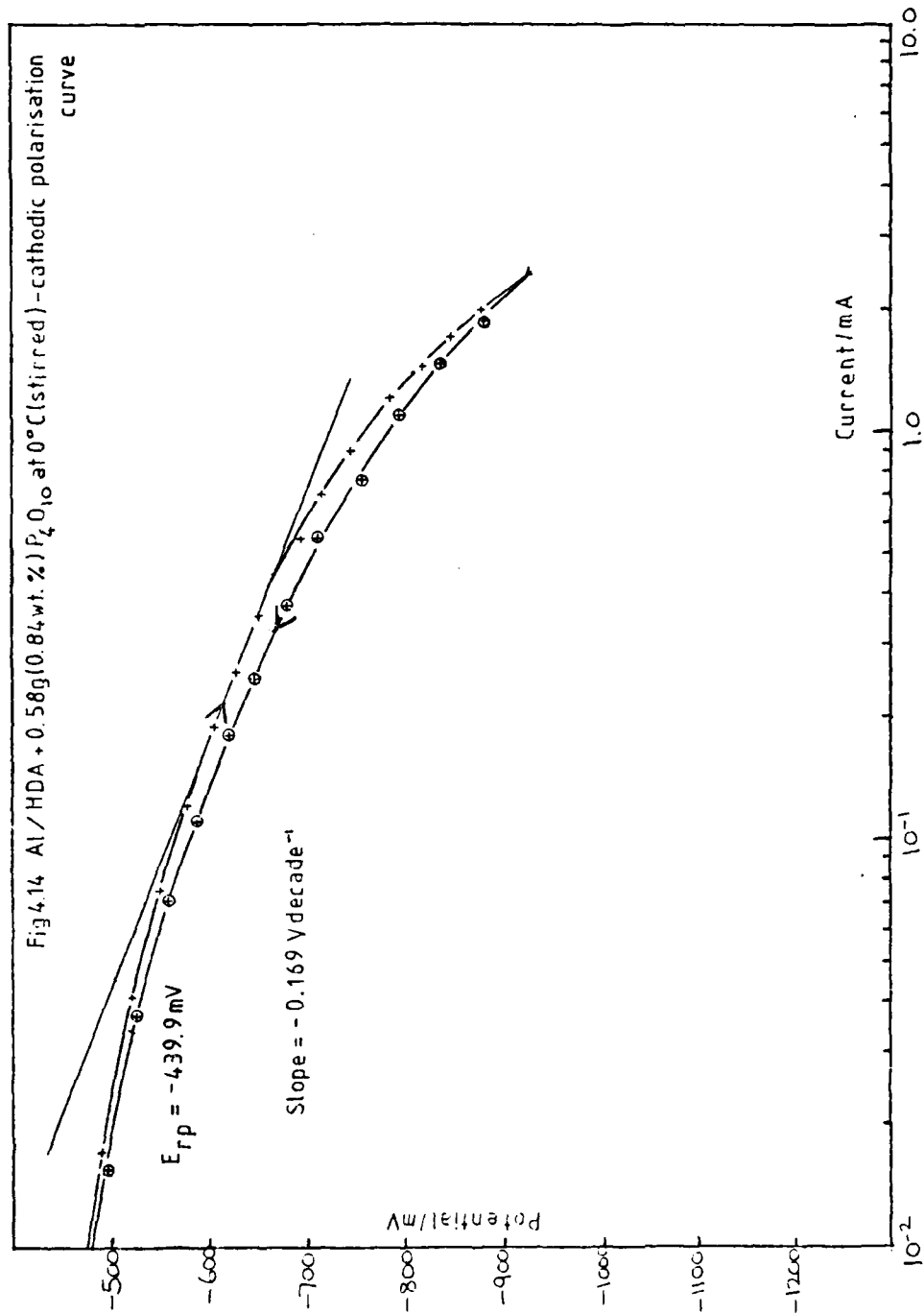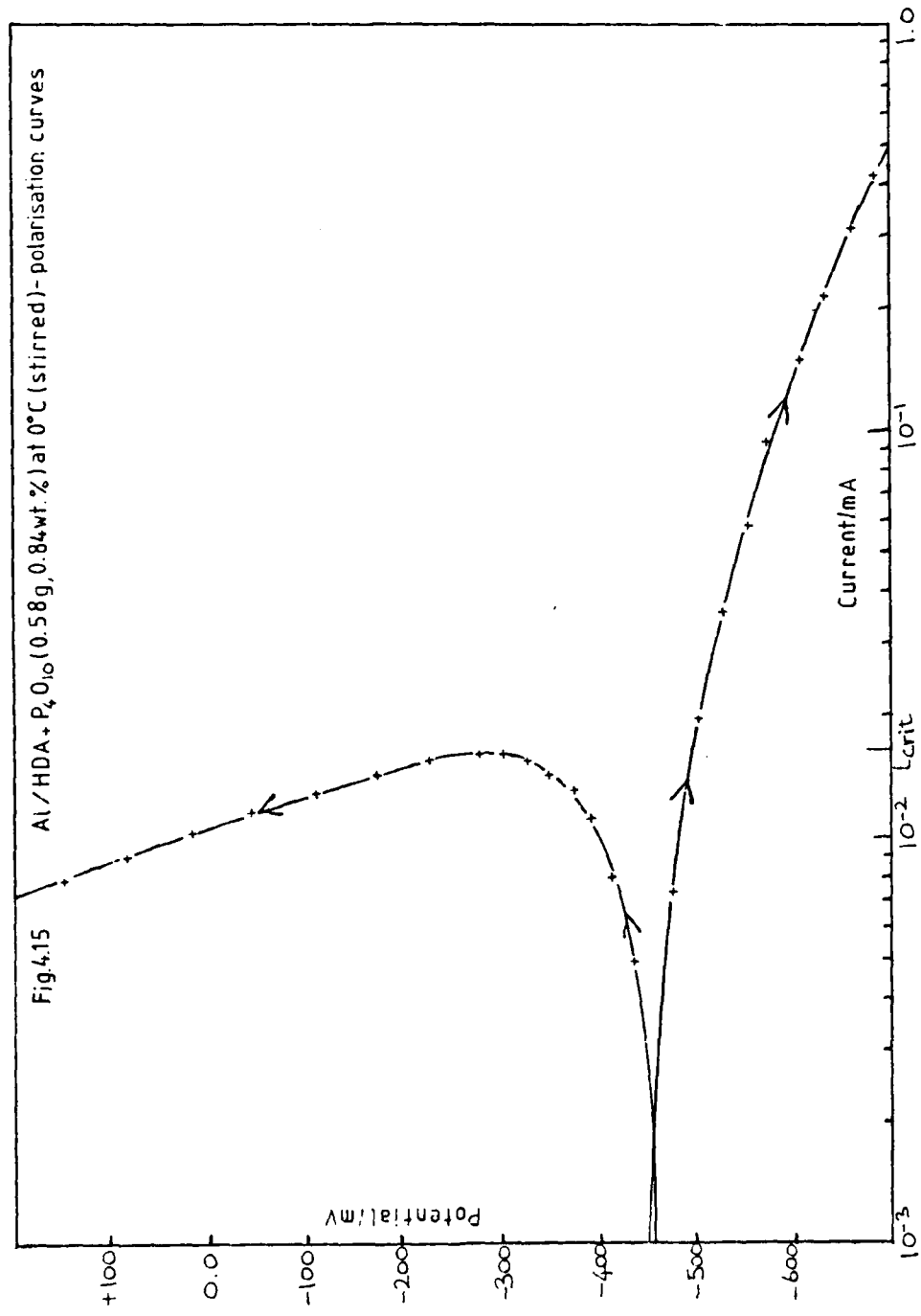
Al in HDA + P_4O_{10} (1.4 wt%)

The aluminium was pretreated as described on P.50 of this report. The P_4O_{10} in HDA solution was prepared by adding the required amount of HDA to a known weight of P_4O_{10} and stirring the mixture for 3 hours before immersing the electrode assembly in the medium. The instantaneous corrosion rate of aluminium in this medium was determined periodically using the polarisation resistance (PR) method. After 8 days it was not possible to make further PR measurements due to the shifting corrosion potential. The highest corrosion rate was observed after 5 days (Fig. 4.16). After 15 days (E_{rp} was periodically monitored during the 8-15 day period) the electrode assembly was removed from the medium and a sample of acid withdrawn for examination by ^{31}P n.m.r. spectroscopy. Only one peak was observed in the ^{31}P spectrum ($\delta_{85\%H_3PO_4}$ = -2.05 ppm) which was assigned to protonated orthophosphoric acid ($H_4PO_4^+$).

A freshly polished aluminium working electrode was fitted to the electrode assembly which was then immersed in the acid. The system was left overnight and the polarisation characteristics of aluminium in the medium were then investigated. (Fig. 4.17). The corrosion current (i_{corr}) was determined by the Tafel extrapolation method. The low i_{corr} value indicates that orthophosphoric acid is providing very effective inhibition, better in fact than HF and PF_5 (see Sections 4.2(g) and (h). The rest potential (E_{rp}) is however very similar to that observed

Fig. 4.16   Graph of Corrosion Rate vs. Time for P_4O_{10}-inhibited HDA (1.4 wt %)

Corrosion Rate × 10^4 (g m^{-2} hr^{-1})

Time/days
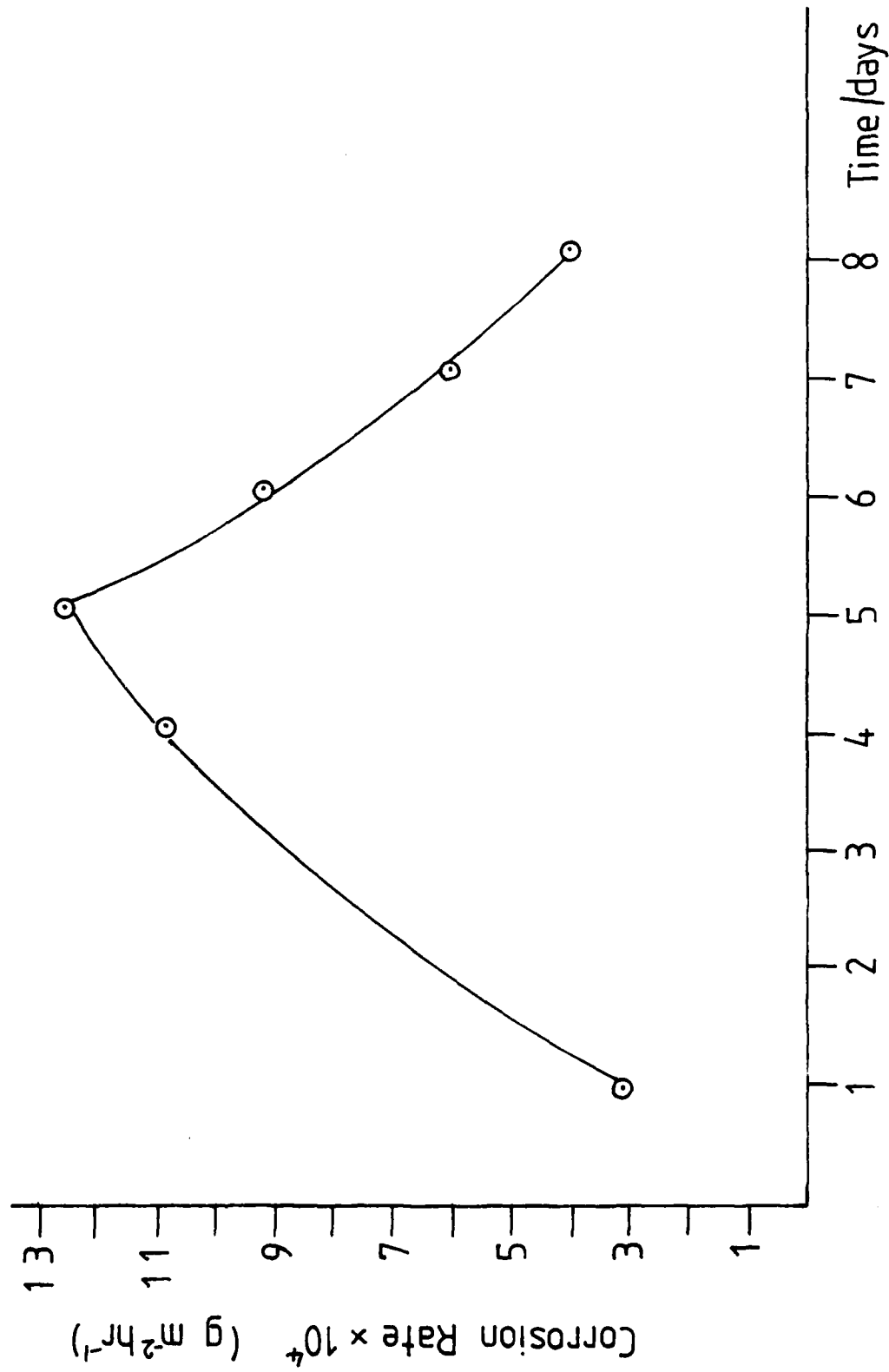
Fig. 4.17 Polarisation Curve of Al in HDA + 1.4 wt% P₄O₁₀

Temp. 22.5°C, Step Time 120 s
Step Voltage 50 mV, Scan Rate 0.42 mV s⁻¹
S/V 0.04 cm⁻¹

$F_{rp} = -715$ mV

$i_{corr} = 5.05 \times 10^{-8}$ A cm⁻²
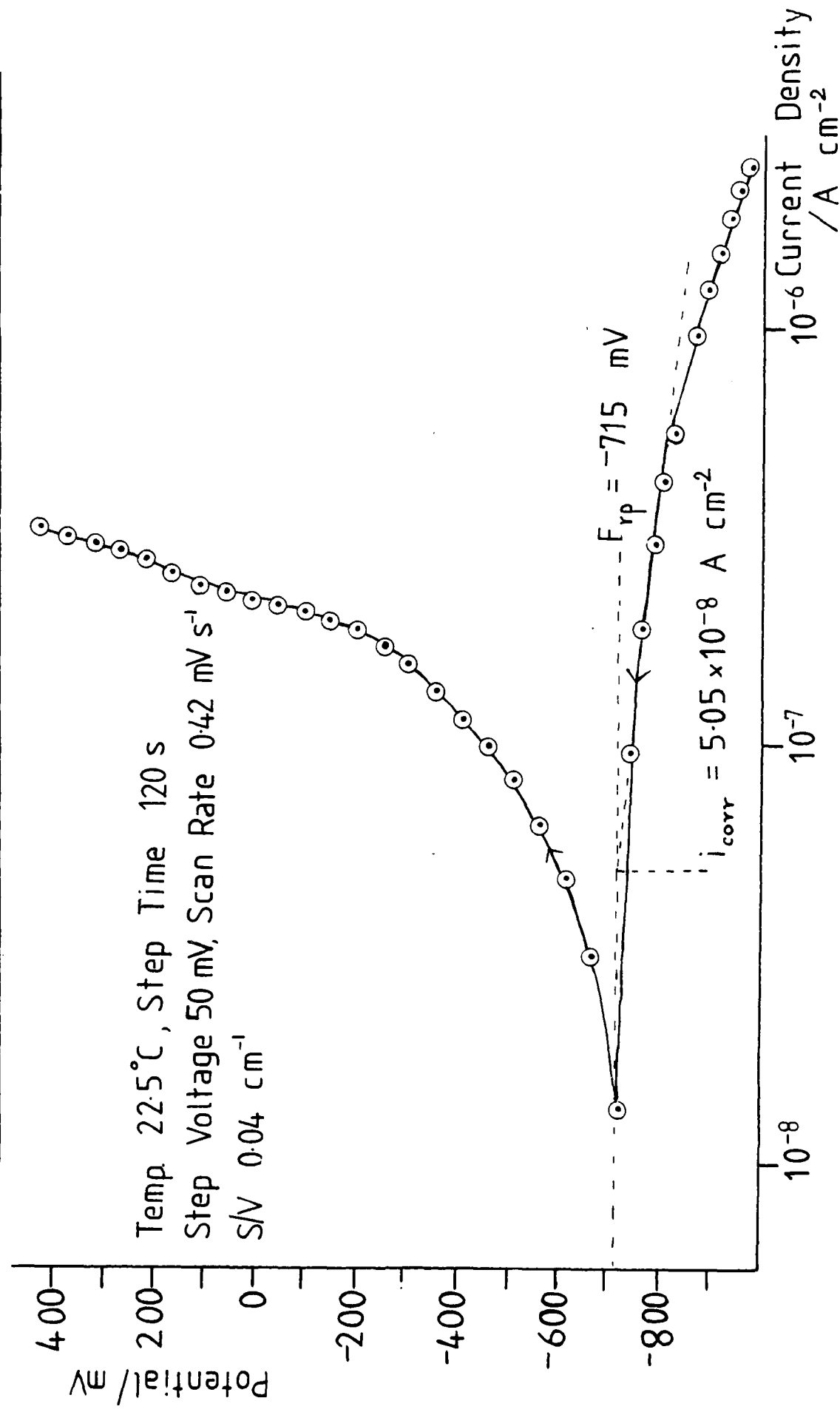
in HDA. The rest potential of the system was observed to decrease throughout the duration of this experiment. This effect may be due to inhibition of the cathodic reaction (rather than the anodic reaction) taking place. Clearly the effectiveness of P_4O_{10} as an inhibitor will depend upon the nature of the species in solution. Results indicate that the greater the extent of hydrolysis of P_4O_{10}, the better the inhibition.

(e) <u>Al in HDA + H_3PO_4</u>

Some figures are given below (Table 4.7) for Al in HDA + H_3PO_4 of different concentrations and purity. Once again, it can be seen from the cathodic curve (Fig. 4.18) that only one reaction occurs, in contrast to Al/100% $HNO_3+P_4O_{10}$. From the table it would appear that 0.60 wt% of 95% H_3PO_4 provides better inhibition than 1 wt% of 89% acid,

. The anodic curve (Fig. 4.19
shows only a small degree of secondary passivation in the
7 wt% case which is not observed in the 0.6 wt% case (Fig.4.20)

Fig.4.20 shows that a voltage of
<u>ca</u> +680 mV the current reached a maximum value but then decreased. It is not known why this should occur, but the film formed by H_3PO_4 could possibly delay the growth of the normal anodic   film and cause it to be formed at much higher potentials, which would explain the decrease in current;

Table 4.7 Electrochemical Parameters for Al in

HDA + 0.60 wt% H_3PO_4 (95% Purity) (S/V = 0.091 cm^{-1}) At 0°C

Date	Soln.	Tafel Slope /V decade^{-1}	Rest Potential /mV	i_{corr} /Acm^{-2}
31/3/80	(1)	-0.090	-195.44	6.64×10^{-7}

HDA + 1 wt% H_3PO_4 (ca 89% purity) (S/V = 0.089 cm^{-1})

Date	Soln.	Tafel Slope /V decade^{-1}	Rest Potential /mV	i_{corr} /Acm^{-2}
20/2/80	(2)	-0.158	-262.8	11.01×10^{-6}
20/2/80	(2)	-0.150	-265.9	8.45×10^{-7}

HDA + a further $0.81gH_3PO_4$ 89% purity added (2.17 wt %)

Date	Soln.	Tafel Slope /V decade^{-1}	Rest Potential /mV	i_{corr} /Acm^{-2}
22/2/80	(2)	-0.185	-226.0	1.06×10^{-6}

Fig.4.18 Al/HDA+0.69g(1wt.%)H₃PO₄ at 0°C (stirred)-cathodic polarisation curve

$E_{rp} = -262.8mV$

Slope = -0.158Vdecade^{-1}

Potential/mV

Current/mA

Fig. 4.19   Al/HDA + 0.69g(1wt.%)H₃PO₄ at 0°C (stirred)–polarisation curves

Fig.4.20 Al/HDA+0.60wt%H₃PO₄ at 0°C(stirred) - anodic polarisation curve

Fig.4.21 Al/HDA+0.36wt.%H₂PO₃F at 0°C (stirred) - cathodic polarisation curve

$E_{rp} = -104.48$ mV

Slope① = -0.1405 V decade⁻¹
Slope② = -0.095 V decade⁻¹

or the effect of the anodic film becomes more pronounced here.

Corrosion Rate of Al in HDA Containing 0.60 wt% H_3PO_4 (95% concn.) at $0^{\circ}C$

The corrosion current found (6.64×10^{-7} A cm^{-2}) corresponds to a weight loss of 2.23×10^{-3} gm^{-2} hr^{-1}. This is a factor of ca 3 less corrosive than Al in UHDA at $0^{\circ}C$. The polarisation resistance figure obtained was 2.12×10^{-7}A cm^{-2} ($7.10 \times 10^{-4} gm^{-2} hr^{-1}$).

(f) HDA + 0.36 wt% 'H_2PO_3F'

The H_2PO_3F used in these experiments was unfortunately exceedingly difficult to purify and an nmr spectrum taken on the sample prepared for thisstudy revealed the presence of H_3PO_4 and certain polymeric species. The H_3PO_4 was a permissible constituent, since it is present in Modified HDA of modest added water content,[4.9] but the presence of polymeric species was undesirable. Nevertheless, it was considered that an assessment of the system could still be made with some degree of success.

Table 4.8 lists all the important parameters concerning Al/HDA + 'H_2PO_3F' (0.36 wt%) at $0^{\circ}C$.

Table 4.8

Electrochemical Parameters for Al in HDA + 0.36 Wt%
'H_2PO_3F' at $0^{\circ}C$

Date	Tafel Slope	Rest Potential
13/3/80	-0.1295	
	-0. 102	-134.10
13/3/80	-0. 130	
	-0.1005	-127.70
14/3/80	-0.1405	-104.48
	-0. 095	(after anodic pol)
17/3/80	-0.1435	
	-0. 103	-103.85
17/3/80	-0. 138	
	-0. 102	-106.56

Fig. 4.21 shows the cathodic polarisation curve of Al in HDA + 0.36 wt% 'H$_2$PO$_3$F'. Two linear portions can be seen of slopes -0.1405 and -0.095 V decade^{-1}.

The anodic polarisation curve is shown in Fig. 4.22 and shows clearly that metal dissolution has been severly inhibited compared to Al/UHDA. The polarisation curve (2) indicates that a film is present on the Al surface, this film being quite stable in solution, since (2) was taken 16 hours after (1).

Corrosion Rate of Al in HDA + 0.36 wt% 'H$_2$PO$_3$F' at 0°C

The corrosion rate was impossible to obtain by the Tafel extrapolation method since there were two cathodic slopes, however, a polarisation resistance measurement, using cathodic and anodic slopes of 0.036 and -0.095 V decade^{-1} respectively, gave a figure of 1.59 x 10^{-8}A cm^{-2} (5.39 x 10^{-5}gm^{-2}hr^{-1}).

(g) HDA + 0.65 wt% PF$_5$ (MHDA)

This system was studied at various temperatures, and the relevant figures are given in Table 4.9. The duration of time for which the system was kept at a certain temperature, and also the total length of time from initial immersion is given.

The corrosion currents are based on polarisation resistance measurements, taking -0.090 and 0.036 V decade^{-1} (at 0°C) as the cathodic and anodic slopes respectively. No definite conclusions can be drawn from the above data, as there are too many variables one must consider, particularly the effect of time on the corrosion rate; this may be the dominating factor and temperature effects a secondary consideration. It will be

- 74 -

Table 4.9

Electrochemical Parameters for Al in HDA + 0.65 Wt% PF$_5$ (MHDA) at 0°C (S/V = 0.096 cm^{-1})

Date	Temp/ °C	Tafel Slope/ V decade	Rest Potential/ mV	i_{corr}/ Acm^{-2}
13/5/80	0 (left for 1 day; total of 1 day)	-0.100 / -0.088	-282.65	1.71x10^{-7}
19/5/80	15.4 (left for 3 days; total of 7 days)	-0.1275 / -0.086	-172.20	4.20x10^{-8}
16/5/80	-2.5 (performed on same day; total of 4 days)		-300.00	1.63x10^{-7}
16/5/80	4.6 (as above)		-273.30	3.41x10^{-7}
16/5/80	7.4 (as above)		-234.60	5.31x10^{-8}

Fig.4.22 Al/HDA+0.36wt.% H_2PO_3F at 0°C (stirred)
– anodic polarisation curve

② taken 16hrs. after ①

Fig.4.23 Al/MHDA at 15.4°C (stirred)
– cathodic polarisation curve

E_{rp} = –172.2 mV

slope① = –0.1275 V decade⁻¹
slope② = –0.086 V decade⁻¹
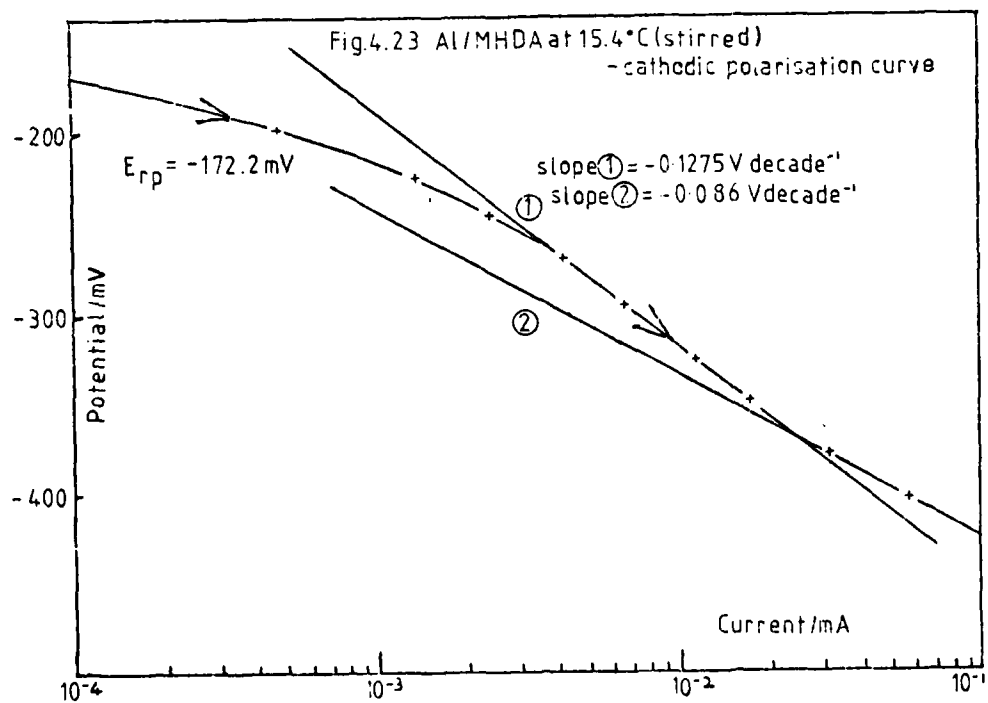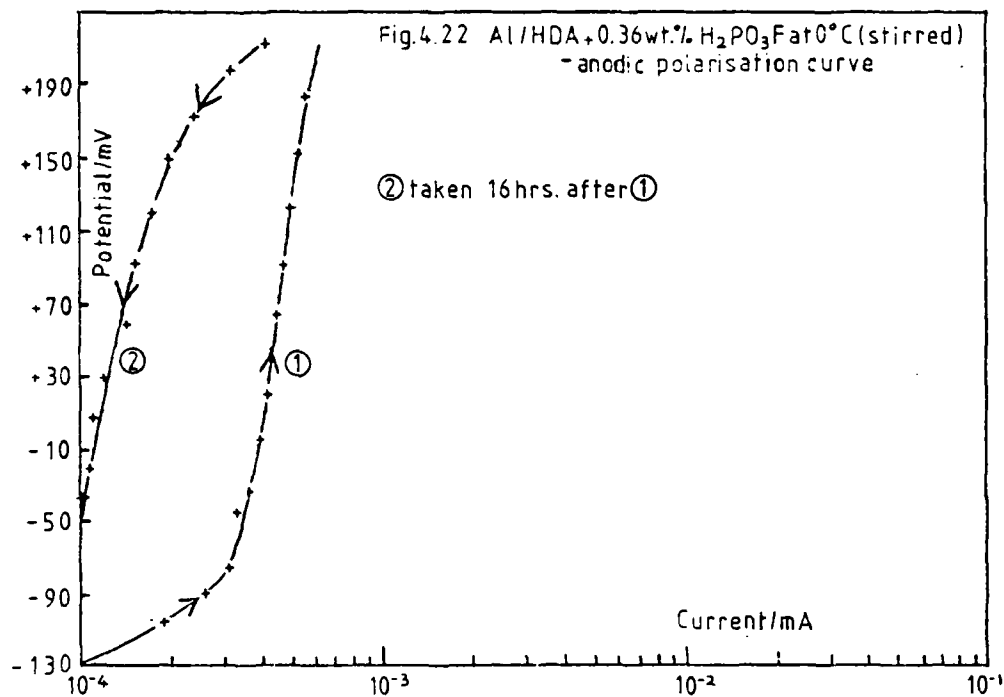
necessary to run the electrochemical cell at a certain temperature for some weeks in order to establish the full significance of temperature. Storage problems with the MHDA in the cell were also found, and a better sealed cell is required.

However, it can be said that the familiar double slope is present in this system as well (Fig. 4.23). It is interesting to note that at $0^{\circ}C$ the two slopes almost converge (Fig. 4.24). This phenomenon of two cathodic slopes has been observed by Våland and Nilsson[4.10] working with Al in an aqueous fluoride system, thus suggesting that this behaviour is due to some fundamental property of the fluoride ion when in contact with Al_2O_3, and is not due to the nature of the solution.

When one considers the anodic polarisation curve at $0^{\circ}C$ (Fig. 4.25) it can be seen that no passivation behaviour is exhibited, although at ca + 350 mV the anodic current decreases, in similar manner to the curve in Fig. 4.20 (0.60 wt % H_3PO_4). This kink is not seen in the anodic curve at $15.4^{\circ}C$.

In comparison with H_2PO_3F it seems that Al in MHDA has a greater corrosion current.

Al in MHDA at Room Temperature

The specimen was chemically pretreated (see p. 65, this report). The system was left for ca 1 day, in order to stabilize, after which time its polarisation characteristics were

Fig.4.24 Al/MHDA at 0°C (stirred)
-CATHODIC POLARISATION CURVE

$E_{rp} = -282.65$ mV

① = slope -0.100 V decade^{-1}
② = slope -0.088 V decade^{-1}

Fig.4.25 Al/MHDA at 0°C (stirred)
-ANODIC POLARISATION CURVE

$E_{rp} = -249.0$ mV
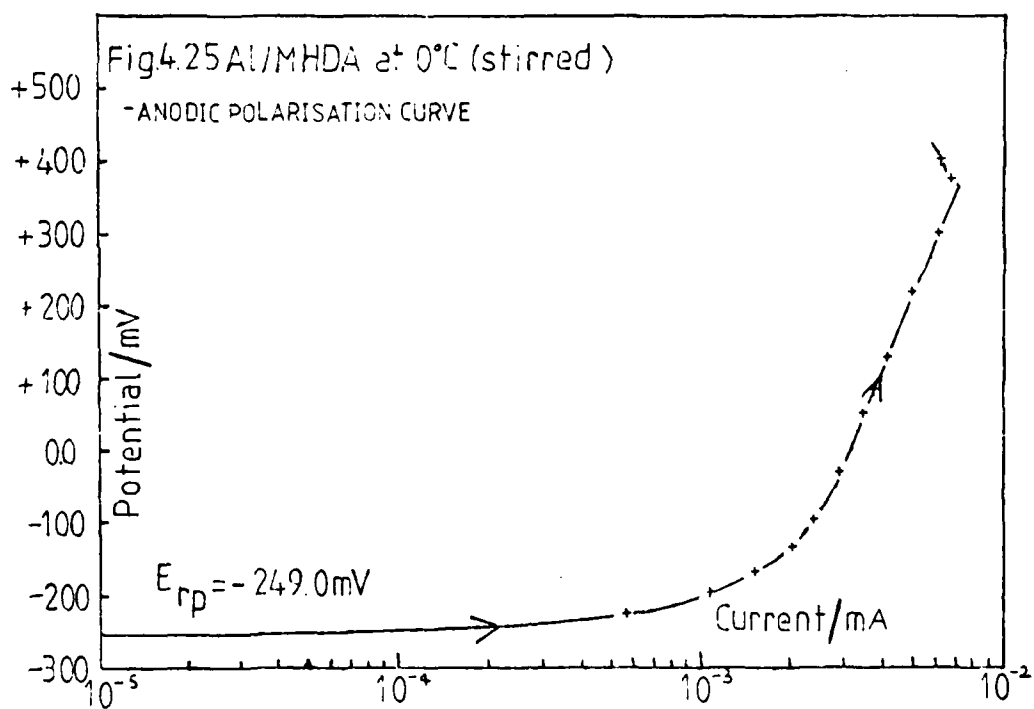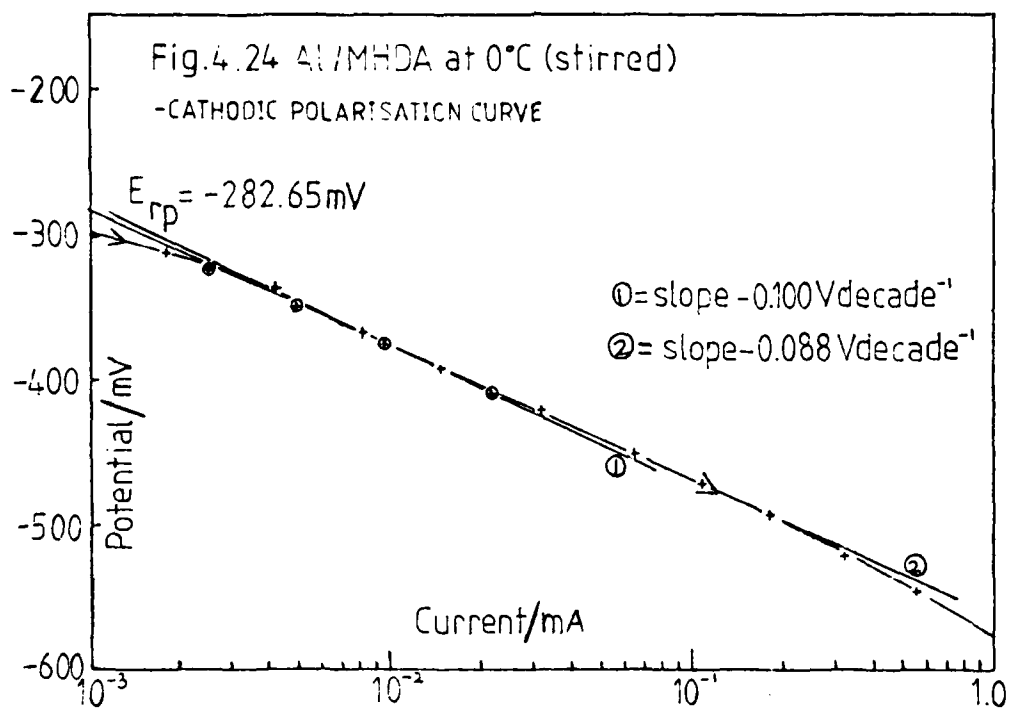
investigated. The curves obtained (Fig. 4.26) demonstrate
that aluminium is passive in this medium. The corrosion current
(i_{corr}) is an order of magnitude lower than the value obtained
for aluminium in HDA. The rest potential (E_{rp}) is considerably
more noble (i.e., more positive) in MHDA than in HDA (-265 mV
vs -695 mV). These results indicate that anodic inhibition
is occuring. The anodic portion of the curve is almost vertical
indicating that as the specimen is   polarised, the film grows
thicker. The cathodic portion of the curve between 50 and 200 mV
cathodic overpotential displays Tafel behaviour consistent with
a 1 electron reaction.

(h) Al in SHDA

The specimen was prepared using the chemical treatment
described on p.65 of this report. After immersing the electrode
assembly in the medium the rest potential of the aluminium
electrode (relative to a platinum reference electrode) was
monitored using a chart recorder (attached to the cell via a
high impedance DVM). The potential increased smoothly and
stabilised at ca -220 mV after 15½ hours. A series of
polarisation experiments were then carried out. At room
temperature the curve obtained (Fig. 4.27) was almost identical
with the curve plot obtained in MHDA (Fig. 4.26). Changing
the steptime (step times in the range 20-990s were investigated)
had little effect upon the shape of the polarisation curve.
These results indicate that HF is acting as an anodic inhibitor.

Fig. 4·26 Polarisation Curve of Al in MHDA

Temp. 22°C, Step Time 22s
Step Voltage 25 mV
Scan Rate 1·14 mV s⁻¹
S/V 0·04 cm⁻¹

$E_{rp} = -265$ mV

$i_{corr} = 1·27 \times 10^{-7}$ A cm⁻²

Potential / mV

10^{-6} Current Density / A cm⁻²

Fig. 4.27 Polarisation Curve of Al in SHDA

Temp. 20.5°C, Step Time 80 s
Step Voltage 40 mV
Scan Rate 0.5 mV s^{-1}
S/V 0.04 cm^{-1}

$E_{rp} = -305$ mV

$i_{corr} = 1.15 \times 10^{-7}$ A cm^{-2}

Potential/ mV

Current Density/A cm^{-2}
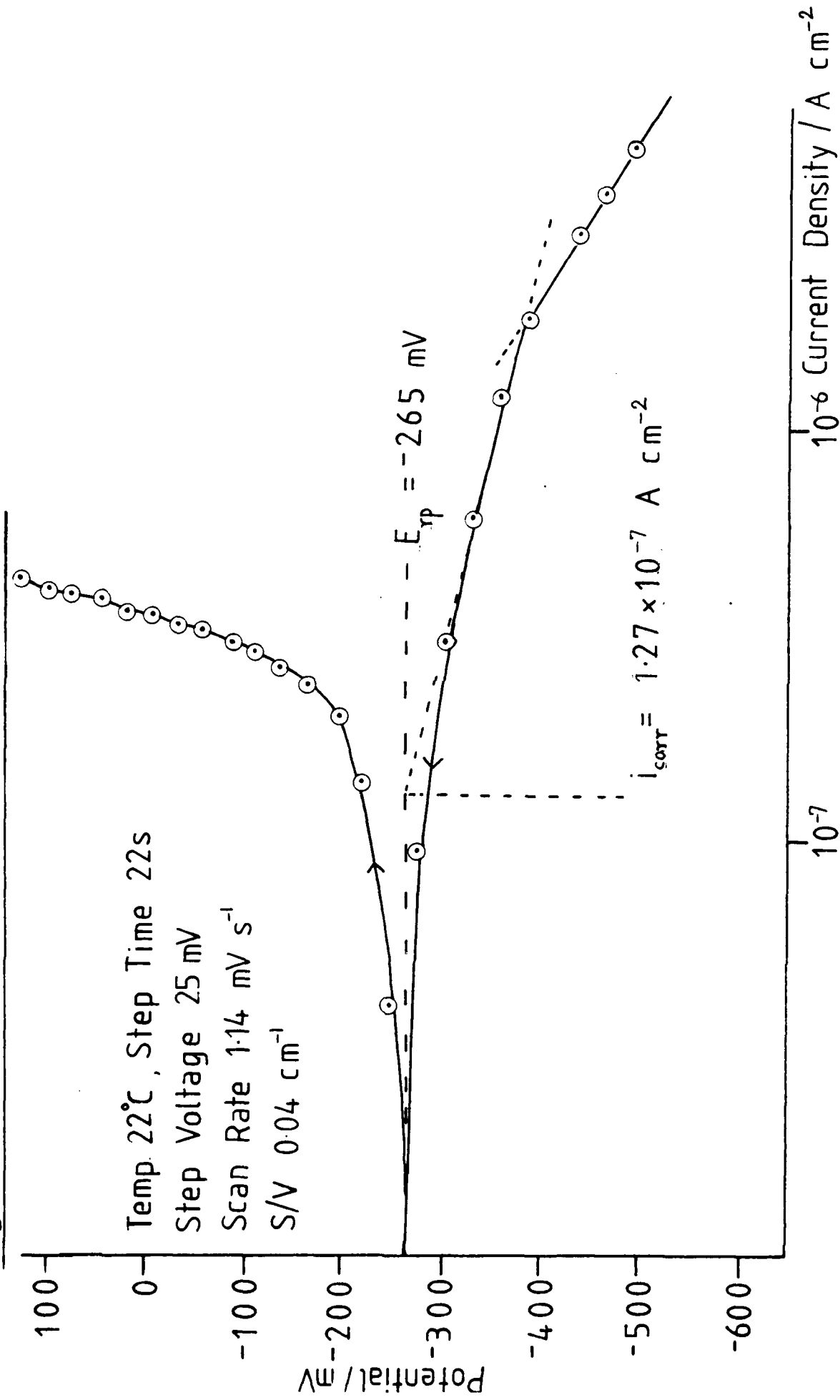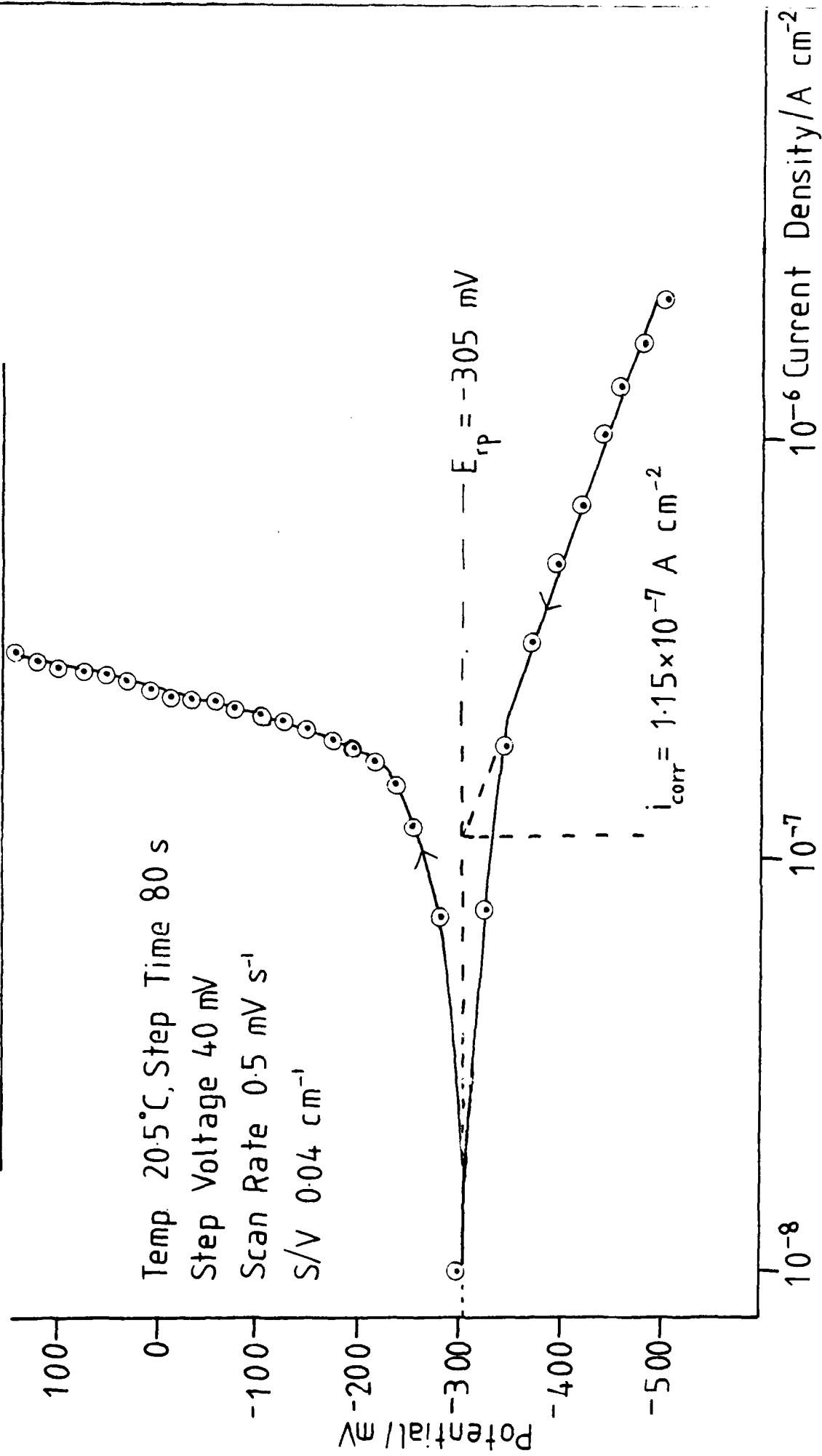
Upon polarising, the passive film formed in this medium grows thicker as was observed in the Al/MHDA system.

The behaviour of the system at $0^{\circ}C$ is very similar to that at room temperature, (Fig. 4.28).   There are a few differences:- the rest potential at $0^{\circ}C$ is less noble, the shape of the anodic portion of the curve is slightly different and its position is shifted to slightly higher current densities. These observations indicate that there is a thinner, less protective film at $0^{\circ}C$ than at room temperature.

(i)   Potential/Time Studies

The aluminium was pretreated by the polishing technique (p.50, this report). The corrosion potentials of aluminium in various media were monitored as a function of time using a chart recorder (via an impedance matching device).

The following media were investigated:- uninhibited HDA containing 0.7 wt% PF_5 (MHDA), HDA containing 0.6 wt% HF (SHDA) and HDA containing 0.4 wt% PF_5. The latter was investigated because corrosion rate data[4.11] indicates that 0.4wt% is the optimum PF_5 concentration. The results are summarised in Table 4.10. At the end of the experiments the aluminium specimens were retained and subsequently examined by S.E.M.   On the basis of the potential/time experiments the following conclusions can be drawn:-

Fig. 4.28 Polarisation Curve of Al in SHDA at 0°C

Step Time 180 s, Step Voltage 50 mV
Scan Rate 0.28 mV s⁻¹, S/V 0.04 cm⁻¹
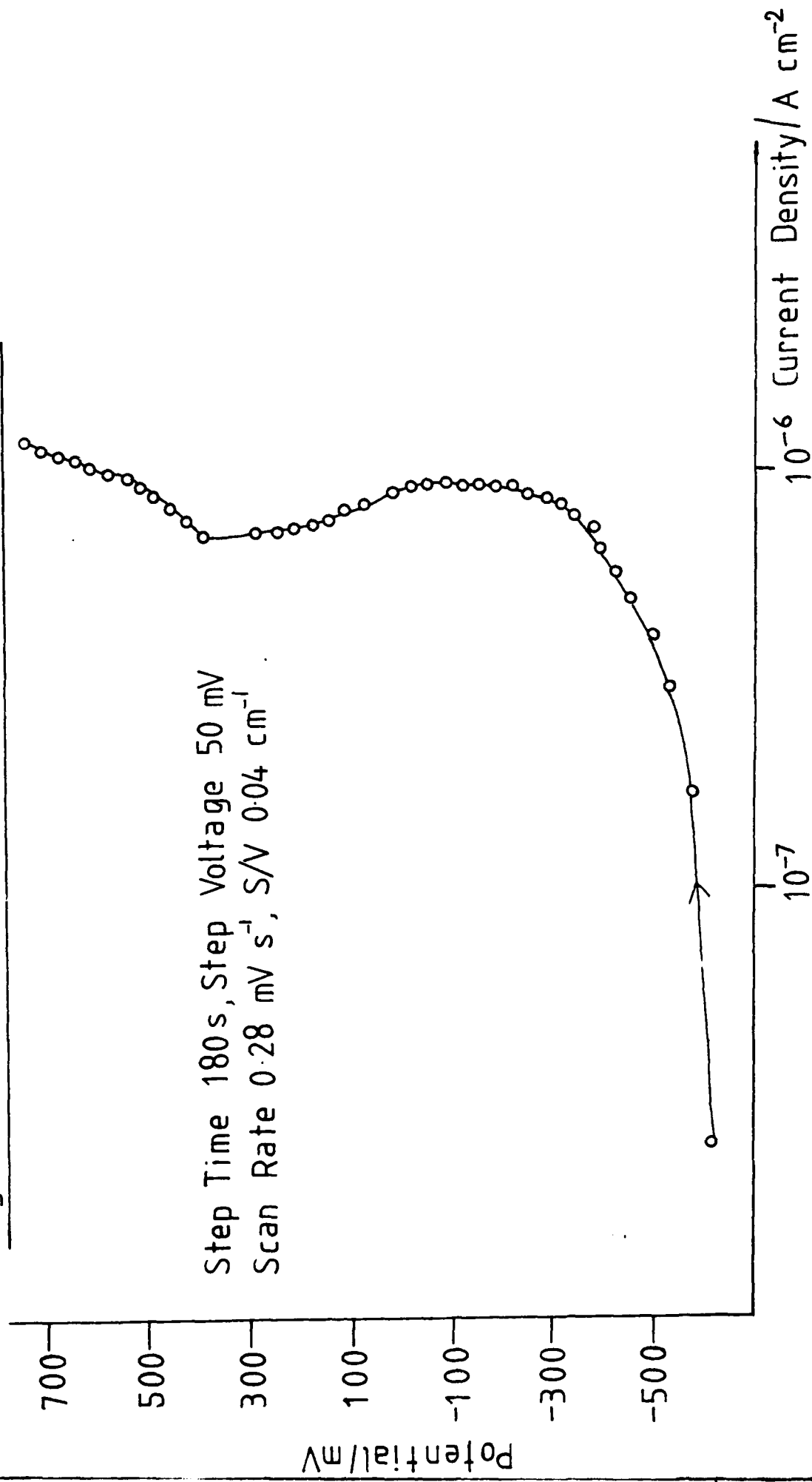
Table 4.10

Summary of Potential/Time Results For Aluminium in Various Media

	MHDA	HDA + 0.4 Wt% PF_5	SHDA	UHDA
Inital Potential (mV)	-318 (after 1 minute)	-168 (after 2 minutes)	-160 (after 1 minute)	-400 (after 1½ minutes)
Final Potential (mV)	-185	-60	-320	-700
Duration of Experiment (Hours)	239	555	238	132

(1) With inhibitors (HF and PF_5) present more noble values of E_{rp} are obtained. This behaviour is characteristic of anodic inhibitors (passivators).

(2) In inhibited systems a potential shift in the positive direction is observed immediately. This indicates that an inhibiting effect is conferred very quickly.

(3) The final potential obtained for 0.4 wt% PF_5 in HDA is more noble than that observed for MHDA, which is more noble than that observed for SHDA. This indicates that the passivating film is thicker in HDA containing 0.4wt% PF_5 than in MHDA and that the film in MHDA is thicker than in SHDA.

(4) In all systems sudden decreases in potential were observed. Following a sharp drop the potential gradually returned to a more noble value. These observations indicate that in all systems some form of random corrosion event (e.g., pitting or cracking and flaking of the surface film) occurs.

S.E.M. Observations

Consistent with previous results[4.12], an S.E.M. investigation of the aluminium specimen exposed to HDA (micrograph 4.1) revealed the presence of pits. No pits were observed on the surface of aluminium exposed to HDA containing 0.4 wt% PF_5 (micrograph 4.2). The whole surface

is covered with a film and certain regions with a thick

deposit (micrograph 4.3). Results obtained for aluminium

exposed to SHDA and MHDA are intermediate between the

uninhibited HDA and 0.4 wt% PF_5 cases. Although pits are

observed (micrographs 4.4 and 4.5) they are fewer in number

(per unit area) for SHDA and MHDA than for uninhibited HDA.

There are also regions covered with a thick deposit on the

aluminium surfaces exposed to SHDA and MHDA. The S.E.M. results

confirm conclusions drawn concerning film thickness on the

basis of potential/time experiments.

Note

All polarisation experiments in this Section were conducted

on a Thompson Ministat precision potentiostat using the potential

step method (see Sec. 3.2). Work with non-fluoride containing

systems was mostly conducted in glass apparatus similar to that

described elsewhere.[4.13] Work with fluoride containing systems

was carried out in fluoroplastic cells, the design of which

has been previously reported.[4.14]

(j) Conclusions

The electrochemical investigations carried out

indicate conclusively that HF and PF_5 function as anodic

inhibitors for aluminium in HDA. This inhibition takes

place by the formation of an insoluble surface film. Long

term rates can not be obtained electrochemically because

film formation is a lengthy and complex process.

The formation of colloidal material in solution
probably occurs when the protective film flakes off.
As a result, the corrosion is likely to be non-uniform. H_2PO_3F,
0.4 wt % PF_5 and P_4O_{10} (at concentrations around 1 wt %)
may provide better short-term inhibition than either
0.6 wt % PF_5 or 0.6 wt % HF. Long-term predictions,
based upon electrochemical results, are unwise but electro-
chemistry does allow a comparative assessment of short-
term inhibitor effectiveness to be made.

4.3 X-ray Photoelectron Spectroscopic (XPS) Studies

(C.L.E. Cole)

An introduction to XPS theory has been given already
(Ref. 4.1, p. 30).   This introduction requires a little
expansion, however, in the light of recent work.

Throughout the period of time in which XPS has been used
as an analytical tool by our research group, one of the main
problems that beset us was the lack of resolution afforded
by the instrument. The resolution can be enhanced by
selecting a lower analyser energy (the analyser provides a
means of analysing the energies of the electrons released by
X-   radiation), but this means that the magnitude of signal
detected is decreased. Clearly, a form of compromise must be
established, and it is common practice for operators to use
50 eV analyser energy and a time for full scan of 300 seconds.
These parameters were also adopted by the present research
group until recently when it was decided to experiment with
lower analyser energies and longer scan times in an effort,
primarily, to detect the expected existence of a peak on the
high binding energy side of the Al_2O_3 peak, denoting the
presence of fluoride.

The lowest analyser energy (10 eV) was used combined
with long scan times (1000 and 3000 seconds).

Another method of improving the resolution slightly is
to change the source of X-rays, i.e., from AlK_α to MgK_α;

this reduces the contribution of the inherent line width
from the source by approximately 0.2 eV.

XPS has been used to investigate the surface of Al after
exposure to:

(a) Uninhibited HDA

(b) $'H_2PO_3F'$

(c) HDA + 10% HPO_2F_2

(d) Pure HPO_2F_2

(e) Modified HDA

(f) Standard HDA

For control purposes the metal itself was examined. Various
pretreatments, including that described on p. 50,
were studied. The latter consisted of
abrading on SiC paper, and polishing on 8μ and 1μ diamond wheels,
followed by a further polish with 0.1μm Al_2O_3 paste. The spectrum
of the Al surface then showed a substantial amount of carbon,
and a smaller amount of silicon. The carbon could arise from
a number of sources, i.e., the diamond wheels, hydrocarbons,
adsorbed CO_2 and the SiC paper. It has been found that the
best pretreatment for use prior to XPS work involves using
an ultrasonic technique which cleans the surface, and considerably
reduces the C and Si peaks. In a number of cases, however,

these peaks still remain quite intense, and it is thought

that the SiC from the abrasive paper becomes so embedded

in the Al surface that even ultrasonic cleaning does not

remove it. Clearly, the use of SiC paper should be minimised.

Even assuming that the C level is negligible up to this

point, it has been observed that carbon contamination can still

occur inside the ESCA spectrometer. For example, Fig.4.29

shows the surface of an Al specimen that has undergone the

above pretreatment, and been kept in an inert Ar atmosphere

up to the point of entry into the spectrometer. The CIs

peak is intense and Si2p and 2s peaks are also visible. Fig.

4.30 is the XPS spectrum taken after approximately $3\frac{1}{2}$ hours,

and shows a more intense Cls peak and less intense Al 2p,

Al2s and O 1s peaks. It must be emphasised that no treatment

was given to the Al during the $3\frac{1}{2}$ hour period. It can be

seen that this carbon contamination, which almost certainly

comes from the pump oil, presents a problem during quantitative

analysis of a spectrum, unless one makes the dubious

assumption that the areas of the Al and O peaks are reduced

to the same extent by the presence of carbon (See p.89).

Consider the XPS spectrum of Al, pretreated as described above

and left overnight in a sample tube, although no attempt was

made to fill the tube with Ar (Fig.4.31). The Al peak can

easily be seen occurring to the low BE side of the Al_2O_3.

A computer deconvolution was taken of the spectrum (Fig.4.32) and

the relevant parameters are recorded in Table 4.11. Calibration of

Fig.4.29

(i)

Fig.4.30

C_{1S}

O_{1S}

(ii)

O_{Auger}

Si_{2S}

Si_{2P}

Al_{2P} Al_{2S}

Binding Energy
/eV

100   200   300   400   500   600   700   800   900

X P S spectra of AL (i) 'as received' (ii) after 3½ hrs. in spectrometer

Fig. 4.31

AL 2p

Au 4f

$\times 10^3$ c.p.s.

70   80   Binding Energy /eV
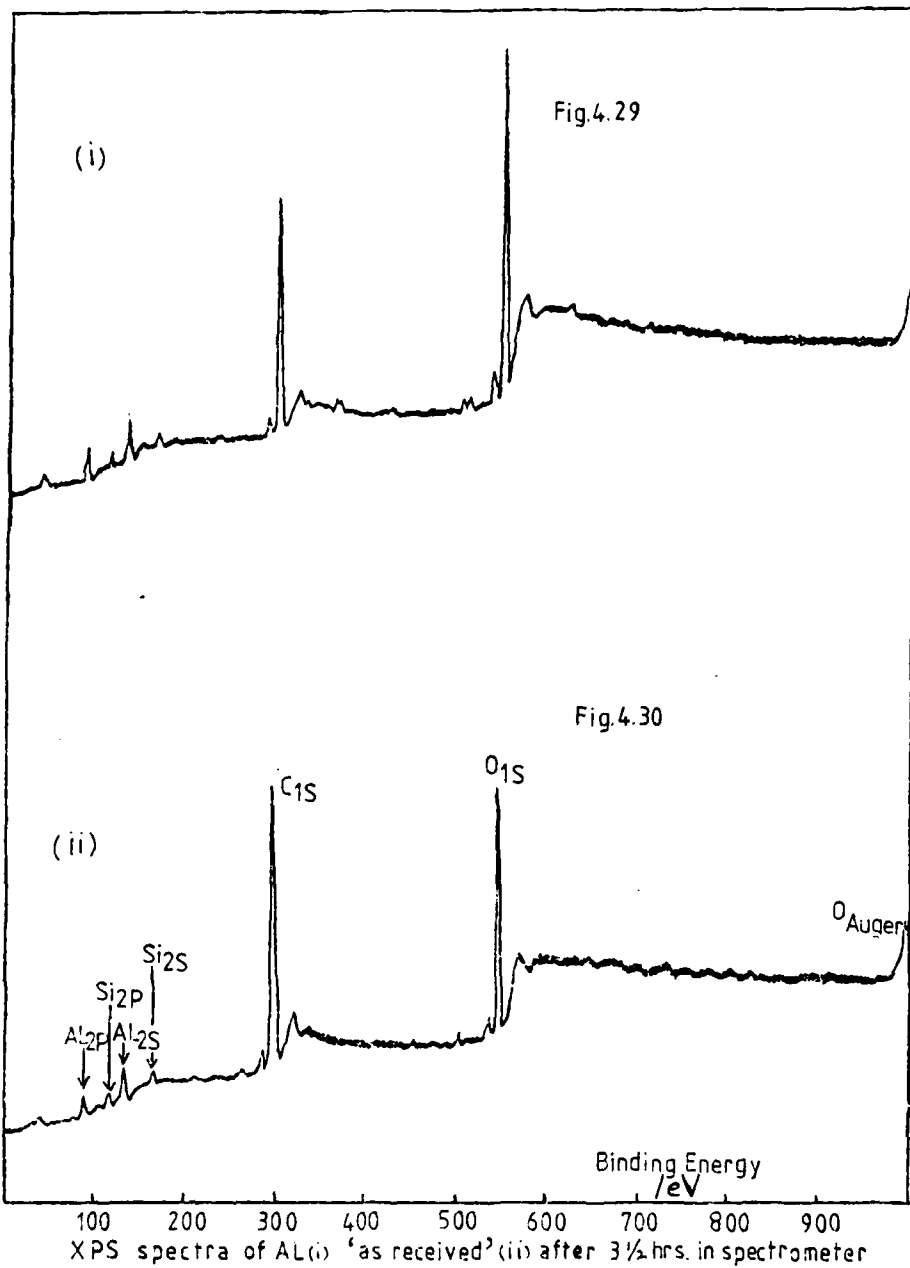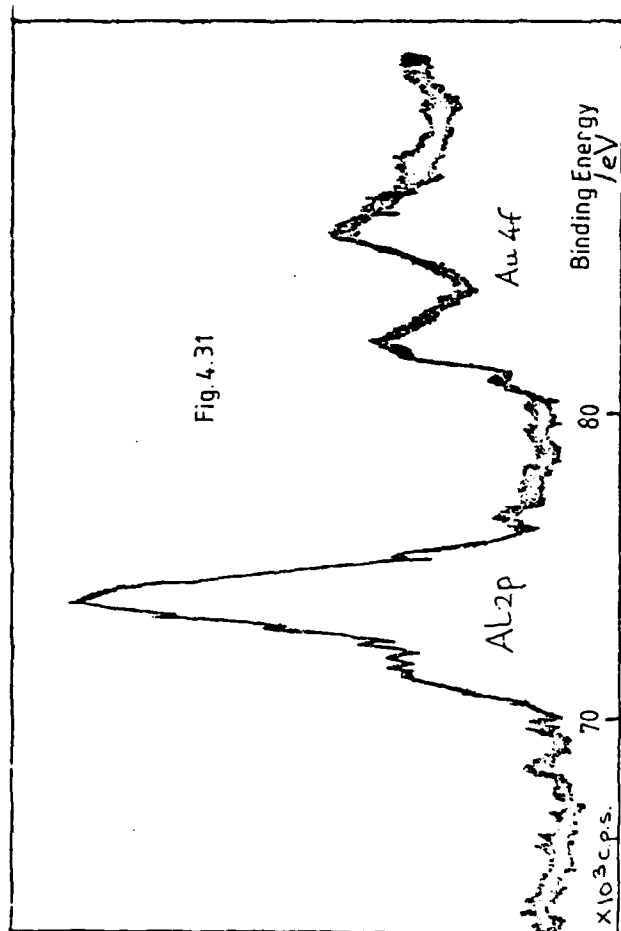
XPS spectrum of Al using 50eV analyser energy.

EXPERIMENTAL DATA

INDIVIDUAL CURVES

1412.7 VOLTS

AL2p

1414.9 VOLTS

Au 4f

1399.7 VOLTS

1403.6 VOLTS

Kinetic Energy(ev)

1404
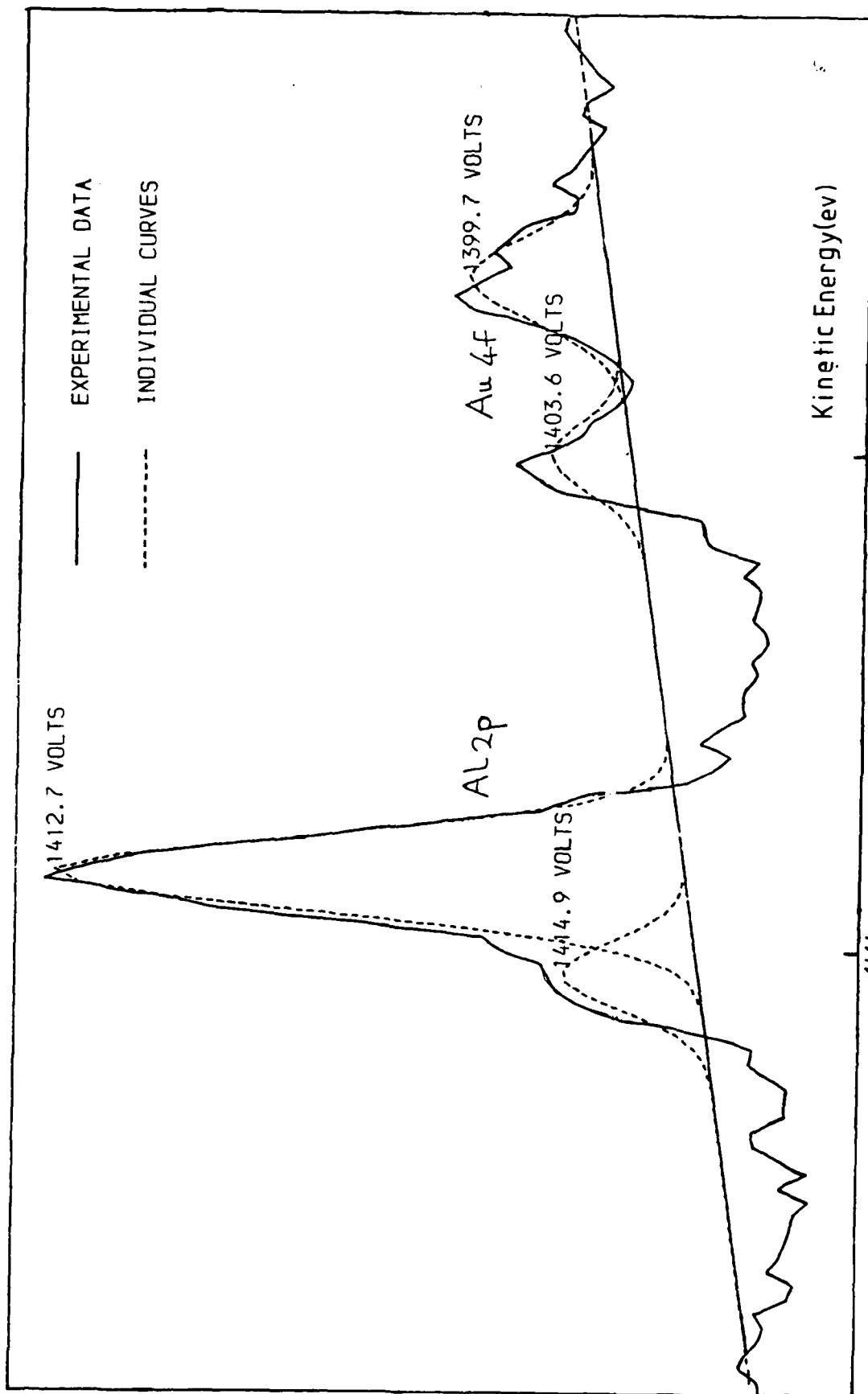
1414

Fig 4·32 Deconvolution of AL2p and Au 4f peaks.

Table 4.11   Deconvolution of XPS Spectrum of Al: Peak Parameters

Peak	Peak Height /counts sec^{-1}	Peak Position Kinetic Energy / eV	Width at half Height / eV	Area /counts sec^{-1}
Al	4.9096×10^2	1414.9	1.7381	9.08×10^2
Al$_2$O$_3$	2.2700×10^3	1412.7	1.9142	4.625×10^3
Au4f7/2	2.8825×10^2	1403.6	1.7381	5.333×10^2
Au4f5/2	4.9948×10^2	1399.7	2.0783	1.105×10^3

Table 4.12   Corrected Binding Energies (C 1s Standard)

Peak	Peak Position Binding Energy / eV	Literature Value[4.15]
Al	73.0	72.4
Al$_2$O$_3$	75.2	74.5

the spectrometer was accomplished using gold as external standard and assigning a BE of 84.0eV to the Au 4f7/2 photoline. The CIs line was also measured and had a value of 283.72eV. Taking the value of the CIs photoline as 285.00eV the correction factor for charging effects is 1.28eV, compared to 1eV for the Au 4f7/2 line. Taking the CIs as the standard, the corrected values for the spectrum are shown in Table 4.12. The figures obtained are reasonable compared to the literature values, and the separation between the Al and Al_2O_3 peaks (2.20eV) is close to the literature value of 2.1eV. The program output suggests that another peak was present close to the Al2p line and from the deconvolution curve it is possible to place an additional peak between the Al and Al_2O_3 peaks. This could correspond to an $Al(OH)_3$ or $AlO(OH)$ species, since the relative position is correct, and would mean that water from the atmosphere has reacted with the barrier layer of Al_2O_3. An attempt was made to fit an extra peak into the spectrum but this met with little success. It is still believed, however, that an additional species is present, and there is some evidence to show that inert atmosphere technique suppresses the formation of this species; however, the most recent spectra still need to be deconvoluted.

It is possible to calculate the thickness of the Al_2O_3 using the equation:[4.16]

$$A^{2p}_{Al_2O_3} / A^{2p}_{Al} = (1 - \exp(-d/\lambda)) / \exp(-d/\lambda)$$

Where A represents peak area obtained directly from the spectra, d is the oxide film thickness and Λ is the escape depth.

For an electron KE of 1389 eV the escape depth of Al_2O_3 is $13 \pm 2Å$.[4.16] If the same value is assumed for the metal then a direct estimate of the thickness of oxide film may be made.[*] Two other assumptions have been made, however, principally that although the deconvolution gives a sloping background, and cuts off a small base area on all the peaks, the relative area of $Al^{2p}_{Al_2O_3}/Al^{2p}_{Al}$ will remain approximately the same. The second assumption is that the area due to the additional peak is small enough to be neglected.

(a) Al in Uninhibited HDA

Figures 4.33 to 4.35 show the surface of Al after 53 days' exposure to uninhibited HDA. A small N(1s) peak, probably due to adsorbed nitrogen gas from the atmosphere, is visible in Fig.4.33. Surprisingly, after 36 minutes etching (Fig.4.34) there is still no sign of aluminium metal on the surface. It is necessary to etch for 47 minutes (Fig.4.35), with a typical argon ion current of $65\mu A$, to expose the metal. These results confirm that a very thick oxide film forms on the surface of Al exposed to uninhibited HDA. It is well known that certain solutions can provide an environment in which the thickness of the porous oxide layer formed on Al can extend over thousands of Ångstroms. It is suggested that uninhibited HDA is such a solution.

[*] The value obtained is $23 \pm 2Å$

Fig. 4.33

(i)

N_{1S}

O_{1S}

Fig. 4.34

O_{Auger}

(ii)

AL_{2P}

AL_{2S}

$Au_{4}f$

Au_{4d}

O_{2S}

C_{1S}

BindingEnergy
/eV

100   200   300   400   500   600   700   800   900
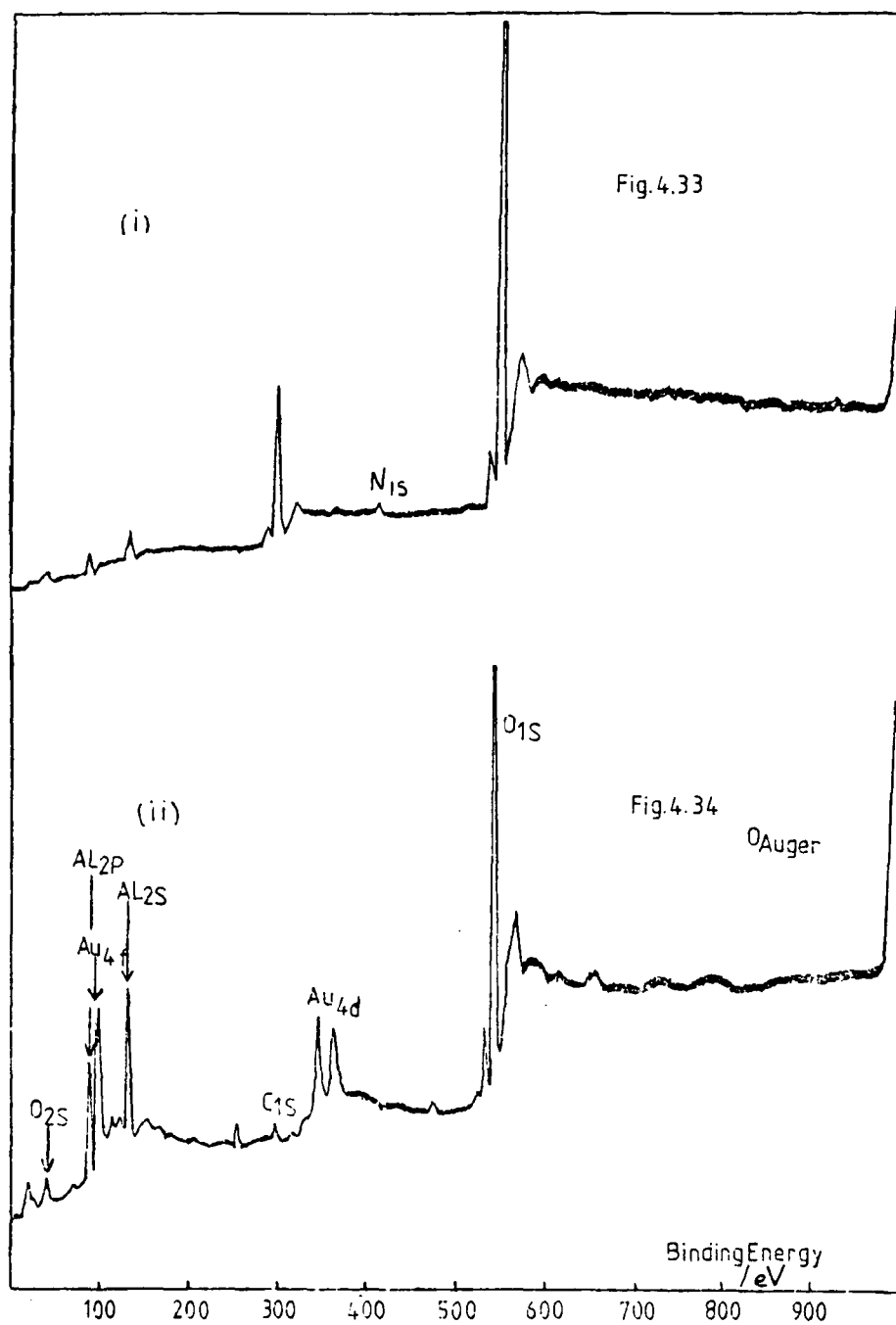
XPS spectra of AL/UHOA* (i) 'as received' (ii) after 36 min. etch (70 µA)

* left for 53 days

Fig.4.35

(i)

Au 4f

Al₂ₚ

3×10³ c.p.s.   70   80   90

(ii)

O1s   F1s

O Auger

F Auger

Al₂ₛ

Al₂ₚ P₂ₚ
          P₂ₛ   C1s   Fig.4.36
Au 4f
O₂ₛ

Binding Energy
/eV

100 200 300 400 500 600 700 800 900
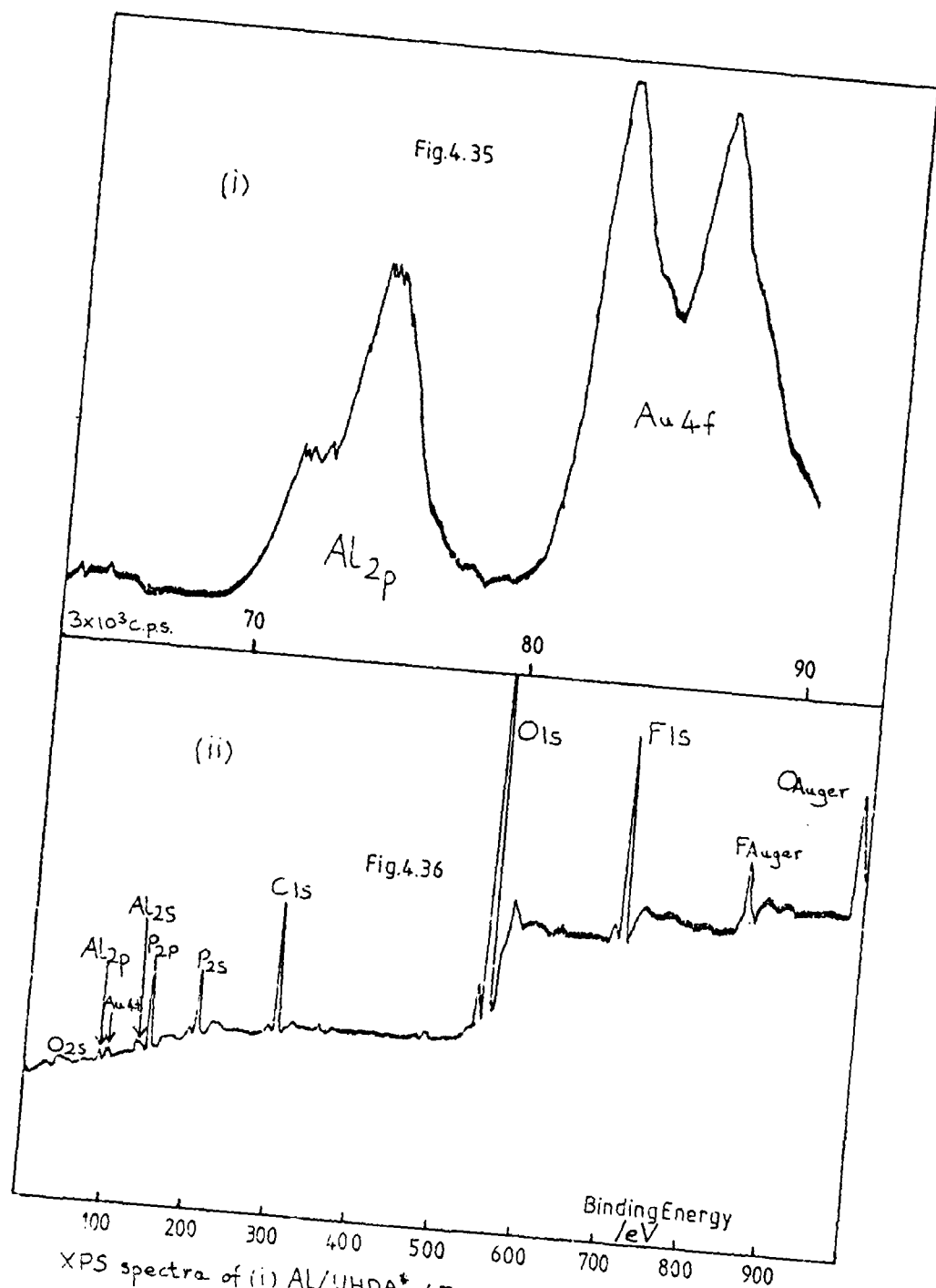
XPS spectra of (i) AL/UHDA*, 47 mins.etch (65μA) using 50eV
analyser energy, and (ii) AL/HPO₃F* ('as received'.
* Left for 53 days   ** Left for 2 days.

An interesting observation is that the intensity of the O(1s) line increases upon etching, reaching a maximum at about half the film depth, suggesting that surface impurities, e.g. carbon, decrease the intensity of the line.

It is hoped in future work to obtain a quantitative estimate of the film thickness by relating $A_{Al_2O_3}^{2p}/A_{Al}^{2p}$ to various periods of etching at a specified current, so leading to a figure that will give the amount of Al_2O_3 removed per μA of current. A number of difficulties are present however, principally:

(i) non-uniform etch. This is perhaps the most serious problem and involves the tendency for the ion beam to form pits or craters on preferential sites. Argon-ion etching, as a technique for estimating film thickness, has been used with a surprising amount of success, however.[4.17]

(ii) Reduction of the oxide to metal. This is a serious problem with many oxides, but with Al_2O_3, providing that the target current and energy are reasonably low, no such problem is envisaged owing to the very high bond energy.

(b) <u>Al in 'H_2PO_3F'</u>

The impure H_2PO_3F referred to in Section 4.2(f) was used.

With Al in 'H_2PO_3F' the 'as received' (i.e., non-etched surface) spectrum (Fig. 4.36) shows both phosphorus (2p and 2s) and fluorine (1s and Auger) peaks. Depth profile analysis revealed a greater concentration of P and F, as indicated by the

increased intensity of these peaks in the spectrum. Even
after 25 minutes etching time ($100\mu A$ target current) the
intensities of both the P and F peaks were still slightly
greater than in the 'as received' spectrum: this indicates
a considerable penetration. Fig.4.37 shows that after 15
minutes etching time the intensities of the P and F peaks are
considerably increased. It appears that the intensities of
the P and F peaks rise to a maximum and then decrease as the
etching time increases.

(c) Al in HDA + 10% HPO_2F_2

Fig.4.38 shows the 'as received' spectrum revealing a
small F peak that increases in intensity after a 2 minute etch
(Fig.4.39). This is to be expected, since in Fig.4.38
considerable surface contamination suppresses the appearance
of the Al(2p and 2s) peaks. However, after 5 minutes total
etching time at $\underline{ca}$ $60\mu A$ (cf. Fig.4.39) the F peak decreased
significantly in intensity, and this indicates that surface
penetration of F did not occur to the same extent here as with
neat 'H_2PO_3F'. This may have been due to the dilution effect
of HPO_2F_2 with HDA. ^{31}P n.m.r. spectroscopy has shown that
HPO_2F_2 undergoes some hydrolysis to H_2PO_3F and HF in HDA (see
Section 2.2(d) and Table 2.5). Since the reaction of 10% HPO_2F_2
in HDA with aluminium was carried out in a glass vessel, the
presence of the Na and Mg peaks visible in Figures 4.38 and 4.39,
and attributable to attack on glass, can be understood.

(i)

O2S F2S P2p P2S

Fig.4.37

(ii)

450 Na 1s AL2S Si2p AL2p Au 4f Si 2S C 1s mg Auger Au 4d N 1s Na Auger O1s F1s F Auger O Auger

Fig.4.38

Binding Energy /eV

100 200 300 400 500 600 700 800 900
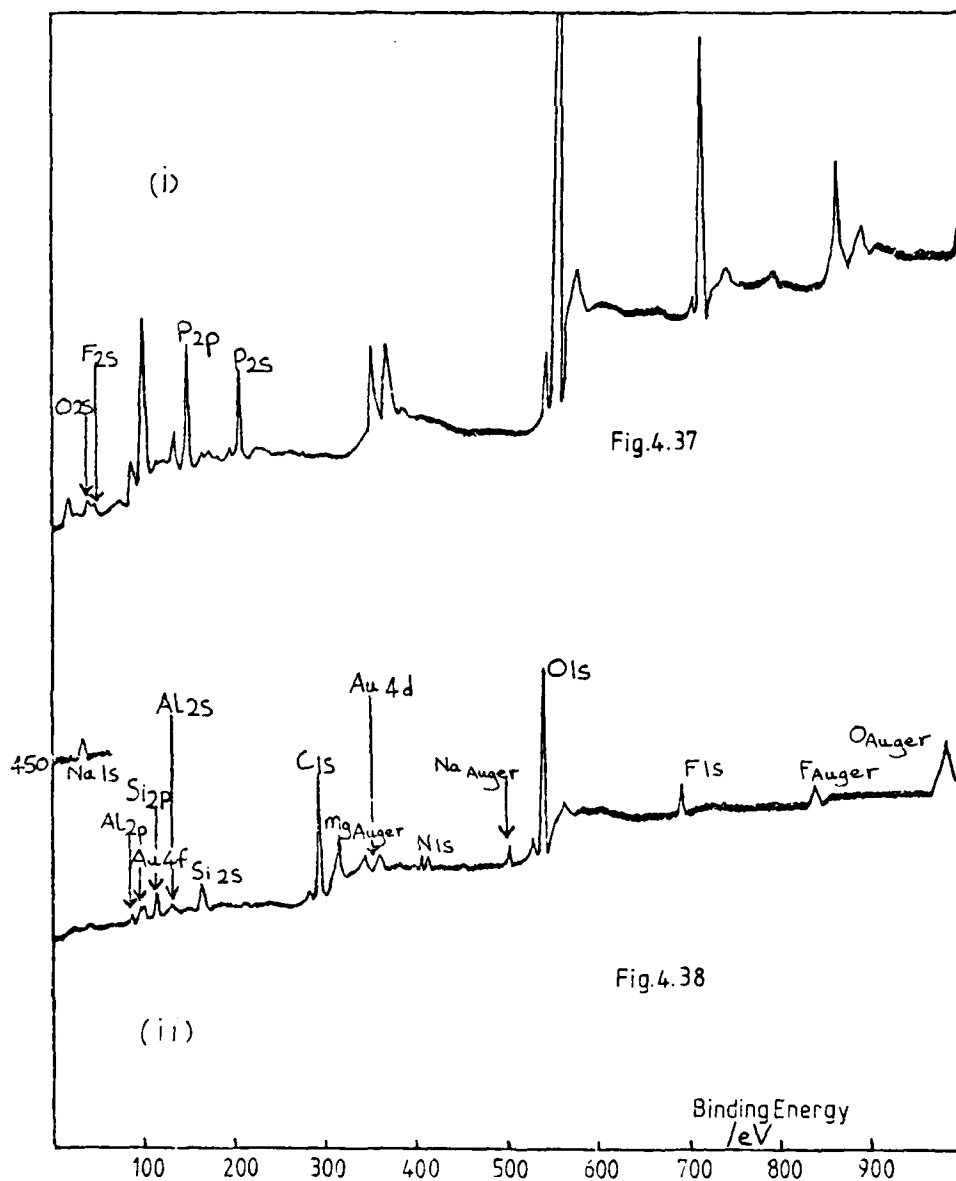
XPS spectra of (i) AL/H₂PO₃F* 15 min. etch, and (ii) AL/HDA
+ 10% HPO₂F₂*, 'as received'.
*Left for 2 days.

Fig.4.39

Fig.4.40

(i)

Mg Auger

Na Auger

(ii)

O Auger

F 1S

F Augers'

O 1S

C 1S

Al 2S

Au 4f

Al 2p Si 2S

Si 2p

F 2S

O 2S

B

P 2s

Au 4d N 1S

Binding Energy
/eV

100   200   300   400   500   600   700   800   900
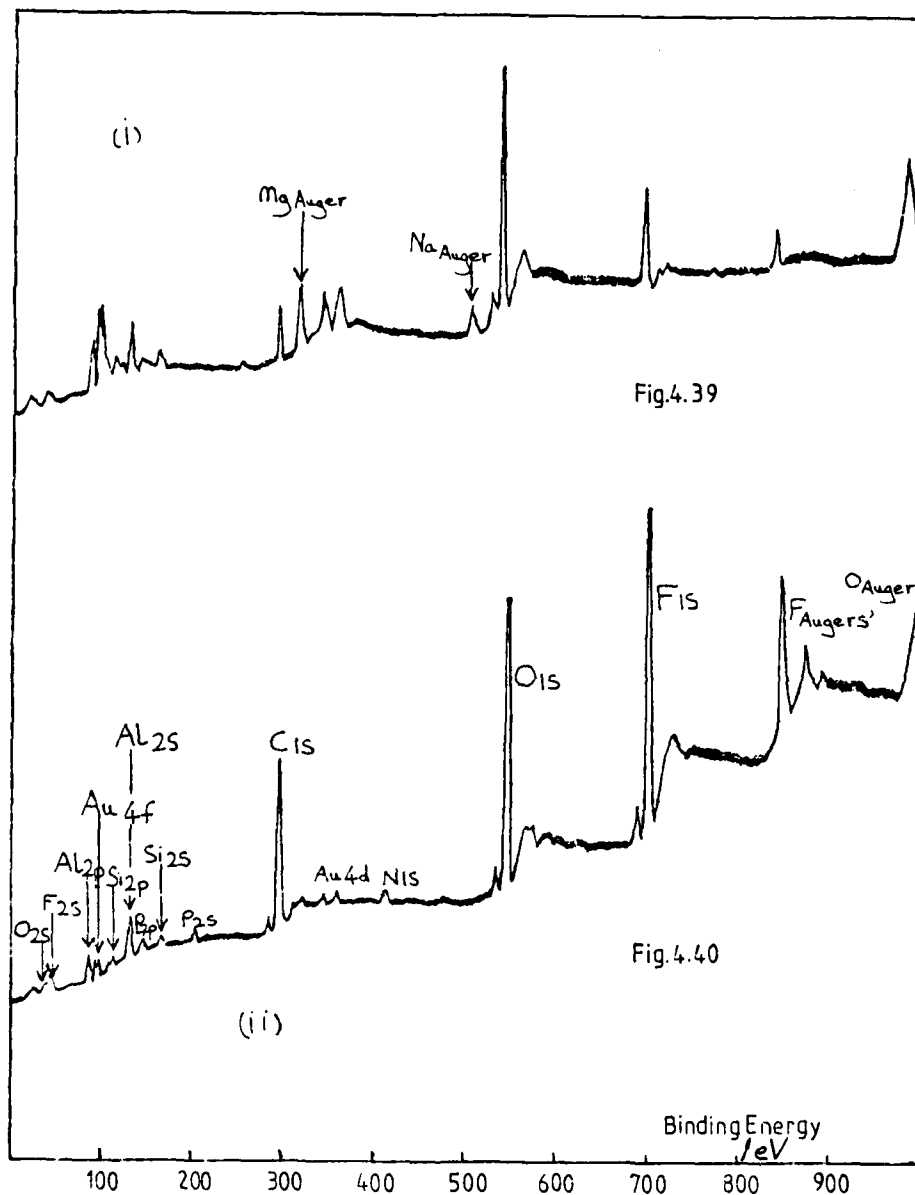
XPS spectra of (i) AL/HDA + 10% HPO₂F₂* after a two
minute etch (ca. 60μA), and (ii) AL/HPO₂F₂** 'as received'
* left for 2 days, ** left for 11 days

No P peaks were observed, indicating that only the fluoride ion penetrated the surface; not a fluorophosphate species. This contrasts with the above result for H_2PO_3F. It is to be expected that the F^- anion will enter the Al_2O_3 lattice and replace O^{2-}, owing to almost identical ionic radii ($F^- = 1.36\text{Å}$, $O^{-2} = 1.40\text{Å}$)[4.18], as recently proposed by other workers.[4.10]

(d)   Al in Pure HPO_2F_2

Pure HPO_2F_2 was vacuum distilled onto the Al specimen in a fluoroplastic vessel in order to eliminate hydrolysis and consequent attack on glass, and the residual acid was distilled off after a period of 11 days.

Figures 4.40 to 4.43 show the surface of Al after this duration of exposure to neat HPO_2F_2. Fig.4.40 shows a very intense fluoride peak, which suggests that Al might be capable of

Fig.4.41
(i)

Labels on spectrum (i): O2s, F2s, Al2p, Si2p, Si2s, Al2s, Au4f, C1s, Au4d, O1s, F1s, F$_{Auger s'}$, O$_{Auger}$

Binding Energy /eV

Fig.4.42
(ii)

Analyser Energy =100eV

Al$_{2p}$

Au 4f

×10^4 c.p.s.   70   80   90
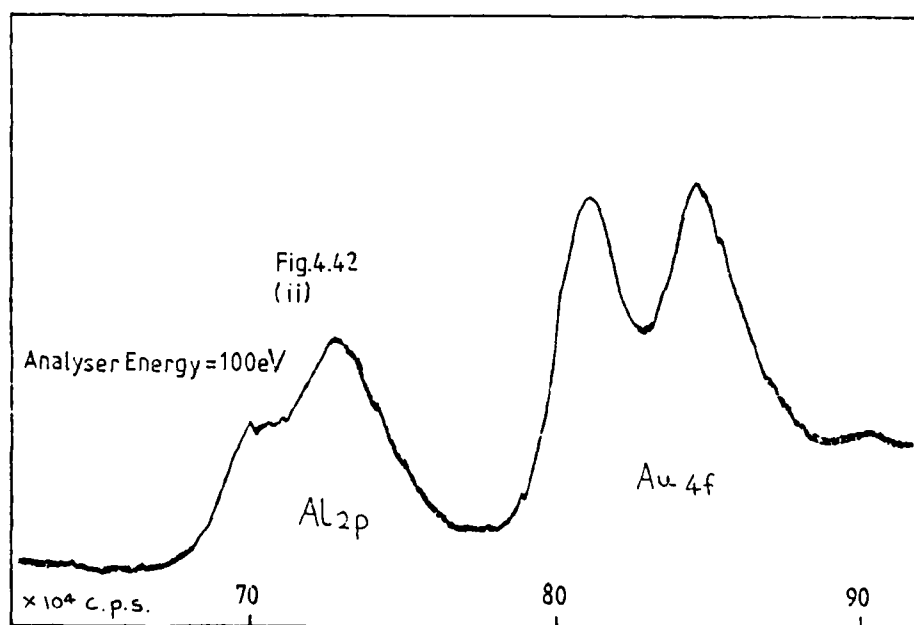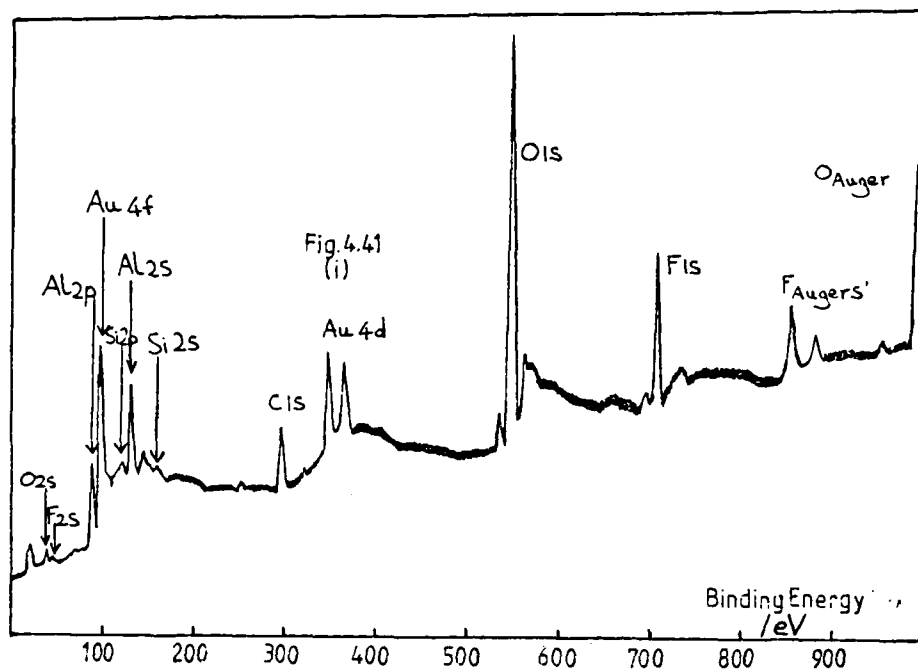
XPS spectra of (i) AL/ H PO$_2$F$_2$* after a two minute etch (ca. 60μA)
and (ii) AL/HPO$_2$F$_2$* after a 30 s etch (ca. 60μA)
* Left for 11 days.

Fig.4.43

(i)

Analyser Energy = 100eV

AL 2s

$\times 10^4$ c.p.s.

P 2p

3×10^3 c.p.s.

Fig.4.44

(ii)

O 1s

O Auger

F 1s

F Auger

C 1s

Au 4f

Al 2s

Al 2p

P 2p

P 2s

O 2s

Binding Energy /eV
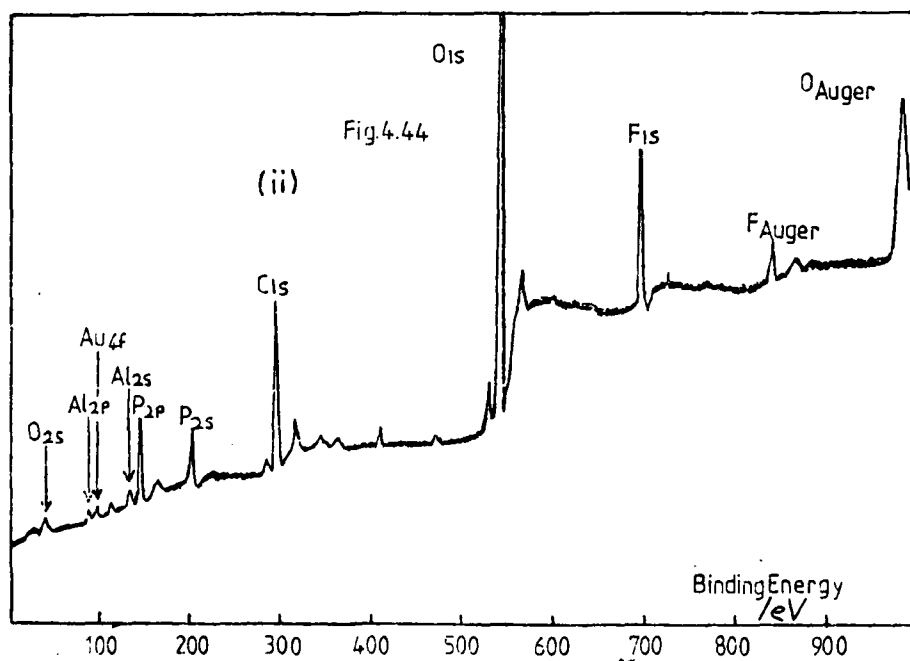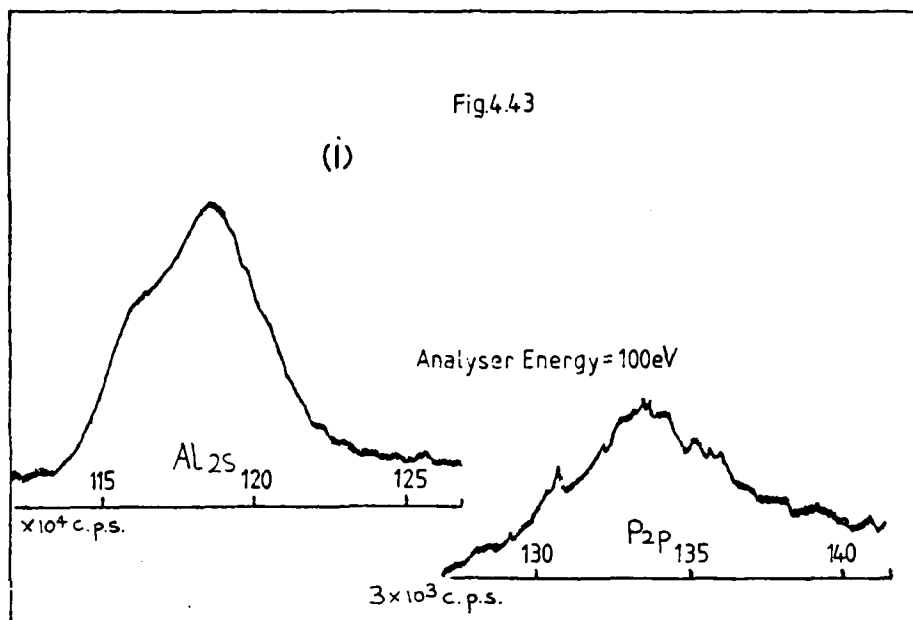
XPS spectra of (i) Al/HPO$_2$F$_2$* after a 30s etch, and (ii) Al/HPO$_2$F$_2$ 'as received'
*left for 1 days. **left for 7 days

abstracting fluoride from HPO_2F_2, causing degradation of the acid. This was supported by the detection of a relatively small amount of phosphorus; much less than that found in the $Al/'H_2PO_3F'$ spectrum.

The weak N(1s) peak is probably mostly due to adsorbed nitrogen gas, although even after 30 seconds of etching time a N(1s) peak was still just visible, suggesting that a nitrate species could also be present.

The Al(2p) and Al(2s) peaks (Figs.4.42 and 4.43) show the shoulder due to Al metal becoming apparent after only 30 seconds etching, showing a relatively thin film.

A more recent spectrum of Al/HPO_2F_2, after 7 days exposure of the metal to the acid shows, however, a high phosphorus content. (Figs.4.44 to 4.47). The level of P is still significant after 110 seconds of argon ion etching (Fig.4.47). Evidence of a thin film is again found in Fig.4.46, where the Al metal peak can be seen.

Discussion of the apparent inconsistency in phosphorus levels obtained from two samples at different times, will be postponed until the next section when the Al/Modified HDA system will be discussed.

(e)   Al in Modified HDA

Figures 4.48 to 4.51 show the surface of Al exposed to MHDA for 12 days. Of particular interest is the presence of phosphorus (Figs.4.48 and 4.49) on the surface, although this element was not detected on the surface of Al exposed to MHDA for 3 years (Ref.4.1, Section 3.3).   It is possible that

-92-

Analyser Energy = 50eV

Fig.445

P_{2p}

130   135   140

P_{2s}

190   195

Fig.446

Al_{2p}

Au 4f

Binding Energy
/eV

70   80   90
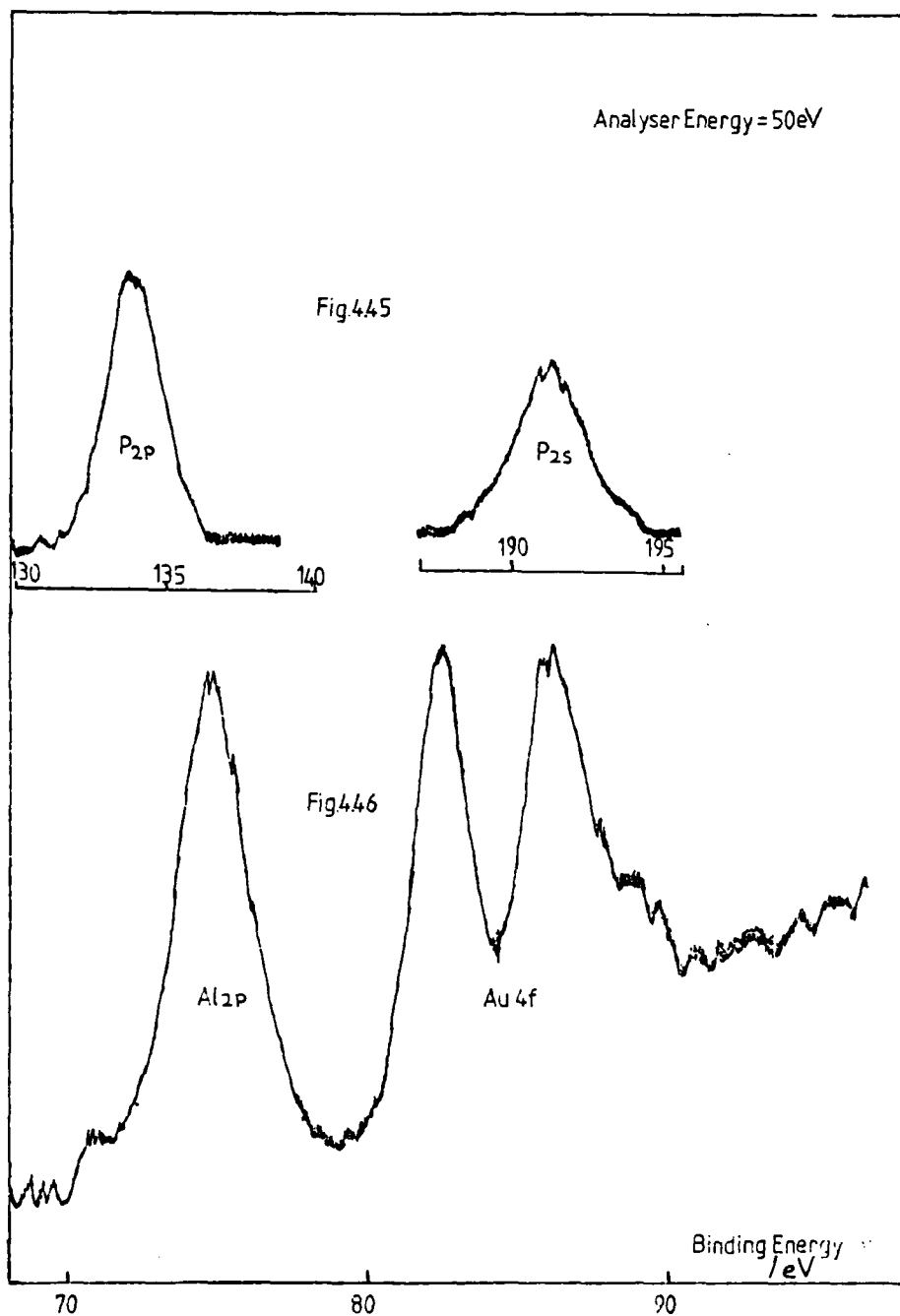
XPS spectra of *Al/HPO$_2$F$_2$ 'as received'
*left for 7days

Fig 4.4.7

XPS spectrum of *Al/HPO$_2$F$_2$ after a 110s etch(ca.60μA)
*left for 7days

Fig.4.48

Fig.4.49

Analyser Energy=100eV

P_{2p}

3×10^3 c.p.s.

Al_{2s}

3×10^3 c.p.s.

Binding Energy / eV
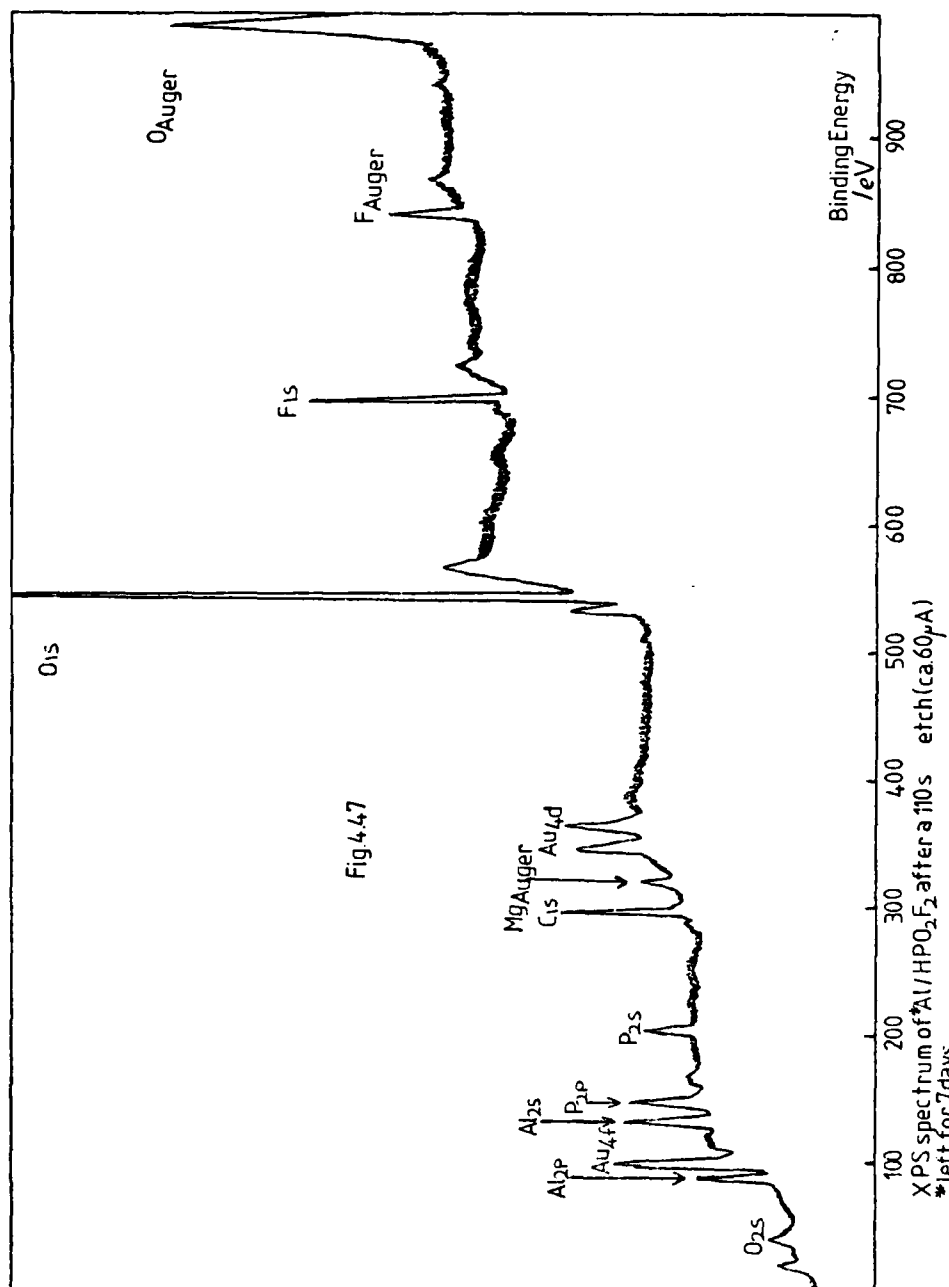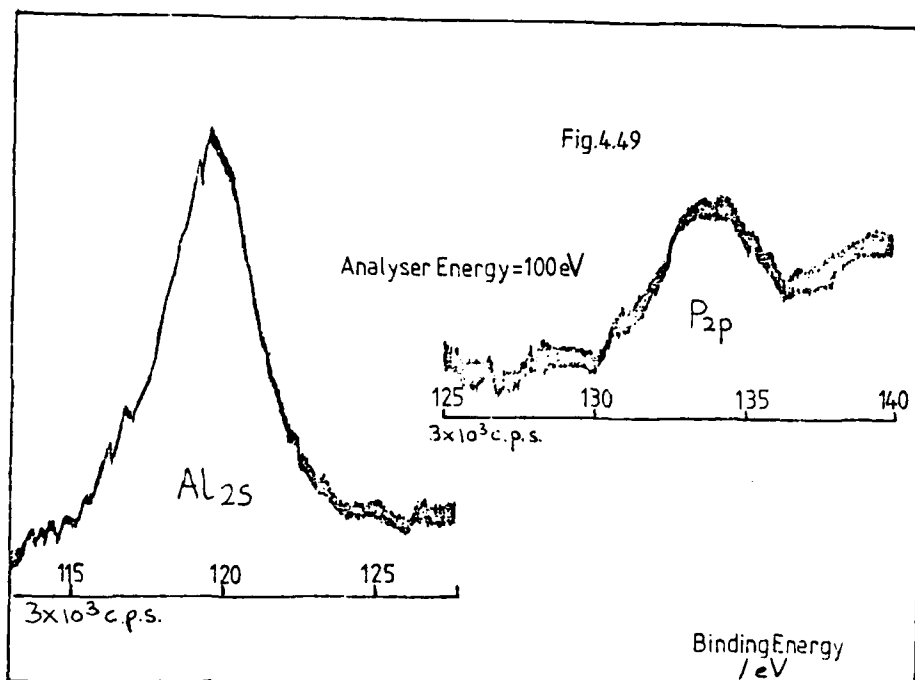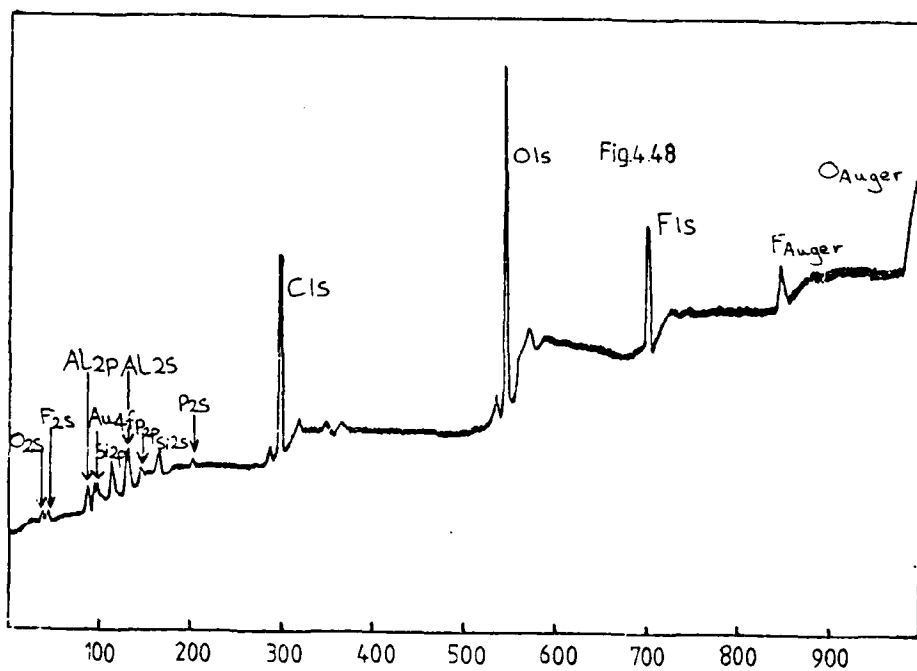
XPS spectra of Al/MHDA 'as received', left for 12 days

because of the great affinity of Al for fluoride, the F$^-$ anion gradually replaces any phosphorus on the surface, over a period of years. A similar situation could exist for the Al/HPO$_2$F$_2$ system, where the longer exposure time revealed a lower phosphorus content than for the shorter exposure time.

It is not known exactly which phosphorus species is present in the oxide layer, but it is interesting to note that all the spectra of P-containing reactants studied, i.e., HPO$_2$F$_2$, H$_2$PO$_3$F and MHDA, with the exception of 10% HPO$_2$F$_2$, show a high oxygen level, consistently higher than that in the Al/SHDA system. It is hoped that by obtaining more spectra, the levels of oxygen can be related to a fluorophosphate or phosphate species.

Samples will also be investigated over different time periods, as the time factor does appear to be significant in relation to the amount of P detected on an Al sample. Al metal can just be discerned without etching (Fig. 4.50) and the Al(2p) peak clearly reveals Al$_2$O$_3$ and the Al metal (Fig. 4.51) after only 30 seconds etching time, which shows

Fig.4.50

(i)

AL2p

Au 4f

3×10^3 c.p.s.

70   80   90

Fig.4.51

(ii)

AL2p

Au 4f

$\times 10^4$ c.p.s.   70   80   Binding Energy —
/ eV
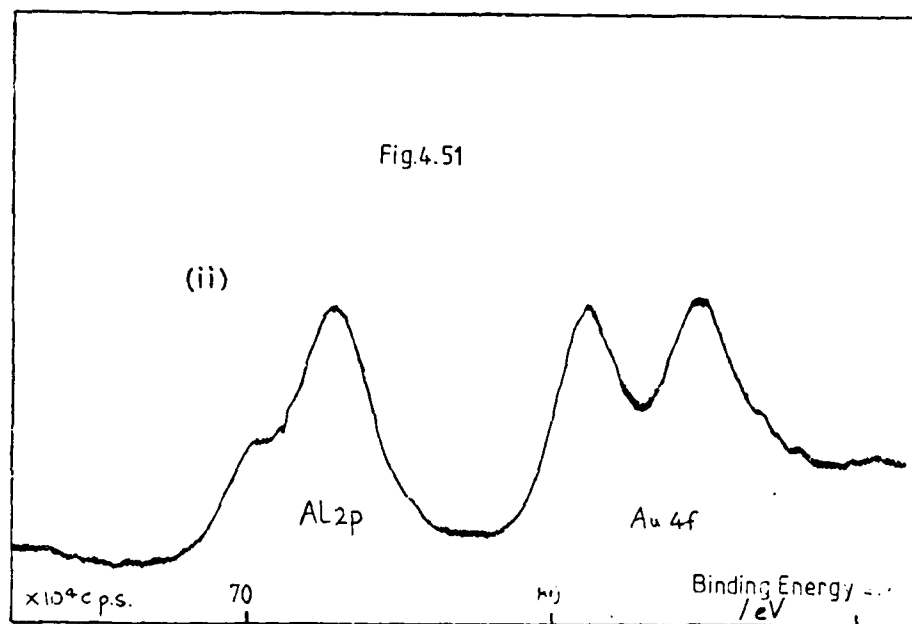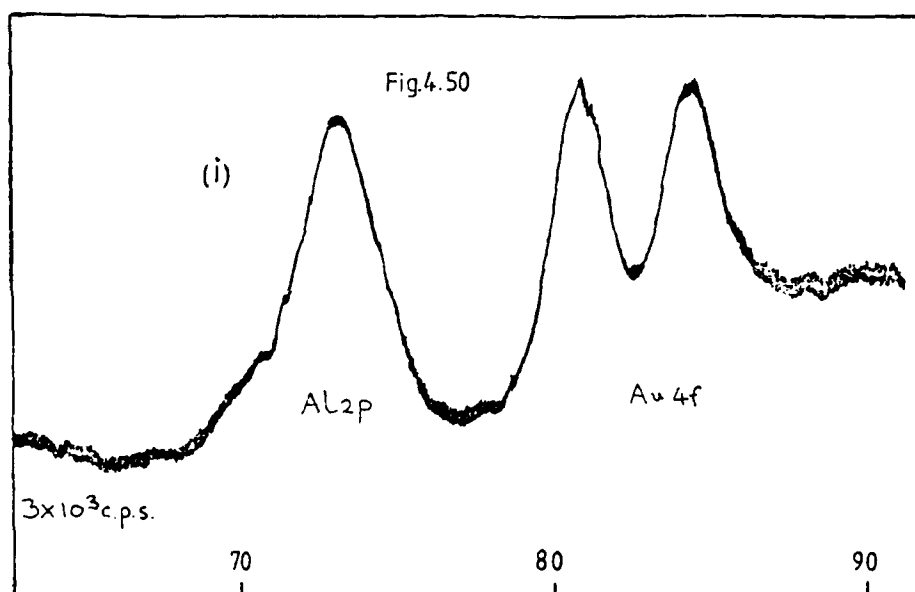
XPS spectra of (i) Al/MHDA 'as received', and (ii) after a 30s etch (ca. 60µA)
*left for 12 days. Analyser energy for both (ii) and (i) = 100ev

that the film formed in MHDA is much thinner than that formed in uninhibited HDA after two minutes etching time the concentration of Al is approaching that of the oxide (Fig. 4.51). Nitrogen was not detected on the surface, although it has been found on other samples exposed to MHDA for longer periods of time. In these cases the N(1s) peak did not disappear on etching which suggests that a nitrate species has been incorporated into the film.

The latest results include a spectrum of Al exposed to MHDA for 72 days (Figs. 4.52 to 4.55). The P level is higher than that found on the Al sample already discussed above, although less than that found on a sample exposed to MHDA for 15 days. Obviously the situation is more complex than originally envisaged, however, it appears that P is gradually displaced by F over long periods of time,

Possibly the answer to this problem lies in the nature of the film initially present on the Al, before immersion in the MHDA; this will vary according to the humidity and exposure of air to the sample. The best way to elucidate the situation would be to periodically monitor the P level by means of XPS, studying only the surface content and avoiding argon-ion etchin . This, however, has the obvious disadvantage of possible

(i)

Fig.4.52

(ii)   Analyser Energy = 50eV

Fig.4.53

Al$_{2P}$

Au$_{4f}$

×10³ c.p.s.   75   80   85   90

(iii)

Fig.4.54

O$_{1s}$

F$_{1s}$

O$_{Auger}$

F$_{Augers}$

C$_{1s}$

O$_{2s}$ F$_{2s}$ Al$_{2P}$ Al$_{2s}$ P$_{2P}$ P$_{2s}$

Al$_{uv}$

Birding Energy /eV

100   200   300   400   500   600   700   800   900
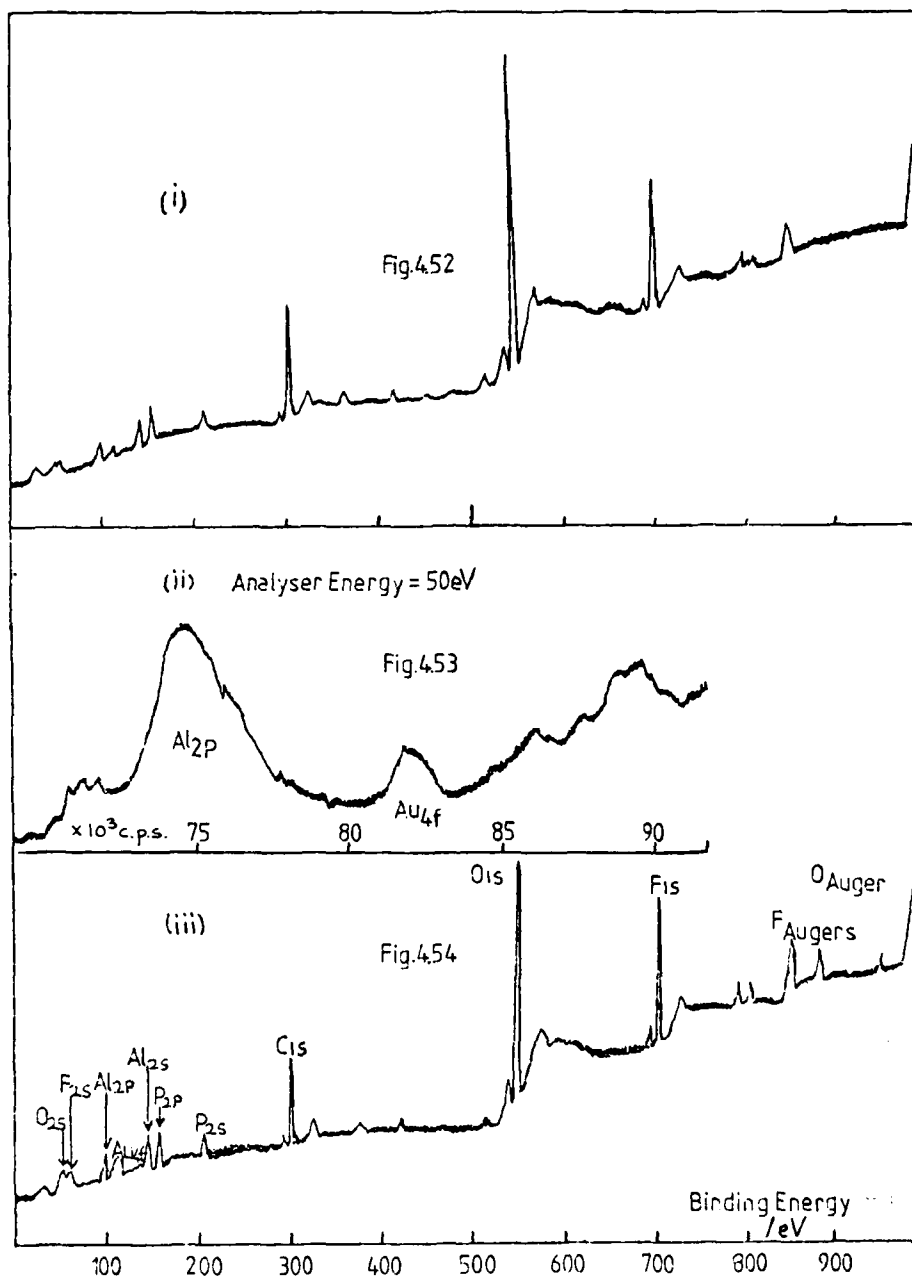
XPS spectra of Al/MHDA*, (i)and(ii)'as received', (iii)after a 10s   etch(ca. 50μA)
*left for 72 days

(i)

Fig.4.55

Al₂p

Au₄f

Analyser Energy = 50eV

×10³ c.p.s.

75   80   85   90   95

F₁s

Fig.4.56

F Augers

(ii)

O₁s

C₁s

Al₂p Al₂s

F₂s

Binding Energy / eV

100 200 300 400 500 600 700 800 900
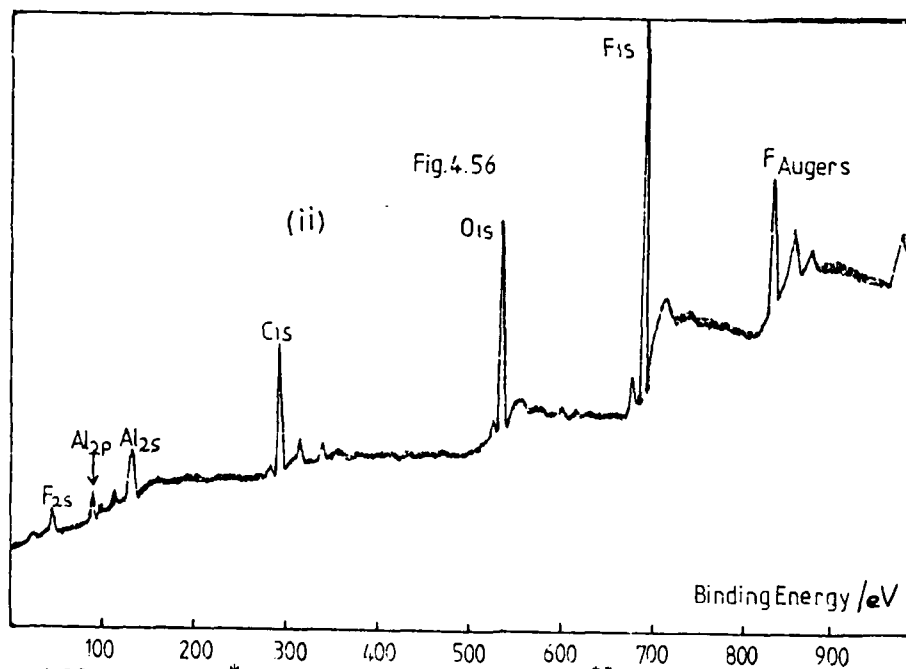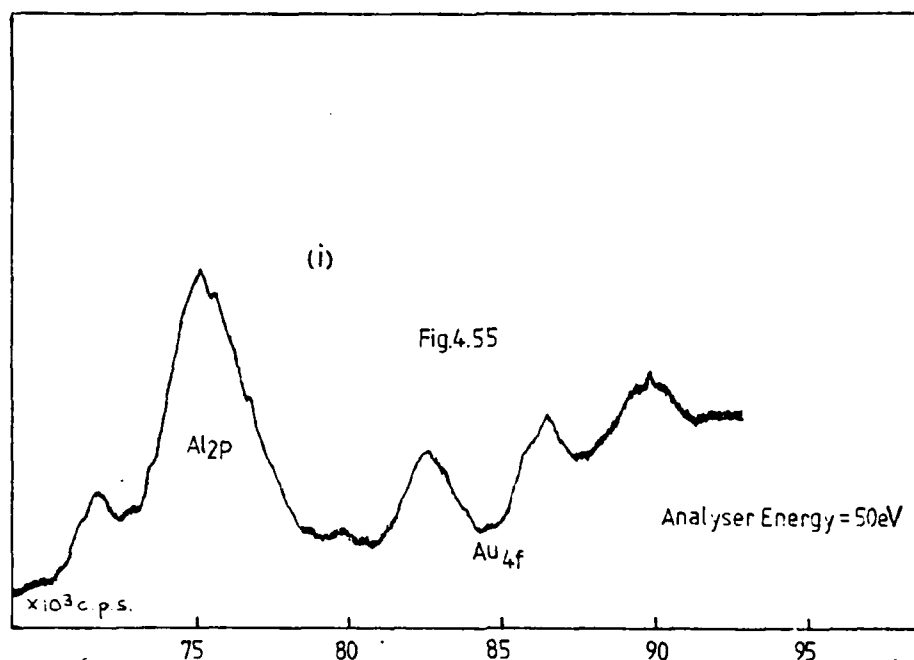
XPS spectra of (i)*Al/MHDA after a 10s   etch and(ii)Al/SHDA'as received'
* left for 12 days   ** left for 51 days.

contamination of the sample while it is out of solution
and also the possibility of oxide growth. It is thought
that these disadvantages could be overcome using inert
atmosphere techniques. Alternatively, samples need to be set
aside for at least one year and the P level measured after
this time.

The Al2p peak shown in Fig. 4.53 is significant
in that it shows a distinct Al metal peak, indicating a
thin film of Al_2O_3. The peak is well resolved and some
way (3.84eV) from the Al_2O_3 peak; in fact these results suggest
that this particular sample possessed one of the thinnest films
so far observed with the exception of those formed in the
Al/SHDA system. (See below).

(f) Al in Standard HDA.

Figures 4.56 to 4.63 show spectra of Al after exposure
to SHDA for various periods of time. Figure 4.57 shows a
remarkably high level of Al metal considering that argon-
ion etching was not employed to produce it, and only
approximately the top 20Å are being sampled.

The separation between the metal and oxide (plus, presumably
fluoride) peaks is considerable and amounts to 4.56 eV. The
literature value for the separation between Al and Al_2O_3 is

(i)

Fig.4.57

×10³ c.p.s.

Al₂p   Au₄f

(ii)

Fig.4.58

Al₂p   Au₄f

×10³ c.p.s.   Binding Energy/eV

70   75   80   85   90
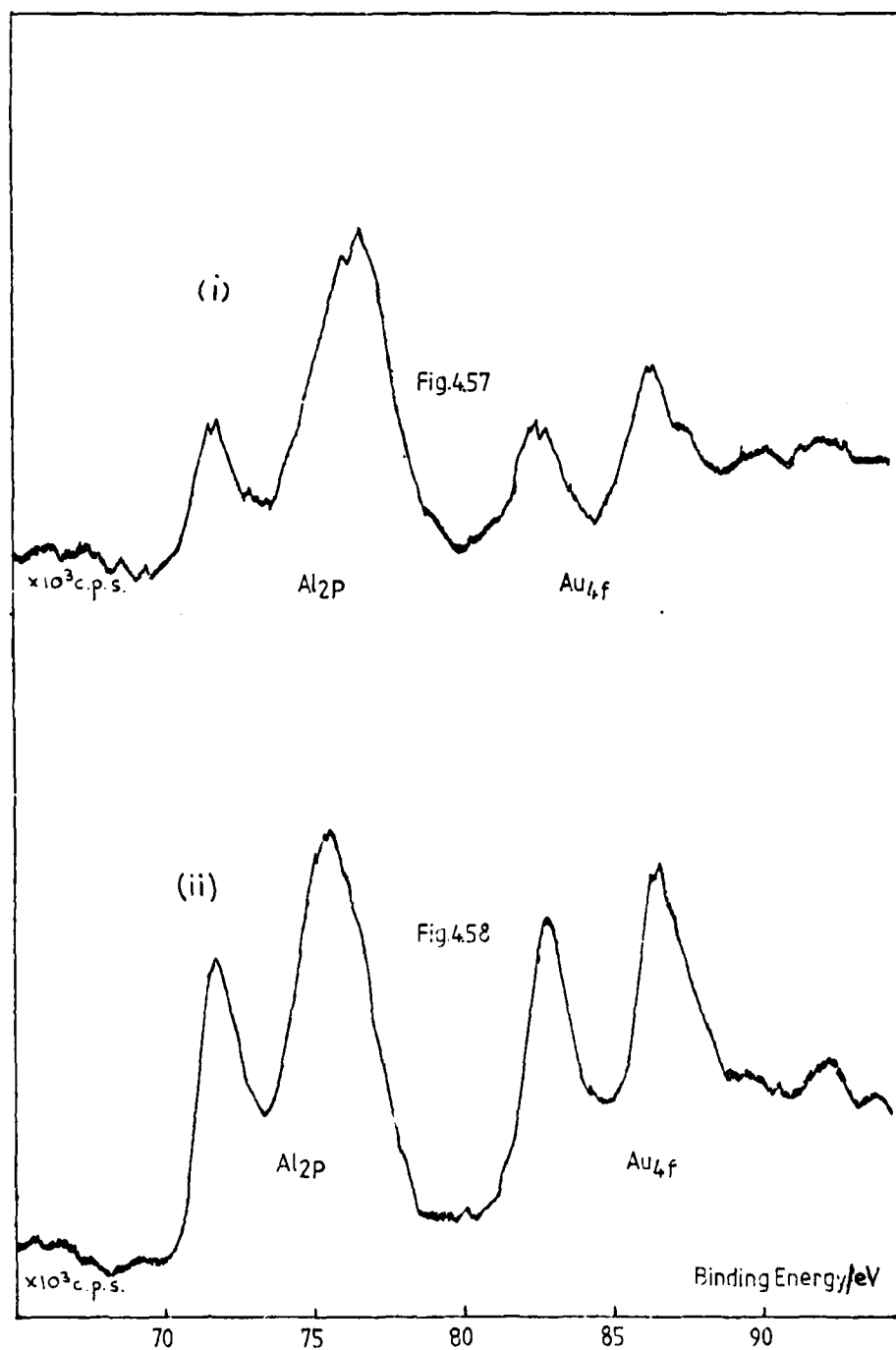
XPS spectra of (i) Al/SHDA 'as received', and (ii) after a 10s   etch (ca.100μA)
*left for 51 days. Analyser energy for both (i) and (ii) = 50eV

(i)

Fig.4.59

Al$_2$P

Au$_4$f

x10^{3}c.p.s.

70   75   80   85   90

(ii)

Fig.4.60

Al$_2$P

Au$_4$f

Binding Energy/eV

x10^{3}c.p.s.

70   75   80   85   90   95
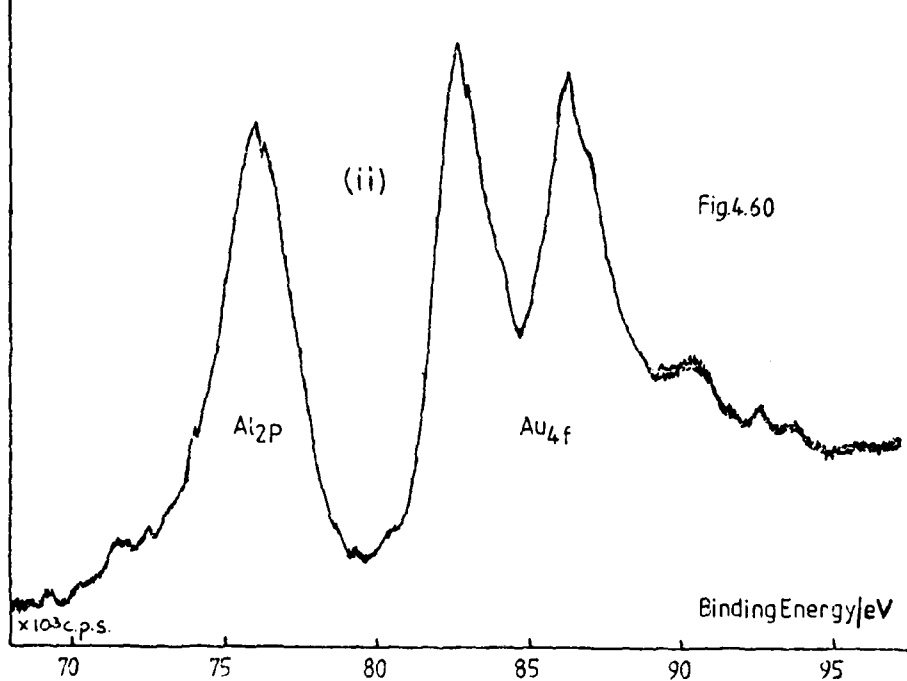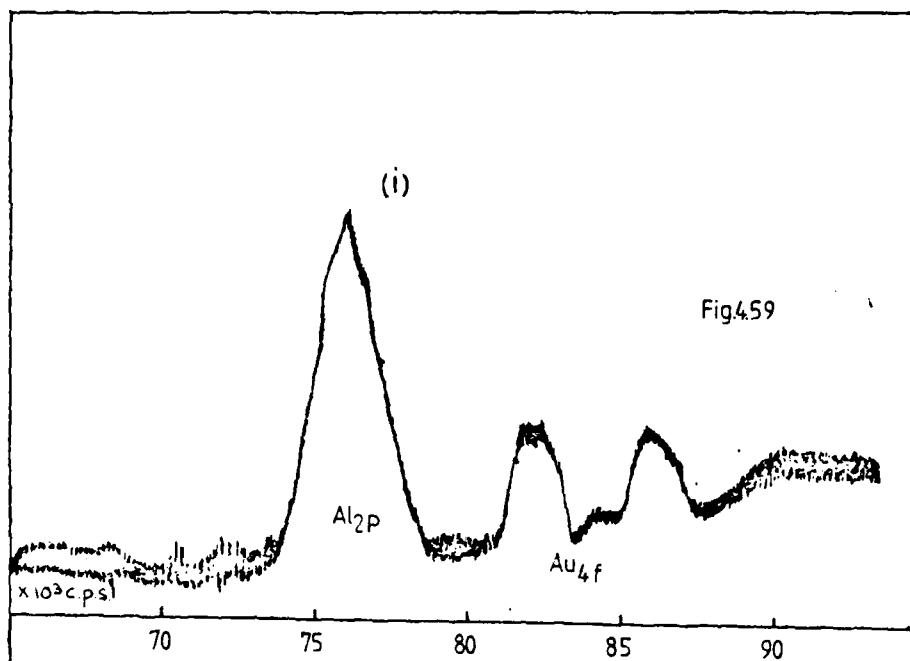
XPS spectra of (i) Al/SHDA 'as received' and (ii) after a 45 s   etch (ca. 38 μA)
*left for 14 days. Analyser energy for both (i) and (ii) = 50 eV

Fig.4.61

(i)

O_{1s}

C_{1s}

O_{Auger}

F_{1s}

F_{Auger}

Si_{2p} Si_{2s}

Al_{2p} Al_{2s}

100 200 300 400 500 600 700 800 900

Fig.4.62

Al_{2p}

Au_{4f}

×10³ c.p.s.

Analyser Energy = 50eV

Binding Energy/eV

70   75   80   85   90   95
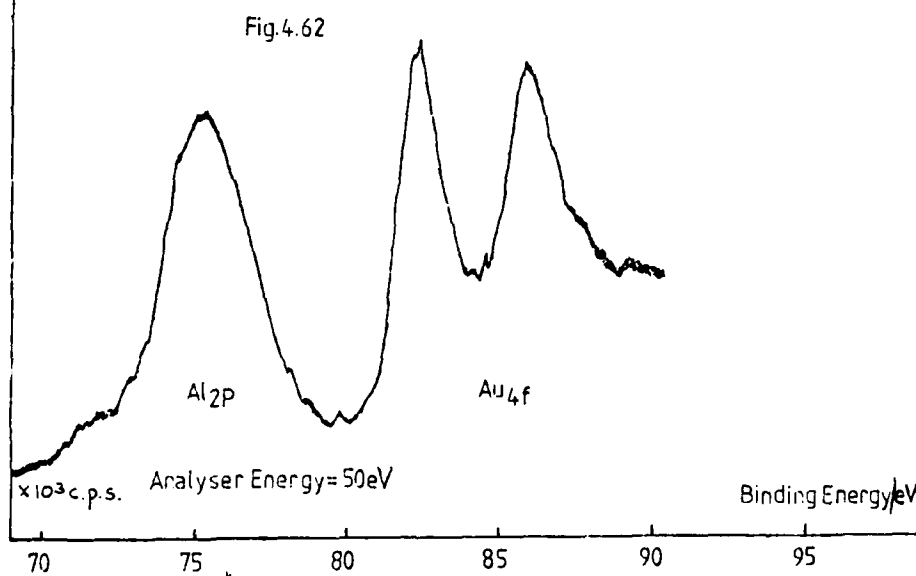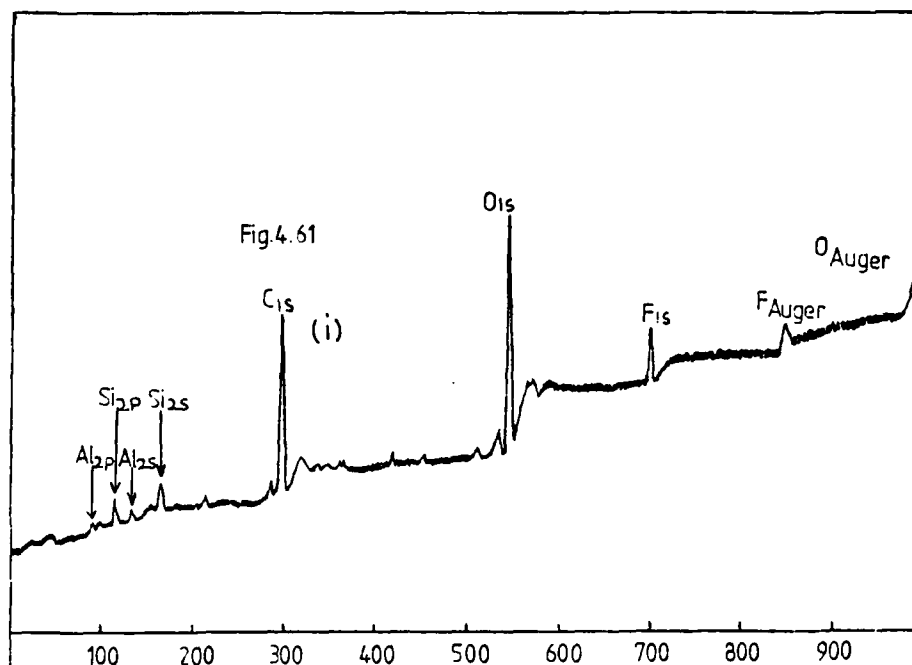
XPS spectra of (i) Al/SHDA 'as received', and (ii) after a 14s etch(ca.60μA)
*left for 41 days.

Analyser Energy = 50eV

Fig. 4.63

(i)

Al$_{2P}$

Au$_{4f}$

70   75   80

×10^3 c.p.s.

85   90

×10^3 c.p.s.

Fig. 4.64

(ii)

Al$_{2P}$

Analyser Energy = 50eV

Analyser Energy = 20eV

separation ① = 0.84eV

"   ② = 1.32eV

"   ③ = 1.44eV

①

② ③

Al$_{2P}$

×10^3 c.p.s.

3×10^2 c.p.s.

Binding Energy/eV

70   75

70   75   80
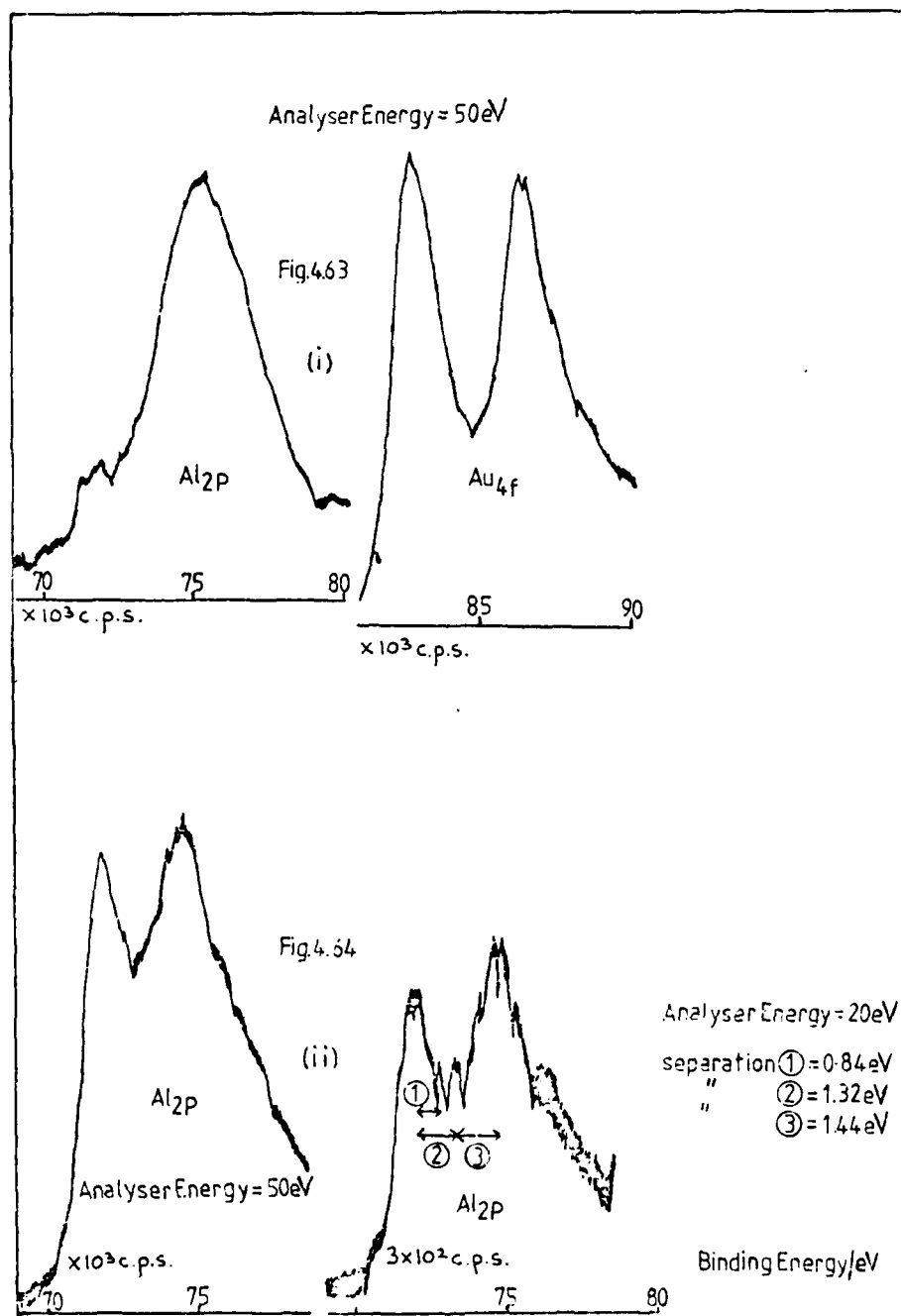
XPS spectra of (i) Al/SHOA after a 30 s   etch (ca. 60 μA), and (ii) after a 6 min. etch (ca. 60 μA)
*left for 41 days.

2.1 eV and appears to indicate that the fluoride present

in the Al2p peak can significantly affect peak distances.

It may also be significant that the fluoride content in the

sample is one of the highest measured of all the systems

studied.

Generally, it can be said that all the inhibited systems

containing fluoride have Al metal - Al_2O_3 (+ fluoride)

separations of about 3 eV or greater; this figure could

ultimately depend on the amount of fluoride present.On the other

hand the energy separation for Al uninhibited HDA appears to be ca

2.30eV, close to the literature value.

The large Al metal peak in evidence in Fig. 4.57 should

be put in perspective and compared to untreated Al (Fig. 4.31),

where it can be observed that there is at least an equal

amount of Al metal. We can therefore infer that the film

thicknesses are of the same order; perhaps about 30Å.

This represents a very thin film, and a possible explana-

tion for this thin film could be in the aggressive action of

F^- towards Al_2O_3. The F^- ion could attack the Al_2O_3 through

cracks and flaws in the oxide film, so undermining it and

causing film stripping. There is some evidence of this

taking place from potential time studies as described in

section 4.2(i).

The mechanism of film stripping can be found in the

literature in relation to fluoride in aqueous solutions.[4.19]

It is possible that some of the problems associated with

colloid formation in rocket fuel lines are due to this phenomenon.

Some evidence for decreasing film thickness with time can be seen upon comparison of Figures 4.60 and 4.62. The sample exposed to SHDA for only 14 days shows a slightly thicker film than that exposed for 41 days, as evinced from the fact that in the former, 45 seconds of argon-ion etching are required to expose the Al metal while in the latter spectrum only 14 seconds are required (both etches were carried out at ca 60μA target current.) Other samples left in SHDA for different times tend to show that the film thickness decreases with time. However, one sample left for only 9 days showed a very thin film, although not as thin as that giving rise to Fig. 4.57. It is possible in this particular case that the air-formed film was initially thin itself, and as been shown by a number of spectra, this film will not grow as the oxide when fluoride is present (cf UHDA). The question of air-formed films was raised in the section on MHDA. It was, therefore, decided to obtain spectra of two samples after similar lengths of time exposed to SHDA. Samples exposed for 41 ard 42 days were investigated and the latter was found to have a thinner film that cannot be realistically attributed to the difference in exposure time; it is therefore suggested that initial film formation plays an important role, although only more measurements taken over longer time intervals will clarify the situation.

Figures 4.64-4.69 show attempts to resolve the fluoride peak on Al2p. Comparisons between Fig. 4.65 and Fig. 4.66 show the effective use of the lower analyser energy and longer scan time. These figures, in fact, show a fairly complex Al2p peak, composed of possibly 5 different constituent peaks. The Al metal peak is easy to identify and occurs at the lowest binding energy. Adjacent to Al metal in Fig. 4.67 occurs a very small spike (at ca 1.20eV from the metal) which is present in several spectra of Al2p at high resolutions; this merges into a larger peak at ca 1.86eV from the Al metal. At approximately 2.76eV it is thought Al_2O_3 appears, shifted by about 0.66eV from its position ascribed by the literature. The peak 1.32eV from the oxide is thought to be due to AlF_3, although the literature value is 2.00eV removed from Al_2O_3.

The two peaks remaining to be assigned are of interest since they indicate the existence of two more compounds of aluminium. There is a possibility that the peak 1.86eV from Al is due to $Al(OH)_3$ since it is in the correct position relative to metal and oxide. Another possibility is that the peak represents the oxofluoride, AlOF, however, XPS data on this compound have not been found in the literature and it is impossible at present to state whether the peak will occur to the high or low binding energy side of Al_2O_3. The small peak remaining defies assignment until more data is available regarding the peak at 1.86eV from the metal.

Fig.4.65

Analyser Energy=50eV

Al$_{2P}$

Au$_{4f}$

70   75   80   85   90

×10^{3}c.p.s.

×10^{3}c.p.s.

Fig.4.66

Analyser Energy=10eV

Al$_{2P}$

×10^{2}c.p.s.

70   75

Binding Energy/ev

XPS spectra of *Al/Si DA after a 2½ min. etch (ca. 60μA)
*left for 42 days.

separation ① =2.76eV
" ② =1.74eV
" ③ =1.20eV
" ④ =4.56eV

Fig.4.67

(i)

Al$_{2P}$

Al$_{2S}$

70   75

×10² c.p.s.

115   120   125

×10² c.p.s.

separation ① =1.86eV
" ② =0.90eV
" ③ =1.32eV

Fig.4.68

(ii)

Fig.4.69

Al$_{2p}$

F$_{1S}$

Binding Energy/eV

70   75   80

×10² c.p.s.

685   690
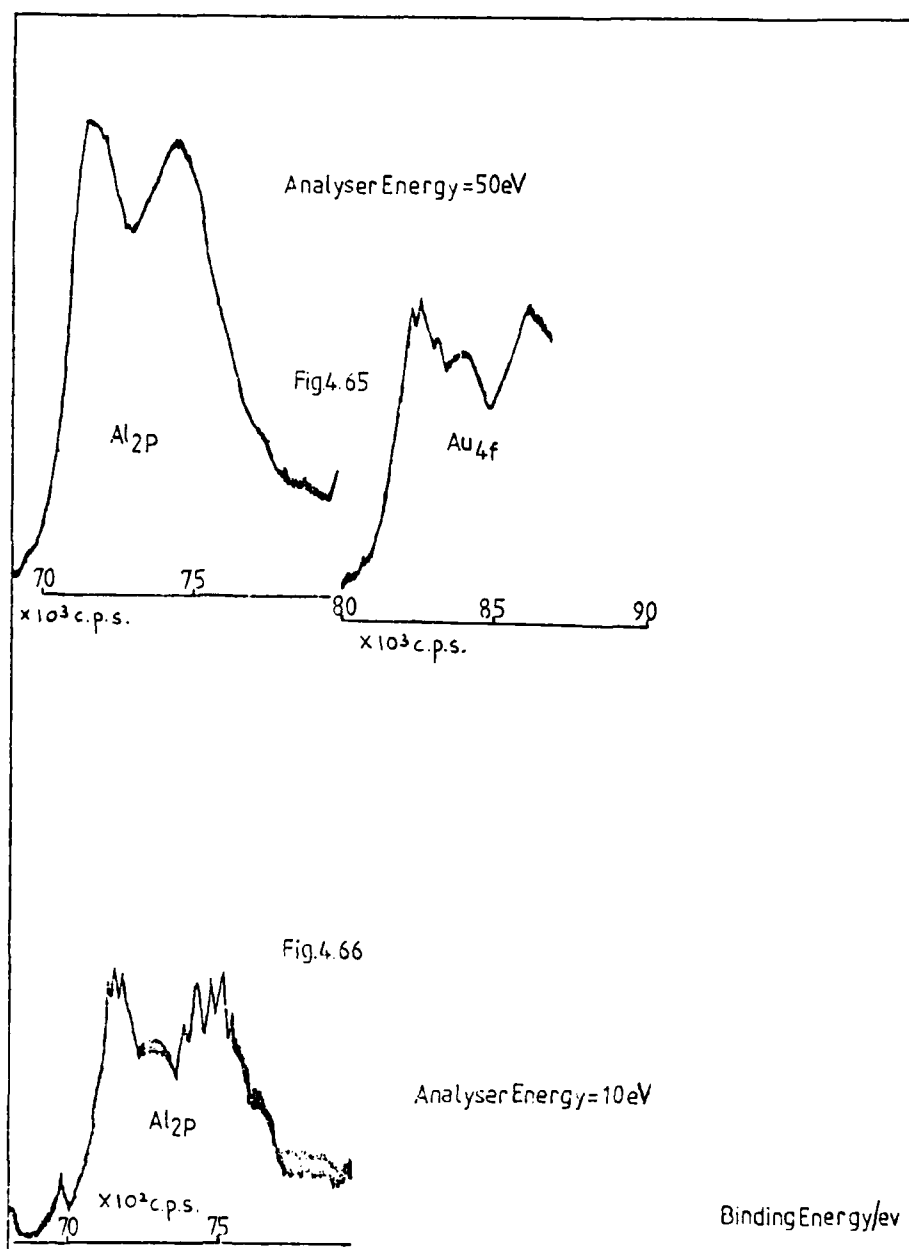
×10² c.p.s.
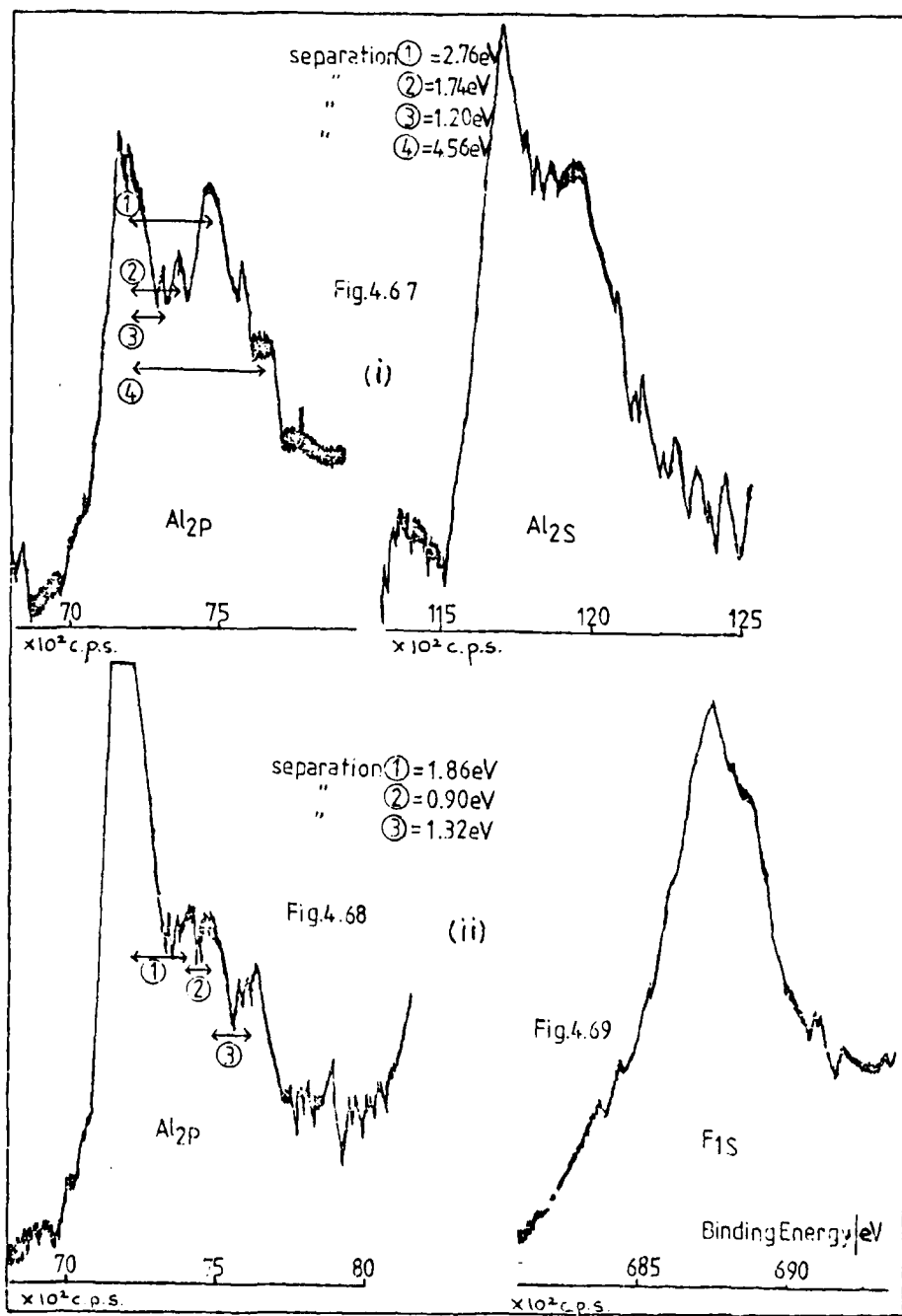
XPS spectra of (i) Al/SHDA after a 3min.etch(ca.5CµA), and (ii) after a 5min.etch(ca.60µA)
*left for 42 days. Analyser energy =10ev for (i) and (ii).

The possibility of two species of fluoride led to speculation regarding the symmetry of the F1s peak at high resolution. It was hoped that a shoulder or small peak would be seen on the main peak so indicating the presence of another fluoride. Some evidence (Fig. 4.69) was found for this effect, although it should be stressed that more spectra need to be run, and on different systems, in order for any conclusion to be drawn.

In summary, these results indicate that the film thickness on Al is much higher after exposure to UHDA compared to MHDA, but the thickness in the latter case is comparable to that following exposure to HPO_2F_2. Aluminium exposed to H_2PO_3F produces a much thicker and/or more resistant film than either MHDA or HPO_2F_2, but is thinner than in the UHDA case. The film in SHDA appears to be the thinnest of all, and this may be reflected in its higher corrosion rate for Al, at least for short periods of time, compared to MHDA. (see e.g. Table 4.1 and Fig.4.1).

The fluoride peak on Al2p has been resolved, using lower analyser voltages and longer scan times, after shorter intervals of argon-ion etching. The etching is necessary because the oxide tends to mask any fluoride present until sufficient Al_2O_3 is removed to reveal the former.

It is suggested that an oxofluoride may be present in the Al/SHDA system; this has also been mentioned as a
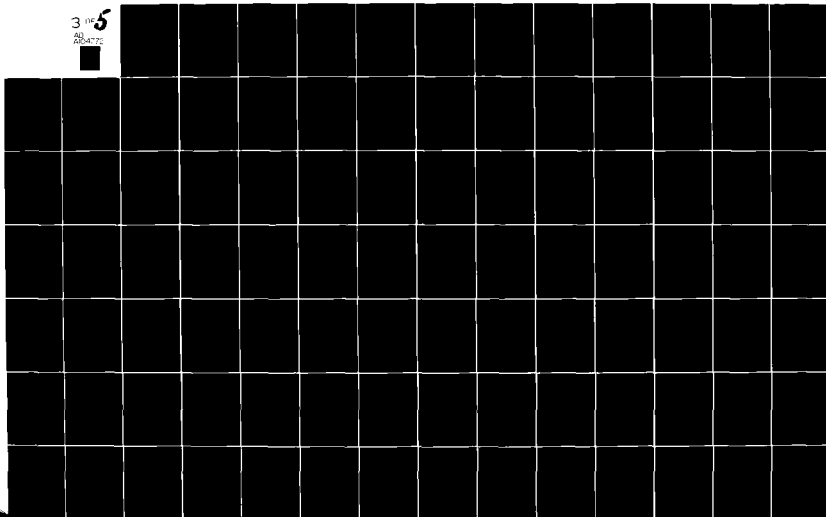
possibility in aqueous fluoride systems, and a mechanism for
AlOF formation has been proposed consisting of replacement
of O^{2-} by F^- in the Al_2O_3 lattice.

In future work XPS spectra of individual compounds
e.g. $Al(PO_2F_2)_3$, $AlPO_4$ and AlF_3 should be obtained in order to
assist identification of the species present on Al exposed to
MHDA and SHDA. An XPS spectrum of AlOF would also be desirable,
however, AlOF is very difficult to prepare.[4.20]

The possibility of film cracking and undermining has been
discussed in relation to certain XPS spectra and also the
possibility of time dependency of these phenomena. More
experiments should be conducted over various periods of
time in an effort to clarify the situation. Future work should
also involve the application of deconvolution to existing
spectra to indicate the number of possible peaks involved and
their associated binding energies.

(g) Conclusions

The XPS studies demonstrate that upon exposure to
uninhibited HDA a very thick film forms on the surface of aluminium.
This is in agreement with the conclusions reached as a result
of electrochemical investigations. In standard HDA and
modified HDA XPS provides evidence that, in the initial stages
of corrosion, a thin film exists on the aluminium surface and,
in the case of SHDA, a film stripping process occurs. This
process must be followed by a film growth process since the
film formed on aluminium after long term storage in standard
HDA is known to be very thick (Section 4.1). Furthermore,
the thickness of the film formed in standard HDA appears to be

influenced by the thickness of the air-formed film initially
present on the aluminium surface.

5. THE CORROSION OF STAINLESS STEELS IN HNO_3/N_2O_4 MIXTURES
(P.G. Cheeseman and R.C. Hibbert)

5.1 Introduction

A thorough electrochemical investigation has now been carried out to determine the precise nature of the corrosion of stainless steel by the NO_2^+ ion in HNO_3/N_2O_4 media. 321 stainless steel, titanium stabilised, was the particular steel studied, being very similar in composition to the 347 stainless steel, niobium stabilised, which is/used also to contain these oxidising acid mixtures. This Section describes the various electrochemical techniques used in this study and also presents a general discussion of the results.

The apparatus and experimental techniques used in polarisation and corrosion potential studies have already been described (Section 3). The polarisations recorded in this Section were carried out using a Wenking PCA72 potential control amplifier, with an external overpotential provided by a linear sweep generator (supplied by Chemical Electronics Co.). As described in Section 3, a Luggin capillary arrangement was used to give greater sensitivity, and to avoid contamination the counter electrode was contained in a separate compartment. Figure 5.1 shows a schematic diagram of the electrochemical cell with position of electrodes. The stainless steel working electrode is shown with it s planar face positioned close to the Luggin capillary;cylindrical and planar faces of the stainless steel specimens were prepared with abrasive papers followed by an 8 and 1 μm diamond wheel polish.

Fig 5.1   Glass electrochemical cell

Platinum
counter electrode   Working
electrode   Luggin capillary

Rhodium ref
electrode

(glass _____)

(glass
frits)
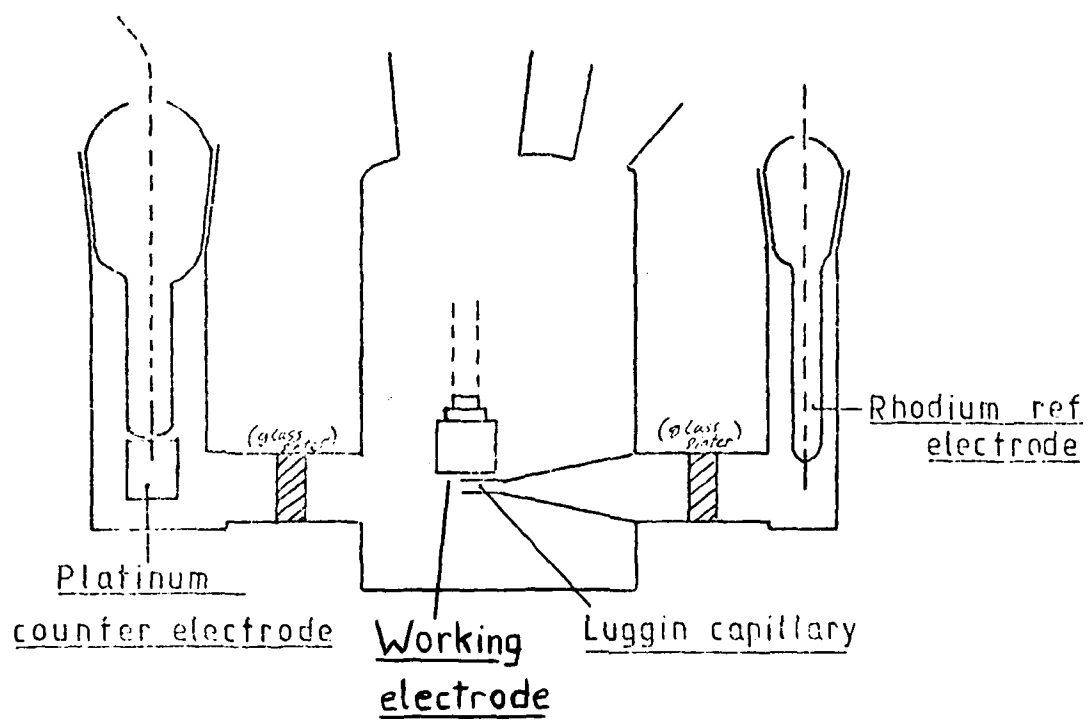
In corrosion potential-time experiments, the potential was monitored using a high impedance digital voltmeter, which measured potential to the nearest 0.1 mV.

5.2 Passivation

Previous corrosion studies in uninhibited HNO_3/N_2O_4 media[5.1] have established that after an induction period, stainless steel corrodes at a rate determined by the N_2O_4 and H_2O content, principally at the grain boundaries (see Section 3 for the effect of H_2O and N_2O_4 on the thermodynamics of the system). Potential-time studies have shown that the induction period is related to the formation of a film on the stainless steel which thickens logarithmically with time until a certain critical thickness or critical potential is reached: The film then breaks down primarily at the grain boundaries and corrosion ensues. A plot of E vs logt is a straight line, as seen for 321 stainless steel in HDA at $0^{\circ}C$ (Figure 5.2). A comparison of $dE/d(\log t)$ for different N_2O_4 and H_2O concentrations and temperature can give useful information on rates of reaction of stainless steel in these media; in this case the reaction is that of passivation.

S.E.M. and E.D.A.X. studies provide firm evidence that this film is predominantly Cr_2O_3 at its outer surface, with increasing amounts of Fe further into the film, possibly as $FeCr_2O_4$. S.E.M. has indicated a film thickness of ca 3 μm.

In an aqueous system, the following mechanism of passivation can be considered. (Mechanism 1).

Figure 5·2   Potential vs log t for stainless
steel (321) in H.D.A. at 0°C. Slope =
S = 52·5 mV decade^{-1}

H.D.A. at 15°C, S = 160 mV decade^{-1}

100 % HNO_3 at 0°C, S = 90 mV decade^{-1}

4·2 wt% N_2O_4-HNO_3 at 0°C, S = 70 mV decade^{-1}

Potential of 321 S.S. vs 0·1 molal
N_2O_4 - HNO_3/mV

log (t/hr)

2·0

1·0

-260

-210

-160

-110

Mechanism 1

ANODE

$$M \cdots O \overset{\displaystyle H}{\underset{\displaystyle H}{}} \longrightarrow M\!\!-\!\!O^{\displaystyle H}$$

CATHODE $\quad e^- + H^+ \rightarrow \tfrac{1}{2} H_2$

Another proton can then be lost to form the oxide.
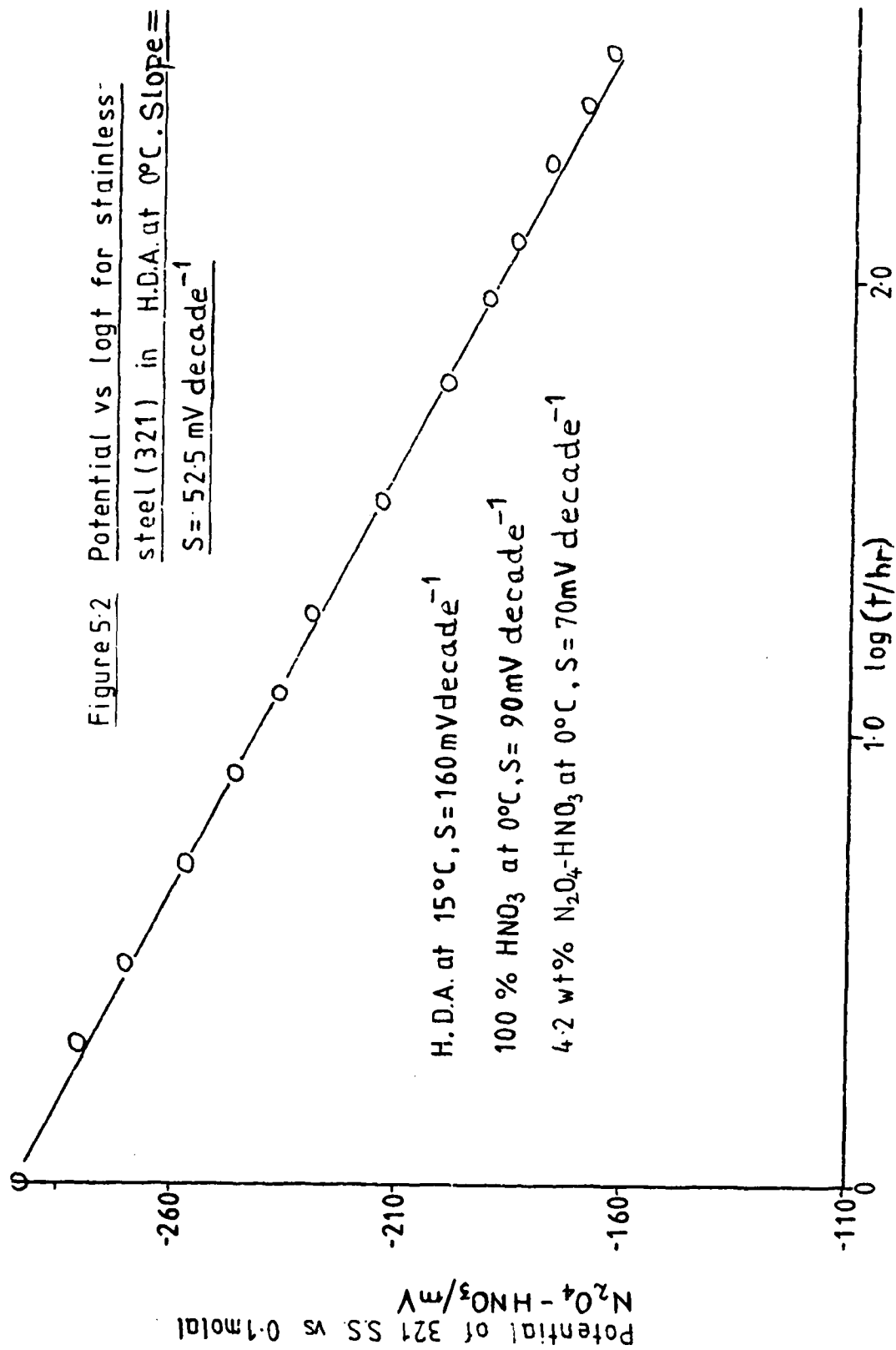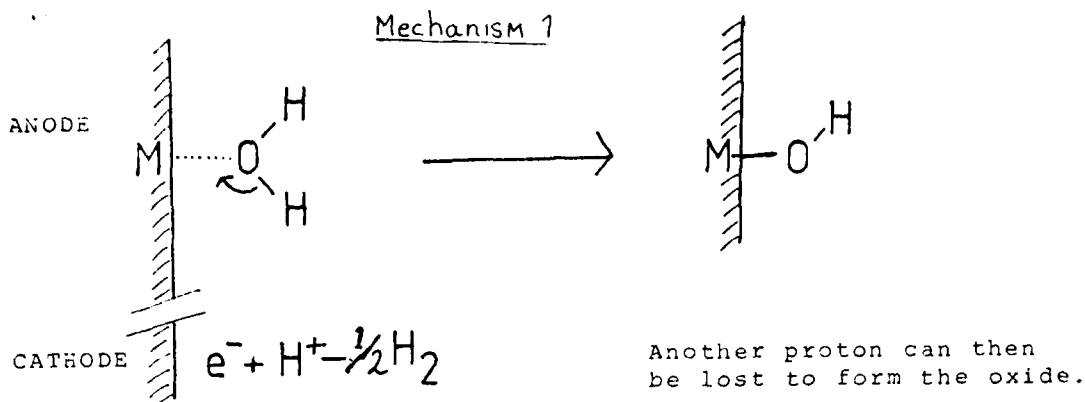
Similarly in nitric acid we can envisage the following

Mechanism 2

ANODE

$$M \cdots O \overset{\displaystyle NO_2}{\underset{\displaystyle H}{}} + NO_3^- \longrightarrow M\!\!-\!\!O^{\displaystyle NO_2} + HNO_3$$

(A similar mechanism can be written for nitrate alone)

CATHODE $\quad e^- + NO_2^+ \rightarrow NO_2 \ (or \ \tfrac{1}{2} N_2O_4)$

Similarly, NO_2^+ may then be lost to form the oxide.
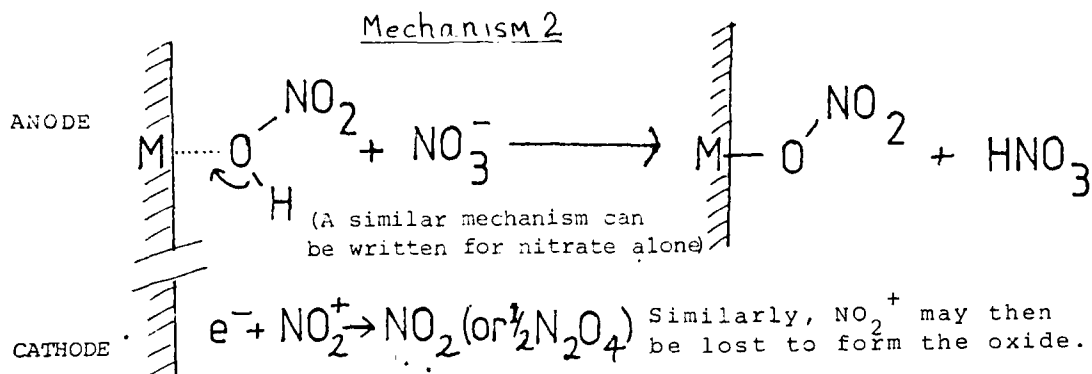
If there is sufficient solvation the metal nitrate effectively formed on the surface of the metal may dissolve into the acid mixture to give a solvated metal nitrate; this is found to be the case with copper. Alternatively NO_2^+ may be lost in a similar fashion to the 2nd H^+ (Mechanism 1) to give the metal oxide, and this is the case for the chromium in stainless steel. From a thermodynamic study of heats of formation of nitrates and oxides it should be possible to predict whether oxide or nitrate is the favoured corrosion product with regard to the surface reaction. It should be noted at this point (from Mechanism 2) that the cathodic reaction involves a one-electron rate-determining step to give the NO_2 radical as the reduced species. This remains for a time on the stainless steel surface as an adsorbed species before combining with another adsorbed NO_2 radical to give N_2O_4 in solution.

5.3 Transpassive Breakdown

If stainless steel is coupled with platinum in a
HNO_3/N_2O_4 solution the potential of the couple after only
a few minutes attains the potential of platinum alone,
i.e., the thermodynamic potential of the system. Platinum
acts as a highly efficient cathode whilst stainless steel
corrodes as the anode. In 4 wt % N_2O_4 in HNO_3, the coupling
of stainless steel with platinum (area ratio 4:1 respec.) had
the effect of increasing the corrosion rate by up to
15 times. Coupling with platinum takes the stainless steel
into the transpassive region (see Section 3 and below)
artificially and this would be a useful technique in the
accelerated production of corrosion products.

The equilibrium between chromium (III) oxide, Cr_2O_3,
(solid) and chromium (VI) oxide, CrO_3, (dissolved) was usefully studied
using this technique. Artificial breakdown was effected
in the stainless steel by coupling with platinum in pure
nitric acid. After one minute the stainless steel was
decoupled and the film repair process followed by potential
monitoring. The rate of repair was found to be more rapid if
Chromate ions were externally added to the solution in the
form of $K_2Cr_2O_7$. Corrosion experiments recently carried out
have shown that small additions of $Cr_2O_7^{2-}$ to nitric acid
will inhibit the corrosion of stainless steel in nitric acid.

These results together provide firm evidence for the
following equilibrium at the stainless steel surface.

Cr(III) solid oxide $\rightleftharpoons$ Cr(VI) dissolved oxide
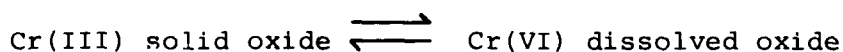
In nitric acid containing N_2O_4, the situation is more complicated as N_2O_4 reduces Cr(VI) to Cr(III). Work currently in progress is examining the reaction between N_2O_4 and $Cr_2O_7^{2-}$ in nitric acid. A preliminary study has shown that the reaction is not immediate but is still continuing toward equilibrium after 24 hours. Unpublished work carried out in these laboratories has provided evidence for the oxidation of Cr(III) to Cr(VI) by N_2O_5 and an equation for the overall equilibrium in solution can be written.

$$Cr(III) + 3N(V) \rightleftharpoons Cr(VI) + 3N(IV).$$
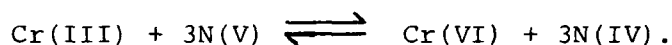
The corrosion of stainless steel by the oxidation of insoluble Cr(III) oxide to soluble Cr(VI) oxide is termed the trans-passivation effect, and is well documented in aqueous systems, where water is available to take part in the oxidation.

$$Cr_2O_3 + 4H_2O \rightleftharpoons Cr_2O_7^{2-} + 8H^+ + 6e^-$$
$$E = 1.168 - 0.0788pH + 0.0098 \log\left[Cr_2O_7^{2-} \right]$$
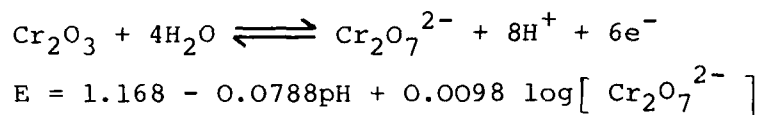
Anodic polarisation experiments for stainless steel in HNO_3/N_2O_4 media have substantiated this transpassivation theory, and Figure 5.3 shows a typical anodic polarisation curve.

The onset of breakdown is indicated by an increase in $^{di}/dt$ for constant potential as shown by the horizontal arrows in Figure 5.3. As breakdown proceeds the film is stripped off, and as this resistance to corrosion is removed the corrosion current correspondingly increases. On depolarisation the situation is the opposite, as the stainless steel specimen is depolarised the film is thinner at any given potential compared to its thickness at that same

Figure 5.3

Anodic Polarisation Curve for 321
Stainless Steel in 0.26 molal
$N_2O_4 - HNO_3$

$\begin{bmatrix} T = 0°C \\ dV/dt = 20\ mV.min^{-1} \end{bmatrix}$

Secondary Passivation

Current drift
→ Film Formation
← Film Dissolution

Transpassive breakdown

Passivation

current density/$\mu A.cm^{-2}$

10   100

Potential/mV versus Rh | 0.26 molal $N_2O_4 - HNO_3$

-40   -80   -120   -160
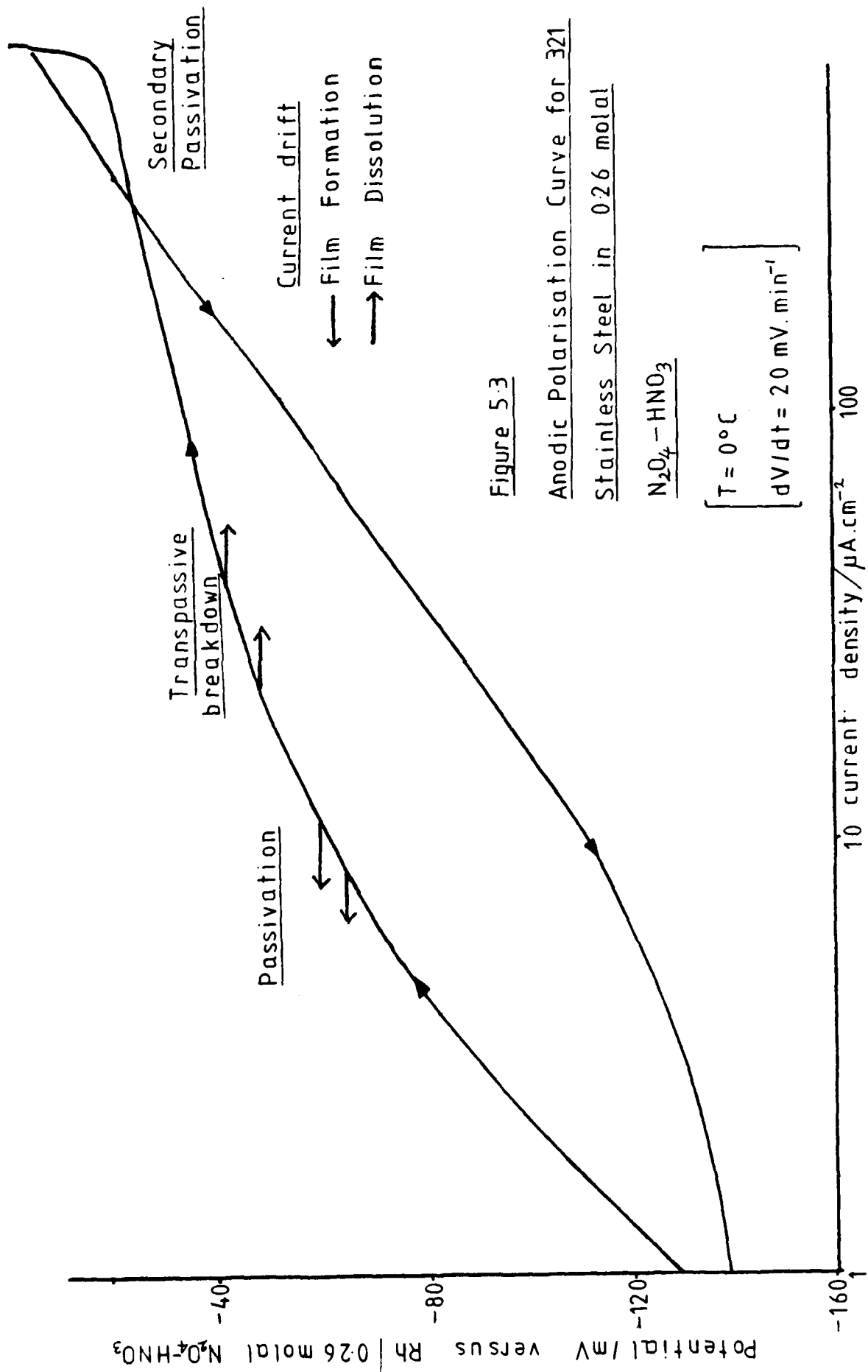
potential during polarisation and $^{di}/dt$ is negative as to some degree the film repairs itself. At high overpotentials the current reaches a limiting value and the curve levels off ($\underline{ca}$ $10^{-3}A\,cm^{-2}$). This phenomenon is termed secondary passivation and is associated with the saturation of the boundary layer adjacent to the stainless steel surface with Cr(VI) oxide in its dissolved form.

To establish exact breakdown potentials for stainless steel films in these media, corrosion current $\underline{vs}$ time plots have been obtained at different potentiostatically set potentials. Figure 5.4 shows results obtained for a solution of 8.0 wt % N_2O_4 in HNO_3 and Figure 5.5 is a plot of potential against $^1/t_b$ (t_b = time to breakdown) deriv ed from the data of Figure 5.4, yielding a breakdown potential of -152mV. It is supposed that at lower potentials than this breakdown occurs only at specifically susceptible sites, i.e., grain boundaries, as is observed in real corroding situations. The curves shown in Figure 5.4 tail off at a limiting current density, the value of which can be converted to give an accurate estimate of the corrosion rate for that particular concentration and potential. Furthermore, activation energy (E_A) can easily be determined from observation of the change in limiting current density with temperature. This may be determined in a few hours as opposed to the weeks required in classical corrosion rate studies. The results for 321 stainless steel in a 30 wt % N_2O_4-HNO_3 mixture are illustrated in Figure 5.6.

FIGURE 5.4

Corrosion current/time curves for 321 stainless steel in 8wt% N_2O_4-HNO_3 at 0°C.

FIGURE 5.5

E vs $1/t_b$
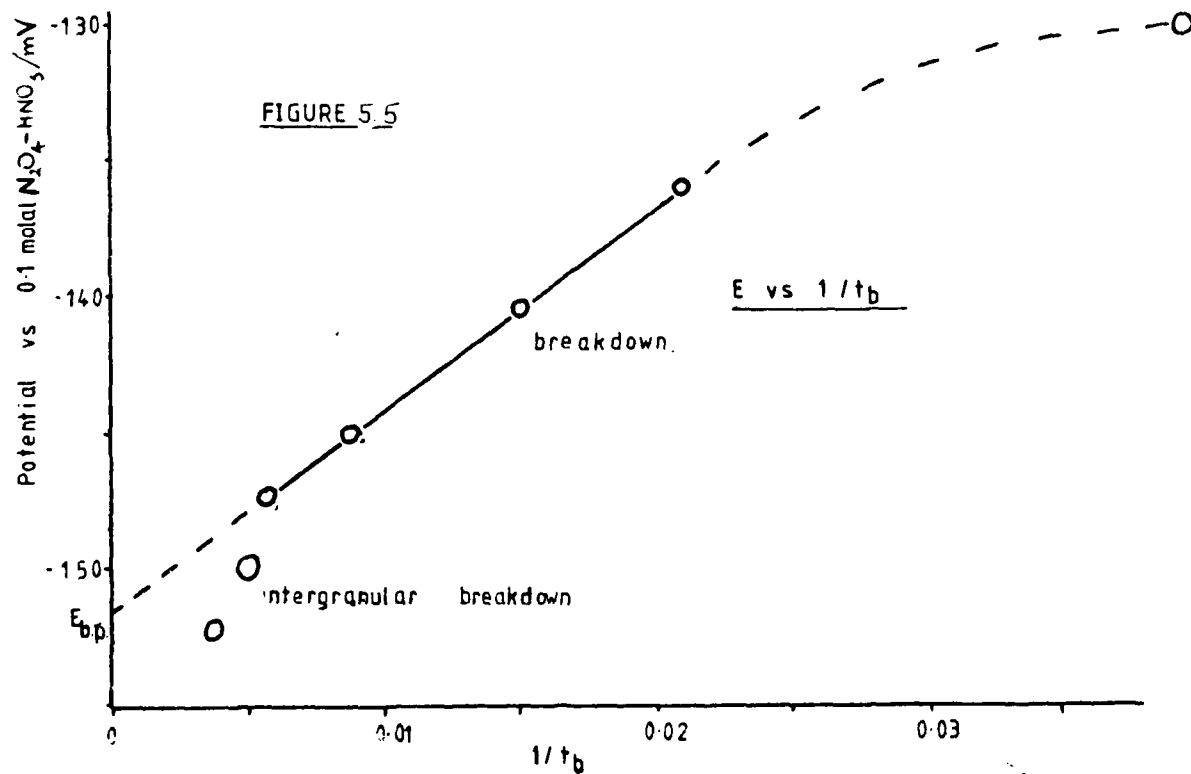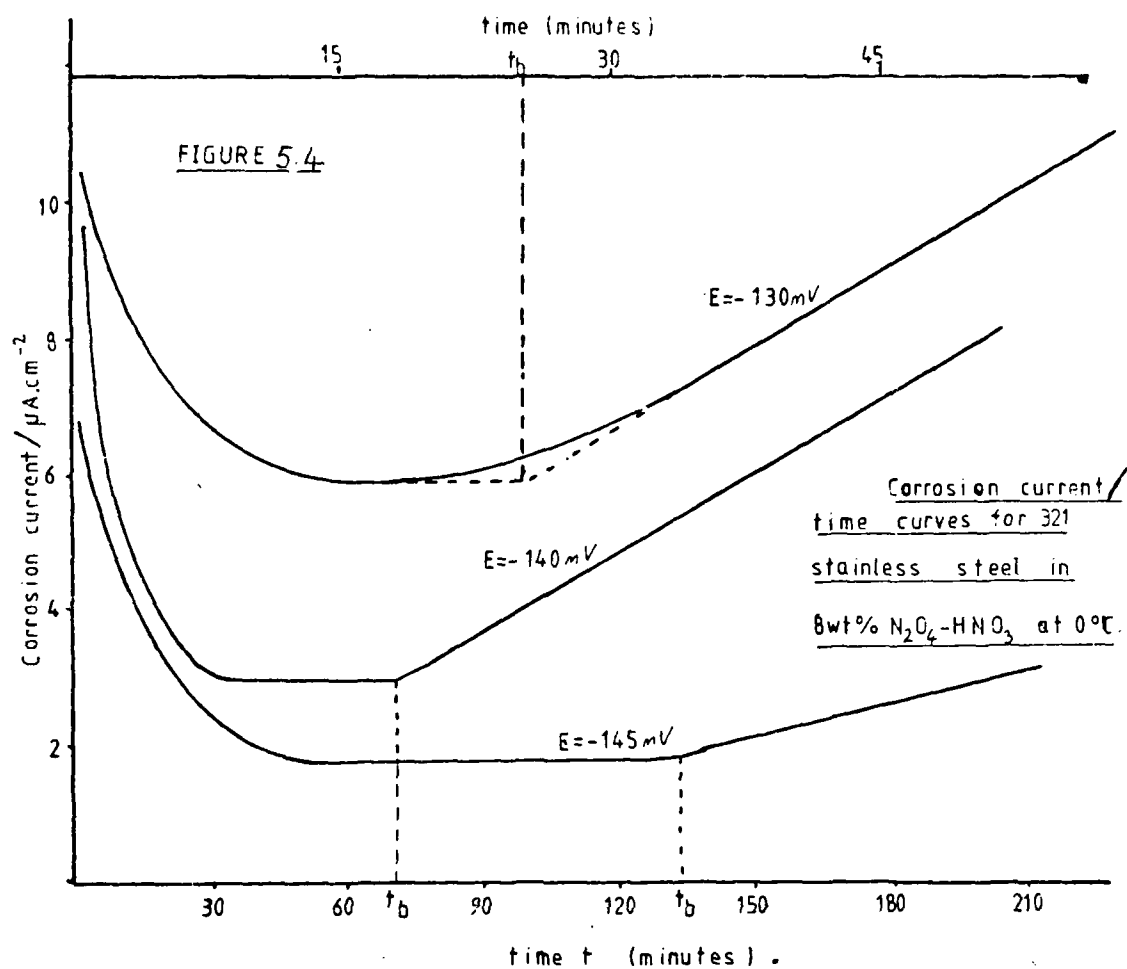
Figure 5.6

Log (corrosion current) vs (temperature)$^{-1}$ for 321 stainless steel in 30wt% N_2O_4–HNO_3.

$Rate = k \exp(E_A/RT)$

$gradient = E_A/R$

E_A (30wt%) = -102 kJ.mol^{-1}

$i_{corr} = \mu A.cm^{-2}$

$\log i_{corr}$

$T^{-1}/K^{-1} \times 10^3$
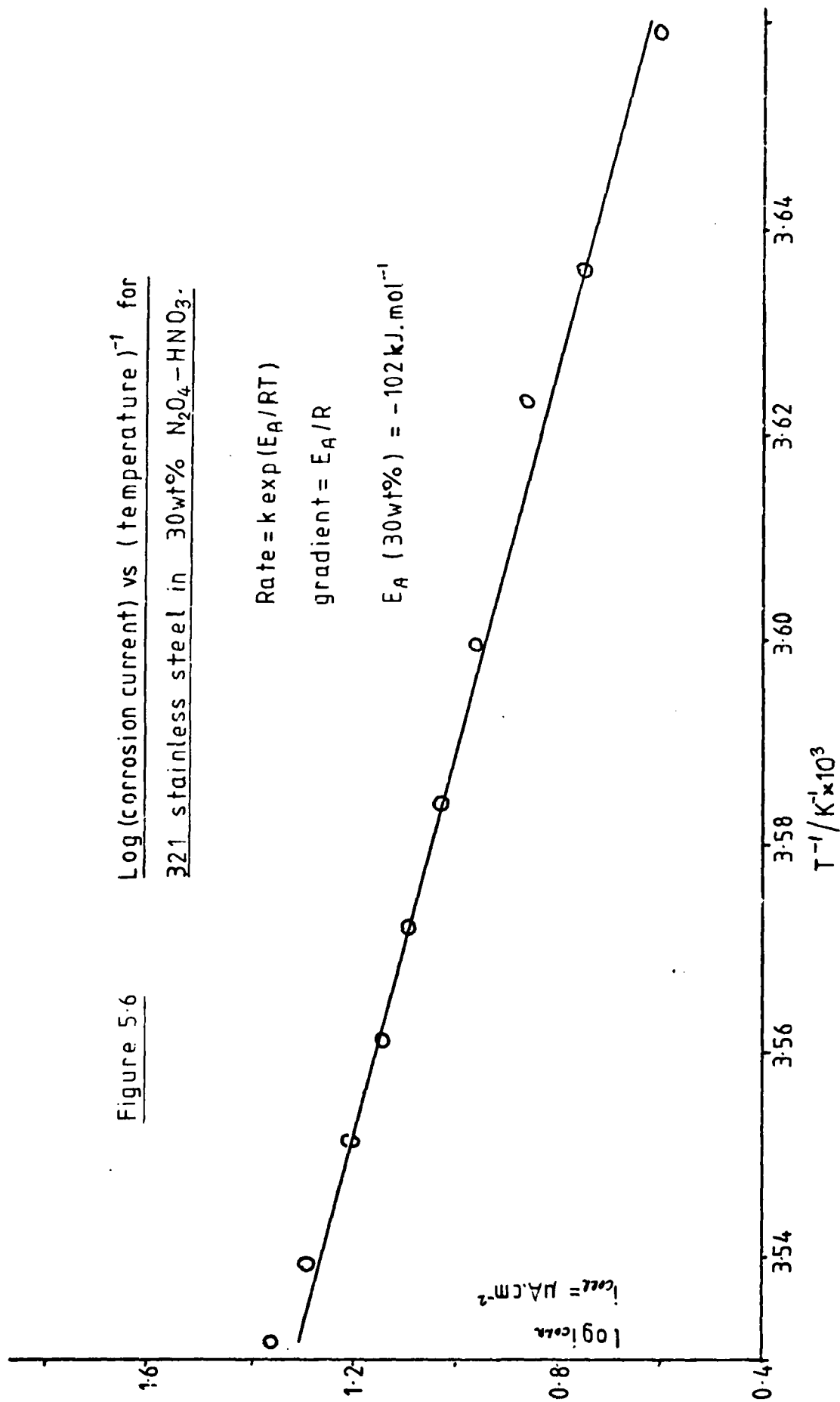
The viability of these techniques has been proved but their further development largely depends on the requirement for this particular type of information.

5.4 The Cathodic Protection of Stainless Steel

In the previous section the concept of breakdown potential was discussed. Stainless steel in this system can in theory be protected by artificially lowering its potential well below the transpassivation potential into the stable passive film region. Although the protection effected is in the cathodic direction this is not strictly cathodic protection as it is the anodic reaction that is principally influenced. As with cathodic protection in other systems, in these media it can be afforded in two ways, i.e., by using an external power source or by coupling the metal in question with another of more base potential, so that the resultant mixed potential is lower than the former corrosion potential. A preliminary investigation has been made into both types of protection.

(a) Use of an external power source

A 321 stainless steel electrode was polarised cathodically in a 0.19 molal N_2O_4-HNO_3 solution and kept at a potential of -275 mV with respect to a 0.1 molal N_2O_4-HNO_3 reference solution. This potential is about 120 mV more negative than the rest potential (as attained by the stainless steel after 8 hours in the solution.) Cathodic protection was afforded by standard polarisation equipment (Accuron) and was potentiostatic in nature with a protection current varying from 1-4 μA. cm^{-2} over an 11 day period at $0^{\circ}C$. An identical

specimen was allowed to corrode without protection as a control.

After the afore mentioned period the control specimen had acquired the characteristic black appearance associated with serious corrosion, also showing extensive intergranular attack under the microscope. The specimen had lost weight and the presence of green Cr(III) and/or Ni(II) was clearly visible in solution. In contrast, the cathodically protected specimen was found to have remained lustrous in appearance, had, in fact gained a little weight and had not changed the colour of the solution.

Even as a preliminary experiment this has established the viability of cathodic protection as a protection method for stainless steels in nitric acid and related media. A long term experiment is planned for future work involving a stainless steel tank of previously described design[5.3] but containing the appropriate electrodes to effect cathodic protection of the tank by an external E.M.F., as illustrated in Figure 5.7(a). Note that the Teflon tops and bases of the tank assemblies illustrated in Figure 5.7 are clamped in position, so as to give a leak-proof seal, by means of stainless steel end-plates secured by stainless steel bolts and nuts (see Figure 2.12 of Ref.5.3).

(b) Coupling with a metal of more base potential

The second method for cathodic protection involves a stainless steel couple with a more base metal. Many such metals are obviously available but the main corrosion problem in HDA propellant systems has been the build up of insoluble

-109-

Pt connecting wires

teflon top

inspection port

platinum wire (counter electrode)

stainless steel tank

teflon base

Rhodium reference

12 cm

5 cm

teflon

rhodium reference electrode

Aluminium rod

·A

B
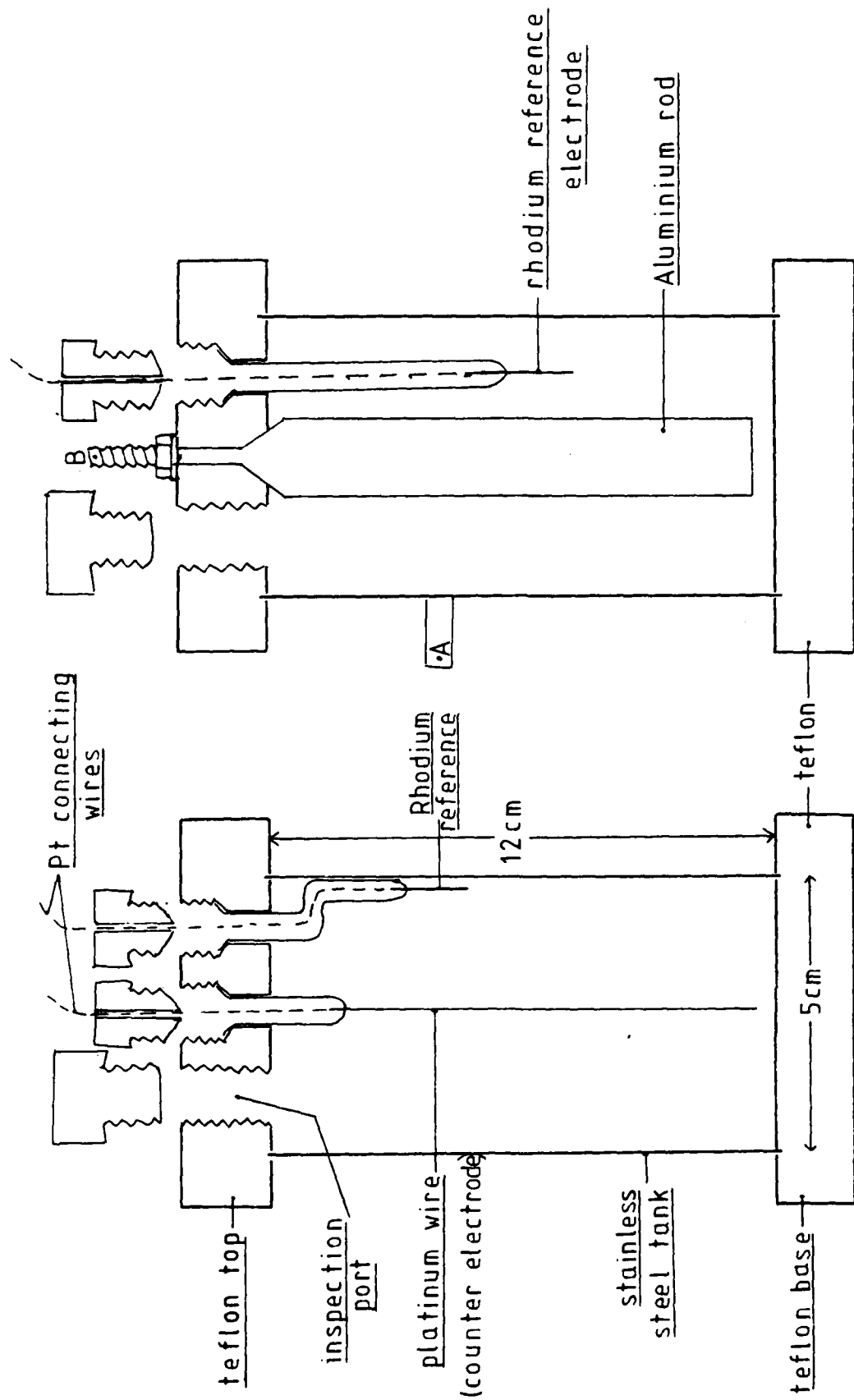
a) Tank protected by external E.M.F.   b) Tank protected by aluminium couple.

(external connection made between A & B)

Figure 5.7

corrosion products and this must be the primary consideration in such a closed system.

Silver is one possibility as it is estimated that only a few percent by area of silver coupled to stainless steel would be necessary to give a mixed potential which would be, and remain, less than the breakdown potential. This estimate is based on experiments carried out in 5 wt % N_2O_4-HNO_3 in which stainless steel has a potential of ca -150 mV and silver -850 mV. The mixed potential is electrode-area dependent but for equal areas its value is approximately 5/6 of the way towards the silver corrosion potential. For silver to be effective in this way, the solution would have to be saturated with silver nitrate (<0.2 wt %) to prevent the silver corroding. The silver nitrate crystals could be easily filtered out, however, before the oxidiser was used in a rocket motor, unlike the gelatinous or colloidal reaction products found at present to cause so many problems.

Aluminium also may be used to cathodically protect stainless steel in these media. This has previously been observed by other workers on this system[5,4] and recent potential measurements have provided an explanation for this protection. Figure 5.8 shows the result of coupling stainless steel and aluminium of equal areas together in HDA. The mixed potential of ca -400 mV is ca 1/3 of the way between the individual potentials of stainless steel and aluminium. The effect of stainless steel-aluminium coupling is to protect the stainless steel by holding it away from the transpassive region. The effect on aluminium is not so easily predicted
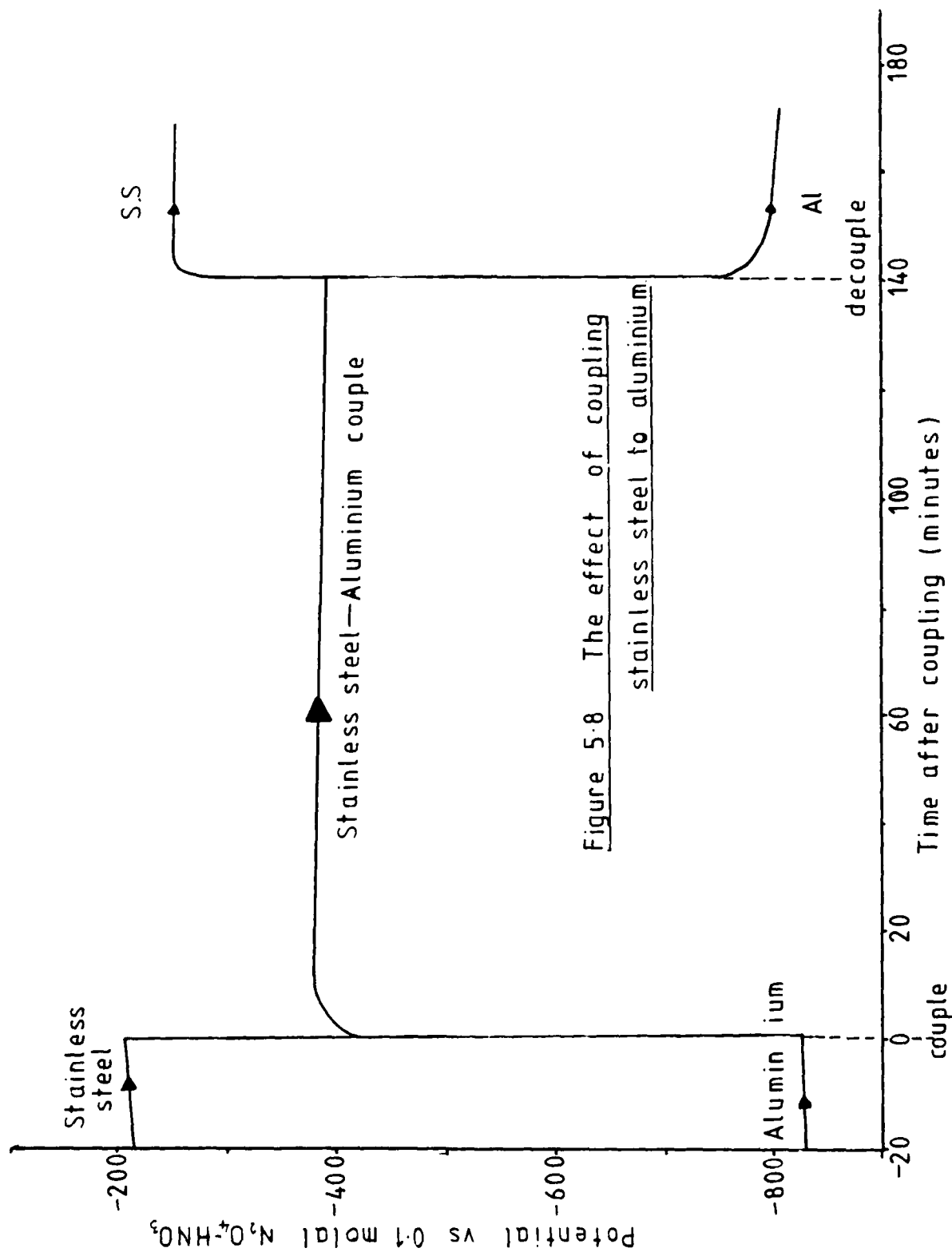
Figure 5·8 The effect of coupling
stainless steel to aluminium

but it is to be expected that at this more noble potential a thicker Al_2O_3 film will be present on the aluminium surface, which may increase the likelyhood of the pitting normally observed on aluminium which corrodes in this system. No corrosion experiments have yet been performed to verify these latter speculations concerning aluminium but some long term tank experiments are planned for future work. A stainless steel tank fitted between two teflon blocks will have an aluminium rod, which will be coupled to the stainless steel, positioned in the centre. It is planned to analyse the acid for Al^{3+}, Fe^{3+} and Cr^{3+} by atomic absorption over a 1 year period, comparing the results with a control tank in which the aluminium rod and stainless steel cylinder are not externally in contact, (Figure 5.7(b)).

The effect of coupling platinum (Section 5.3), silver (this Section) and aluminium (this Section) with stainless steel has been described. It has been shown that full protection through to greatly accelerated corrosion may be the result, depending on the nature of the coupling metal. In a real rocket propellent storage or engine situation a wide range of metal alloys are joined together in the complete complex system. This renders an academic study of any particular alloy of dubious relevance to the understanding of the overall corrosion problem. Transpassive breakdown potential will differ from steel to steel and the exchange current density of NO_2^+ reduction will also differ depending on the metal alloy (cathode effectiveness). The situation of large cathode, small anode can have particularly disastrous results and is a situation met too often in corrosion problems.

5.5 The Protection of Stainless Steel by Inhibitors

This Section is divided into three sub-Sections according to the approach that has been used in the study of particular inhibitors. Section 5.5(a) deals with H_2SO_4, P_4O_{10} and KF as inhibitors in N_2O_4-HNO_3 solutions and presents a general discussion on inhibitor mechanisms. This first sub-Section is more academic in its approach and is the result of work carried out on the N_2O_4-HNO_3 system in general rather than HDA in particular. Section 5.5(b) deals with electrochemical studies carried out specifically in HDA containing propellent specification quantities of HF and PF_5 as established inhibitors. The inhibitors dealt with in these first two sub-sections are anodic filming inhibitors in type, in contrast to As_2O_3 which is discussed in Section 5.5(c) and has been found to operate by a different mechanism. Work on As_2O_3 is included in this report because of its possible use in conjunction with a fluoride-based anodic filming inhibitor.

(a) H_2SO_4, P_4O_{10} and KF

In early studies[5.5] it was discussed that additions of 1 wt % H_3PO_4 or 2 wt % H_2SO_4 reduced the corrosion of stainless steel in 99 wt % nitric acid by a factor of 10. Recent electrochemical and surface studies in our laboratories have indicated the precise nature of this inhibition and have provided insight into the general inhibitor mechanism which operates in the nitric acid - dinitrogen tetroxide system. In the work reported here sulphuric acid has been chosen as the model inhibitor.

Figure 5.9 shows potential-time curves for 321 stainless steel in 15 wt % N_2O_4-HNO_3 for different amounts of H_2SO_4 inhibitor. With increasing additions of H_2SO_4 the build up of oxide film on the surface is increasingly retarded, as the sulphate ion is able to inhibit oxide formation at the anodic areas as shown in Mechanism2 (Section 5.2). The slope $\Delta E/\Delta t$ does not appear to change with the concentration of sulphuric acid, suggesting that the efficiency of NO_2^+ reduction on the stainless steel surface (the cathodic reaction) is not impaired by the presence of sulphuric acid. A 347 stainless steel sample was prepared for X-ray photoelectron spectroscopy (XPS). A disc 7 mm diameter and 2mm thick was machined from 347 stainless steel rod; the two flat surfaces were first abraded and then polished with 8 and 1 μm diamond wheels. This specimen was placed in 5 cm^3 of 15 wt % N_2O_4-HNO_3 containing 2 wt % H_2SO_4 and left for two weeks at room temperature. After this period the specimen was removed and washed with acetone and inhibisol before storing under 1 cm^3 of inhibisol to prevent atmospheric contamination. A small quantity of green precipitate was observed near and on top of the stainless steel specimen, on removal from the acid. This was not analysed but a similar precipitate, presumed to be a metal sulphate was observed in early inhibitor experiments.[5.5]

Figure 5.10 shows an XPS scan for 347 stainless steel after immersion in uninhibited 15 wt % N_2O_4-HNO_3 solution, and a 1 minute Argon ion etch. Notable features are the strong chromium peaks indicating protection by Cr_2O_3 or $FeCr_2O_4$.

FIG 5·9   Potential vs time curves for 321 stainless steel in 14% N_2O_4-HNO_3 with H_2SO_4 added.

Legend:
- ○ 0 wt% H_2SO_4
- ● 0·9 wt% "
- □ 1·4% "
- ■ 3·0% "

Y-axis: Potential / mV vs rhodium in 14% N_2O_4 - HNO_3

X-axis: Log time (minutes)
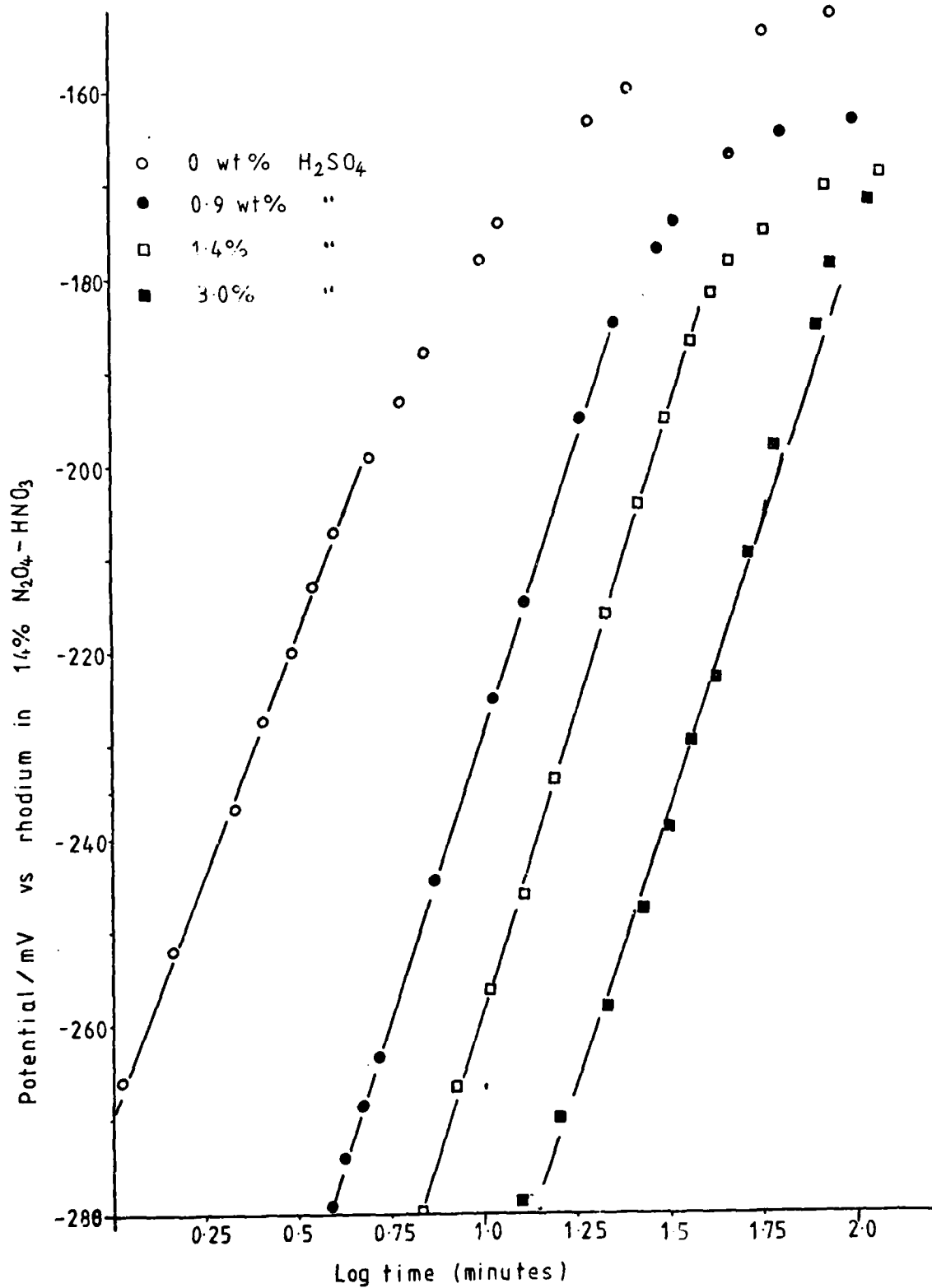
FIGURE 5·10

X.P.S. scan after 1 min Ar ion

etch for 321 stainless steel

after exposure to uninhibited

15 wt% N_2O_4-HNO_3

Binding energy (eV)
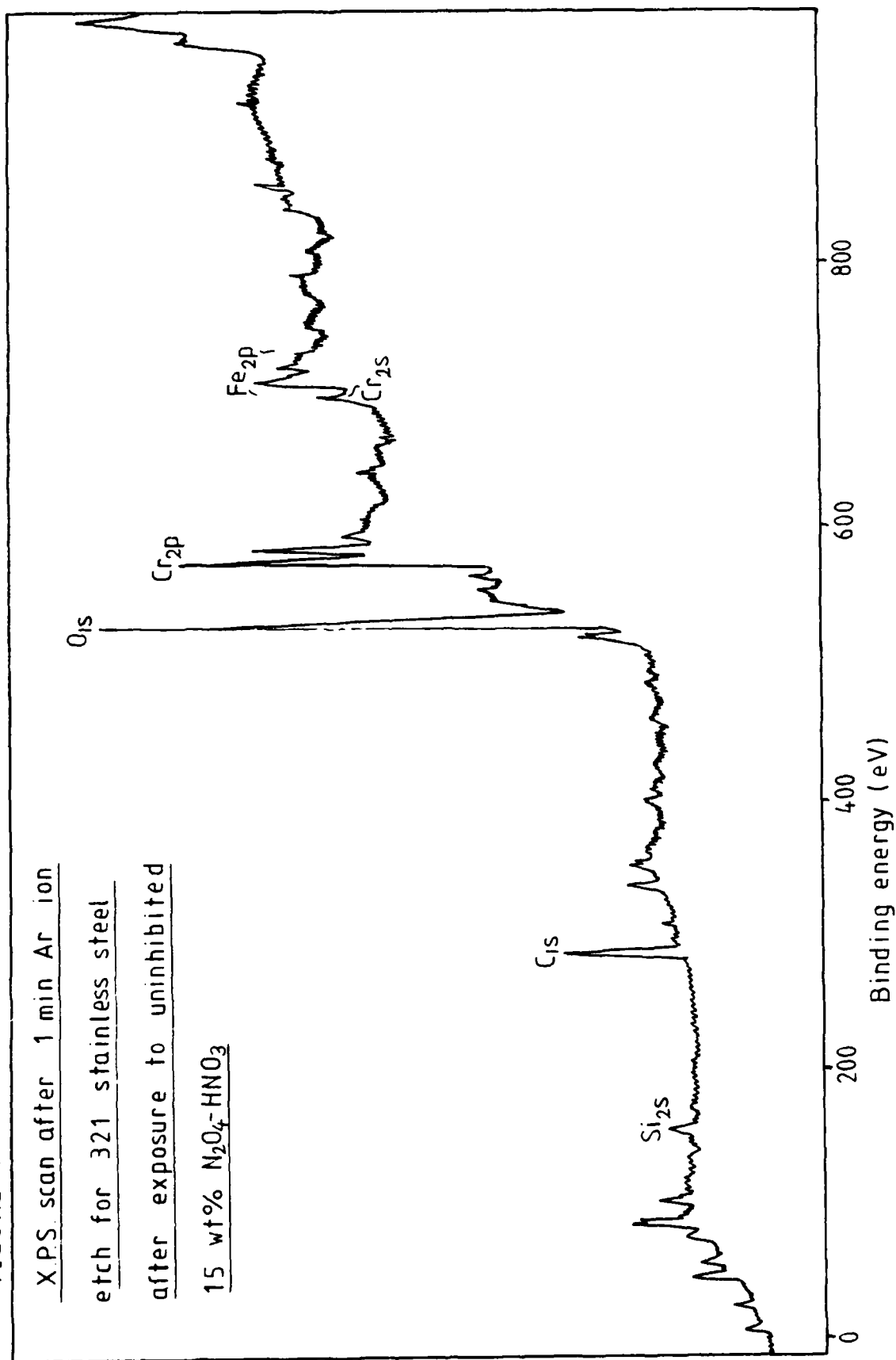
Figure 5.11 shows the XPS scan of the surface of 347 stainless steel after exposure to the H_2SO_4-inhibited acid. S_{2p} and S_{2s} peaks are present suggesting the presence of a sulphate film and in contrast to Figure 5.10 the Cr_{2p} peak is relatively small, whereas the Fe_{2p} peak is more prominent. It seems probable that H_2SO_4 operates as an inhibitor by forming the insoluble $Fe_2(SO_4)_3$ at the anodic areas, which consequently reduces the corrosion rate. The effect of additions of H_2SO_4 on the anodic polarisation character of 347 stainless steel in 15 wt % N_2O_4-HNO_3 is seen in Figure 5.12. The anodic polarisation curves at different H_2SO_4 concentrations are superimposed on one another and the following features are important to note.

I) The area between polarisation and depolarisation curves narrows with increasing H_2SO_4 concentration.

II) The onset of secondary passivation (SP) occurs at lower overpotentials and for lower currents, the higher the concentration of H_2SO_4.

III) The rest potential after polarisation is less noble the more sulphuric acid is present.

The general shape of the polarisation curves is indicative of breakdown and is similar to that observed for 347 stainless steel in uninhibited systems. Optical microscopy of electrodes exposed to this polarisation breakdown has shown an electrode surface covered with pits. The presence of the sulphate anion prevents intergranular attack but as an aggressive anion in the system, causes pitting corrosion of the stainless steel.

Figure 5.11

XPS scan of 321 Stainless steel
after exposure to 15% $N_2O_4-HNO_3$
+ 2.0 wt% H_2SO_4
(scan after 30 sec Ar ion etch.)

Binding energy (eV)

O_{1s}

Fe_{2p}

Cr_{2p}

Fe augers

O auger

C_{1s}

Au_{4d}

S_{2s}

S_{2p}

Au_{4f}

Fe_{3p}

Figure 5·12

Anodic polarisation curves for

321 Stainless Steel in 15wt%

N₂O₄–HNO₃ at 0°C.

——— Uninhibited

—·—· +2·0wt% H₂SO₄

Current / μA·cm⁻² (log scale)

Overpotential ηₐ / mV
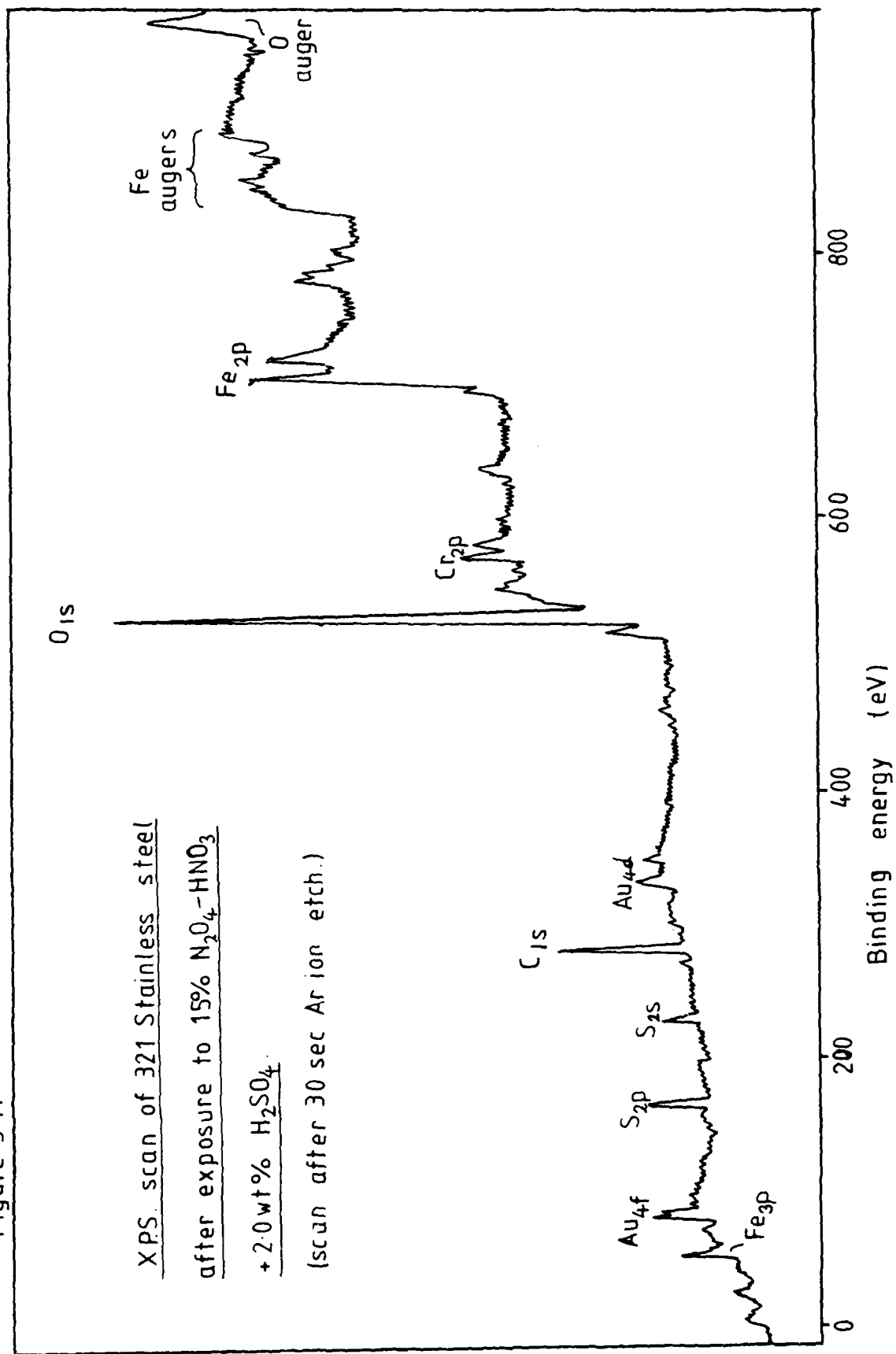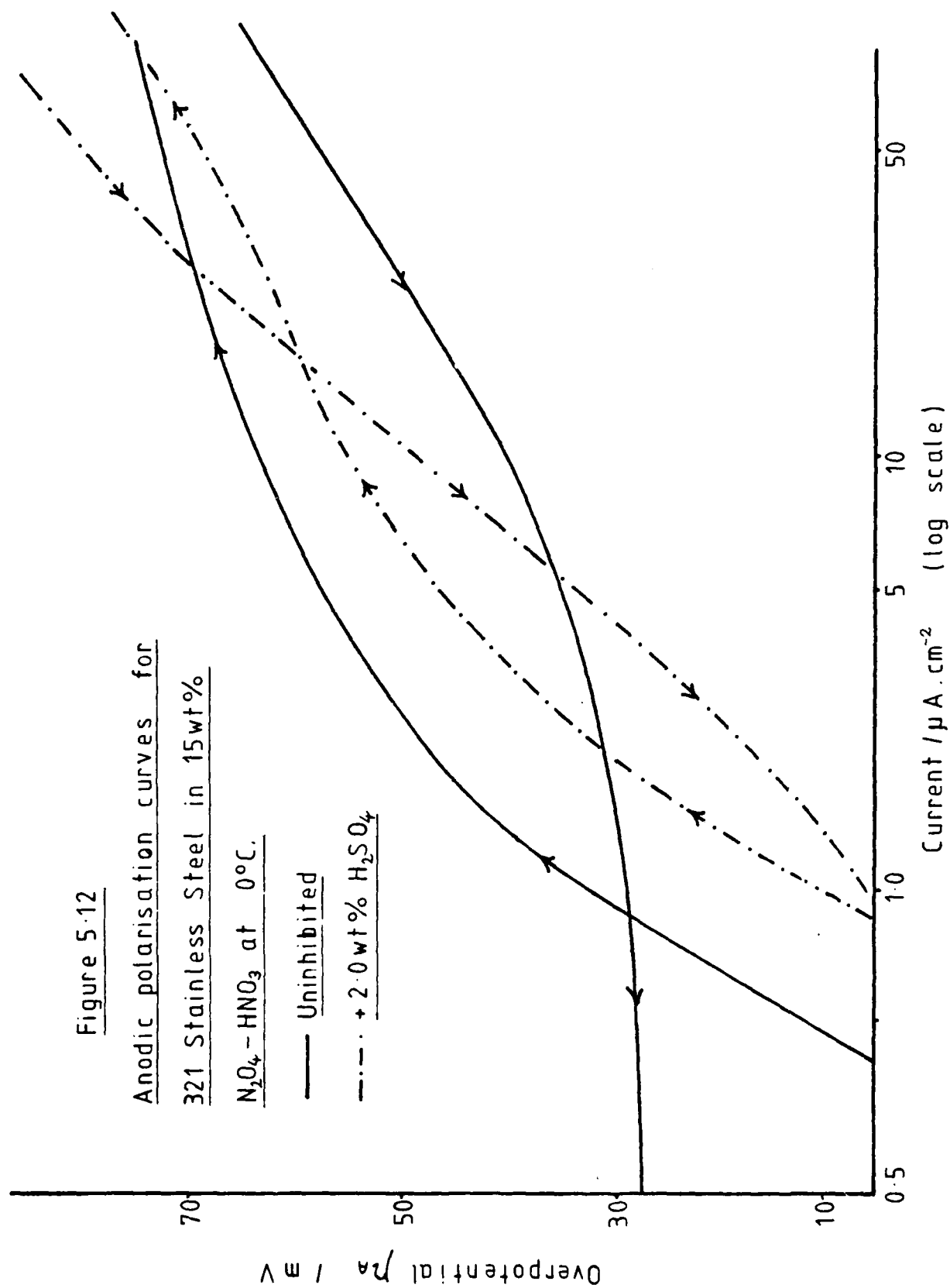
Sulphate anion reduces the attack at the anodic sites on a
stainless steel surface by the formation of Iron sulphate,
but the reduction in corrosion is not sufficient for H_2SO_4
to be considered as a viable inhibitor. Large quantities
of metal sulphate, formed at the metal surface, and initially
adhering to it, eventually break away to form metal sulphate
precipitates in solution.

Sulphate, phosphate and fluoride have very similar inhibitor
mechanisms but the degree and effectiveness of fluoride as an
inhibitor far exceeds the protection offered by the other two.

Figure 5.13 shows a potential-time curve for 347 stainless
steel in 15 wt % N_2O_4-HNO_3 containing 0.6 wt % F^- (as KF).
The displacement of the curve to the right indicates the
greater effectiveness of fluoride as an anodic inhibitor.
It is also significant to note that the presence of fluoride
enhances the cathodic reaction; this is indicated by the
steeper passivation slope $\Delta E/dlnt$. Figure 5.14 shows a cathodic
polarisation curve for 347 stainless steel in this inhibited
system. The curve is very well defined with a Tafel slope
of - 110 mV, to be expected from the one-electron reaction
$$NO_2^+ + e^- \longrightarrow \tfrac{1}{2}N_2O_4.$$
The greater efficiency of this reaction on the fluoride film
could be due to two reasons:-

I)   increased   ionic conductivity of the film,

II) easier adsorption of reduced and oxidised species.

Figure 5·13
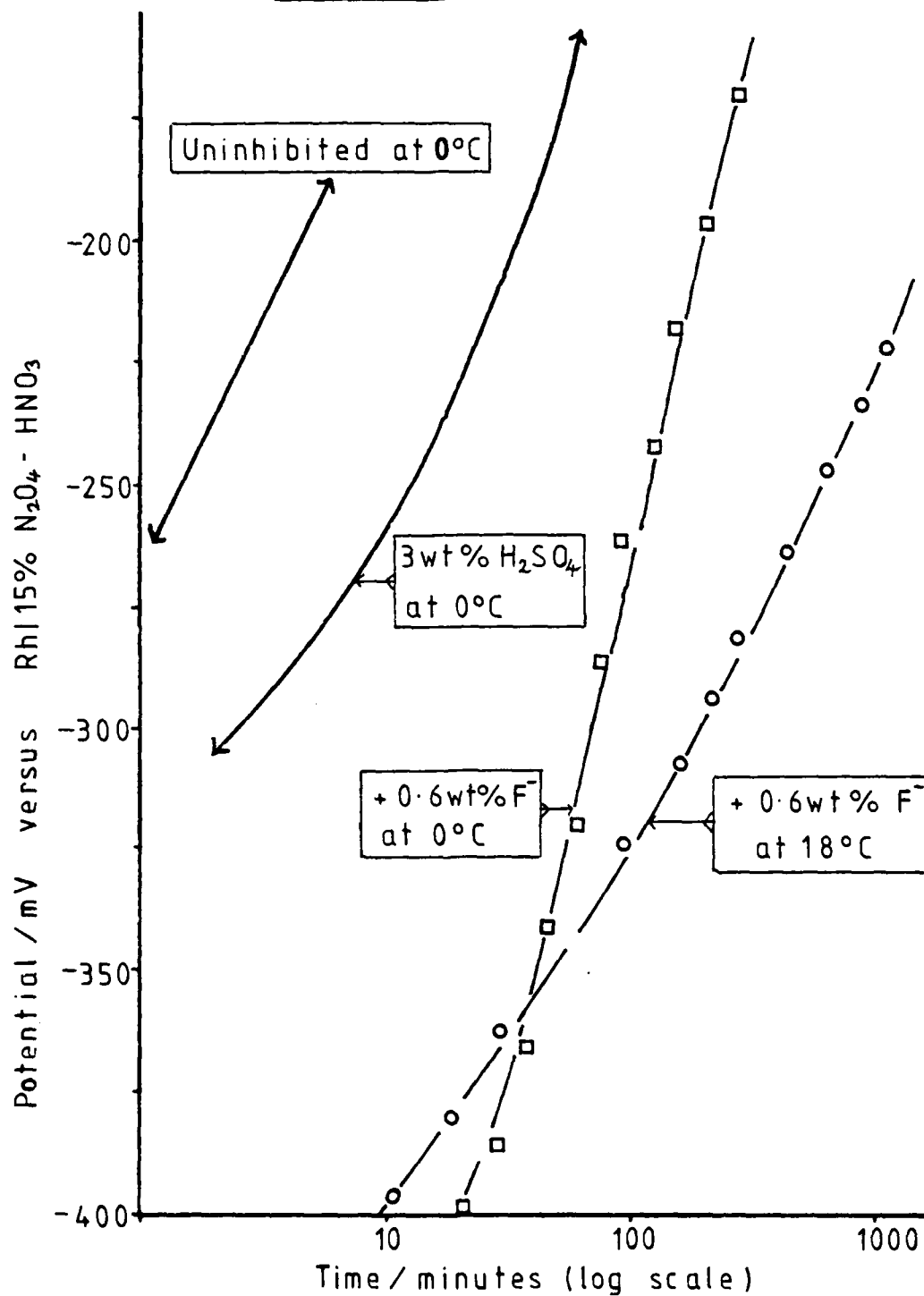
Potential / time curves for 347 Stainless Steel in 15 wt% N_2O_4-HNO_3

Figure 5.14

Cathodic Polarisation curve for 347
Stainless Steel in 15wt% N_2O_4 - HNO_3
Inhibited with 0.6wt% F^- (as KF)

$(T = 0°C, S/V = 0.1 cm^{-1}, d\eta/dt = 80 mV.min^{-1})$

$i_{corr} = 5 \times 10^{-8} A.cm^{-2}$
$= 4.4 \times 10^{-4} g.cm^{-2}.year^{-1}$
$b_c = -112 mV.decade^{-1}$

Current / $\mu A.cm^{-2}$ (log scale)

Potential / mV against Rh | 15% N_2O_4 in HNO_3
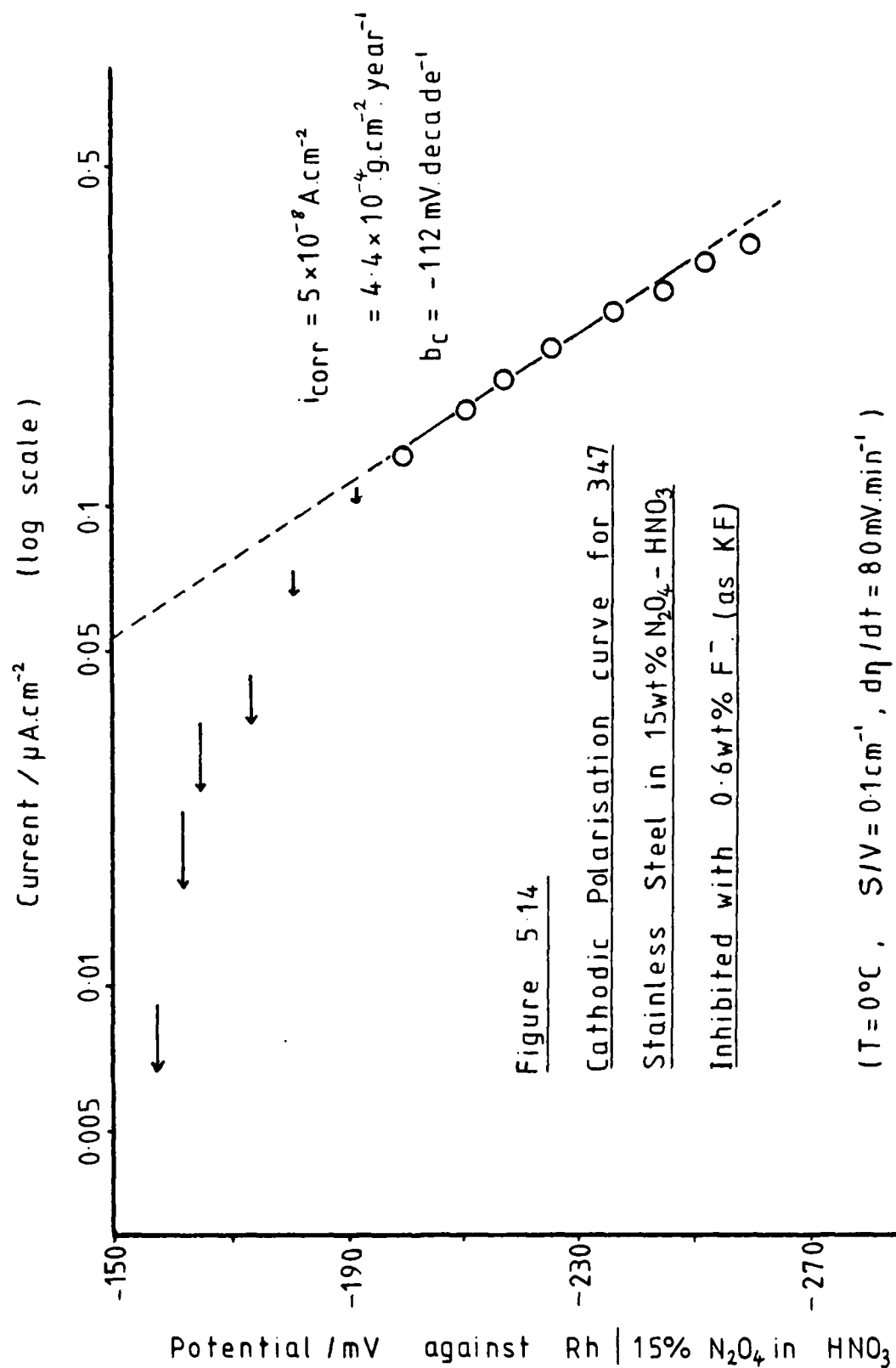
Figure 5.15 shows an anodic polarisation curve for 321 stainless steel in F^--inhibited 15 wt % N_2O_4-HNO_3. No breakdown characteristics are evident and the film on the stainless steel surface appears to be presenting a very protective barrier to the corrosion. The fluoride ion acts as a very efficient anodic film-forming inhibitor, initially reacting at the anodically active sites to form a metal fluoride which then effectively blocks further attack. Figure 5.16 shows an XPS scan after 30 sec Argon ion etch for 321 stainless steel exposed to 15 wt % N_2O_4-HNO_3, containing 0.6 wt % F^-, for 2 weeks. The significant difference between this scan and that for sulphate inhibition (Figure 5.11) is the greater prominence of the chromium peaks (Cr_{2p}) after immersion in the fluoride-inhibited medium. It would appear that with time, build up of insoluble metal fluoride at the anodic areas causes it to be dispersed into the solution. This, however, is a much slower process than the precipitation observed in the H_2SO_4-inhibited system.

Conclusion

The filming inhibitors described are essentially anodic in their mechanism of action and exert their action by the formation at the anodic areas of highly insoluble corrosion products, which subsequently stifle further attack. Build up of these corrosion products with time leads to their suspension in the liquid to form colloidal solutions or gelatinous solids which cause severe filtration problems.
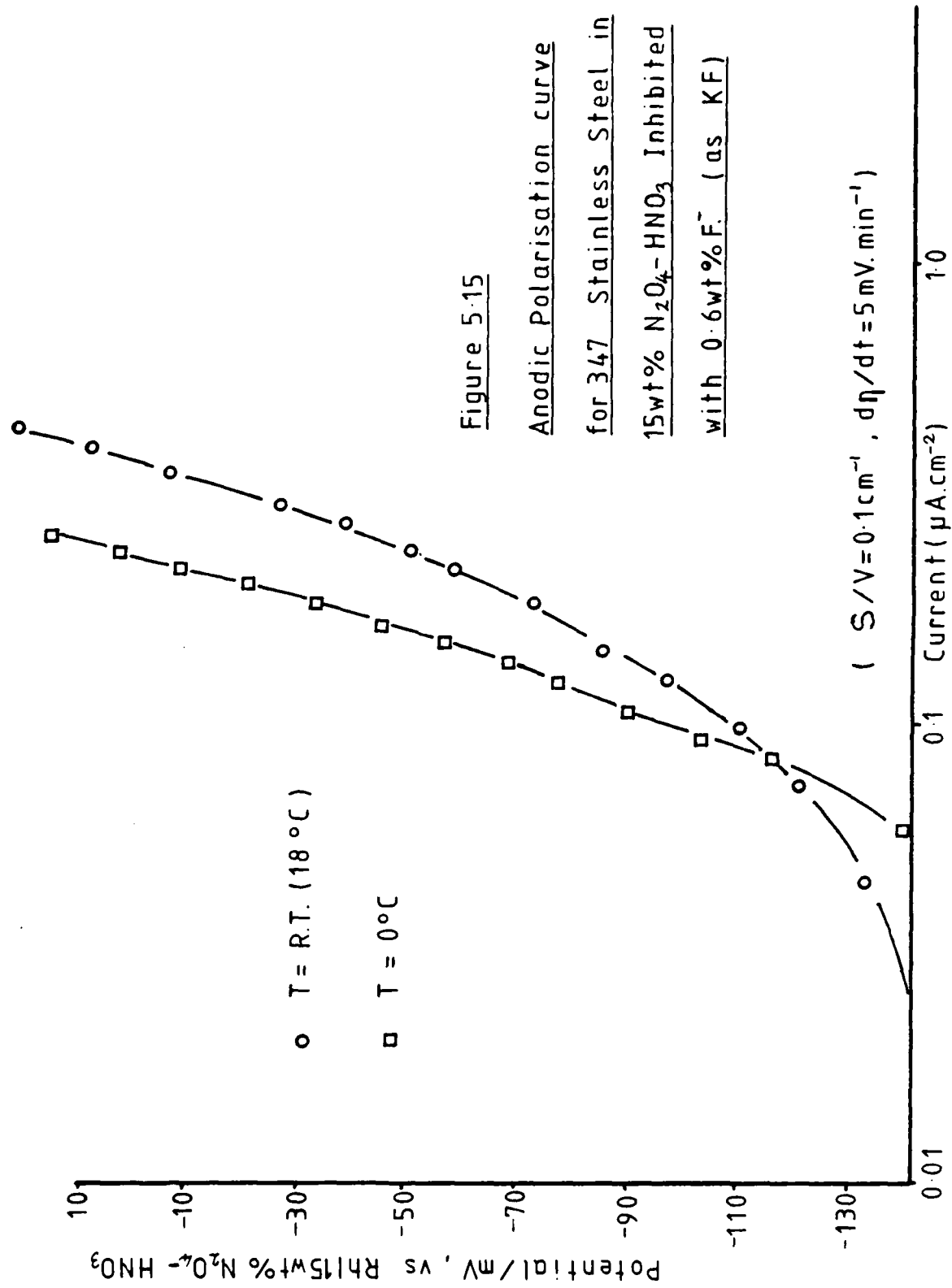
Figure 5.15

Anodic Polarisation curve
for 347 Stainless Steel in
15wt% N_2O_4 – HNO_3 Inhibited
with 0.6wt% F^- (as KF)

(S/V=0.1cm^{-1} , dη/dt=5mV.min^{-1})

Current(μA.cm^{-2})

Potential/mV , vs RH15wt% N_2O_4– HNO_3

o   T = R.T. (18 °C)

□   T = 0°C

Figure 5.16

XPS scan after 30 sec Ar etch

for 321 stainless steel after exposure

to 15wt% N_2O_4–HNO_3 + 0.6wt% F^-

Binding energy (eV)
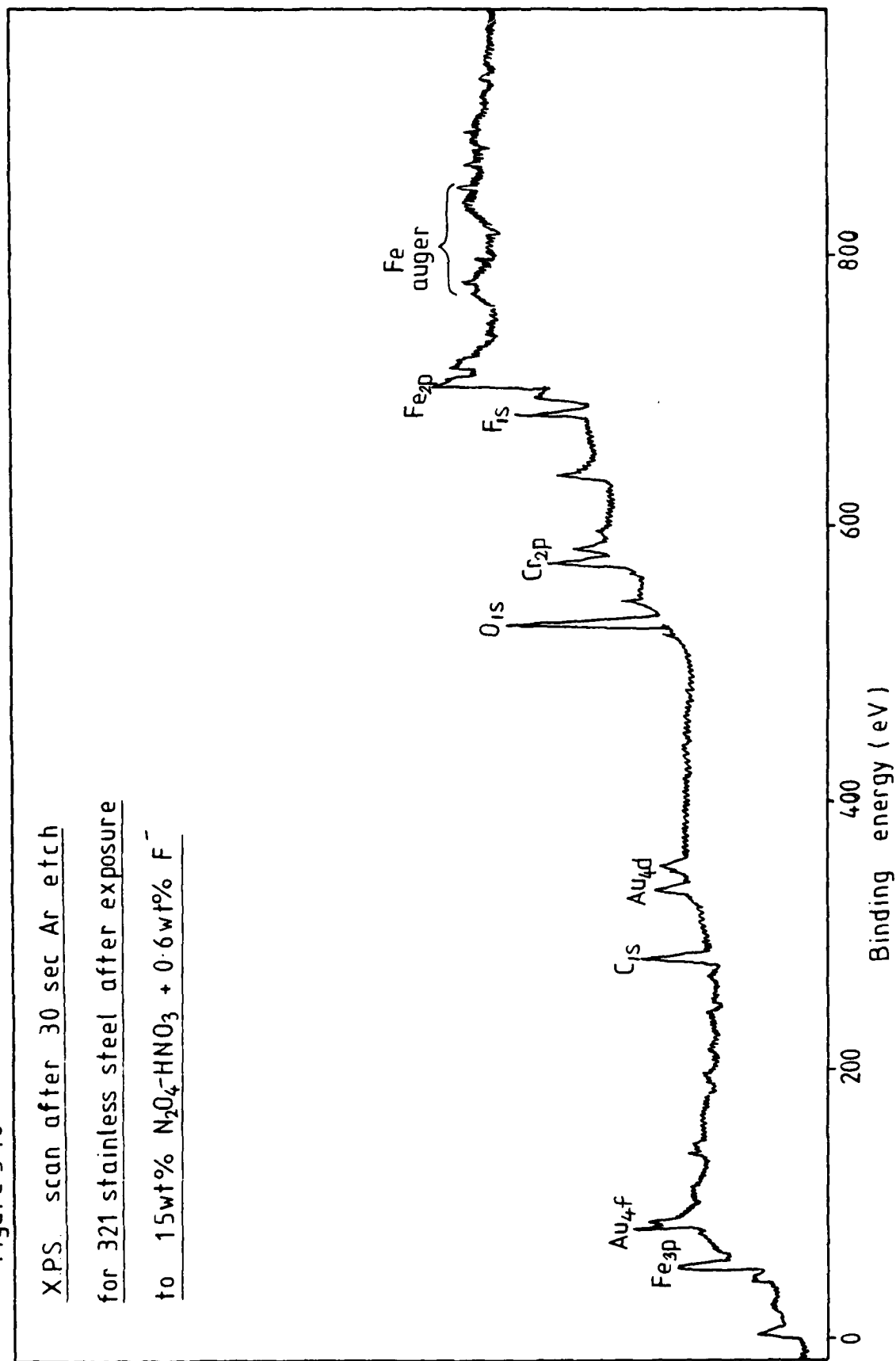
It is our opinion that in a closed system an inhibited HNO_3/N_2O_4 solution, stored for a long period of time, will inevitably deposit insoluble solid matter if the inhibitor used is of the anodic film-forming type.

Note:-

In all electrochemical experiments in HNO_3/N_2O_4 solutions containing added fluoride it has been assumed, with reasonable confidence , that the operation of rhodium and platinum reference electrodes is unimpaired by the presence of fluoride. However, this assumption has not been validated and experiments have yet to be performed to assess the behaviour of rhodium and platinum when fluoride is present.

(b) HF (SHDA) and PF₅ (MHDA)

(i) Polarisation Studies of 321 Stainless Steel

The polarisation behaviour of 321 stainless steel in SHDA has been briefly reported and the fluoroplastic cell used in electrochemical studies involving inhibitors described.[5.3]

A series of polarisation curves for 321 stainless steel in both SHDA and MHDA has been obtained. The stainless steel electrodes were in the form of machined discs. The surface pre-treatment employed is described in Section 5.1 of this report. Polarisation experiments were conducted using a Thompson Ministat precision potentiostat, using the potential step method. (See Section 3)

The potential of the working electrode, relative to the platinum reference electrode, was monitored over a period of 24 hours prior to the commencement of the polarisation experiments. A number of anodic and cathodic polarisation curves were then obtained at room temperature, the rest potential (E_{rp}) being recorded before and after each polarisation run. The cell was then surrounded in ice and a number of anodic polarisation studies were carried out at $0^{\circ}C$.

At room temperature the curves obtained for SHDA and MHDA (Figure 5.17 and Figure 5.18) are similar, and the influence of step time on the shape of the curve is slight. The cathodic portions obey the Tafel equation (i.e., give rise to a linear portion) between 50 and 200 mV cathodic overpotential. The cathodic Tafel slopes are consistent with a 1 electron process (i.e., $NO_2^+ + e^- \longrightarrow \frac{1}{2}N_2O_4$).

The curvature of the anodic portion is attributed to insufficient time being allowed between potential steps for the current to decay, even when using the longest step time ($\sim 1,000s$) available (when recording automatically).

At $0^{\circ}C$ only very slight curvature is observed for the stainless steel in SHDA system (Figure 5.19). The influence of step time on the shape of curve has also been investigated (Figure 5.20). Pronounced curvature is observed when the step time is too short but when it exceeds 600s the anodic curves display an almost vertical portion. In MHDA the form of curve obtained at $0^{\circ}C$ is different (Figure 5.21). The

Fig. 5.17 Polarisation Curve of Stainless Steel in SHDA

Temp. 21°C, Step Time 990 s
Step Voltage 20 mV, Scan Rate 0.02 mV s^{-1}
S/V 0.013 cm^{-1}

$E_{rp} = -265$ mV

$i_{corr} = 175 \times 10^{-7}$ A cm^{-2}

Fig. 5.18 Polarisation Curve of Stainless Steel in MHDA

Temp. 19.5°C, Step Time 20 s
Step Voltage 20 mV, Scan Rate 1 mV s^{-1}
S/V 0.04 cm^{-1}

$E_{rp} = -265$ mV

$i_{corr} = 2.1 \times 10^{-7}$ A cm^{-2}

Current Density/ A cm^{-2}

Potential / mV
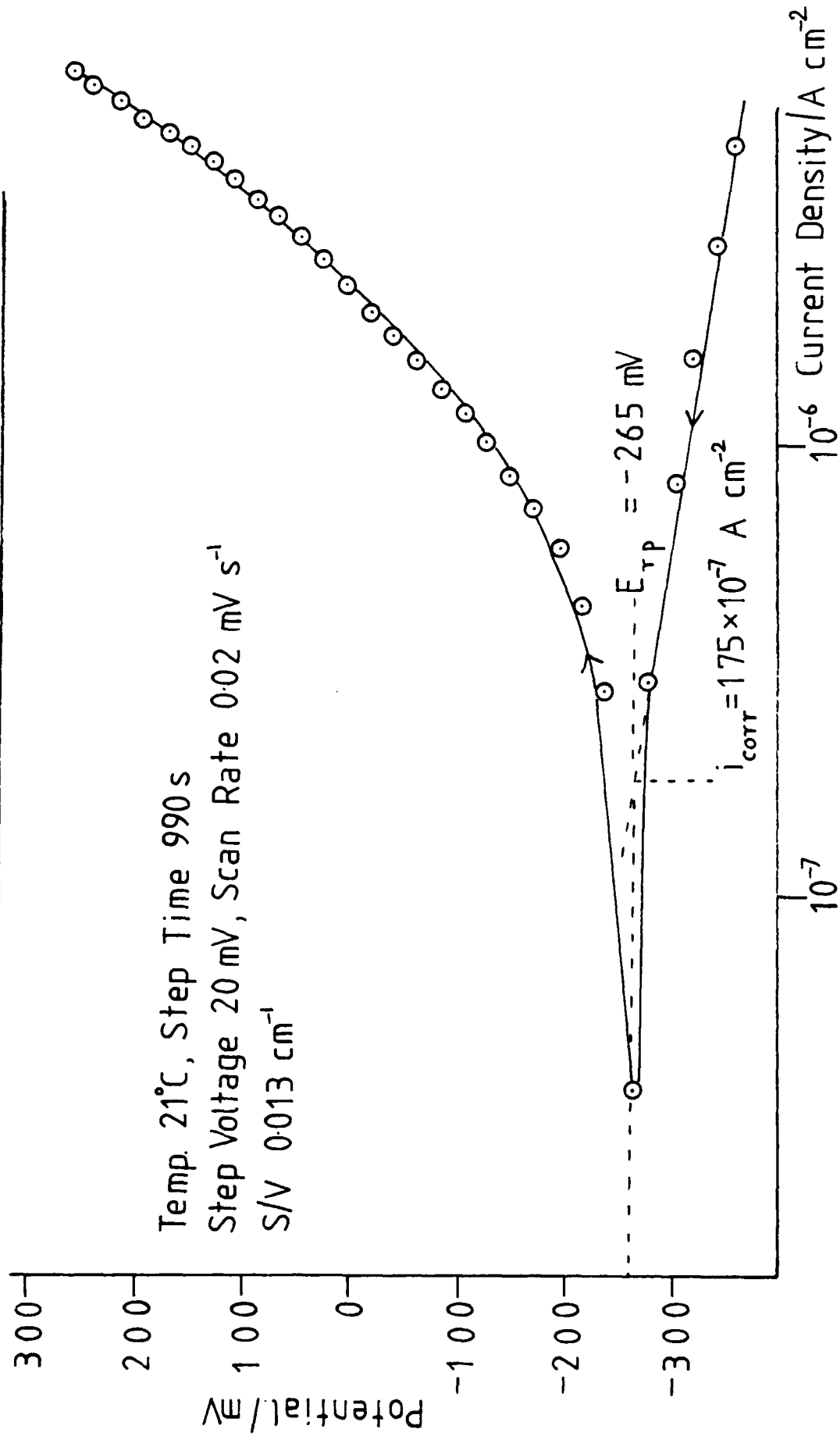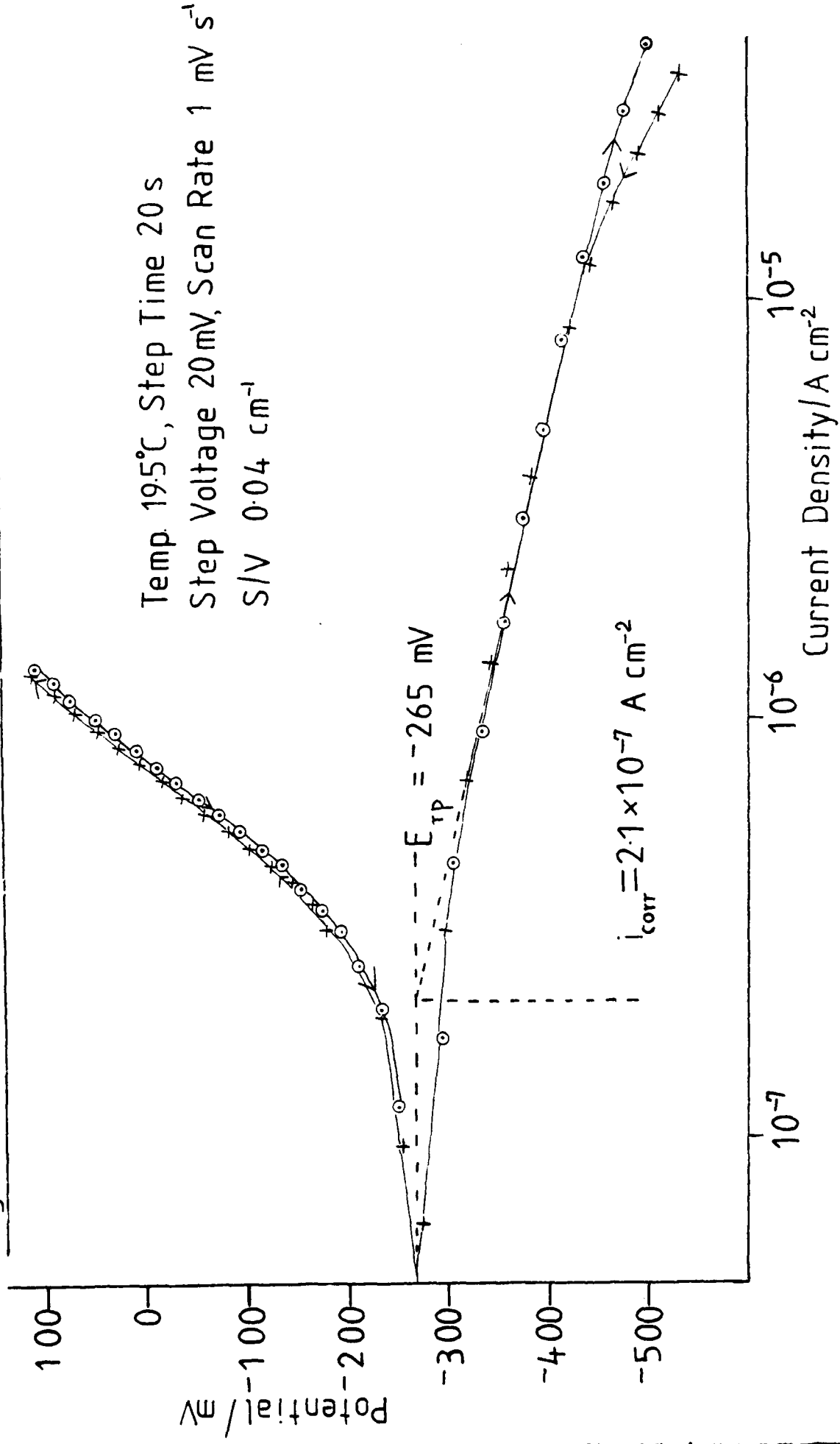
Fig 5.19 Anodic Polarisation Curve of Stainless Steel in SHDA at 0°C

Step Time 990 s, Step Voltage 58 mV
Scan Rate 0.06 mV s⁻¹, S/V 0.013 cm⁻¹
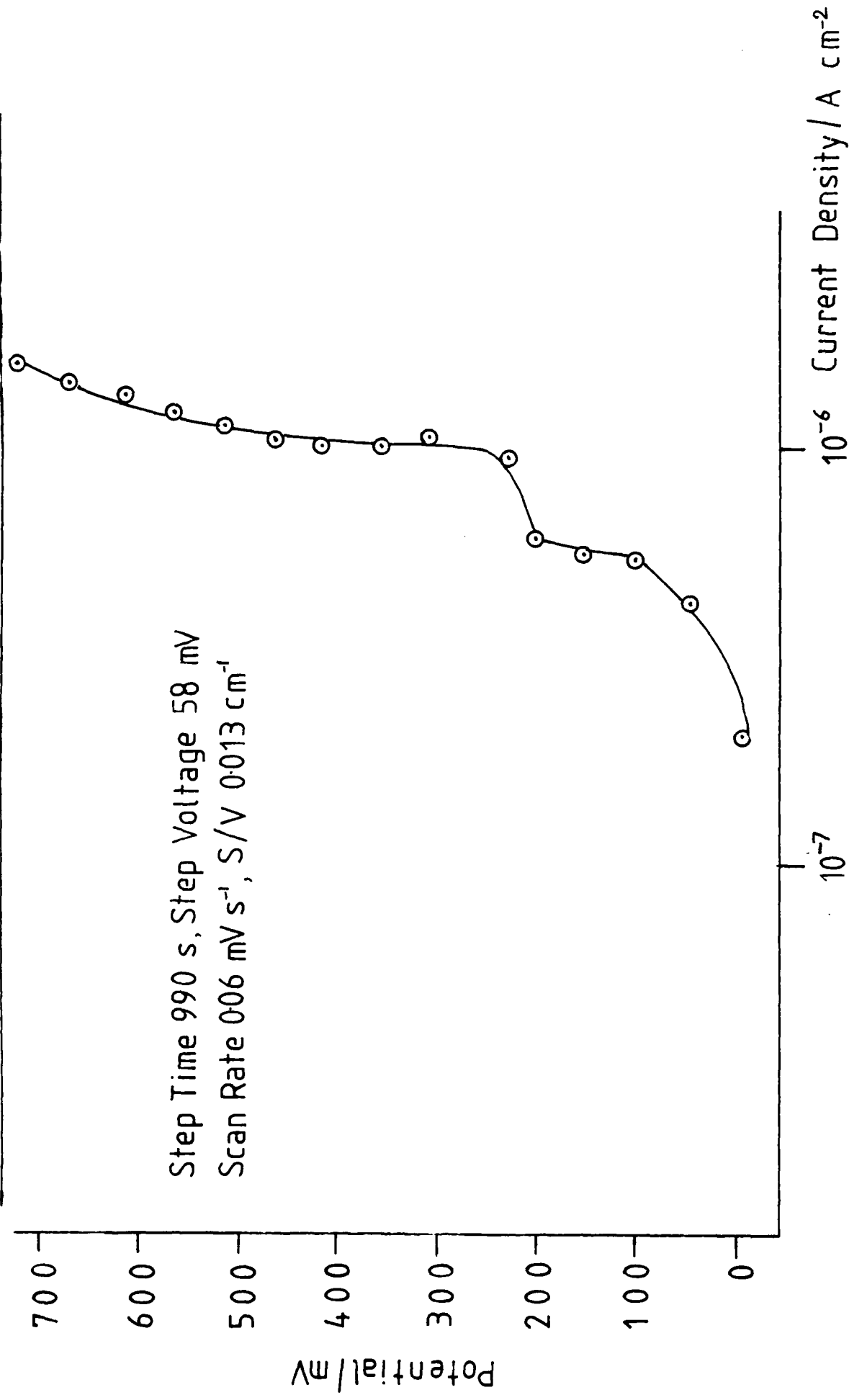
Fig 5·20 Effect of Step Time upon the Stainless Steel / SHDA

Polarisation Curve

Temp. 19°C

Step Time	Step Voltage	Scan Rate
□·····600 s······	32 mV······	0·05 mV s^{-1}
⊙····990 s······	50 mV······	0·05 mV s^{-1}
+·····120 s······	95 mV······	0·79 mV s^{-1}

$S/V = 0·013$ cm^{-1}

Current Density / A cm^{-2}

Potential / mV
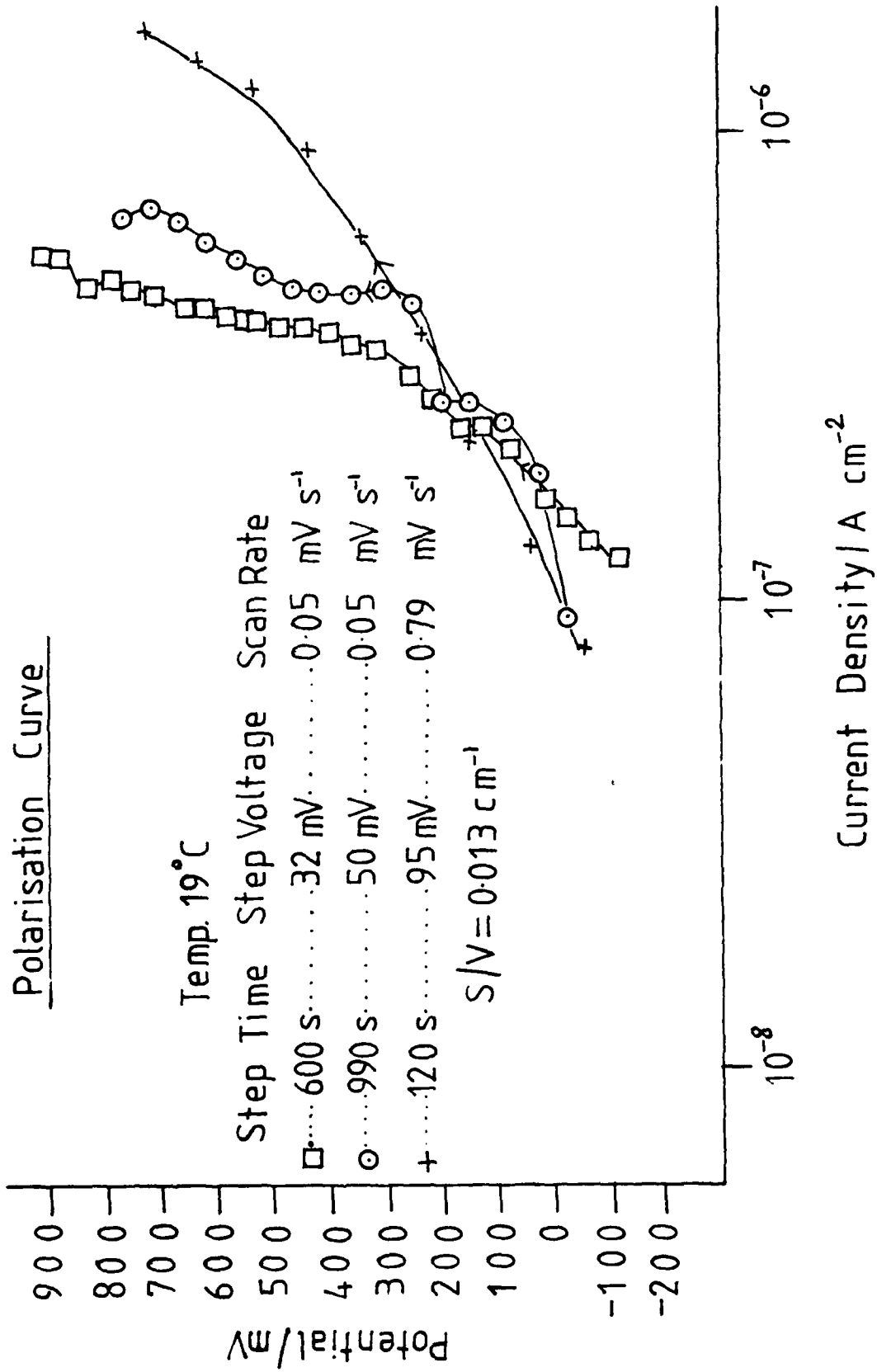
Fig. 5:21 Anodic Polarisation Curve of Stainless Steel in MHDA at 0°C

Step Time 990s, Step Voltage 70 mV
Scan Rate 0·07 mV s⁻¹, S/V 0·04 cm⁻¹
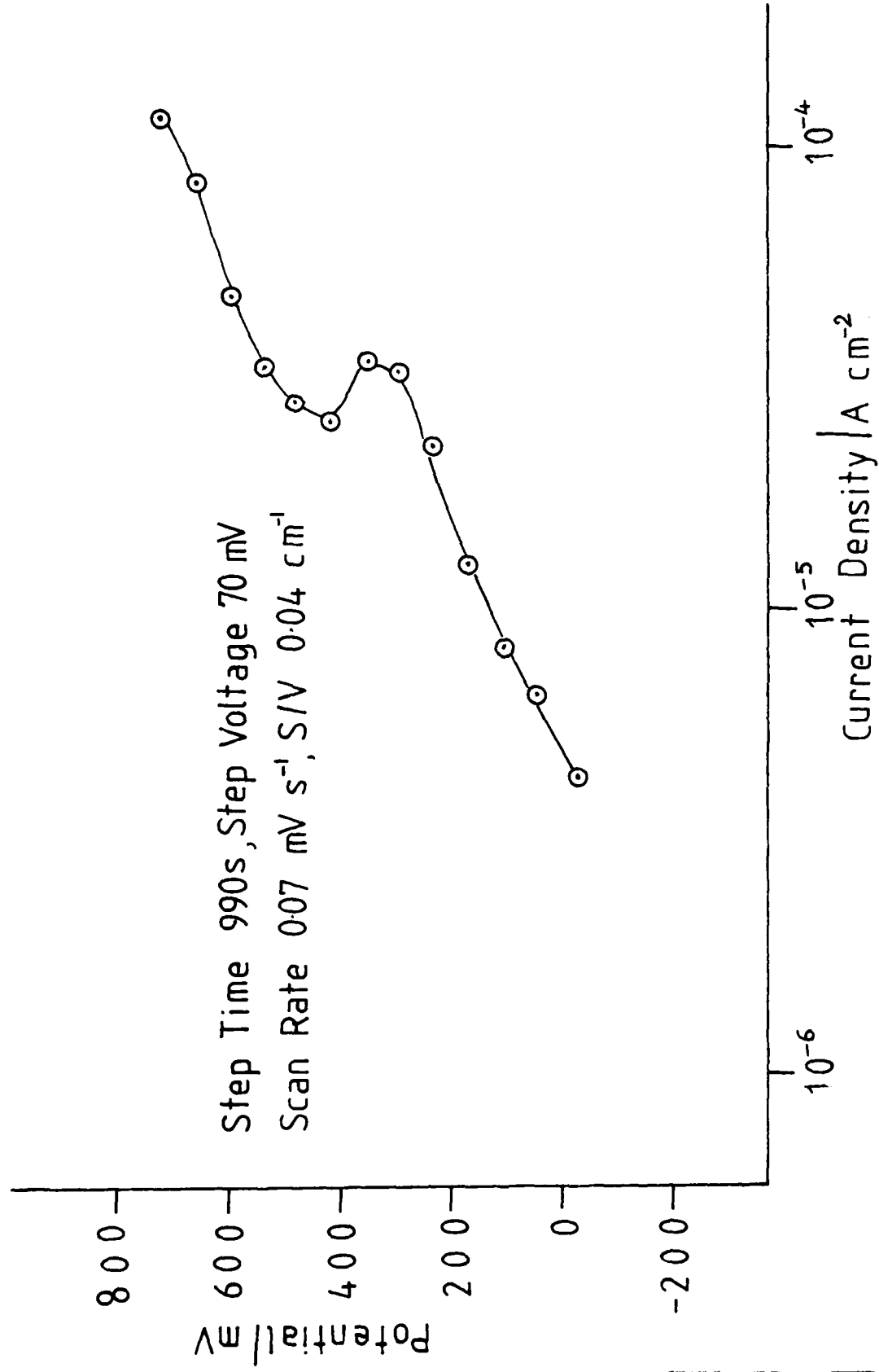
effect of temperature on this system is also marked. E_{rp} moves
from -245 mV at room temperature to -136 mV at 0^OC. This
change implies that the film is thicker at 0^OC than at room
temperature. The stainless steel/SHDA system exhibits only
a small temperature effect; E_{rp} changes from -320 mV at
room temperature to -294 mV at 0^OC. Thus in the SHDA system
the film displays similar properties at room temperature
and 0^OC.

The corrosion current (i_{corr}) values (obtained by the
Tafel extrapolation method, see Section 3) for SHDA and MHDA
at room temperature indicate very low corrosion rates.
"Experimental" and electrochemical rates are compared in Table
5.1. Direct qualitative comparisons between "experimental" and
electrochemical rates are difficult because the influence of
many factors (e.g, surface area/volume ratio and surface pre-
treatment) is unknown. However, provided the corrosion is
uniform, the accuracy of the Tafel extrapolation method would
be equal to or greater than conventional techniques such as
weight loss.

(ii) Potential /Time Studies of 347 Stainless Steel

The surface preparation of the stainless steel was carried
out as outlined in Section 5.1 of this Report. The variation

Table 5.1   Comparison of Electrochemical and "Experimental"* Corrosion

Rates for 321 Stainless Steel

At Room Temperature

	SHDA	MHDA
Electrochemical corrosion rate ($g\ m^{-2}\ h^{-1}$)	1.2×10^{-3}	1.5×10^{-3}
Surface area/volume ratio (cm^{-1})	0.013	0.03
"Experimental" corrosion rate ($g\ m^{-2}\ h^{-1}$	1.3×10^{-3}	2.4×10^{-4}
Surface area/volume ratio (cm^{-1})	0.22	0.95
Time after which experimental rate measured (days)	42	28

*
The "experimental" corrosion rate data were obtained from non-electrochemical experiments, further details of which can be found in Refs. 5.1 (SHDA) and 5.3 (MHDA).

of the potential of the working electrode (relative to a platinum reference electrode) was monitored using a chart recorder (connected to the cell via an impedance matching device). The results are summarised in Table 5.2.

The cell was maintained at a temperature of $25^{\circ}C$ throughout the duration of the experiment.

In the SHDA system the potential initially increased i.e., became more positive, reaching -190 mV after 1 hour, but then began to decrease. This decrease (down to -335 mV) was relatively smooth for 90 hours. After this time, there is some evidence for film breakdown-repair processes. Sharp decreases in potential, followed by gradual rises of the order of 50 mV, being observed. After 200 hours the potential remained relatively stable, fluctuating between -400 and -420 mV.

In the MHDA system, an initial increase in potential was also observed, the most noble potential reached being -158 mV (after 4 hours). The potential then decreased smoothly until it stabilised at -260 ± 20 mV after about 50 hours.

(iii) Conclusions

In SHDA and MHDA the presence of an inhibitor keeps the protective surface film thin. In uninhibited HDA, the chromium oxide film grows and corrosion eventually takes place because of the transpassivation effect, but in media containing HF and PF_5 this is prevented. Potential/time studies suggest

Table 5.2   Summary of Potential/time Results for

347 Stainless Steel

At Room Temperature

	SHDA	MHDA
Initial potential (mV) after 12 minutes	-217	-238
Final potential (mV)	-410	-250
Duration of experiment (hours)	260	160

that a thicker film is formed in MHDA than in SHDA and that
the growth of these films is a multistage process. The type
of film formed probably depends on the nature and concentration
of potentially inhibitory anions (e.g., F^-, $PO_2F_2^-$) in the
system. Polarisation studies indicate that although HF and
PF_5 produce a similar effect (particularly at room temperature)
the properties of the actual films formed are considerably
different.

(c) $\underline{As_2O_3}$

As_2O_3 was one of the corrosion inhibitors for WFNA
studied[5.5] in 1955 and was discovered to have very good
inhibiting properties in the liquid phase, offering protection
that can be 3-100 times greater than that afforded by
sodium fluoride. However, As_2O_3 was disregarded as an
inhibitor, presumably on account of its poisonous nature as
well as the lack of protection it afforded stainless steel
exposed to the vapour phase. As_2O_3 is, nevertheless, of consid-
erable academic interest as an inhibitor and this, inspired
by the earlier Report,[5.5] has prompted an investigation in our
laboratories. This has involved electrochemical and surface
studies, which have shown As_2O_3 to be a different type of
inhibitor which may be used to complement fluoride inhibitors
to give much better all-round protection.

It is well documented that in concentrated nitric acid,
As_2O_3 is oxidised to As_2O_5. This oxidation occurs very rapidly
in pure nitric acid and the development of a yellow colour in

the nitric acid indicates reduction to NO_2/N_2O_4. It is probable that As_2O_5 hydrolyses to an arsenic acid, but the exact character of As(V) in solution has not yet been determined. Electrochemical and spectroscopic studies are planned to determine the extent of oxidation and hydrolysis.

In the presence of metal (i.e., reducing agent) in HNO_3/N_2O_4 solutions, the redox equilibrium
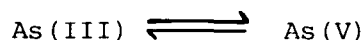
$$As(III) \rightleftharpoons As(V)$$

will *exist* . Stainless steel placed in HNO_3/N_2O_4 solution will take up a negative rest potential relative to the $NO_2^+/\frac{1}{2}N_2O_4$ redox potential of the solution. At the surface of the metal specimen the As(III)/As(V) equilibrium will be substantially more displaced towards As(III) than it will be in the bulk solution and As_2O_3 (or, more likely, a hydrolysed derivative, designated hereafter as "As_2O_3") will be the favoured product at the metal surface. A dynamic equilibrium will therefore exist between "As_2O_3" on the stainless steel surface and an As(V) species in solution.

Figure 5.22 shows a series of potential-time curves for 347 stainless steel in 15 wt % N_2O_4-HNO_3 for different inhibitors. Curve (a) represents the uninhibited system and curve (b) the same system inhibited by 0.3 wt % As_2O_3. The rest potential reached after a few days was between -20 and -50 mV lower than the $NO_2^+/\frac{1}{2}N_2O_4$ redox potential of the system, indicating that with time the equilibrium at the stainless steel surface remains more in favour of As(III) than the equilibrium in bulk solution.
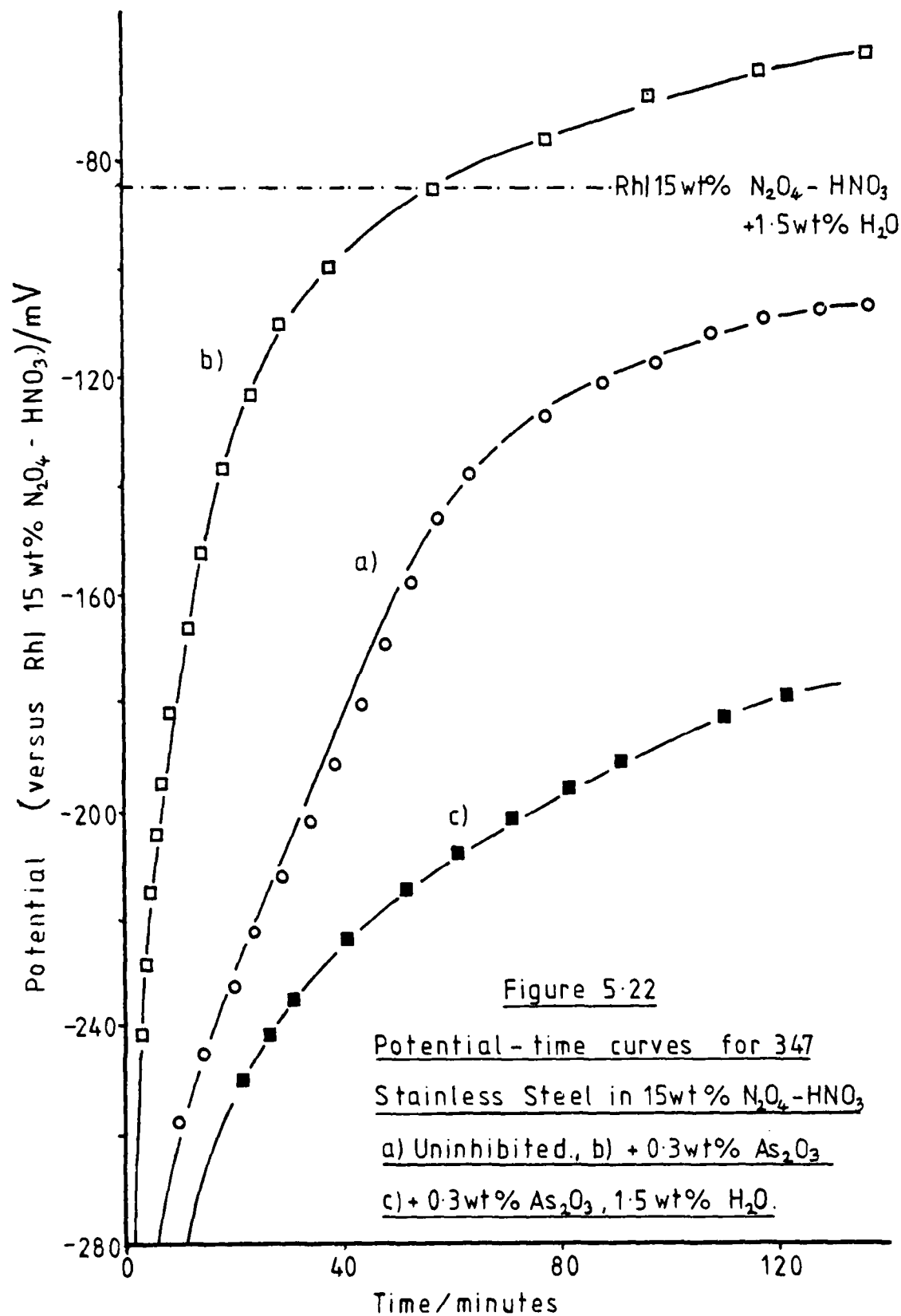
Figure 5.22

Potential-time curves for 347 Stainless Steel in 15wt% N_2O_4-HNO_3

a) Uninhibited., b) + 0.3wt% As_2O_3

c) + 0.3wt% As_2O_3, 1.5 wt% H_2O.

A 347 stainless steel specimen was prepared for XPS examination as already described. It was then placed in a 15 wt % N_2O_4-HNO_3 mixture containing O.3 wt % As_2O_3 at room temperature and set aside for 2 weeks. Figure 5.23 shows the 'as received' XPS scan of the stainless steel surface. The As(3p) and As auger peaks are clearly observed and the relative absence of chromium or Iron peaks suggests the presence of an oxide or oxo-acid of arsenic rather than a metal arsenate(V) or metal arsenate (III). The specimen was argon ion etched for 30 seconds and Figure 5.24 shows the subsequent XPS scan. The arsenic oxide or oxo-acid layer has been completely removed as indicated by the complete absence of an arsenic peak. The chromium and iron peaks are similar in relative intensity to those in Figure 5.10 for the surface of stainless steel exposed to uninhibited 15 wt % N_2O_4-HNO_3. These results suggest deposition of a very thin film of 'As_2O_3' on top of the air-formed film of Cr_2O_3/$FeCr_2O_4$. This 'As_2O_3' film as indicated by the short argon ion etch time needed to remove it, is probably no more than $10\mathring{A}$ thick. This action whereby As(V) is reduced to As(III) at the negative metal surface is similar to the action of As_2O_3 in acid aqueous solutions. As(III) present as AsO^+ is reduced by a negative metal surface to form a thin layer of elemental arsenic all over the metal. The arsenic is depcsited as an amorphous film which is estimated to be only 5-6 monolayers thick.

A preliminary polarisation study of the As_2O_3-inhibited system has been made. Figure 5.25 shows a schematic diagram

Figure 5.23

X.P.S. scan of 321 Stainless steel
after exposure to 15 wt% N_2O_4–HNO_3
+ 0.3 wt% As_2O_3.
(scan-as received)
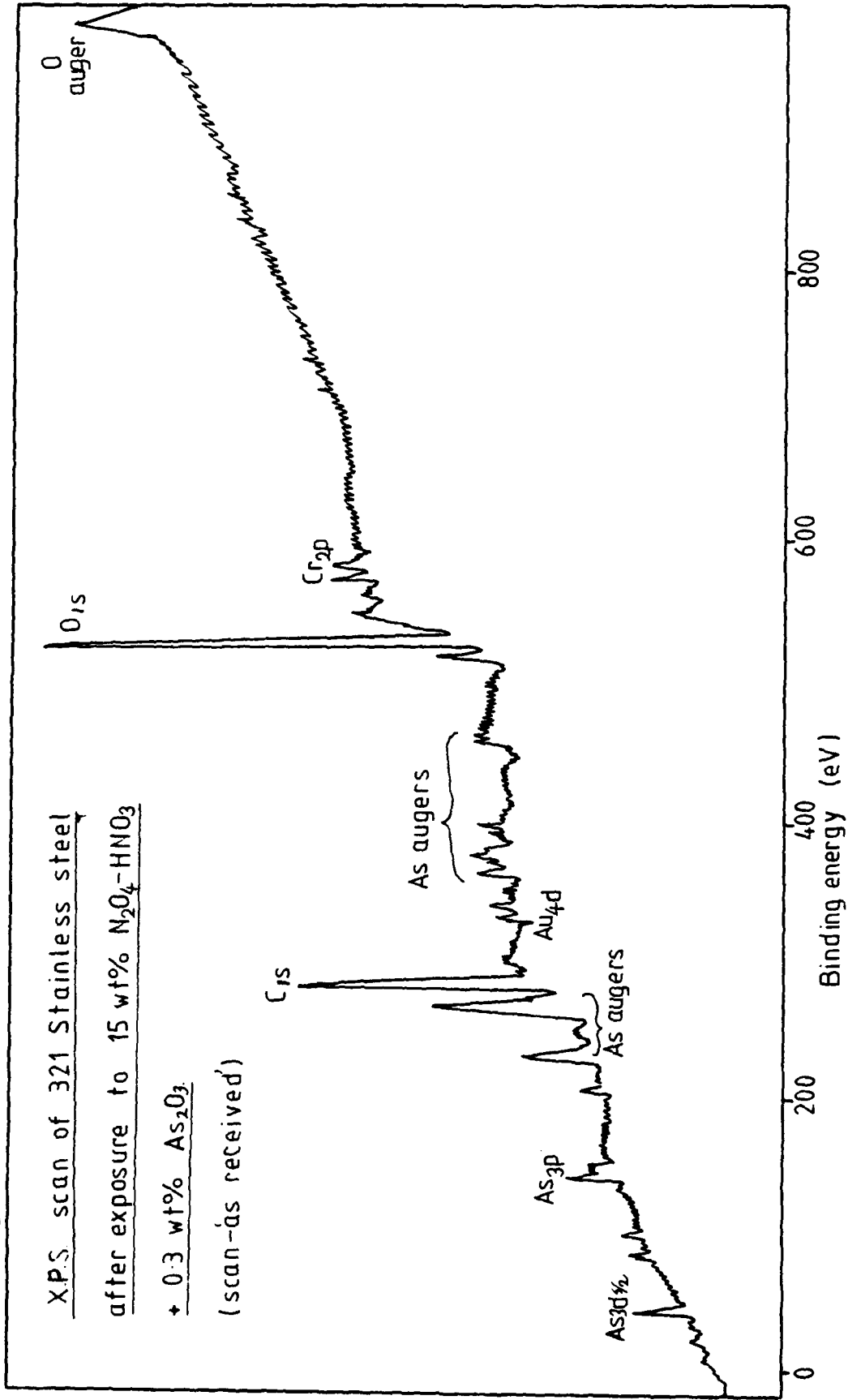
Figure 5.24

X.P.S scan after 30 sec Ar ion

etch for 321 stainless steel

after exposure to 15 wt%

$N_2O_4-HNO_3 + 0.3$ wt% As_2O_3

Binding energy (eV)

Au_{4f}

C_{1s}

Au_{4d}

O_{1s}

Cr_{2p}

Ni auger

Fe auger

Fe_{2p}

Ni_{2p}
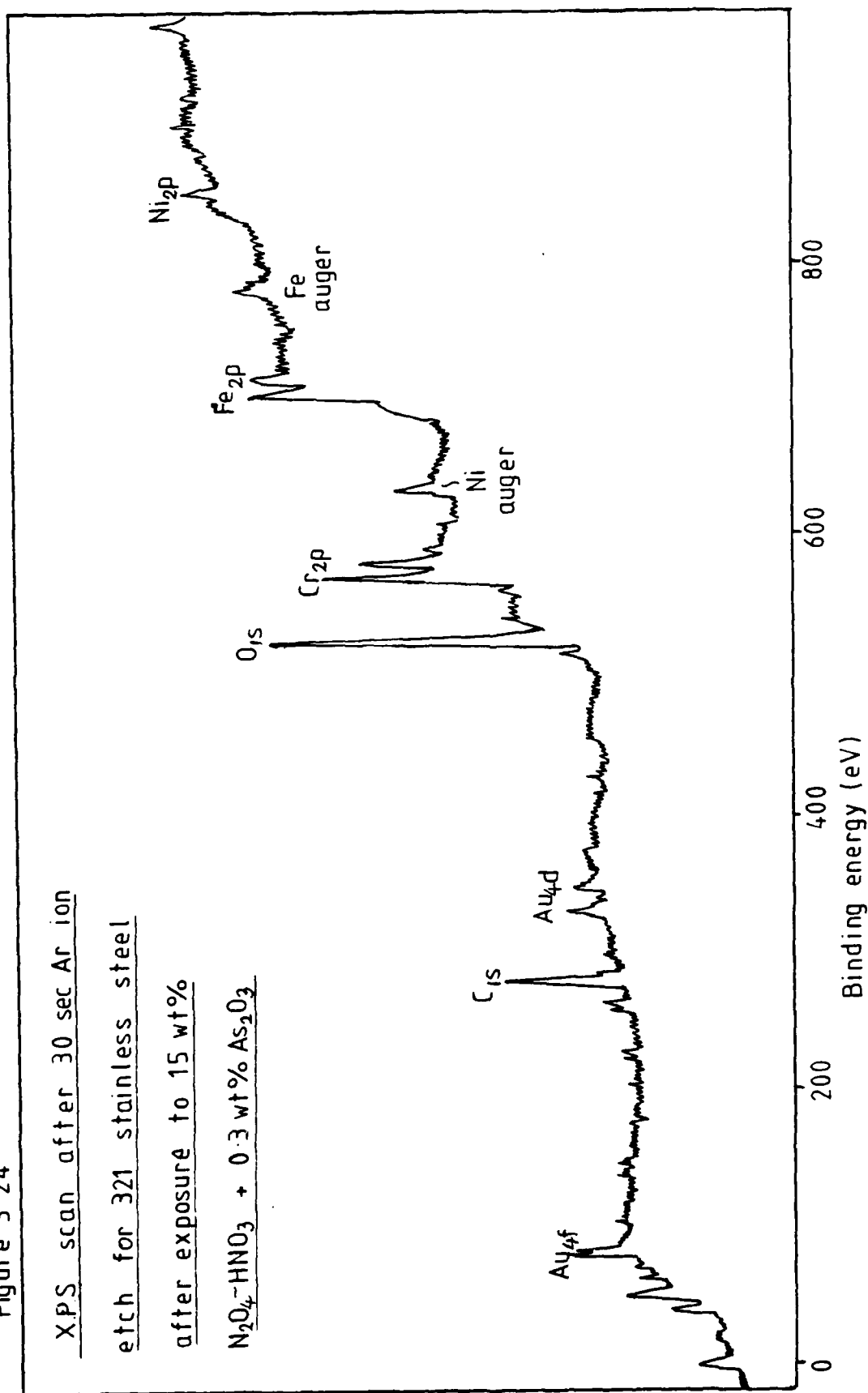
of the polarisation behaviour of 347 stainless steel in

15 wt % N_2O_4-HNO_3 containing 0.3 wt % As_2O_3. No value is

yet available for the corrosion current (i_{corr}) but it is

known to be less than 10^{-7} A.cm^{-2}. The breakdown potentials

quoted were obtained from polarisation curves which used

a polarisation rate of ca 10 mV/min . Curve (b) of

Figure 5.25 shows the effect of adding 1.5 wt % water on the polarisation

behaviour.

The anodic breakdown observed occurs at a potential 20-50 mV

above the NO_2^+/½N_2O_4 redox potential in anhydrous 15 wt %

N_2O_4-HNO_3. The value of 50 mV was obtained after leaving the

specimen in the As_2O_3-inhibited acid for a day, whereas the value

of 20 mV was obtained after only an hour. This breakdown is

caused by the oxidation of the 'As_2O_3' film to a soluble As(V)

species; the unprotected stainless steel is then in the trans-

passive region and the metal is seriously attacked. The current

density peak at ca -20 mV is probably due to the anodic film

inhibitor action of the arsenates (V) in solution (cf phosphates,

sulphates) with the subsequent formation of insoluble metal

arsenates (V). This is verified by the deleterious pitting that

is observed on the stainless steel surface after this

polarisation treatment. The effect of water (curve(b)) is apparently

to stab ilise the 'As_2O_3' film so that higher anodic over-

potentials are then necessary to effect oxidation breakdown.

The effect of adding 1.5 wt % H_2O to 15 wt % N_2O_4-HNO_3 is to

reduce the NO_2^+/½N_2O_4 potential by 60 mV. This reduction in the

oxidising power of the medium causes the As(III)/As(V)

(b)

(a)

As$_2$O$_3$ oxidation $\longrightarrow$ As(v) in solution.

−20
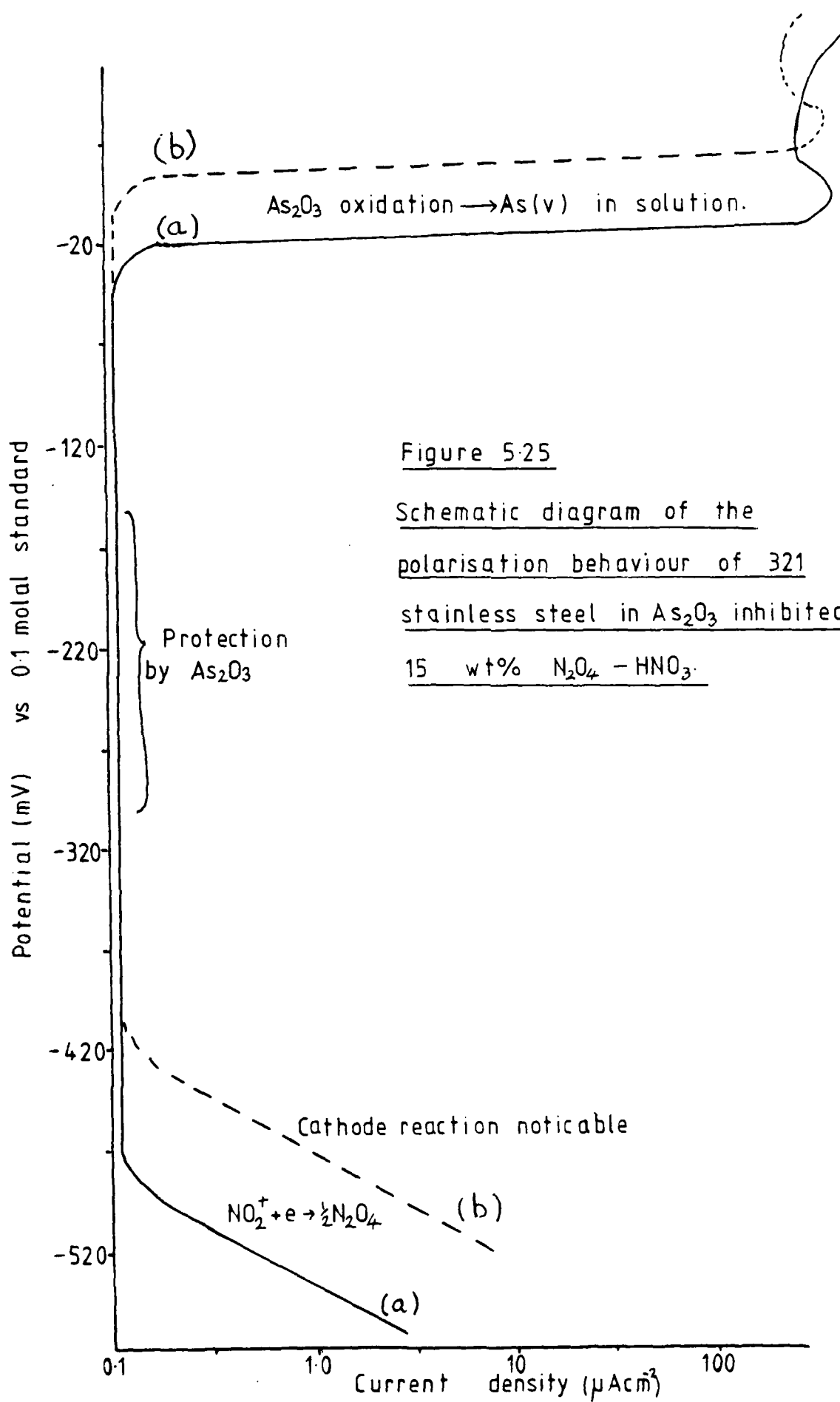
Figure 5·25

Schematic diagram of the

polarisation behaviour of 321

stainless steel in As$_2$O$_3$ inhibited

15 wt% N$_2$O$_4$ − HNO$_3$.

−120

Protection
by As$_2$O$_3$

−220

−320

−420

Cathode reaction noticable

NO$_2^+$ + e → $\frac{1}{2}$N$_2$O$_4$

(b)

−520

(a)

Potential (mV)   vs   0·1 molal standard

0·1   1·0   10   100

Current   density (μAcm^{-2})

equilibrium in solution to shift in favour of As(III) which will stabilise any 'As$_2$O$_3$' film formed on a negative metal surface.

The cathodic breakdown, apparently observed, is less easy to interpret and a full study has not yet been undertaken.

Solubility of As$_2$O$_3$ in N$_2$O$_4$-HNO$_3$ Solutions

0.3 wt % As$_2$O$_3$ appears to dissolve completely in 15 wt % N$_2$O$_4$-HNO$_3$. After 24 hours, however, a milky white colloidal solid is observed at the bottom of the cell. The addition of 1·5 wt % H$_2$O removes this solid permanently. For As$_2$O$_3$ to have a practical use as an inhibitor, solid formation would have to be eliminated completely by correct choice of inhibitor concentration with respect to the water concentration of the N$_2$O$_4$-HNO$_3$ solution.

5.6   The Corrosion of Stainless Steel in Standard HDA
(B. Mellor)
(a)   Experimental

A series of experiments in polypropylene vessels concerning the corrosion rate of stainless steel in SHDA at 25°C, have been reported previously.[5.6]   The stainless steel samples were in the form of coupons and the rates were determined by periodic sampling and analysis of each solution for Fe, Cr and Ni content by atomic absorption spectroscopy.

The analysis of the solution samples showed that the relative concentrations of Fe, Cr and Ni vary appreciably with time.   Fig.5.26 shows the variation of the relative concentrations of Fe/Cr and Ni/Cr normalised to their relative proportions in the steel.   (The broken lines in the Figure denote the ratio found in the steel).   The general observation may be recorded that in the early stages of the experiments, the Ni concentration is disproportionately high (relative to the composition of the steel, 70% Fe, 18% Cr, 10% Ni), compared with the Fe and Cr levels.   The relative Fe level varies somewhat, but is generally higher than the Cr level.

A series of experiments in Teflon vessels, at 20°C, have also been reported[5.7].   Solution analysis revealed that in the early stages the iron and more especially the nickel content, were disproportionately higher than the corresponding chromium concentration, compared with the relative content of these three elements in the steel.   As the experiments proceeded, however, the respective concentrations tended to converge to relative levels close to those of the steel composition i.e. (70% Fe,
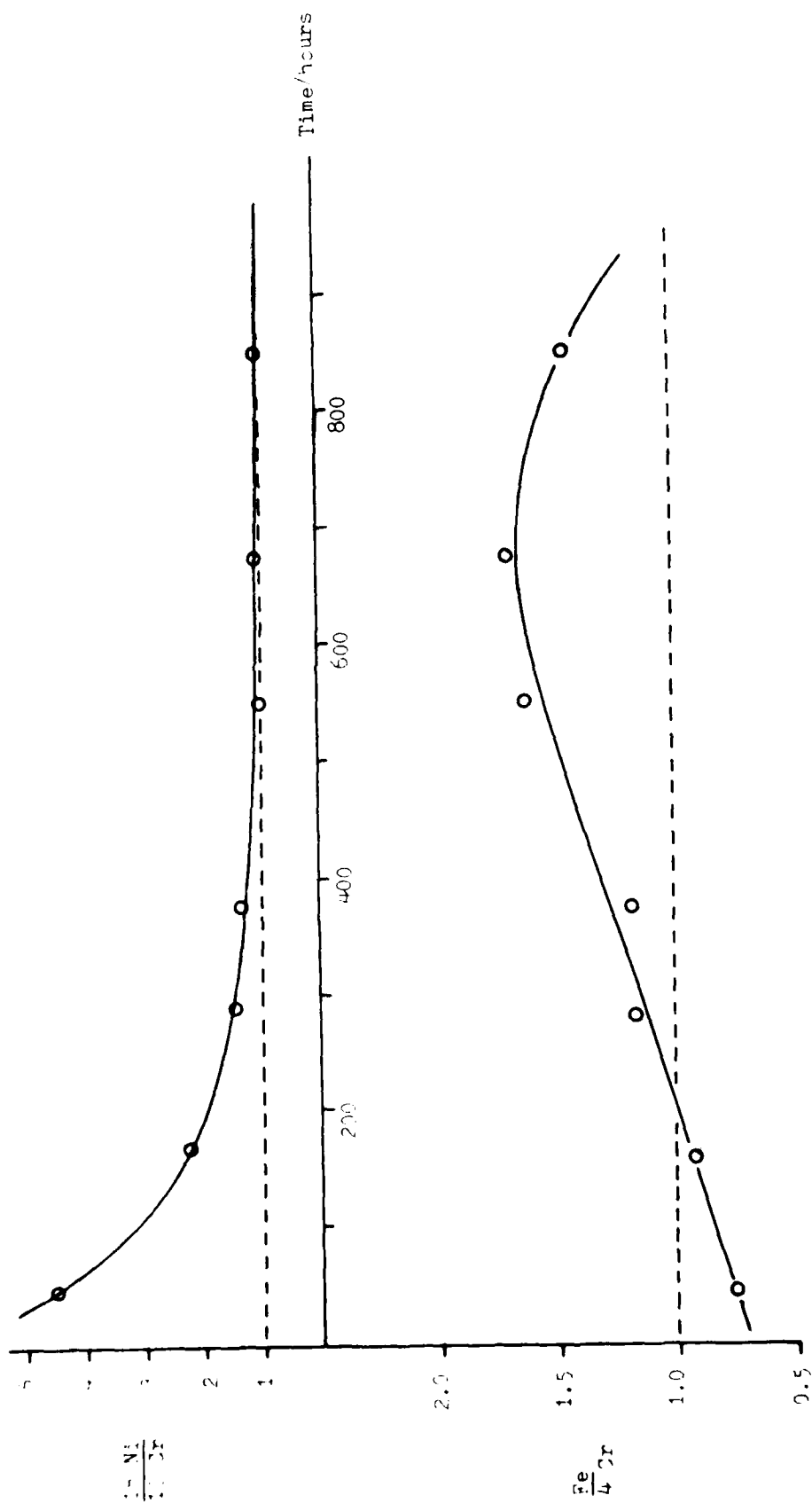
Fig.5.26 Relative Concentrations of Metals in Solution in Standard HDA at 25°C

18%Cr, 10%Ni).   Fig.5.27 shows the Fe, Cr and Ni concentrations normalised to allow for their relative proportions in the steel.

(b)   Conclusions

The results (Figs 5.26 and 5.27) show that stainless steel corrodes in a preferential manner initially, iron and more especially nickel, going into solution more rapidly than chromium.   This behaviour is consistent with the formation of a protective surface layer in which, presumably, chromium species play a major role.   This would account for the rapid loss of iron and nickel from the surface of the metal, which would continue until the chromium-rich protective film had formed, controlling the rate of further corrosion.   These conclusions are entirely consistent with the observations reported in Section 5.5.   The Potential/Time experiment involving the stainless steel/SHDA system demonstrated that the establishment of a stable film was a process extending over many hours.   Also the XPS scan of 321 stainless steel exposed to 15 wt % N_2O_4 - HNO_3 containing 0.6 wt % F^- (Fig.5.16) demonstrated the prominence of chromium in the surface film. In the early stages of corrosion, iron fluoride may form on the anodic sites but is then dispersed into solution. Chromium fluoride appears to be much more coherent and becomes incorporated into the oxide film (which would exist on the steel surface prior to immersion in SHDA).   Nickel is lost from the anodic sites because soluble nickel nitrate $(Ni(NO_3)_2 \cdot 2H_2O)$ forms in preference to nickel fluoride[5.8] and thus the presence of fluoride does not inhibit nickel corrosion in SHDA.   The anodic sites become plugged with (primarily) chromium fluoride, this plugging preventing the
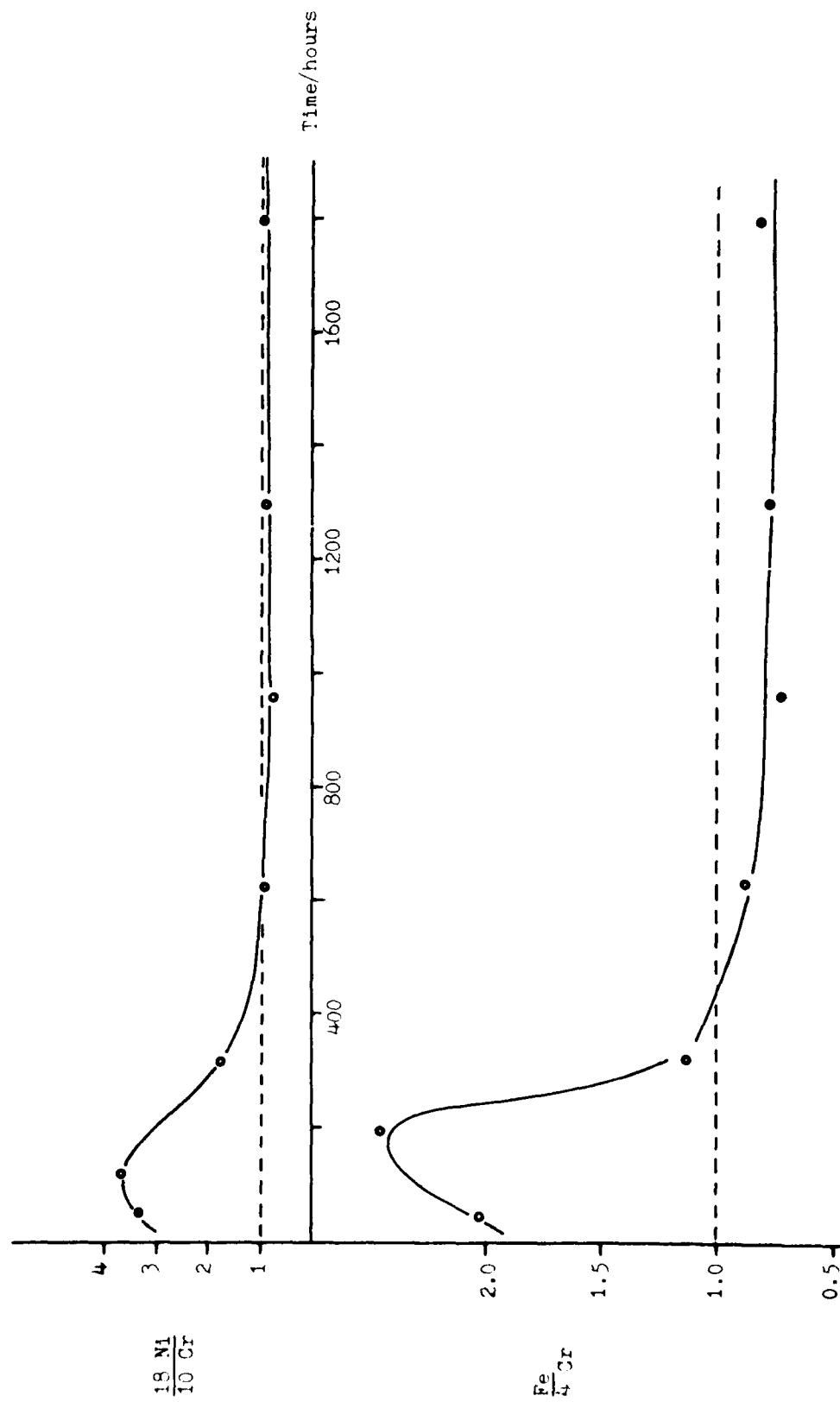
Fig.5.27   Relative Concentrations of Metals in Solution in Standard HDA at 20°C

growth of the chromium oxide film. Thus, breakdown of the film, due to the transpassive effect, is not observed in SHDA.

6.   CORROSION PRODUCTS

6.1 Studies Relevant to Standard HDA   (A.A.M. Moharum,

     R.C. Hibbert and B. Mellor)

The stainless steel/Standard HDA corrosion product has
been shown to consist principally of the new phase $FeF_3.xH_2O$
($0.5<x<1$) and extensive investigations involving iron(III)
fluorides in nitric acid media have already been reported.[6.1]
In contrast, until very recently (see Section 6.1 (a) (ii))
no authentic aluminium/Standard HDA corrosion product had
been isolated in our laboratories and during the second
year of the Grant period, attention was concentrated on the
behaviour in HDA of aluminium, chromium and other relevant
metals, in the presence of HF.

(a) Aluminium

(i) Experiments involving synthetic corrosion products
     The 'titration' of Al in HDA with HF

The work described here, and that in Section 6.1 (b)
involving chromium are continuations of similar studies,
already reported,[6.1] but involving 100% HNO_3. In those
studies, the complexing of M^{III} (M = Al, Cr, Fe) with
fluoride in the nitric acid was investigated by carrying
out a titration, i.e., by adding small known amounts of
HF to a solution of M^{III} of known concentration, while
monitoring the reaction by infrared spectroscopy, in order

to detect the appearance of HF in the vapour phase, i.e.,
the "end point". The previous report[6.1] included detailed
accounts of the experimental procedure and equipment used
in conducting these titration reactions[6.2] and the
technique for detection of HF by infrared spectroscopy.[6.3]
The "titration" experiments in 100% HNO_3 indicated the
formation and stability of AlF_6^{3-}, CrF_6^{3-} and FeF_6^{3-} in this
solvent medium, in contrast to aqueous systems where there
is a tendency to form the MF_5^{2-}(aq) anions. Extension of
the experiments from 100% HNO_3 to the more technologically
relevant HDA was of obvious importance but there are, however,
a number of difficulties encountered in performing HF
titrations in HDA. Foremost is that the partitioning of HF
between the liquid phase and the vapour phase is different
for 100% HNO_3 and HDA. Whereas in HNO_3, less than 1 mg HF
added to 11g HNO_3 in a 20 mm O.D. Kel-F tube gives rise to
measurable infrared peaks for HF in the 3900-3800 cm^{-1} region
for the vapour phase, in HDA it is found that up to 20 mg HF must be
added to generate detectable peaks under the same conditions.
Nevertheless, by taking account of this "blank" determination
(obtained in the absence of metal in solution) some meaningful
results have been obtained.

Aluminium dissolves only very slowly in HDA,[6.4] and no
carbonyls, which can be used successfully for preparation of
HDA solutions of chromium or iron, are known. Solvolysis of
anhydrous $AlCl_3$ has been used[6.4] to prepare solutions of
aluminium in HDA but was avoided in the study described

here because of the trace amounts of chloride which might remain in solution. Since $Al(NO_3)_3 \cdot 6H_2O$ is known to be a stable species in HDA[6.4], a convenient method of preparing an Al(III) solution involves dissolution of the readily available nonahydrate, $Al(NO_3)_3 \cdot 9H_2O$ in HDA followed by the addition of sufficient N_2O_5 to change the aluminium nitrate composition to $Al(NO_3)_3 \cdot 6H_2O$. This procedure was adopted in the present work. HF was then distilled into this solution in small portions,[6.2] the infrared spectrum of the vapour phase above the solution being monitored by IR spectroscopy[6.3] after each addition. The results are presented in Table 6.1 and clearly indicate the acquisition of six fluoride ligands per aluminium atom in HDA solution, as in 100% HNO_3.[6.1]

Characterisation of gel

When a solution of aluminium in HDA containing an excess of HF (e.g., as produced above), is evaporated down, a gel forms. We have carried out, on such a gel, a second titration with HF (after addition of a further known weight of HDA to dissolve the gel) to the established 6:1 end point. Under these circumstances

$$AlF_x \longrightarrow AlF_6{}^{3-}$$

where x is the F:Al ratio in the gel and

$(6-x) = \dfrac{\text{total weight of HF (second titration) added-blank}}{\text{weight of HF required to give 1:1 ratio of F:Al}}$

The detailed results of such an experiment are given in Table 6.2 and show that the gel produced by Al in HDA, containing HF is a form of AlF_3.

Table 6.1

Al/HDA Titration with HF

Wt of Al/HDA solution taken = 9.877 g

No. Millimoles Al per g HDA = 0.0909

Wt of HF required to give Al:F ratio of 1:1 = 17.96 mg

HF Added/mg	Observation	Peaks in 3900-3900 cm^{-1} region
60	Clear solution	None
83.6	H DA cloudy	None
128	H DA Cloudy, but became clear after shaking overnight	None
143	Clear solution	Two of low intensity

Wt of HF added to HDA alone to give peaks of similar intensity: 33.5 mg (Blank value).

Total wt of HF absorbed by Al/HDA	Blank	Wt HF reacted with Al	Al:F ratio	Theor wt HF for 6:1 ratio
143 mg	33.5 mg	109.5 mg	1:6.1	107.6 mg

Table 6.2

Al/HDA/HF Gel Titration with HF

Wt of gel + HDA = 8.241 g

No. of Millimoles Al in gel = 1.05

Wt of HF required to give Al:F ratio of 1:1 = 21 mg

HF added/mg	Observation	Peaks in 3900-3800 cm^{-1} region
68	Gel dissolved on shaking for 5 hours	-
88	Clear solution	None
95	Clear solution	Two

Blank determined for this experiment: 33.9 mg HF

Total wt of HF absorbed by HDA gel	Blank	Wt HF reacted with Al in gel	(6-x)	Al:F ratio in gel
95 mg	33.9 mg	61.1 mg	2.9	1:3.1

Analysis of solid product

The solid residue investigated in this study was obtained as follows: 6+ moles of HF were added to a solution of aluminium in HDA and then the solution was evacuated to a gel. More HDA was added and the gel titrated once again to the 6 : 1 HF/Al point. This solution was again evacuated to a gel, and the remaining occluded HDA extracted by washing by decantation with dichloromethane. The material was then collected on a filter stick and dried in a stream of argon.

The product was found to be amorphous. The infrared spectrum was similar to that of β-AlF$_3$.3H$_2$O, and no peaks due to NO$^+$, NO$_2$$^+$ or covalent nitrate were observed. The product was analysed for aluminium (Found: 21.2 21.15 AlF$_3$.3H$_2$O requires 19.55, AlF$_3$ requires: 32.14, AlF$_3$.2.4H$_2$O requires: 21.23%), giving a result consistent with a partially dehydrated form of AlF$_3$.3H$_2$O, in accord with earlier observations.[6.5]

Attempted determination of the solubility of β-AlF$_3$.3H$_2$O in SHDA by Millipore" filtration.

No authentic corrosion product had been obtained from the Al/SHDA system when the work described here was carried out, however, AlF$_3$.3H$_2$O was thought to correspond most closely to such a product.[6.5] Solubility determinations on α- and β-AlF$_3$.3H$_2$O in SHDA, using a centrifuge technique, gave anomalously high results attributed to colloid formation.[6.5] In view, however, of the importance of solubility data for such systems it was considered worthwhile to attempt a further

determination on the β-AlF$_3$.3H$_2$O/SHDA system, employing

stainless steel Millipore" filtration equipment

incorporating Teflon membranes down to 0.2 μm pore size.

Approximately 3 g of commercial β-AlF$_3$.3H$_2$O (analysed

as β-AlF$_3$.3.16H$_2$O. Found: Al, 19.15%) was added to SHDA

(82.35 g) in a polythene container. Two teflon coated

magnetic stirring bars were added, the container was fitted

with a screw cap and sealed with Teflon tape and the contents

were stirred at room temperature for two weeks. The Millipore"

equipment was first pressure tested for leaks and the filters

(0.5 (uppermost), 0.3 and 0.2 μm Teflon membranes held

together) were wetted with CH$_2$Cl$_2$. The mixture was then

poured into the apparatus

under a blanket of dry

argon.

The apparatus was then pressurised to 5 psig. Filtration was very

slow so the pressure was increased to 15 psig whereupon only

about 15 cm^3 of filtrate (contaminated with CH$_2$Cl$_2$)

collected in two hours. This first portion was rejected

and the receiver was replaced by a new one maintained at

0°C. In all cases the receiver was protected from atmospheric

moisture by a continuous current of dry nitrogen

Very little filtrate collected over two hours at 15 psig. The

mixture was therefore allowed to filter overnight at 15 psig

whereupon only approximately 15 cm^3 of filtrate collected in the receiver. This was obviously due to blocking of the fine pores of the filters. The unfiltered mixture, held on top of the filters, was poured off into another polythene container under a blanket of dry argon and kept in a freezer at $\sim$ -20 °C. The filtrate collected changed to a greenish gel overnight, after almost complete loss of N_2O_4. This was due to lower solubility of β-$AlF_3 \cdot x H_2O$ in 100% HNO_3 (containing HF) than in SHDA (as indicated by earlier experiments[6.6]). The Millipore apparatus was then evacuated (10^{-3} mm) for 30 min, prior to dismantling in a dry box. A very small amount of finely powdered white solid was found on the filters, but insufficient for analysis.

The remaining unfiltered mixture was again filtered through a 10 µm Teflon membrane in the "Millipore" equipment, after cleaning and drying, precautions being taken to exclude atmospheric moisture. Again, the first 20 cm^3 of filtrate collected, containing a little CH_2Cl_2, was discarded. The second portion of filtrate was collected in another clean and dry polythene receiver at 0 °C and 15 psig. The complete filtration process of this second portion took about two and a half hours. The solid remaining on the 10 µm Teflon membrane was then washed thoroughly three times with dry CH_2Cl_2 and was dried by passing dry nitrogen through it

at 5 psig for 15 minutes. The "Millipore" equipment was then once again dismantled in the dry box. Unlike the pure white and powdery starting material (commercial β-AlF$_3$.3.16H$_2$O), the product was granular, had a very faint pale green tinge and $\underline{ca}$ 0.666 g had been collected. The infrared spectrum of the product (Table 6.3) was found to be similar to those of β-AlF$_3$.3H$_2$O ex SHDA[6.7] and α-AlF$_3$.3H$_2$O.[6.8] The position of the H$_2$O deformation vibration, δ(H$_2$O), at 1650 cm^{-1} (cf 1660 cm^{-1} for α-AlF$_3$.3H$_2$O[6.8]) is more indicative of the α than the β-form of AlF$_3$.3H$_2$O for which this vibration appears at 1685 cm^{-1}. The shift to lower wavenumber from β to α-forms implies strong hydrogen bonding of water to fluoride in the latter.

Also, the H$_2$O wagging vibration, ρ_w(H$_2$O), showing a frequency at 400 cm^{-1} and a shoulder at 360 is more indicative of the α-form. Unfortunately, the X-ray powder photograph of the material showed no clearly defined lines indicating that the product was amorphous.

The product was analysed for fluoride using a fluoride ion-selective electrode and for aluminium content using atomic absorption spectroscopy. (Found: Al, 20.7; F, 41.3. AlF$_3$.3H$_2$O requires: Al, 19.6; F, 41.3. AlF$_3$.2.5H$_2$O requires: Al, 20.9; F, 44.2%.)

On addition of excess sodium hydroxide solution to a solution of the product in dilute nitric acid, the colour of the solution became yellowish brown, and a pale brown gelatinous precipitate was deposited on standing, leaving a colourless solution. This precipitate also dissolved in

Table 6.3

Infrared Spectrum of Solid Residue After "Millipore" Filtration
(10 μm Membrane) of   β-AlF$_3$.3.16 H$_2$O/Standard HDA Mixture

cm^{-1}		Assignment
3400-3000	(vs, b)	ν(OH)
2580	(sh, b)	$\delta + \rho_r$(H$_2$O)
2260	(w, b)	
1650	(vs, b)	δ(H$_2$O)
1300	(vw, sp)	
1250	(vw, b)	trace NO$_3^-$
1160	(vw, b)	
940	(vw, b)	
720- 570	(vs, b)	ν(Al-F)
520	(sh)	
400	(s, sp)	ρw(H$_2$O)
360	(sh)	

dilute nitric acid and the resulting solution gave positive tests for iron(III) with potassium ferrocyanide and ammonium thiocyanate. This iron undoubtedly arose from the action of Standard HDA on the Stainless Steel "Millipore" apparatus during the long periods of contact during filtration and this also accounts for the pale green tinge of the product. The amount of iron impurity in the product, determined by atomic absorption spectroscopy was found to be of the order of 0.3%.

The "solubility" was determined by measuring the Al content (by atomic absorption spectroscopy in the SHDA filtrate after passage through the 0.5, 0.3 and 0.2 μm teflon membranes in the first filtration process. A portion of this filtrate (6.574 g) was exposed to the atmosphere in an open weighing bottle in a fume cupboard. After 30 minutes the filtrate had set to a rigid orange gel which, after 1½ days had become orange-green after loss of a substantial amount of N_2O_4. The gel was digested in water to give an orange solution which was transferred to a 100 cm^3 volumetric flask. This solution was then diluted fifty times for analysis by atomic absorption spectroscopy. The "solubility" was thereby found to be 0.8365 g of Al in 100 g of Al/SHDA solution, i.e., 8365 ppm. The filtrate showed a slight Tyndall effect and a duplicate solubility determination to that described above gave rise to the same observations and a value of 0.9517 g Al in 100 g of Al/SHDA solution, i.e., 9517 ppm.

These results support the earlier conclusions[6.5] that the aluminium fluoride trihydrates become colloidal in

Standard HDA and it must therefore be recognised that
conventional filtration techniques, even using the smallest
filter pore sizes available, will be ineffective in removing
such contaminants from the oxidiser.

(ii) Authentic corrosion products

The contents of the aluminium tanks used in the long
term corrosion rate experiments (see Section 4.1) were
filtered after 28 months, using an aluminium "Millipore"
filtration apparatus. The contents of the Standard HDA
tank were filtered through a 0.5 µm Teflon membrane. A very
small amount of a white solid was obtained, sufficient only
for an infrared spectrum, although it proved impossible to
obtain a satisfactory mull. It was noticed, however, that
the walls of the tank were coated with a thick film of
white solid, which could be removed by gentle scraping with
a small spatula. Sufficient material was collected in this
way from the region exposed to the liquid phase for
examination by both X-ray powder diffraction and infrared
spectroscopy. It was also possible to obtain sufficient
material from the region exposed to the vapour phase to
obtain an X-ray powder photograph. Both samples were,
however, contaminated with aluminium powder which made the
preparation of an infrared/mull from the liquid phase sample,
very difficult. A satisfactory infrared spectrum could
only be obtained using a x5 ordinate expansion in the region
1700-400 cm^{-1}; it proved impossible to obtain good definition
in the O-H stretching region (3800-3000 cm^{-1}). The spectrum
(Fig. 6.1 and Table 6.4) is particularly interesting in that

Fig.6.1 Infrared Spectrum of SHDA Tank Sample (Al)
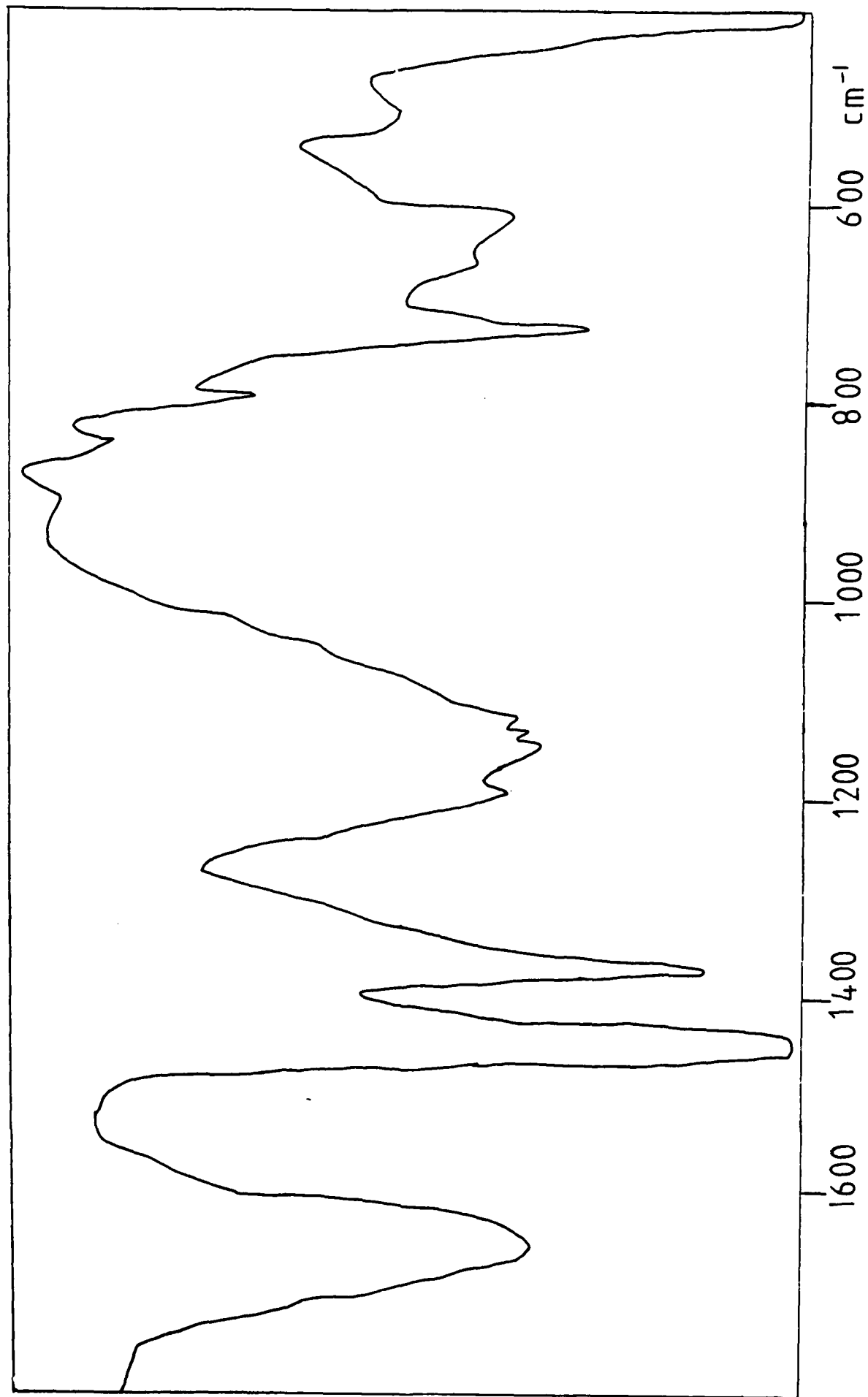
Table 6.4

Infrared Spectrum of Standard HDA/Al Tank Sample (Liquid Phase)

Wavenumber/cm^{-1}		Assignment
1655	(vs, b)	$\delta(H_2O) + \nu(NO_3)$?
1450	(vs)	Nujol
1370	(vs)	Nujol
1190	(s)	
1145	(s)	$\nu(NO_3)$?
1130	(s)	
1115	(s)	
905	(w, b)	$\rho_r(H_2O)$
845	(w)	$\rho_r(H_2O)$
800	(m, sp)	$\pi(NO_3)$?
730	(vs, sp)	$\nu(AlF) + \nu(AlO) + \delta(NO_3)$?
715	(sh)	
660	(s)	$\nu(AlF) + \rho_w(H_2O)$
615	(s)	
515	(m)	

it differs significantly from the spectra of aluminium

fluoride trihydrates reported earlier,[6.5] and shows a

number of well-defined absorption bands, tentative

assignments of which are given in Table 6.4.

The X-ray powder photograph of the liquid phase

sample contained lines attributable to aluminium metal

but a number of other lines where also observed

(Table 6.5). All the lines observed for the vapour phase

sample corresponded to those for aluminium metal. Thus the

vapour phase film probably consists of one or more amorphous

compounds. The most intense lines of α-AlF$_3$.3H$_2$O occur only

weakly in the X-ray powder photograph of the liquid phase

sample. The two most intense lines, observed for this

sample, probably arise from the overlapping of the two most

intense lines of α-AlF$_3$ and αAlF$_3$.H$_2$O. There is a broad

diffuse halo (centred at a d spacing of ca 5.6Å) which

may be due to aluminium hydroxofluorides of the type

AlF$_x$(OH)$_{3-x}$ (where $2 \geqslant x \geqslant 1$). Investigations of the corrosion

of aluminium by inhibited red fuming nitric acid (IRFNA,

approximately 83% nitric acid, 14% dinitrogen tetraoxide,

2% water and 0.7% hydrofluoric acid by weight) have resulted

in the isolation of corrosion products.[6.9] Several samples

of powder and flake deposits from long term storage bottles

have been analysed. The average analytical figures are

Al, 26.1% and F, 45.7%, yielding an Al:F ratio of 1:2.5. These

figures indicate that at least one component, other than

simple hydrated aluminium fluorides, (AlF$_3$.nH$_2$O) is present

in the IRFNA products. Some suggested components are the

Table 6.5

X-Ray Powder Data for the Standard HDA/Al Tank Sample

(Liquid Phase) and Related Compounds

Tank Sample[*]		α-AlF$_3$[**]	
$d/\overset{\circ}{A}$	I/I_O	$d/\overset{\circ}{A}$	I/I_O
4.65	5	3.52	100
4.00	weak	2.119	20
3.56	100	1.759	25
3.05	weak	1.587	15
2.55	weak		
1.78	50		

α-AlF$_3$.H$_2$O[**]		AlF$_{1.96}$(OH)$_{1.04}$[**]	
$d/\overset{\circ}{A}$	I/I_O	$d/\overset{\circ}{A}$	I/I_O
3.55	100	5.56	100
2.05	13	2.90	15
1.78	37	2.78	15
1.59	26	1.96	11
1.26	13	1.85	13
		1.70	11

α-AlF$_3$.3H$_2$O[**]	
$d/\overset{\circ}{A}$	I/I_O
4.63	100
4.04	70
2.54	80

* - excluding lines due to aluminium metal

** - only the most intense lines are included

oxide Al_2O_3 (several amorphous forms are known), the
oxofluoride, AlOF, fluorohydroxo- or hydroxo-species
e.g., $AlF_3(OH)_{3-x}$, $Al(OH)_3$, $Al(OH)_4^-$ or hydrates of
aluminium (III) nitrate (the presence of $Al(NO_3)_3.9H_2O$
has been postulated[6.9] and $Al(NO_3)_3.6H_2O$ is known to
separate from HDA[6.4]). Such compounds are likely to be
present also in the SHDA/Al tank sample and its infrared
spectrum appears to be consistent with this. XPS investigations
(Section 4.3(f), however, give little evidence for the
formation of nitrate on the surface of aluminium exposed to
SHDA. It seems likely, therefore, that the vapour phase film
is an amorphous form of aluminium oxide (which may well contain
a substantial quantity of fluoride) and this may also be
a component of the liquid phase film. Conclusive and detailed
characterisation of the liquid phase film is not possible on
the basis of the evidence presently at our disposal but we
tentatively propose that α-AlF_3 and α-$AlF_3.H_2O$ are its
principal components.

An X-ray diffraction study has been performed upon an
authentic corrosion product, isolated by other workers[6.16]
on a 10μm filter after 3642 hours exposure of aluminium to
SHDA at 23^OC. The 2 strongest lines in the powder pattern
of this sample occurred at d spacings of 3.48 and 1.785 $\overset{O}{A}$. As
can be seen from Table 6.5, these are almost identical in
position to the two strong lines for the SHDA/Al tank sample
discussed here. The major difference between the powder
patterns of the two samples is that the tank sample pattern
contained weak lines assignable to α-$AlF_3.3H_2O$ and the filtered
sample pattern contained weak lines attributable to β-$AlF_3.3H_2O$.
However, the α-form is known to be metastable in the solid

state or in aqueous solution.[6.17] It may be that if the film "flakes off", and passes into solution, conversion of α-AlF_3.$3H_2O$ into β-AlF_3.$3H_2O$ takes place. An important observation, however, is that AlF_3.$3H_2O$, in any form, is not a major component of the surface film.

No material could be isolated (even after filtration through a 0.5 m Teflon membrane) from the Modified HDA tank. Also, the surface film was much thinner than in the SHDA case and could not be removed by scraping.

(b) Chromium

(i) Experiments involving synthetic corrosion products

The titration of Cr in HDA with HF

Similar experiments to those described above for aluminium (Section 6.1(a) (i)) have been performed with solutions of chromium in HDA (prepared by dissolution of the hexacarbonyl,

$Cr(CO)_6$). The titration summarised in Table 6.6 confirms the formation of CrF_6^{3-} in HDA solution, as in 100% HNO_3.[6.1]

Characterisation of gel (solid)

On evaporating solutions of Cr in HDA containing excess HF, a gel has been observed only once. On all other occasions, the product has gone directly to a solid, which is easily soluble in water. A sample of this solid has been titrated with HF, after addition of UHDA, and the results are presented in Table 6.7.

These results suggest that the solid produced on evaporating Cr/HF/HDA solutions is a tetrafluorochromate.

Analysis of solid product

The chromium product, prepared as described in Section 6.1 (a)(i) for aluminium, was found to have an infrared spectrum similar to that of α-CrF_3.$3H_2O$. No peaks due to NO^+, NO_2^+ or covalent nitrate were observed. The product was analysed for chromium and fluoride (found: Cr, 28.8; F, 42.2%; F/Cr ratio 4.0. CrF_3.HF.$3H_2O$, which could also be written as H_3O^+.CrF_4^-.$2H_2O$, requires: Cr, 28.4; F, 41.5%).

(c) Reactions of other metals with Standard HDA

DM Tallett[6.10] investigated qualitatively the reactions of 19 metals with 100% HNO_3 and uninhibited HDA, these being magnesium, calcium, titanium, vanadium, chromium, manganese, iron, cobalt, nickel, copper, silver, zinc, cadmium, mercury, aluminium, tin, bismuth, uranium and 321 stainless steel. B Mellor[6.11] performed similar investigations on the reactions of 10 metals with Standard HDA, these metals being iron, chromium,

Table 6.6

Cr/HDA Titration with HF

Wt of Cr/HDA solution taken = 9.256 g

No of millimoles Cr per g HDA = 0.0615

Wt of HF required to give Cr:F ratio of 1:1 = 11.38 mg

HF added/mg	Observations	Peaks in 3900–3800 cm^{-1} region
91.5	Solution turned from dark green to pale green	None
103.5		Two broad peaks of weak intensity

Blank determined as 32.9 mg HF

Total wt of HF absorbed by Cr/HDA	Blank	Wt HF reacted with Cr	Cr:F ratio	Theor. Wt HF for 6:1 ratio
103.5 mg	32.9 mg	70.6 mg	1:6.2	68.4 mg

Table 6.7

Cr/HDA/HF Solid titration with HF

Wt of solid + HDA = 7.308 g

No. millimoles Cr in Solid = 0.57

Wt of HF required to give Cr:F ratio of 1:1 = 11.4 mg

Total wt of HF absorbed by HDA +solid	Blank	Wt HF reacted with Cr in Solid	$(6-x)$*	Cr:F ratio in Solid
47 mg	24 mg	23 mg	2.0	1:4.0

*See Section 6.1(a)(i)

nickel, manganese, cobalt, copper, zinc, magnesium, barium
and strontium. Certain results relevant to stainless steel,
i.e., the reactions of iron and chromium, including weight
loss $\underline{vs}$ time curves, have already been reported, but with
the use of metals other than aluminium and 300 series
stainless steels, it is relevant to note some of this work
on other metals. The reactions of five of these metals,
manganese, cobalt, nickel, copper and zinc, with UHDA and
SHDA, are reported in Table 6.8, although care should be
taken in comparing the results, as the form of metal, and
particularly the surface to volume ratio, is not the same
in all cases.

Table 6.8

Reactions of Some Metals with Standard and Uninhibited HDA

Metal	Reaction with Standard HDA	Reaction with Uninhibited HDA
Manganese	Instant vigorous reaction, effervescence, darkening of liquid, metal dissolved completely in minutes.	Instant effervescence, very vigorous reaction, viscous solution, slightly darker in colour, forms after a day, metal completely dissolved in 2 days.
Cobalt	Instant reaction, effervescence, purple coloration of liquid, metal dissolved completely in minutes.	Instant purple coloration of solution, vigorous effervescence, slows down after a few minutes, and almost stopped after 10 minutes.
Nickel	Instant reaction, green coloration of liquid, metal dissolved in minutes.	Slow reaction, green solution formed, No further reaction after a week.
Copper	Slow, visible, reaction of metal, blue-green coloration of liquid, metal dissolved slowly.	Instant green coloration of liquid, no effervescence, opaque, dark green viscous solution formed in 2 days, no further change after a week.
Zinc	Instant vigorous reaction, effervescence, no coloration of liquid, metal dissolved in minutes.	Metal dissolved completely to give pale yellow solution within 2 hours.

It is notable that all of these dipositive metals react equally if not more, readily with Standard HDA than Uninhibited HDA and this can attributed to the high solubility of the M(II) fluorides (M = Mn, Co, Ni, Cu and Zn), compared to those of Al(III) and Cr(III) which give passivity in Standard HDA.

6.2   Studies Relevant to Modified HDA   (RC Hibbert)

Experiments involving synthetic corrosion products

The experiments described here extend those presented in the previous Scientific Report[6.12], a number of which involved the reactions of metal solutions in HDA with PF_5. N.m.r. spectroscopic studies (see, for example, Ref 6.1, Section 6, and this Report, Section 2.2) revealed that the reaction of PF_5 with HDA generates hexafluorophosphate, PF_6^-, difluorophosphoric acid, HPO_2F_2, and hydrofluoric acid, HF, as principal products, together with a small proportion of monofluorophosphoric acid, H_2PO_3F. Hydrolysis of PF_6^- to HPO_2F_2 and HF then occurs with time in HDA. PF_6^- is a rather inert anion with little coordinating ability whereas $PO_2F_2^-$ and F^- are good ligands. It is now clear, therefore, that corrosion products generated in reactions of metals with PF_5/HDA solutions (e.g., Modified HDA) are likely to be mixtures, principally of difluorophosphates and fluorides. The products of such reactions, carried out under closely similar synthetic conditions, might therefore be expected to give somewhat variable analytical results and this was found to be the case for iron.[6.13]

Chemical and structural knowledge of metal difluorophosphates, reported in the literature, is not extensive. In view of this the synthesis of some aluminium, chromium and iron difluorophosphates was undertaken in our laboratories ⟨ from reactions of $AlCl_3$ or $CrBr_3$ or $FeCl_3$ with difluorophosphoric acid (the obvious reagent for the preparation of difluorophosphates), either neat or in diethyl ether solution, and the products

of these reactions have already been described.[6.12] The further studies, now reported, involve reactions of metals with pure HPO_2F_2 or with HPO_2F_2 in HDA solution. The metals chosen (indicated below in brackets) are those present in alloys, known to make contact with propellant HDA, i.e., stainless steels (Fe, Ni), Haynes 25 (Mn, Co) and 17-4 PH steel (Cu). Metallic aluminium and chromium are excluded since they are passivated by HPO_2F_2 under these conditions.

Since metal difluorophosphates are potential corrosion products from Modified HDA, the interactions of difluoro-phosphates with pure HF and of fluorides with pure HPO_2F_2 are also of interest and relevance. Thus far, attention has been directed largely to the latter and representative fluorides of all the relevant metals mentioned above have been examined.

(a) The Reactions of Metals with Pure HPO_2F_2

The reactions of HPO_2F_2 with a number of pure metals, namely Fe, Ni, Co, Mn and Cu (each of which is a major or minor component of alloys present in rocket propulsion systems employing HDA as oxidiser), have been studied.

A quantity of metal was placed in a pre-weighed Schlenk tube containing a Teflon-coated stirring bar (Fig 6.2). The Schlenk tube was then re-weighed so that the weight of metal taken was accurately known. An excess of HPO_2F_2 was then distilled on to the metal under static vacuum (usually 5-10 times that required for a metal: HPO_2F_2 mole ratio of 1:3). The reaction vessel was then filled with dry argon, a P_4O_{10} guard tube was fitted, through which the vessel was vented to the air, and the reaction mixture was stirred magnetically until reaction appeared to have ceased.

Iron

As the HPO_2F_2 melted on to the metal bubbles of gas (H_2) would be seen rising from the metal powder. A white material appeared on the walls of the reaction tube and the liquid phase was a pink colour. The white product (contaminated by small f iron metal) was collected on a filter stick using counter-current. The liquid phase was also collected, removed by distillation in a static vacuum was isolated. Both solids were dried in been repeated a number of times but it tain the white compound totally free ave Fe, 15.5; P, 25.9%. This III), Fe(III) difluorophosphate of
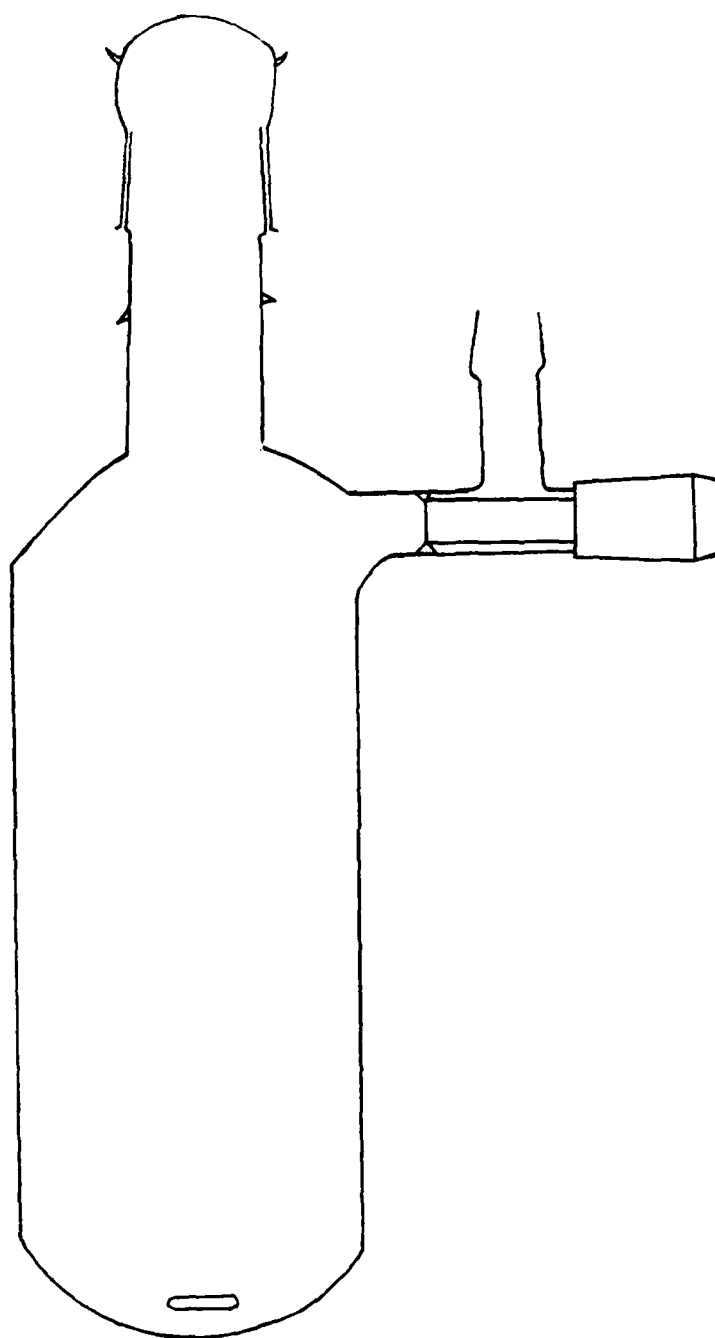
Fig 6·2   Schlenk tube used in metal /
HPO_2F_2 reactions

the form $Fe(II)_n Fe(III)_m (O_2PF_2)_{(2n+3m)} \cdot (HPO_2F_2)_n$. Its infrared spectrum (Fig 6.3 and Table 6.9) is similar to that of the blue-grey compound (Fig 6.4 and Table 6.10) which has been formulated as $Fe(II)Fe(III)(O_2PF_2)_5 \cdot HPO_2F_2$ (Found: Total Fe, 15.5; Fe(II) 7.9; P 25.1. Requires: Total Fe, 15.5; Fe(II), 7.8; P, 25.9%). Both spectra gave evidence for both coordinated difluorophosphate and solvating difluorophosphoric acid. During analysis for Fe(II) the blue-grey compound was dissolved in 2.5% H_2SO_4 and a very small amount of a white product remained, which only dissolved upon the addition of orthopnosphoric acid. No Fe(II) analysis was carried out on the white compound (precipitated by the action of HPO_2F_2 on Fe metal), owing to its insolubility in 2.5% H_2SO_4 even after the addition of orthophosphoric acid. The reaction of Fe with HPO_2F_2 in the absence of oxygen has also been investigated using a specially designed reaction vessel consisting of two Carius tubes joined via a 5-15μ sintered glass plate (Fig 6.5). Fe metal was placed in the left hand tube and HPO_2F_2 was distilled on to it under static vacuum. The reaction was allowed to commence with the apparatus still attached to a vacuum frame. The hydrogen evolved as the reaction proceeded was vented from time to time through the vacuum frame. The solution phase remained clear throughout the course of the reaction. Unreacted Fe metal was collected on the sinter by removing the apparatus from the frame, rotating it through 90° and cooling the collection tube with cotton wool soaked in liquid nitrogen. The apparatus was then re-attached to the vacuum line and excess HPO_2F_2 was distilled out of the collection tube under static vacuum. The residual white solid was analysed. (Found: Fe(as Fe(II)), 15.5; P, 25.8. $Fe(O_2PF_2)_2 \cdot HPO_2F_2$ requires: Fe, 15.5; P, 25.5%).
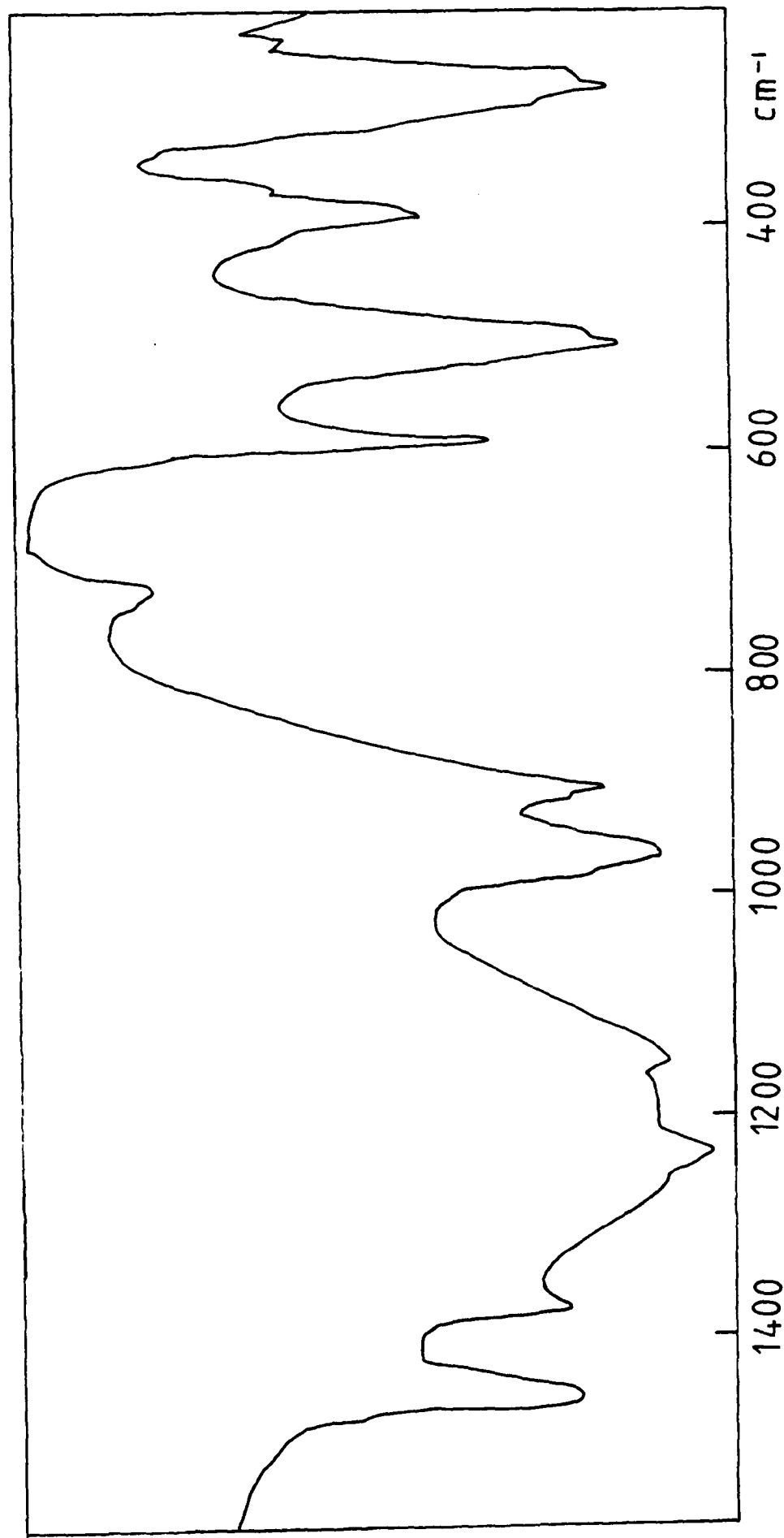
Fig.6.3 Infrared Spectrum of the white product from the Fe/HPO$_2$F$_2$ reaction

Table 6.9

Infrared Spectrum of the White
Compound from the Fe/HPO_2F_2 reaction

Absorption Band (cm^{-1})		Assignment	
3500-2000 w, vbr		ν	O-H
1260	st, sh	ν	P=O
1235	st	ν_{as}	PO_2
1145	st	ν_s	PO_2
967	st	ν_{as}	PF_2 (HPO_2F_2)
914	st	ν_s	PF_2 $(PO_2F_2^-)$
906	st		
590	st	δ_s	PO_2
500	st	δ	POF
492	st		
388	m	δ_s	PF_2

Fig. 6·4   Infrared Spectrum of $Fe^{II}Fe^{III}(O_2PF_2)_5.HPO_2F_2$

Table 6.10

Infrared Spectrum of $Fe^{II} Fe^{III} (O_2PF_2)_5 \cdot HPO_2F_2$

Absorption Band (cm^{-1})		Assignment
3500-2000	w, vb	ν O-H
1307	st, sh	ν P=O
1237	st	ν_{as} PO_2
1145	st	ν_s PO_2
1060	st, sh	ν P-O(H)
995	st, sh	ν_{as} $PF_2(HPO_2F_2)$
952	st	ν_{as} $PF_2(PO_2F_2^-)$
903	st	ν_s PF_2
586	m, sh	δ_s PO_2
555	m	
495	m	δ POF
375	m	δ_s PF_2

-158-

Fig. 6.5   Apparatus used to prepare $Fe(O_2PF_2)_2HPO_2F_2$

Sinter

The infrared spectrum of this solid
(Fig. 6.6 and Table 6.11) provides evidence for both covalent
difluorophosphate groups and difluorophosphoric acid of
solvation. The compound is very sensitive to both
moisture (as are all the difluorophosphates reported in this
Section) and air (i.e., oxygen).

Nickel

The metal reacted with HPO_2F_2, H_2 was evolved and a yellow
solution was formed. As HPO_2F_2 was removed by distillation in
a static vacuum at room temperature, a sticky yellow gum was
obtained. The Schlenk tube was then heated to 60 ^{O}C (oil bath)
and a yellow powder was obtained upon prolonged dynamic evacuation
at this temperature. (Found: Ni, 15.7; P, 26.6.$Ni(O_2PF_2)_2.HPO_2F_2$
requires: Ni, 16.2; P, 25.6%). The infrared spectrum of the
yellow powder is illustrated in Fig. 6.7 (See also Table 6.12).

Manganese

A vigorous reaction between the metal and the acid took
place, hydrogen was evolved and the acid became coloured light
brown-yellow. Upon removal of the excess acid a white powder
remained.

(Found: Mn, 15.2; P, 26.1; F, 29.6.$Mn(O_2PF_2)_2.HPO_2F_2$ requires:
Mn, 15.3; P, 25.9; F, 31.8%). The infrared spectrum of the
white powder is shown in Fig. 6.8 (See also Table 6.13).

Cobalt

As the acid melted on to the metal a rapid reaction took
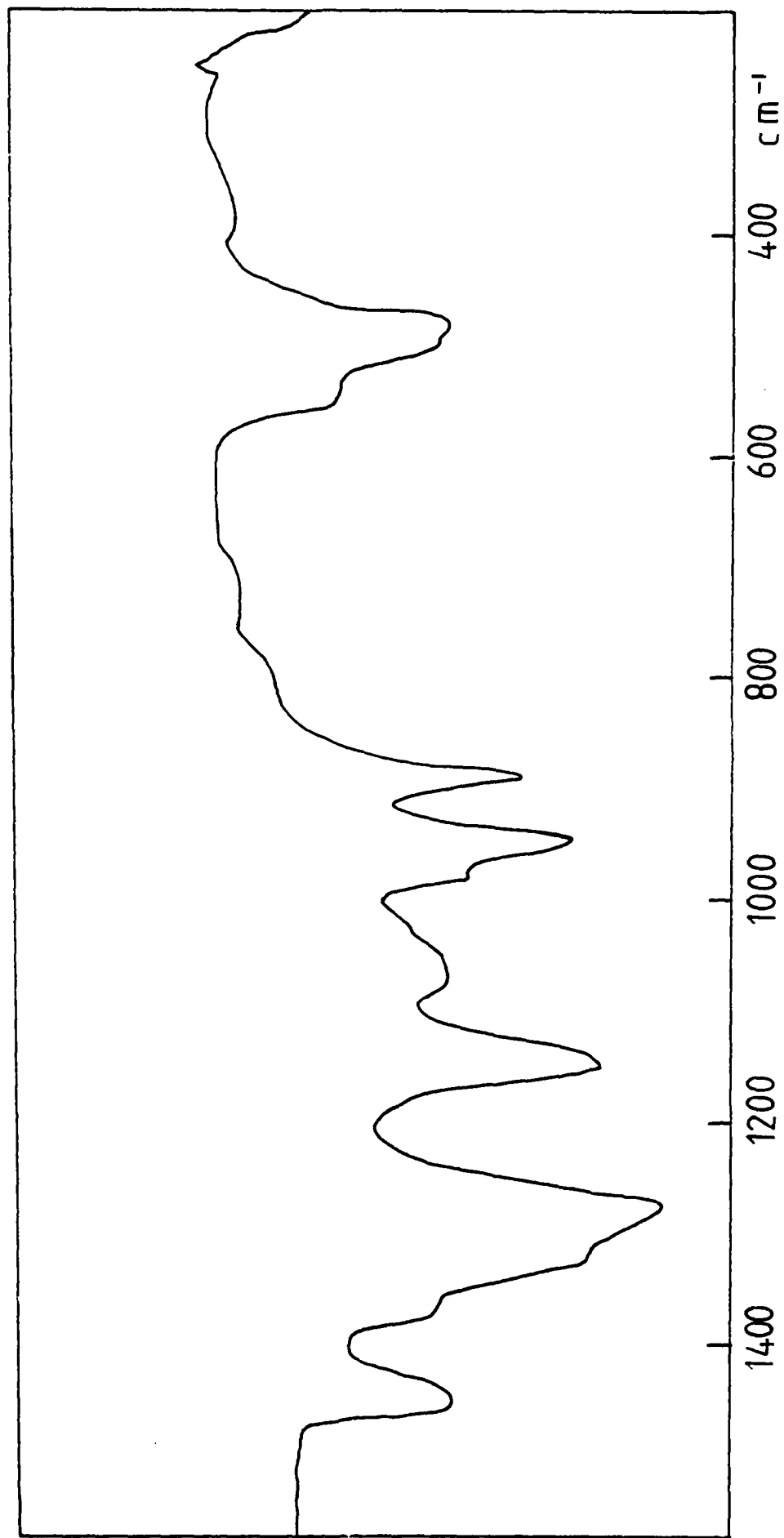
Fig 66   Infrared Spectrum of Fe(O$_2$PF$_2$)$_2$.HPO$_2$F$_2$

Table 6.11

Infrared Spectrum of $Fe(O_2PF_2)_2 \cdot HPO_2F_2$

Absorption Band (cm^{-1})		Assignment	
1320	st	ν	$P=O$
1275	st	ν_{as}	PO_2
1145	st	ν_s	PO_2
1070	m	ν	$P-O$ (H)
977	m	ν_{as}	PF_2 (HPO_2F_2)
943	st	ν_{as}	PF_2 $(PO_2F_2^-)$
888	st	ν_s	PF_2
545	m	δ_s	PO_2
490	m	δ	POF
377	w, vb	δ_s	PF_2

Fig. 6·7   Infrared Spectrum of $Ni(O_2PF_2)_2.HPO_2F_2$

Table 6.12

Infrared Spectrum of $Ni(O_2PF_2)_2 \cdot HPO_2F_2$

Absorption Band (cm^{-1})		Assignment	
1325	st	ν	$P{=}O$
1282	st	ν_{as}	PO_2
1140	st	ν_s	PO_2
1065	st	ν	$P-O(H)$
983	st	ν_{as}	$PF_2(HPO_2F_2)$
943	st	ν_{as}	$PF_2(PO_2F_2^-)$
889	st	ν_s	PF_2
565	m	δ_s	PO_2
525	m, sh		
500	m, sh	δ	POF
481	m		
382	w, b	δ_s	PF_2

Fig. 68 Infrared Spectrum of $Mn(O_2PF_2)_2 \cdot HPO_2F_2$

END
DATE
FILMED
10-81
DTIC

$CovJ$
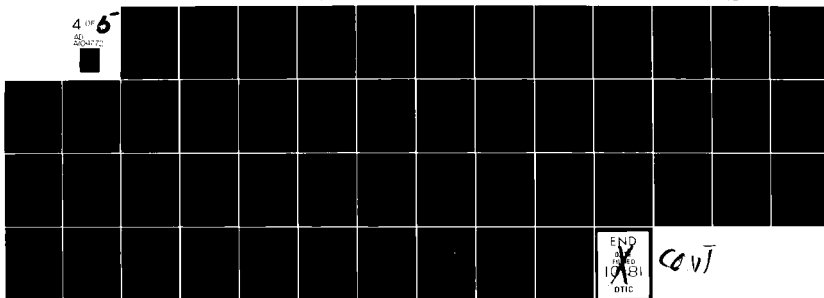
Table 6.13

Infrared Spectrum of $Mn(O_2PF_2)_2 \cdot HPO_2F_2$

Absorption Band (cm^{-1})		Assignment	
1295	st	ν	$P=O$
1273	st	ν_{as}	PO_2
1140	st	ν_s	PO_2
1045	m, b	ν	$P-O(H)$
943	st	ν_{as}	PF_2
888	st	ν_s	PF_2
550	st	δ_s	PO_2
500	st	δ	POF
491	st, sh		
372	w	δ_s	PF_2

place, the acid became red-violet in colour and H_2 gas was evolved. Removal of unreacted HPO_2F_2 yielded a purple powder (Found: Co, 16.6; P, 25.3; F, 28.1.$Co(O_2PF_2)_2.HPO_2F_2$ requires: Co, 16.2; P, 25.6; F, 30.0%) the infrared spectrum of which is shown in Fig. 6.9 (See also Table 6.14).

Copper

No immediate evidence for reaction was observed as the acid warmed to room temperature. After a few hours the acid began to acquire a yellow colour. After one day a pale blue colour was observed which became more intense as the copper dissolved and hydrogen was evolved. Excess acid was removed by distillation under dynamic vacuum with warming of the reaction vessel to $50^{\circ}C$ to remove the last traces of HPO_2F_2. The infrared spectrum of the light blue powder obtained (Found: Cu, 17.5; P, 25.7. $Cu(O_2PF_2)_2.HPO_2F_2$ requires: Cu, 17.3; P, 25.3%) is shown in Figure 6.10 (See also Table 6.15).

Difluorophosphoric acid solvates of metal difluorophosphates are thus formed when Fe, Ni, Mn, Co and Cu react with pure difluorophosphoric acid. These compounds are of interest because they are potential corrosion products (or precursors to corrosion products) from HDA containing PF_5 as corrosion inhibitor. All these compounds are hydroscopic and difluorophosphates are known to hydrolyse rapidly to phosphates via monofluorophosphates in aqueous acidic solutions. They may, therefore, represent initial corrosion products which undergo subsequent hydrolysis.
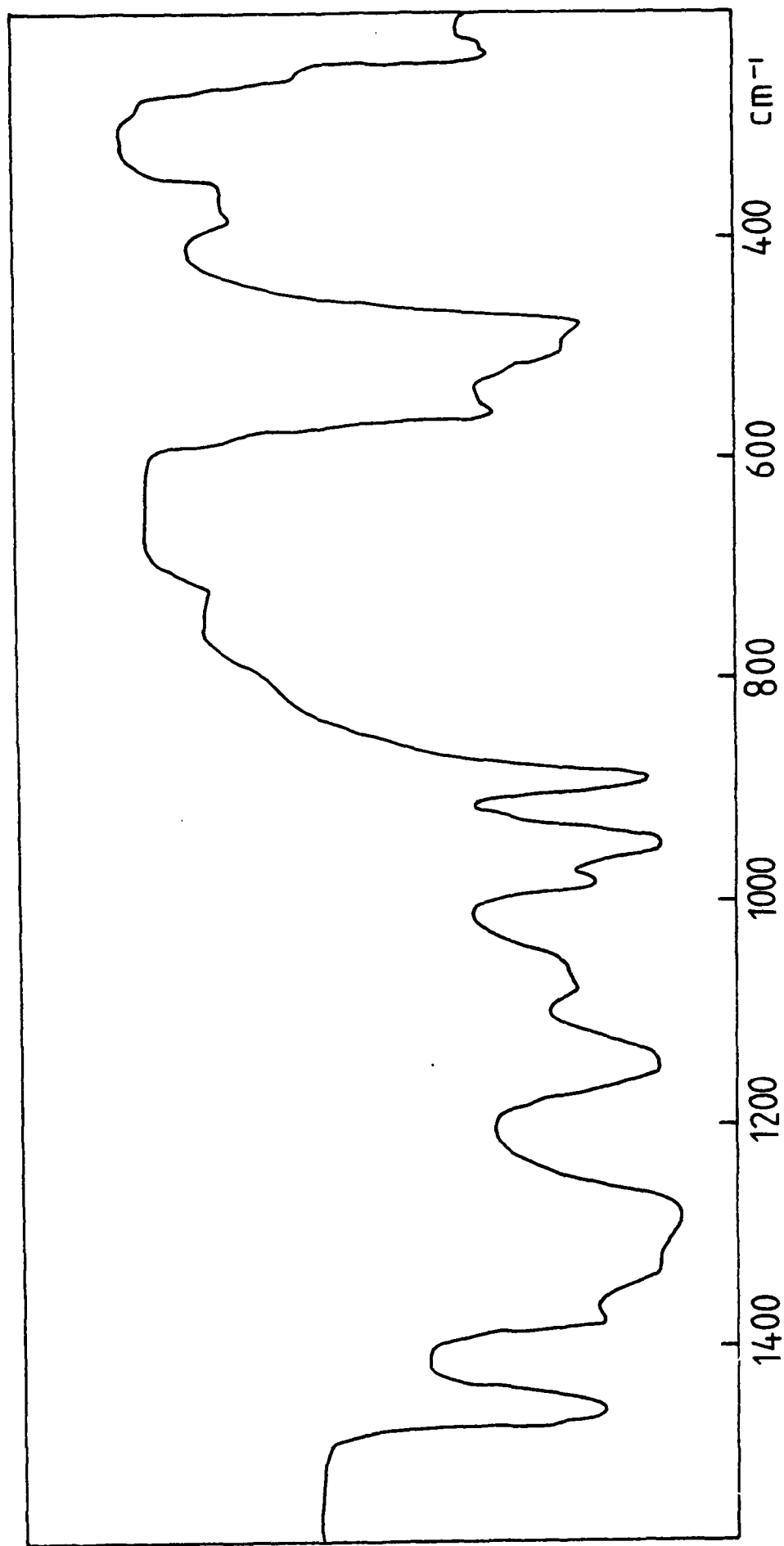
Fig. 6.9 Infrared Spectrum of $Co(O_2PF_2)_2HPO_2F_2$

Table 6.14

Infrared Spectrum of $Co(O_2PF_2)_2 \cdot hPO_2F_2$

Absorption Band (cm^{-1})		Assignment	
1330	st	ν	$P=O$
1280	st	ν_{as}	PO_2
1140	st	ν_s	PO_2
1060	st	ν	$P-O(H)$
980	st	ν_{as}	PF_2 (HPO_2F_2)
945	st	ν_{as}	PF_2 $(PO_2F_2^-)$
887	st	ν_s	PF_2
555	st	δ_s	PO_2
520	s, sh		
500	st	δ	POF
480	st		
365	w	δ_s	PF_2

Fig. 6·10 Infrared Spectrum of $Cu(O_2PF_2)_2.HPO_2F_2$

Table 6.15

Infrared Spectrum of $Cu(O_2PF_2)_2 \cdot HPO_2F_2$

Absorption Band (cm^{-1})		Assignment	
1307	st	ν	$P=O$
1220	st	ν_{as}	PO_2
1165	st	ν_s	PO_2
1140	st		
1020	m	ν	$P-O(H)$
970	st, sh	ν_{as}	$PF_2 (HPO_2F_2)$
955	st	ν_{as}	$PF_2 (PO_2F_2^-)$
905	st	ν_s	PF_2
539	st	δ_s	PO_2
502	st	δ	POF
375	w, br	δ_s	PF_2

(L) <u>Reactions of Metals with HPO_2F_2 in HDA Solution</u>

<u>Iron</u>

HPO_2F_2 (5g) was distilled into a Schlenk tube containing HDA (120g) and iron powder (0.3g) was added to the resulting solution against an argon counter-current (mole ratio $Fe:HPO_2F_2$ 1:9). The reaction mixture was stirred by means of a Teflon coated magnetic "flea" and vented via a P_4O_{10} guard tube. When all the iron had reacted, the white solid product was isolated on a filter stick, using an argon counter-current, and dried in vacuum. Since it has been observed that difluorophosphoric acid undergoes slow hydrolysis in HDA (liberating HF) it was decided to repeat the reaction in fluoroplastic apparatus (to avoid any possible contamination by the reaction products of HF with glass). Iron powder (0.3g) was placed in a PFA screw-cap container fitted with a Kel-F valve by which an attachment to a vacuum frame can be made. HDA (141.49 g) was poured onto the Fe metal against an argon counter-current. The mixture was stirred by means of a Teflon coated magnetic "flea" and the excess pressure vented by opening the valve occasionally for a few seconds. Excess HPO_2F_2 (<u>ca</u>. 10g) was then distilled into the reactor. A white solid compound was formed which was collected and dried as before. X-ray powder photography (Table 6.17) showed that the product formed by both routes was essentially the same. Anaysis showed the compound to be a form of $Fe(O_2PF_2)_3$ (Found: Fe, 15.6; P,25.7. $Fe(O_2PF_2)_3$ requires: Fe, 15.6; P, 25.9%). The infrared spectrum of this product (Fig6.11,Table6.16) was virtually identical with that of the amorphous form of $Fe(O_2PF_2)_3$ reported previously. [6.13]

<u>Nickel</u>

HPO_2F_2 (<u>ca</u>. 35g) was static vacuum distilled into HDA(64g)
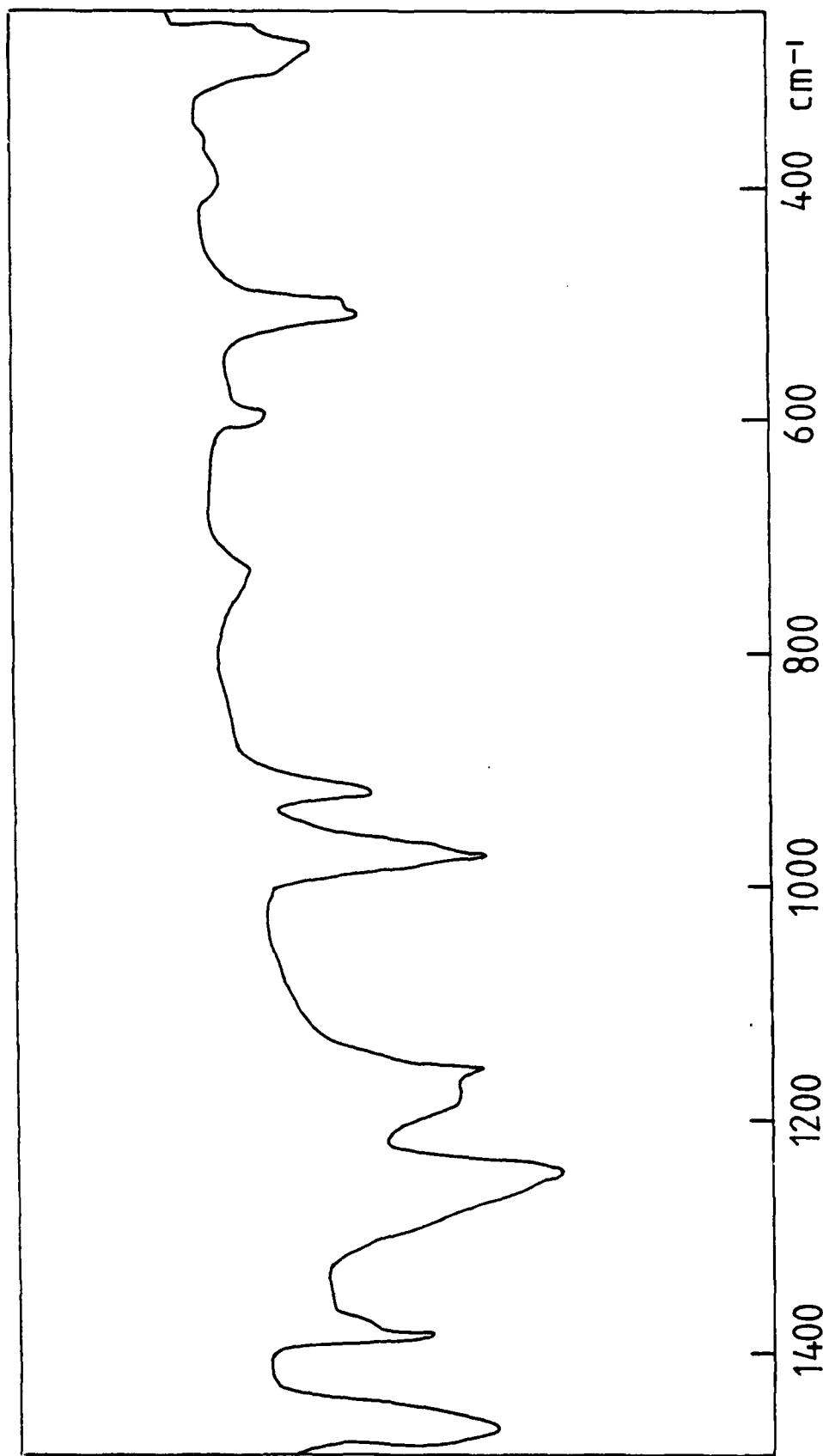
Fig.6.11 Infrared Spectrum of Fe(O$_2$PF$_2$)$_3$

Table 6.16
Infra-red Spectrum of $Fe(O_2PF_2)_3$

Absorption band (cm^{-1})	Assignment	
1245 s	ν_{as}	PO_2
1165 s	ν_s	PO_2
967 s	ν_{as}	PF_2
913 m	ν_s	PF_2
592 w	δ_s	PO_2
503 m	δ	POF
385 w, vb	δ_s	PF_2

Table 6.17   X-Ray Powder Diffraction Pattern of $Fe(O_2FF_2)_3$

d/Å	I/Io
7.511	30
3.730	100
2.825	10
2.222	10
2.047	20
1.992	30
1.926	10
1.865	10
1.246	30

contained in a Schlenk tube. Nickel powder (1g) was added against
an argon counter-current. The reaction mixture was stirred by
means of a Teflon-coated magnetic "flea" and the excess pressure
vented via a P_4O_{10} guard tube. As the nickel was added a vigorous
reaction took place, gas was evolved and a green compound pre-
cipitated. However, after about 30 minutes all of this compound
appeared to have dissolved in the reaction mixture. When reaction
was complete, no solid reaction product had separated and the
mixture was therefore cooled to $-20^{\circ}C$ in a freezer. After storage
at this temperature for about one month, the solution was passed
through a filter stick by means of argon pressure. A pale yellow
powder was obtained   (Found: Ni, 16.0; P, 24.2. $Ni(O_2PF_2)_2 \cdot HPO_2F_2$
requires: Ni 16.2; P, 25.6%), which was shown by X-Ray powder
photography (Table 6.18) to be identical to the product of the
direct reaction between nickel and pure difluorophosphoric acid.
(See above).

The green compound precipitated in the early stages of the
reaction is believed to be $Ni(NO_3)_2 \cdot 2H_2O$ which was obviously
solvolysed to a soluble difluorophosphate in the presence of the
high concentration of HPO_2F_2 employed in this experiment.

(c) Reactions of Metal Fluorides with Difluorophosphoric Acid

The interaction between metal fluorides and HPO_2F_2 is likely
to be of critical importance in PF_5-containing systems. Both
the nature of the film formed in these media and of the corrosion
products generated will depend upon this interaction.

A study of the reactions of metal fluorides with difluorophosphoric

Table 6.18 X-Ray Powder Diffraction Pattern of

$Ni(O_2PF_2)_2 \cdot HPO_2F_2$
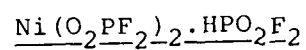
$d/Å$	I/I_o
10.526	30
7.375	10
5.140	10
4.670	5
4.171	5
3.883	5
3.648	100
3.267	20
3.132	5
2.840	5
2.550	5
2.423	5
2.353	5
2.181	5
2.108	5

acid is therefore of considerable relevance to MhDA corrosion Chemistry.

In each experiment the metal fluoride (ca 0.2g) was placed in a 6 mm PTFE tube fitted with a Kel-F valve. HPO_2F_2 (ca. 1 g) was then condensed on the metal fluoride (at liquid nitrogen temperature) and the reaction mixture allowed to warm to room temperature. The vapour phase was examined by infrared spectroscopy to determine whether any HF had been generated. The progress of the reaction was monitored both visually and by periodically recording the inra-red spectrum of the vapour phase in the region 3800-3900 cm^{-1}.

β-FeF$_3$·3H$_2$O

Buff-coloured β-FeF$_3$-3H$_2$O showed no visual sign of reaction with HPO_2F_2 at room temperature and HF was barely detectable in the infra-red spectrum. However, after warming with a hairdryer a colour change of the solid from buff to green was observed and HF was detected in the vapour phase. Upon shaking and further warming, the green colour of the solid faded and a white suspension was formed. The concentration of HF in the vapour phase was observed to increase as the reaction was allowed to proceed overnight. The liquid phase was decanted off and the solid evacuated to dryness. An infrared spectrum of the product was obtained which showed that dehydration had occurred. Bands attributable to $PO_2F_2^-$ groups were also observed. The reaction was then conducted on a larger scale. The white product generated was washed several times with fresh samples of HPO_2F_2 to ensure that complete reaction had taken place. The product was identified as Fe(O_2PF_2)$_3$ on the basis of iron analysis (Found: Fe, 15.8; requires: Fe, 15.6%) and X-Ray powder data which showed the compound to be identical with Fe(O_2PF_3)$_3$ prepared by the reaction of iron

with HPO_2F_2 in HDA (Section 6·2(b)).

$FeF_3.0.86\ H_2O$

Pale green $FeF_3.0.86\ H_2O$ was obtained by the action of HNO_3 upon $\beta-FeF_3.3H_2O$.[6·18] This compound is believed to be the principal corrosion product from long term storage of SHDA in Stainless Steel.[6·14] When HPO_2F_2 was distilled on to $FeF_3.0.86\ H_2O$, no colour change was observed and no HF was detected in the vapour phase. The reaction mixture was left overnight but no observable change occurred. The liquid phase was removed by distillation and an infrared spectrum of the dried solid obtained.

Weak bands assignable to co-ordinated difluorophosphate were observed and the spectrum also indicated that considerable dehydration had taken place. (See Fig. 6.12 and Table 6.19)

FeF_3

The FeF_3 used in this experiment was pale green (although pure FeF_3 is white) and contained a small amount of H_2O. No immediate signs of reaction were observed as the HPO_2F_2 warmed to room temperature and no HF was detected in the vapour phase. The reactants were left in contact for three days and following gentle warming with a hairdryer a small concentration of HF was indicated by the infrared spectrum of the vapour phase. The mixture was then heated to 90 °C whereupon an orange-brown colour was imparted to the acid. The colour deepened after a few minutes heating and the HF concentration in the vapour phase also increased. The tube was then heated for a further 2½ hours during which time the liquid phase turned brown although the HF concentration in the vapour phase remained fairly constant. The liquid phase was distilled off and the solid dried in vacuum. Strong bands attributable to

-172-
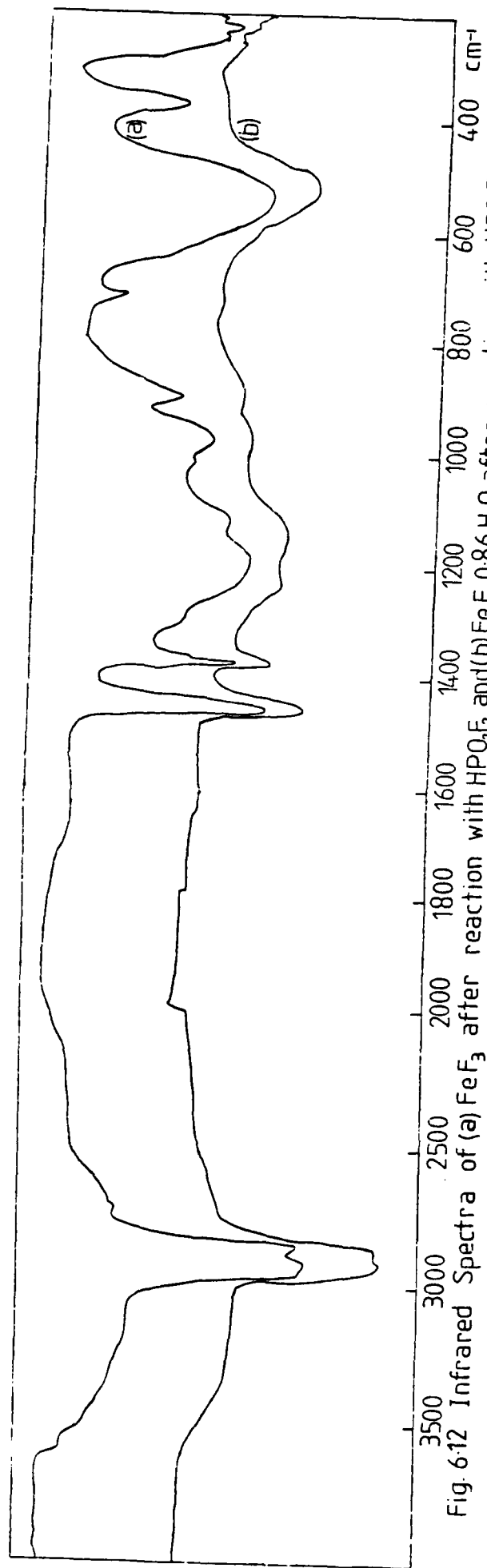
Fig. 6.12 Infrared Spectra of (a) FeF_3 after reaction with HPO_2F_2 and (b) $FeF_3.0.86\,H_2O$ after reaction with HPO_2F_2

Table 6.19

Infrared Spectra of (a) FeF_3 after Reaction with HPO_2F_2 and (b) $FeF_3 \cdot 0.86H_2O$ after Reaction with HPO_2F_2

(a)   (b)

Absorption band (cm^{-1})		Absorption band (cm^{-1})		Assignment	
3500-2500	w, vb	3500-2500	m, vb	ν	O-H
1660	w, b	1622	w	δ	H_2O
1300	m, sh			ν	P = O?
1190	s	1130	w	ν_{as}	PO_2
1120	s	1130	w	ν_s	PO_2
1020	m, sh			ν	P - O(H)?
977	s	965	w	ν_{as}	PF_2
903	m	890	w	ν_s	PF_2
680-430	s, vb	650-430	s, vb	ν	Fe - F
				$+\delta$	$PO_2 + \delta$ POF
374	m			δ_s	PF_2

? tentative assignment

co-ordinated fluoride and co-ordinated difluorophosphate
were observed in the infra-red spectrum. (Fig. 6.12 and
Table 6.19). This spectrum shows certain similarities to
spectra obtained for compounds of the type $M(O_2PF_2)_2.HPO_2F_2$
M = Mn, Fe, Co, Ni, Cu) implying the presence of both
co-ordinated difluorophosphate and solvating difluorophosphoric
acid in this product.

β - $AlF_3.3H_2O$

β - $AlF_3.3H_2O$ (0.1 g) was weighed into a fluoroplastic
tube and HPO_2F_2 was distilled on to it. There was no immediate
evidence for reaction and the mixture was set aside overnight.
The following day definate signs of reaction were observed;
bubbles of gas were seen escaping from the white solid at
the bottom of the tube and weak bands due to HF were identified
in the vapour phase infrared spectrum. After one week, all
the volatiles were removed and the weight change of the tube
determined. The weight of the solid had increased by 0.08 g
providing evidence that reaction had occurred. The reaction
was repeated on a larger scale; excess HPO_2F_2 was distilled
on to $AlF_3.3H_2O$ and the mixture was held at 40 ^{O}C for one
week. HF formed during the reaction was removed by
periodically cooling the reaction tube to -62 ^{O}C (in an
ethoxyethyl acetate/liquid nitrogen slush bath) and pumping
off the HF through a vacuum system. About three quarters of
the HPO_2F_2 was then removed by vacuum distillation and the
remainder decanted off. A fresh portion of HPO_2F_2 was then
distilled on to the solid. The process was then repeated
up to the decantation stage and the white solid product
was dried in vacuum. An infrared spectrum of the product
showed that extensive dehydration had occurred. (See Fig 6.13 and Table 6.29)
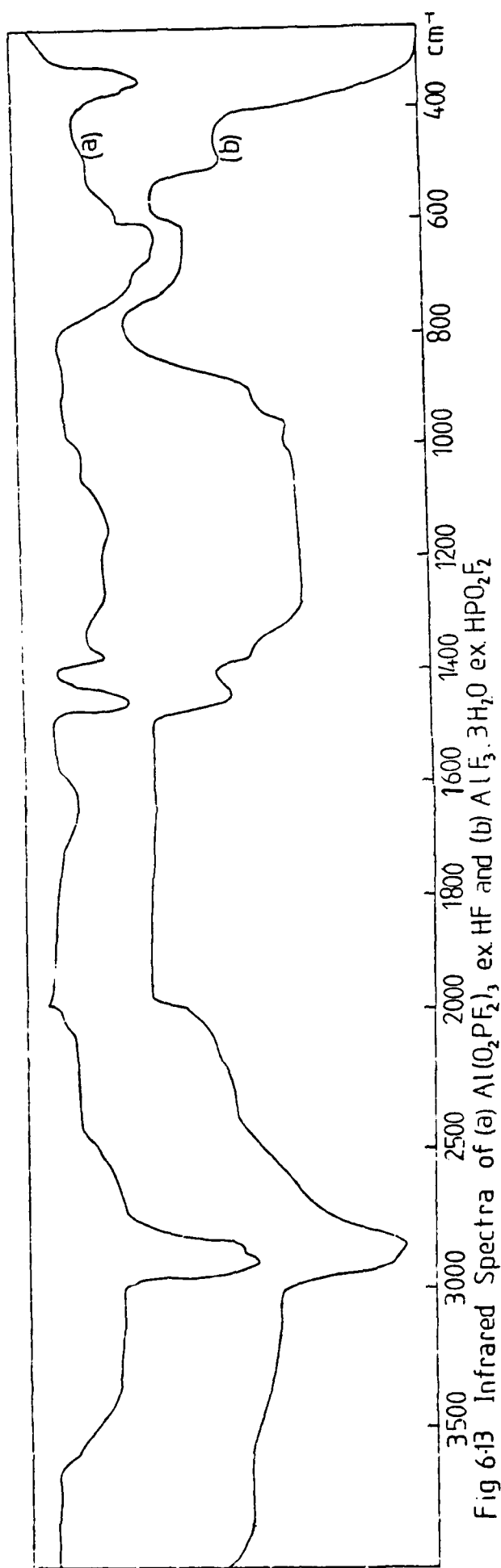
Fig 6·13 Infrared Spectra of (a) $Al(O_2PF_2)_3$, ex HF and (b) $AlF_3.3H_2O$ ex HPO_2F_2

Table 6.20

Infrared Spectra of (a) $Al(O_2PF_2)_3$ Exposed to HF and (b) $\beta\text{-}AlF_3 \cdot 3H_2O$ Exposed to HPO_2F_2

(a) Absorption band (cm^{-1})	(b) Absorption band (cm^{-1})	Assignment	
3500-2500 m, vb	3500-2500 w, vb	ν	O-H
1625 w,b		δ	H_2O
1270 w,b	1330-	ν_{as}	PO_2
1150 w,b	1000 m, vb	ν_s	PO_2
1008 w	965 m	ν_{as}	PF_2
880 w	900 m	ν_s	PF_2
780-550 s,b	760-600 m, b	ν	Al-F
505 m	485 m	δ	POF

No band at 1630 cm^{-1} (due to the H_2O bending mode) was observed. However, strong bands due to metal-fluoride stretching modes were observed indicating that complete conversion of fluoride into difluorophosphate had not taken place, in contrast to the reaction of β-FeF$_3$.3H$_2$O . It was decided to investigate the reverse reaction, namely the reaction of aluminium (III) difluorophosphate with liquid HF.

Some Al(O$_2$PF$_2$)$_3$ was placed in a 6mm PTFE tube, fitted with a Kel-F valve, and HF was distilled on to it. Much effervescence was observed as the reaction proceeded but the solid remained white and did not pass into solution. The HF was decanted off and the solid evacuated to dryness. The infra-red spectrum of the product (Fig 6.13 and Table 6.20) contained bands assigned to fluoride, difluorophosphate and water.

NiF$_2$.4H$_2$O

HPO$_2$F$_2$ was vacuum distilled on to canary yellow NiF$_2$.4H$_2$O. As the acid warmed to room temperature bubbles were observed rising from the green solid, the liquid phase acquired a green-yellow colour and the solid turned green. HF bands were observed in the vapour phase spectrum after a few minutes. Warming of the sample with a hairdryer for a few minutes caused increased effervescence, a darkening of the colour of the solution and a considerably enhanced concentration of HF in the vapour phase. More HPO$_2$F$_2$ was then distilled into the reaction tube and the liquid warmed as before until all the solid dissolved.

The green-yellow solution could not be evaporated to dryness in

vacuum suggesting that dehydration of the $NiF_2.4H_2O$ had resulted in hydrolysis of HPO_2F_2 which generates the involatile phosphorus acids H_2PO_3F and H_3PO_4.

$CrF_3.3\cdot5H_2O$

There were no visible signs of reaction whithin the first day and after one week only very weak bands due to HF were identified in the vapour phase spectrum. The tube was warmed with a hairdryer but the vapour phase infrared spectrum was little affected even though bubbles were seen rising from the solid. After ten days the HF concentration in the vapour phase remained small, the liquid phase was removed by decantation and the solid was washed with dry diethyl ether. After drying in vacuum an infra-red spectrum and an X-Ray powder photograph of the residual solid were obtained.

The X-Ray powder photograph was identical with that of unreacted $CrF_3.3\cdot5H_2O$ and the i,r, spectrum (Figure 6.14 and Table 6.21) indicated that little or no dehydration had occurred. Weak bands due to difluorophosphate were observed in the region 1050-1300 cm^{-1} but the material appears to be largely unreacted $CrF_3.3\cdot5H_2O$

MnF_2

HF was observed in the vapour phase infrared spectrum. After four days the acid has acquired a purple colour and the HF concentration in the vapour phase had increased. The liquid phase was removed by vacuum distillation, followed by decantation, and the residual solid was then washed with a small amount of HPO_2F_2 and dried in vacuum. Bands due to both fluoride and difluorophosphate were observed in the infrared spectrum of this solid residue.
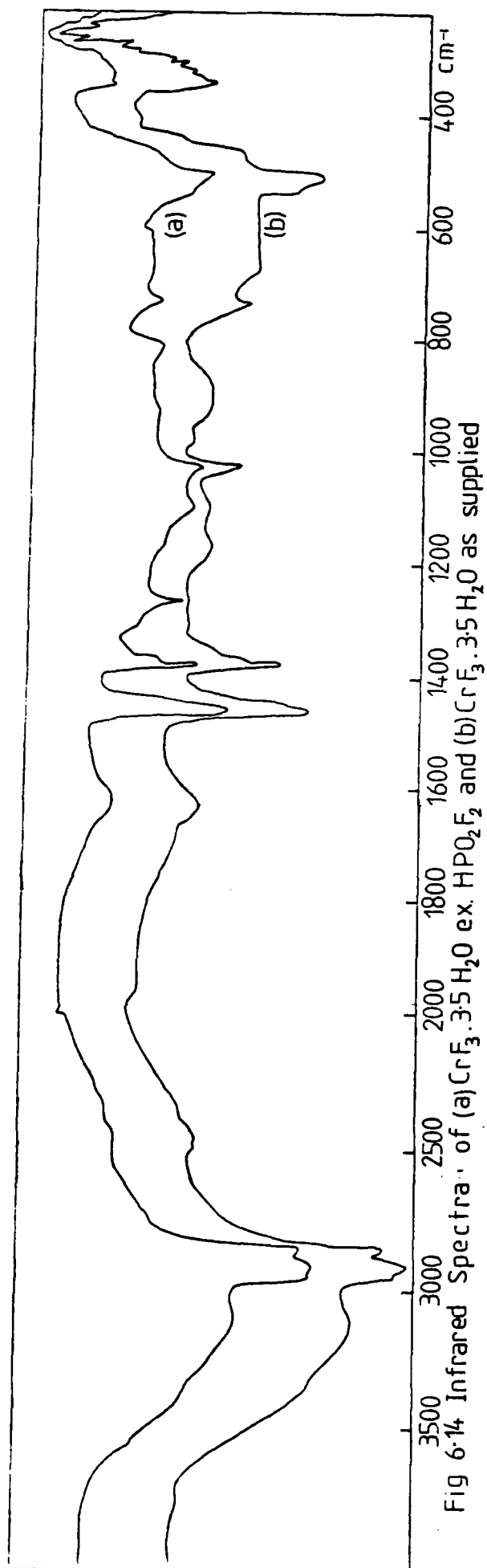
Fig 6·14 Infrared Spectra of (a)$CrF_3.3.5 H_2O$ ex. HPO_2F_2 and (b)$CrF_3.3.5 H_2O$ as supplied

Table 6.21

Infrared Spectra of (a) $CrF_3 \cdot 3.5H_2O$ and (b) $CrF_3 \cdot 3.5H_2O$

Exposed to HPO_2F_2

(a) Absorption band (cm^{-1})		(b) Absorption band (cm^{-1})		Assignment
3500-300	s, vb	3500-3000	s, vb	ν O-H
1640	m, b	1630	m, b	δ H$_2$O
		1262	m, b	ν_{as} PO$_2$
1160		1160	w	
1120	w	1120	w	
1090	w	1090	m	
1020	m	1020	m	
		920	w	ν_{as} PF$_2$
890	w, b	810	w	
725	w	725	w	
700-520	s, b	700-520	s, b	ν Cr-F

MnF_3

The acid acquired a purple colour, however, no other visible signs of reaction were obtained. (The purple colour was likely to be due to contamination of MnF_3 by MnF_2). MnF_3 was found to be unaffected by HPO_2F_2.

$CuF_2 \cdot 2H_2O$

HF was observed in the vapour phase after 20 minutes. The acid took on a green colour which gradually intensified. After four days most of the solid had dissolved, imparting a blue-green colour to the acid. The tube was then heated to $120^{\circ}C$ for 15 minutes causing all the blue $CuF_2 \cdot 2H_2O$ to disappear. The colour of the acid darkened and a small amount of a black solid was deposited at the bottom of the tube. This was almost certainly CuO, formed by thermolysis of an intermediate oxo-salt.

$Co F_2 \cdot H_2O$

Effervescence was observed immediately and HF was observed in the vapour phase after a few minutes. The acid acquired a purple colour which intensified upon standing. After warming with a hairdryer virtually all the solid dissolved in the acid.

$MnF_2 \cdot 2 \cdot 4H_2O$

Vigorous effervescence was seen, and strong bands due to HF were observed in the infra-red spectrum after ten minutes. Upon warming with a hairdryer the rate of reaction increased. After five hours all the solid had passed into solution.

(d) <u>Conclusions to Section 6.2</u>

Depending upon reaction conditions a number of different iron difluorophosphates can be formed (Chart 6.1) . On the basis of its evident stability in HDA solution (see Chart 6.1), the crystalline modification of $Fe(O_2PF_2)_3$ is the product most likely to be akin to the authentic corrosion products reported previously.[6.14]

Although it has not proved possible to perform accurate measurements, the magnitude of the solubility of this compound in both HDA and MHDA is known to be small (ca 50 ppm Fe w/w or less). Therefore, it is likely that this compound will give rise to colloidal material in HDA.

(Chart 6.2)

Experiments with nickel/indicate that the compound $Ni(O_2PF_2)_2 \cdot HPO_2F_2$ must be considered a potential Ni/MHDA corrosion product. It is /generated in a medium where the HPO_2F_2 is in considerable excess as opposed to previous investigations [6.15] where the nickel was in excess. Clearly the $Ni:HPO_2F_2$ mole ratio will control the nature of the product formed. The solubility of $Ni(O_2PF_2)_2 \cdot HPO_2F_2$ in HDA is known to be quite high (ca 5,000 ppm Ni w/w) and, therefore, this compound is unlikely to precipitate from MHDA or be responsible for colloidal matter in solution. However, experiments have shown that $Ni(O_2PF_2)_2 \cdot HPO_2F_2$ does undergo some hydrolysis when left in contact with HDA; nickel monofluorophosphates and orthophosphates are, therefore, also likely to be formed in MHDA.

Difluorophosphoric acid solvates of the type $M(O_2PF_2)_2 \cdot HPO_2F_2$
(Chart 6.2)
(M = Mn,Co,Cu) /are potential corrosion products from the reaction

-180-

Chart 6.1

Synthesis of Iron Difluorophosphates

Fe (powder) $\xrightarrow[\theta_2 \text{ not excluded}]{\text{excess } HPO_2F_2}$ (i) H$_2$ gas

(ii) white solid (see text)

(iii) pink solution

excess HPO_2F_2

O_2 excluded

(i) H$_2$ gas

(ii) colourless solution

Evacuate to dryness

white

$Fe(O_2PF_2)_2 \cdot HPO_2F_2$

Filter evacuate to dryness

blue-grey

$Fe^{II}Fe^{III}(O_2PF_2)_5 \cdot HPO_2F_2$

Fe (powder) $\xrightarrow{HDA}$ brown solution

excess HPO_2F_2 ↓

white

$Fe(O_2PF_2)_3$

(crystalline)

excess HPO_2F_2

$\beta\text{-FeF}_3 \cdot 3H_2O$ buff $\xrightarrow{\text{excess } HPO_2F_2}$ green solid

$FeCl_3$ $\xrightarrow{Et_2O}$ yellow-green solution $\xrightarrow{\text{excess } HPO_2F_2}$ white

$Fe(O_2PF_2)_3$ (amorphous)

-181-

Chart 6.2

Reactions of some Powdered Metals with Difluorophosphoric
Acid

Mn ———excess HPO_2F_2 ————————→ colourless solution

$\downarrow$ evacuate to dryness

$Mn(O_2PF_2)_2HPO_2F_2$

Co ———excess HPO_2F_2 ——————→ purple solution

$\downarrow$ evacuate to dryness

$Co(O_2PF_2)_2 \cdot HPO_2F_2$

Ni ———excess HPO_2F_2 ————————→ yellow solution

$\downarrow$ HDA/HPO_2F_2 mixture

green solid (see text)

$\downarrow$ $\downarrow$ evacuate to dryness

yellow solution ——$-20^{o}C$, one month→ $Ni(O_2PF_2)_2 \cdot HPO_2F_2$

Cu ———excess HPO_2F_2 ————————→ pale blue solution

$\downarrow$ evacuate to dryness

$Cu(O_2PF_2)_2 \cdot HPO_2F_2$

-182-
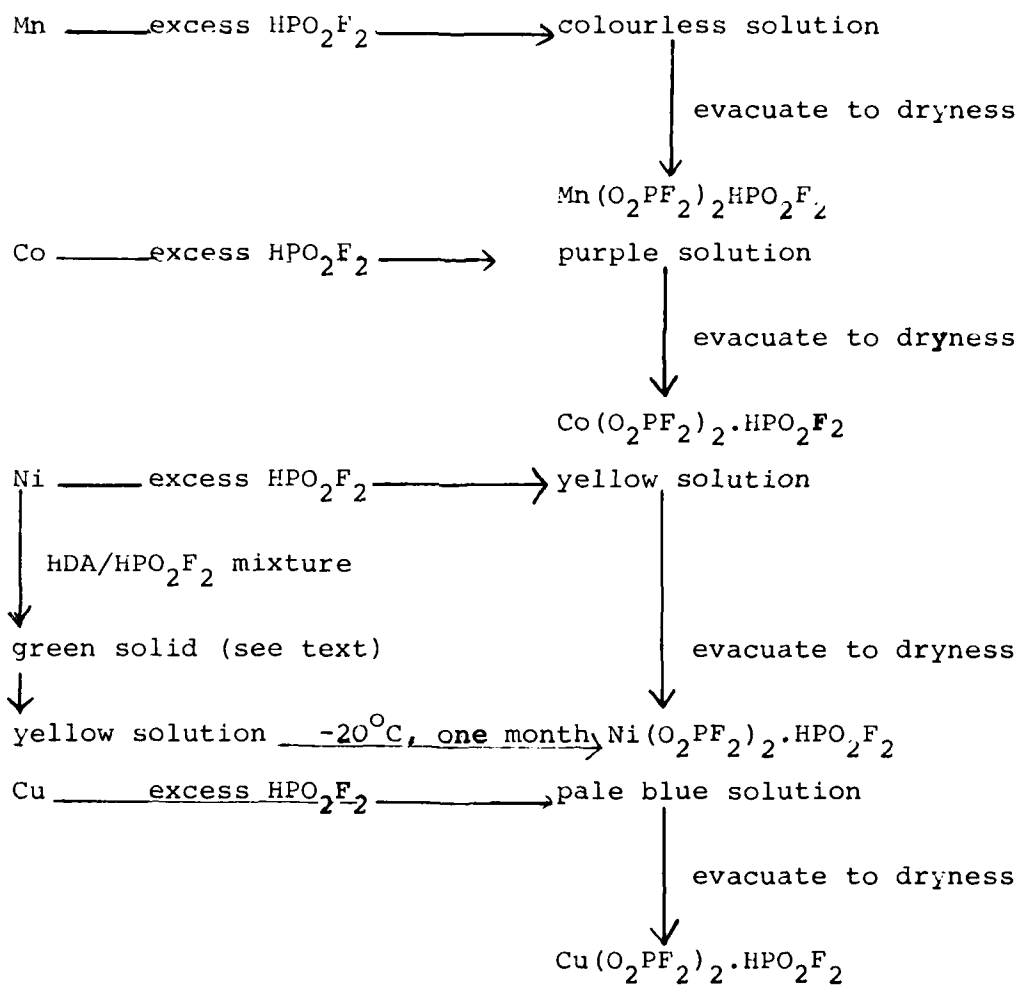
of MHDA with the other metals indicated. All compounds of this type are likely to have a high solubility in MHDA and to undergo some hydrolysis in this medium.

Experiments with some metal fluorides (see Chart 6.3) show that both suspended corrosion products and surface films on metals, in MHDA, are likely to contain both fluoride and difluorophosphate groups. Of particular relevance to the likely nature of surface films are the experiments with β-AlF$_3$.3H$_2$O and CrF$_3$.3.5H$_2$O

The resistance of CrF$_3$.3.5H$_2$O to HPO$_2$F$_2$ gives some indication that the film formed on Stainless steel in MHDA may well be rich in fluoride. Results from the β-AlF$_3$.3H$_2$O/HPO$_2$F$_2$ investigations indicate that the film formed on aluminium is likely to contain a more substantial amount of fluorophosphate.

Chart 6.3

Reactions of Some Metal Fluorides with Difluorophosphoric Acid

(a) **Fluorides which undergo ready reaction with HPO_2F_2**

MnF_2 HF evolved.

Product contained bands due to $PO_2F_2^-$ and F^-.

$CoF_2 \cdot H_2O$
$NiF_2 \cdot 4H_2O$
$CuF_2 \cdot 2H_2O$ HF evolved.
$ZnF_2 \cdot 2.4H_2O$ Product passed into solution.

$\beta-AlF_3 \cdot 3H_2O$ HF evolved.

Extensive dehydration.

Product contained bands due to $PO_2F_2^-$ and F^-.

$\beta-FeF_3 \cdot 3H_2O$ HF evolved (upon warming).

Complete solvolysis and dehydration to $Fe(O_2PF_2)_3$.

(b) **Fluorides which are unreactive towards HPO_2F_2**

MnF_3 No reaction.

$CrF_3 \cdot 3.5H_2O$ Very little reaction.

$FeF_3 \cdot 0.86H_2O$ Reacts to a limited extent.

FeF_3 Reacts under forcing conditions (high temperature).

7. CONCLUDING REMARKS AND RECOMMENDATIONS

Inhibition of metallic corrosion by HF or PF_5 in High Density Acid can be attributed to the formation of protective films of low solubility. The growth of the protective film is a lengthy and complex process and factors such as storage time and H_2O content of the acid are of critical importance. Long term experiments indicate that SHDA can be stored in aluminium with very low levels of corrosion for a considerable length of time (of the order of 18 months to 2 years). However, even this very low corrosion rate is undesirable in view of the insolubility of the corrosion film. The film, the principal components of which appear to be α-AlF_3 and α-$AlF_3 \cdot H_2O$, grows to a significant thickness and, particularly if subjected to even slight mechanical shock, is likely to become detached ('flake off') and colloidal. There is some evidence that in MHDA the film does not, usually, grow to the same thickness as the film in SHDA, which may be an advantage. The levels of aluminium concentration in solution in SHDA and MHDA after 23 months storage were very similar and the long term rate experiments indicated that MHDA offers no advantages over SHDA in terms of corrosion prevention (Section 4.1). It is likely however that H_2O content is a critical factor in deciding the relative effectiveness of SHDA and MHDA. N.m.r. studies (Section 2.2(c) indicate that fairly minor changes in H_2O content (ca 0.2 wt %) significantly affect the relative proportions of fluorophosphate species in MHDA and

-185-

electrochemical studies involving aluminium (Section 4.2) point to the superior inhibitive properties of H_2PO_3F over HPO_2F_2 (at least in the short term). Since increasing the H_2O content of MHDA would increase the H_2PO_3F/HPO_2F_2 ratio, a tolerably high H_2O concentration may well be an advantage in this case.

Both HF and PF_5 are effective inhibitors for the stainless steel/HDA system. It has been established that the corrosion of stainless steel in uninhibited HNO_3/N_2O_4 mixtures occurs because of the transpassive effect. The protective insoluble Cr_2O_3 film breaks down due to the oxidation of Cr(III) to soluble Cr(VI) oxo-species. When HF or PF_5 are present, this transpassive effect does not occur; the different chemical nature of the films in these inhibited systems prevents film breakdown, for example, in SHDA chromium fluoride is incorporated into the oxide film and its ability to plug anodic sites prevents film growth and breakdown.

The cathodic protection of metals in HNO_3/N_2O_4 mixtures, by the use of an external power source or coupling with a metal of more base potential, is an attractive possibility. Preliminary experiments conducted with stainless steel (Section 5.4) are extremely encouraging,having demonstrated that an impressed current, or coupling to aluminium,arrests the corrosion of the stainless steel almost completely. The precise effect of this coupling on the aluminium is not easily predicted but the presence of a thicker film may, or may not, lead to increased protection of this metal also (See Section 5.4).

In the light of the knowledge gained during the course of the work described here, we now conclude this Report with some recommendations for future action. These are aimed at minimising the extent of corrosion of containment metals, and thus the amounts of corrosion products formed, in rocket engine systems employing HDA as propellant oxidiser. So far as the use of chemical (anodic) inhibitors is concerned, the key to the flow decay - type problems associated with the presence of metal corrosion products, appears to be in the establishment and maintenance of a compromise situation i.e. an insoluble surface film on the metal which is coherent and thick enough to give satisfactory corrosion protection, but not so thick as to become easily detached from the metal surface and dispersed into the liquid medium. The recommendations are therefore as follows:-

1. If the use of Standard HDA, i.e. of HF as the inhibitor, must continue, bearing in mind that such inhibitors can only reduce and not entirely eliminate corrosion, the following aspects should be examined

    (a)   The effect of different HF concentrations on corrosion rates and film properties. The effects of small variations in H_2O content and in the proportions of N_2O_4 and HNO_3 would also be relevant.

    (b)   The effect of different pre-treatments of the metal surface (which could include pre-treatment with HF or another fluoride) on aluminium corrosion in Standard HDA. XPS (Section 4.3) shows that the thickness of the film ultimately formed on aluminium in this medium appears to be influenced by the

-187-

thickness of the air-formed film initially present on the metal surface.

(c)   The colloid chemistry of Al, Fe and Cr fluorides in standard HDA.

In a location such as a pump bearing, colloidal metal fluoride may possibly be induced to coagulate (by mechanical or physical rather than chemical effects?) with formation of a suspension or "paste" with poor lubricating properties. Also corrosion in such an area may be accelerated via:

(i)   depletion of the HF content of HDA as fresh metal surfaces are exposed by friction and,

(ii)   poor circulation of lubricant (SHDA) through the bearing.

Presumably the objective should be to maintain the colloidal state of dissoved corrosion products, since it would seem that in this state they can do least harm vis-a-vis for example clogging of filters or abrasion of metal surfaces. In a metal-to-metal bearing, surface films are presumably being continuously formed and removed ie rapid corrosion is occurring in this dynamic situation compared to the slower corrosion in a static system (eg tank).

2.   Concerning Modified HDA, support for a reduction in PF_5 content to 0.4 wt % is now available from two independent sources (See Section 4.2(i) and Ref.4.11).

3.   The preliminary electrochemical and XPS work, described in this Report, on inhibition by HPO_2F_2, H_2PO_3F (aluminium, Section 4) and the non-fluoride inhibitors H_3PO_4, P_4O_{10} (aluminium, Section 4), H_2SO_4 and As_2O_3 (Stainless Steel, Section 5) could be extended to include a study of the tendency, if any, of these compounds to generate suspended

corrosion products.   Many other potential inhibitors

await similar investigations (see Ref.5.5).

Finally, on the basis of the sum total of information

obtained during our two-year programme, we propose that the

corrosion mechanism of Al, Cr and Fe in Standard HDA involves

the steps illustrated in Chart 7.1.

Chart 7.1 Proposed Corrosion Mechanism in Standard HDA

Cathode

$$e^- \quad NO_2^+ \longrightarrow NO_2 \; (\pm N_2O_4)$$

$$\begin{array}{c} -M- \\ -M- \\ -M- \\ -M- \\ -M- \\ \text{Anode} \quad -M- \end{array}$$

$$NO_2 \quad H \underset{O}{\overset{-ONO_2}{\longleftarrow}}$$

$\underline{\text{Electrochemical}}$ Attack $\longrightarrow$

$$\begin{array}{c} -M- \\ -M- \\ -M- \\ -M- \\ -M-O-NO_2 \\ -M- \end{array}$$

Further Attack $\longrightarrow$

$$\begin{array}{c} M \\ M \\ M \\ M \\ M-(ONO_2)_x \\ M \end{array}$$

$\underline{\text{Dissolution}}$

$M(ONO_2)_n \cdot H_2O_x^{(3-n)+}$

Hydration

$\underset{\text{Precipitation}}{\longrightarrow}$ Particulate metal fluoride hydrate in suspension

$\underline{\text{Loss}}$ of NO_2^+ $\longrightarrow$

$$\begin{array}{c} M \\ M \\ M \\ M \\ M=O \\ M \end{array}$$

Fluoride Substitution $\longrightarrow$

$$\begin{array}{c} M \\ M \\ M \\ M \\ M-F_x \\ M \end{array}$$

$\longrightarrow$ Flaking of Film

$\underline{\text{Fluoride}}$ Substitution $\longrightarrow$ Particulate metal fluoride in suspension

fluoride substitution
$$M(H_2O)_6^{3+}$$
$$MF(H_2O)_x^{2+}$$
$$MF_2(H_2O)_x^+$$
$$MF_3 \cdot x\,H_2O$$
$$MF_4(H_2O)_x^-$$
$$MF_5(H_2O)_x^{2-}$$
$$MF_6^{3-}$$

these steps
M=Al, Cr, Fe, (not Ni)

REFERENCES

Section 1

1.1 N Logan, MFA Dove and JW Bailey, "Corrosion Chemistry
in Inhibited HDA", Grant No. AFOSR-78-3717, Final
Scientific Report, 29th November 1979.

1.2 CC Addison and N Logan, "HDA Corrosion Chemistry"
Final Scientific Report, December 1977, AFRPL-TR-77-65.

1.3 N Logan and MFA Dove, "Corrosion Chemistry in Inhibited
HDA", Grant No. AFOSR-78-3717A, Progress Report
No. 4, 30th January 1980; No. 5, 30th April 1980;
No. 6, 31st July 1980.

Section 2

2.1 JDS Goulden and DJ Millen, J Chem. Soc., 1950, 2620.

2.2 DJ Millen and D Watson, J. Chem. Soc., 1957, 1369.

2.3 GW Elverum and DM Mason, J. Phys. Chem., 1956, 60,
104.

2.4 K Nakamoto, "Infrared And Raman Spectra of Inorganic
and Coordination Compounds", Wiley-Interscience, 3rd
Ed., 1978.

2.5 CC Addison, LJ Blackwell, B Harrison, DH Jones, N Logan,
EK Nunn and SC Wallwork, J. Chem. Soc., Chem. Comm.,
1973, 347; LJ Blackwell, EK Nunn and SC Wallwork, J.
Chem. Soc. (Dalton), 1975, 2068.

2.6 K Schaumberg and C Deverell, J. Amer. Chem. Soc.,
1968, 90, 2495.

2.7 N Logan, MFA Dove and JW Bailey, "Corrosion Chemistry in
Inhibited HDA," Grant No. AFOSR-78-3717, Final Scientific
Report, 29th November 1979.

2.8 CC Addison and N Logan, "HDA Corrosion Chemistry", Final
Scientific Report, December 1977, AFRPL-TR-77-65.

Section 3

3.1 JM West, Corrosion and Electrodeposition Processes,
Van Nostrand, 1970.

3.2 M Pourbaix, Atlas of Electrochemical Equilibria, Pergamon,
1966.

3.3 E Crileadi, E Kirowa-Eisner and J Penciner, Interfacial
Electrochemistry, Addison-Wesley,

3.4 ND Tomashov, Theory of Corrosion and Protection of Metals,
Collier-Macmillan, 1966.

3.5 TP Hoar, Corros. Sci, 1965, 5, 279.

3.6 DT Sawyer and JL Roberts, Experimental Electrochemistry
for Chemists, Wiley, 1974.

3.7 JA Von Fraunhofer, and CH Banks, Potentiostat and
its Applications, Butterworths, 1972.

3.8 DJG Ives, and GT Janz, Reference Electrodes, Academic
Press, 1969.

3.9 N Logan, MFA Dove and JW Bailey, Corrosion Chemistry
in Inhibited HDA, Grant No. AFOSR-78-3717, Final Scientific
Report, 29th November 1979.

Section 4

4.1   N. Logan, M.F.A. Dove and J.W. Bailey, "Corrosion
      Chemistry in Inhibited HDA", Grant No. AFOSR-78-3717,
      Final Scientific Report, 29th November 1979, Sect.2.8, p.27.

4.2   Ref. 4.1, Sect. 2.6, Fig. 2.9.

4.3   M.S. Hunter and P.F. Towner, J. Electrochem. Soc.,
      1961, 108, 139.

4.4   J. Albery, "Electrode Kinetics", Clarendon Press,
      Oxford, 1975, p. 109.

4.5   T.M. Salem, J. Horvath and P.S. Sidky, Corr. Sci., 1978
      18, 363.

4.6   H.H. Uhlig, "Corrosion and Corrosion Control: an
      Introduction to Corrosion Science and Engineering",
      New York, Wiley, 2nd Ed., 1971, p. 224.

4.7   Ref. 4.1, Sect. 2.1. p.9.

4.8   Ref. 4.1, Sect. 2.1, p.8.

4.9   Ref. 4.1, Sect. 6.2, p.179.

4.10 T. Våland and G. Nilsson, Corr. Sci., 1977, 17, 449.

4.11 H.Ph. Heubusch   et al, "Propellant Improvement
      Program", Vol. 1, Part 2, Modified HDA Studies, Special
      Technical Report for period May 1972 - July 1973, p. 16.

4.12   Ref. 4.1, Sect. 2.1, p. 11.

4.13   Ref. 4.1, Figs. 7.1 and 7.2.

4.14   Ref. 4.1, Fig. 7.8.

4.15   G.E. McGuire, G.K. Schweitzer and T.A. Carlson,
        Inorg. Chem.,   1973, 12, 2450.

4.16   M.   Klasson, J. Hedman, A. Berndtsson, R.Nilsson
        C. Nordling, and P. Melnik, Phys. Scr., 1972, 5, 93.

4.17   G. Lewis and P.G. Fox, Corr. Sci., 1978, 18, 645.

4.18   F.A. Cotton and G.   Wilkinson, "Advanced Inorganic
        Chemistry," Interscience   , 3rd Ed.,   1972,
        p. 52.

4.19   J.A. Richardson and G.C. Wood, J. Electro Chem. Soc.,
        1973, 120, 193.

4.20   B. Siegel and R.L. Johnson, Nature, 1964, 204, 375;
        1966, 210, 1256.

Section 5

5.1   C.C. Addison and N. Logan, "HDA Corrosion Chemistry",
        Final Scientific Report, December 1977, AFRPL-TR-77-65.

5.2   J.M. West "Corrosion and Electrodeposition Processes",
        Van Nostrand, 1970.

5.3   N.Logan, M.F.A. Dove and J.W. Bailey, "Corrosion
        Chemistry in Inhibited HDA", Grant No. AFOSR-78-3717,
        Final Scientific Report, 29th November 1979.

5.4   H.Ph. Heubusch, Bell Aerospace Textron, Private
      Communication.

5.5   W.H. Bergdorf and E.J. Kinsley, Jr. "Investigation of
      Inhibitors for Fuming Nitric Acid" Wright Air Development
      Centre Technical Report 55-151, March 1955.

5.6   Ref.5.1. p 40.

5.7   Ref.5.1 p.47

5.8   Ref.5.3 p.66.

Section 6

6.1   N. Logan, M.F.A. Dove and J.W. Bailey, "Corrosion Chemistry
      in Inhibited HDA", Grant No. AFOSR-78-3717, Final
      Scientific Report, 29th November 1979.

6.2   See, for example, Ref. 6.1, pp 75-80 and Appendix B.3,
      p. 214.

6.3   Ref. 6.1, Appendix A14, p. 211.

6.4   C.C. Addison and N. Logan, "HDA Corrosion Chemistry",
      Final Scientific Report, December 1977, AFRPL-TR-77-65.

6.5   Ref. 6.1, Section 5.5.

6.6   Ref. 6.1, Table 5.19, p. 139.

6.7   Ref. 6.1, Table 5.22, p. 145, Figure 5.25(b).

6.8   Ref. 6.1, Table 5.21, p. 143, Figure 5.24(a).

6.9   D.R.B. Saw, "Storage Life Assessment of the Packaged Liquid
      Propellants IRFNA and MAF-1", Technical Report PERME TR 143,
      February 1980.

6.10 D.M. Tallett, Ph.D. thesis, University of Nottingham, 1977.

6.11 B. Mellor, Ph.D. thesis, University of Nottingham, 1980.

6.12 Ref.6.1., Sections 5.6-5.9.

6.13 Ref.6.1., Section 5.8

6.14 Ref.6.1., Section 4.1.

6.15 Ref.6.1., Section 5.2.

6.16   E.T. Chang and T. Poston, The Aerospace Corporation,
       El Segundo, California. See Postscript 2, HDA
       Meeting Proceedings, University of Nottingham,
       20-23 May 1980.

6.17   Ref. 6.1, p.128.

6.18   Ref. 6.1, Section 5.4

APPENDIX A. ANALYTICAL, SPECTROSCOPIC AND RELATED TECHNIQUES

A.1 Metal Analysis

Aluminium, chromium, manganese, iron and nickel were determined spectrophotometrically by atomic absorption using a Perkin-Elmer 603 AA Spectrometer. Sodium (ca 35 m molar) in the form of the chloride was added to standard and sample solutions to control ionisation.

Iron as Fe(II) (Section 6.2(a) was also determined by titration with standard potassium dichromate solution using sodium diphenylamine sulphonate indicator. Samples were dissolved in 2.5 % H_2SO_4 (ca 200 cm^3) to which phosphoric acid (5 cm^3) was added.

Cobalt (Section 6 2(a) was determined gravimetrically by precipitation as cobalt tetrathiocyanatomercurate (II) Co Hg(SCN)$_4$.

Copper (Section 6 .(2a) was determined gravimetrically by precipitation as the pyridine thiocyanate complex $\left[Cu(C_5H_5N)_2\right]$ (SCN)$_2$.

A.2 Fluorine Analysis

Fluorine was determined potentiometrically with a lanthanum fluoride ion-sensitive electrode by comparison with standards prepared from Analytical Reagent grade (AR) sodium fluoride (known to be at least 99.6% pure). This was further purified by moistening with A.R. 40% hydrofluoric acid in a platinum crucible, evaporating the acid fluoride to dryness, heating the crucible to a bright red-heat until the fluoride

fused completely for 1 minute and allowing the fused material to cool in a desiccator.

A Tiron (disodium 4.5-dihydroxy-m-benzenedisulphonate)/sodium acetate complexant/buffer solution was used with both standard and unknown solutions to complex the metal and to buffer the pH and ionic strength.

$Mn(O_2PF_2)_2.HPO_2F_2$ (Section 6.2(a)was hydrolysed, prior to analysis, by heating with 4% NaOH (in a sealed Carius tube) at $160^O C$ for 24 hours.

Fluorine was isolated from $Co(O_2PF_2)_2.HPO_2F_2$ (Section 6.2(a) as hydrofluorosilicic acid by distillation from perchloric acid solution.

Fluorine was isolated from metal fluorides by fusing with sodium hydroxide (30 minutes at $650^O C$). The fused residue was cooled, dissolved in warm water and diluted prior to analysis.

A.3   Phosphorus Analysis

Phosphorus was determined gravimetrically as ammonium phosphomolybdate, $(NH_4)_3PMo_{12}O_{40}$. Prior to analysis, fluorophosphate products were hydrolysed in 20% nitric acid containing 2% boric acid (to remove interfering fluoride) at $60-70^O C$ for 2 hours.

A.4   Infrared Spectroscopy

The infrared spectra of solid samples were recorded as Nujol mulls (prepared in a nitrogen filled glove box) between caesium iodide (4000-250 cm^{-1}) or silver chloride windows (4000-330 cm^{-1}) using a Perkin-Elmer 577 grating infrared spectrometer. Attack on the caesium iodide windows by difluorophosphates was slight provided the spectra were run quickly. The spectra were checked by running them again using silver chloride windows. All fluoride spectra were run on silver chloride windows.

A.5 X-Ray Photoelectron Spectroscopy (XPS)

XPS spectra were obtained by means of a Vacuum Generators ESCA 3 instrument using AlK_{α} radiation.

A.6 Scanning Electron Microscopy (SEM)

SEM studies were performed with a Cambridge Instruments S2A scanning electron microscope.

A.7 N.M.R. Spectroscopy

All n.m.r. spectra were obtained with a Bruker WM 250 pulse Fourier transform n.m.r. spectrometer.

A.8 X-Ray Powder Diffractometry

Powder photographs were obtained of finely ground samples which were loaded into 0.2, 0.3 or 0.5 mm diameter glass capillaries in a nitrogen-filled glove box. The capillary was temporarily sealed with grease, then removed from the glove box and flame sealed.

The powder photographs of iron-containing compounds were obtained using FeK_{α} radiation, filtered by manganese, and those of other compounds using CuK_{α} radiation, filtered by nickel, with a 114.83 mm Debye-Scherrer camera.

A.9 Detection of HF in HPO_2F_2 by Infrared Spectroscopy

In the study of the reactions of metal fluorides with HPO_2F_2, HF in the vapour phase was detected by means of two

characteristic bands between 3900 cm^{-1} and 3800 cm^{-1}. All

reactions were carried out in 6 mm i.d. F.E.P tubes sealed

at one end and conected _via_ a compression fitting to a

Kel-F-and-Teflon valve. The infrared spectrum of the vapour

phase was obtained with the tube clamped vertically in the sample

beam of a Perkin-Elmer 577 Spectrophotometer.

To obtain a guide to the sensitivity of this method for

the detection of HF in the presence of difluorophosphoric

acid, HPO_2F_2 (ca lg) was vacuum distilled into an F.E.P.

tube, HF (10 mg) was also distilled in under vacuum and the

vapour phase spectrum, illustrated in Figure Al, obtained.

It was estimated that one tenth of the quantity of HF added

(i.e., 1 mg) would be detectable by this method.

Fig. A1

3900   3800 cm⁻¹
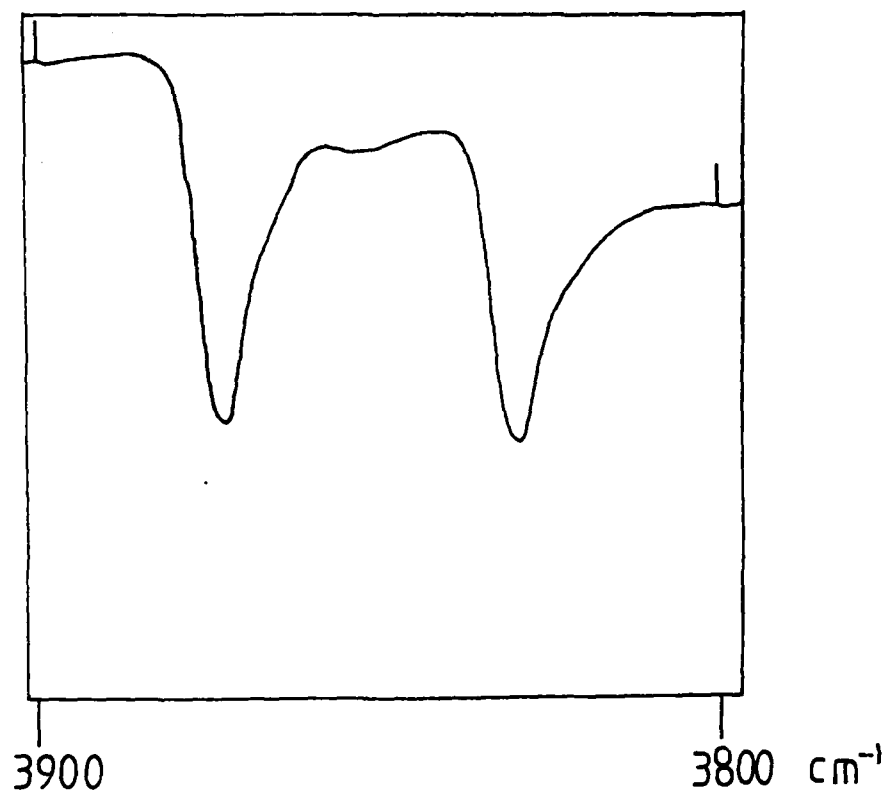
Vapour phase Infrared Spectrum of test
sample containing 1g HPO_2F_2 and 10 mg HF

APPENDIX B.   PREPARATIVE AND MANIPULATIVE TECHNIQUES

B.1.   Preparation of 100% HNO_3

The method and apparatus for the preparation of 100% nitric acid has been described previously.[B1]

B.2.   Purification of Dinitrogen Tetraoxide

The purification of commercial N_2O_4 was also reported earlier.[B1]

B.3.   The Preparation and Manipulation of HF and PF_5

Liquid hydrogen fluoride was obtained from Imperial Smelting Ltd.   The preparation of PF_5 and the vacuum frame used for the manipulation of HF and PF_5 have already been described.[B.2]

B.4.   Preparation of Uninhibited HDA

The preparation of HDA from HNO_3 and N_2O_4 has also been described.[B3]

B.5.   Preparation of Inhibited HDA

Solutions of PF_5 in HDA were prepared by the addition of a pre-calculated amount of PF_5 to the appropriate amount of HDA contained in an FEP reactor fitted with a Kel-F and Teflon valve (Figure B1).

The quantity of inhibitor was calculated by measuring the pressure of gas exerted in a known valume of the fluoroplastic vacuum frame.[B.4]

Fig. B1 Teflon PFA Reactor

Teflon PFA
Vessel
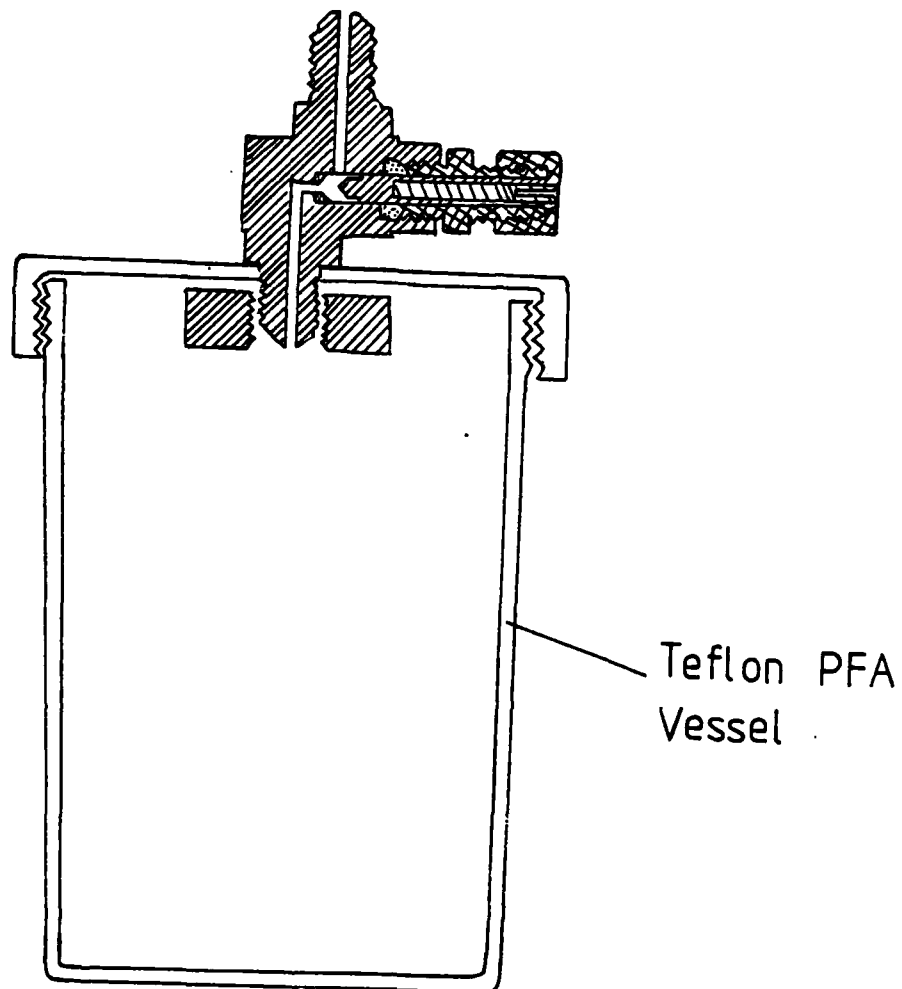
▨ .... Kel-F
▨ .... Teflon
▨ .... Brass
◪ .... Steel

Solutions of PF_5 and HF in HDA have also been prepared by a second method, which has been described previously.[B5]

B.6. Preparation of HPO_2F_2

Difluorophosphoric acid was prepared by the action of hydrofluoric acid on phosphoric anhydride according to the following equation:

$$P_4O_{10} + 6HF \longrightarrow 2HPO_2F_2 + 2H_2PO_3F.$$
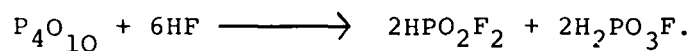
P_4O_{10} was placed in a pre-weighed PFA reactor (Figure B1) which was then reweighed. The required amount of HF was then vacuum distilled onto the P_4O_{10}. Difluorophosphoric acid was separated from involatile monofluorophosphoric acid by vacuum distillation (10^{-4} Torr). The absence of HF in the HPO_2F_2 samples prepared in this way was confirmed by vapour phase i.r. spectroscopy (see Appendix A.9).

The residual involatile monofluorophosphoric acid, prepared by this route, was shown by ^{31}P nmr spectroscopy to be always contaminated by a significant proportion of H_3PO_4.

B.7. Preparation of N_2O_5

The preparation of N_2O_5 has been described previously.[B5]

References, Appendix B

B.1. N. Logan, M.F.A. Dove, and J.W. Bailey, "Corrosion Chemistry in Inhibited HDA", Grant No. AFOSR-78-3717, Final Scientific Report 29th November 1979 (Interim Scientific Report under Grant No. AFOSR-78-3717A), p. 213.

B.2. Ref. B.1. p.214.

B.3. Ref. B.1. p.215

B.4. Ref. B.1. Fig.B3.

B.5. Ref. B.1. p.216

B.6. Ref. B.1. p.217

END

DATE
FILMED

10-81

DTIC

SUPPLEMENTARY

INFORMATION

FOREWORD

This report covers work sponsored by the Air Force Rocket Propulsion
Laboratory, Edwards Air Force Base, California under AFOSR Grant 78-3717.
The period of performance was September 1978 to September 1980. During
this period Lt J. Rendleman (LKCP) and Mr H. Martens (LKCP) were the
Project Managers for AFRPL. The AFRPL Job Order No. was 305810ED.

The work was performed at the University of Nottingham, Nottingham,
NG7 2RD, England under the direction of Drs Norman Logan and Michael
F. A. Dove.

This technical report is approved for release and distribution in
accordance with the distribution statement on the cover and on the
DD Form 1473.

H. H. MARTENS
Project Manager

FORREST S. FORBES, Chief
Propellant Systems Section

FOR THE DIRECTOR

EDWARD E. STEIN, Deputy Chief,
Liquid Rocket Division

DAT FILM